THE UNIVERSITY *of* EDINBURGH

Impacts of anthropogenic aerosols on air quality, climate, and extremes

Yong Zhao

(Also known as Alcide)

THE UNIVERSITY *of* EDINBURGH

Doctor of Philosophy

The University of Edinburgh

November 2019

Declaration

I declare that this thesis has been composed solely by myself and that it has not been submitted, in whole or in part, in any previous application for a degree. I confirm that all works presented here, including published papers and those in review for related journals, are entirely my own unless otherwise stated. I carried out all model experiments, performed all data analysis, produced all materials presented in each of the research chapters, and wrote the whole thesis, Dr David Stevenson and Dr Massimo Bollasina supervised the whole project, contributed to interpreting results, and provided comments on subsequent chapter revisions.

This thesis was submitted for examination on Friday, 19 July, followed by viva examination on Monday, 7 October, and was improved by incorporating suggestions/comments from my PhD examiners Dr Paul Palmer and Dr Nicolas Bellouin. The final version was produced on Monday, 4 November 2019.

November 2019

Abstract

Anthropogenic aerosols have significant impacts on global air quality and climate. However, there are still major uncertainties in our understanding of their characteristics and effects, particularly the mechanisms through which they influence the Earth's climate and the wider environment. Using simulations from the Community Earth System Model (CESM1) for the recent past and future, this thesis seeks to enhance our understanding of the multifaceted impacts of anthropogenic aerosols.

Time-slice model simulations for 1970 and 2010 indicate that once the present-day climate has fully responded to 1970-2010 changes in all forcings including greenhouse gases (GHGs), anthropogenic aerosols and ozone, both the global mean temperature and precipitation responses will be roughly double the transient ones. The temperature response per unit effective radiative forcing (ERF) for short-lived climate forcers (SLCFs) varies considerably across many factors, suggesting that the ERF should be used carefully to interpret the climate impacts of SLCFs. Changes in the probability distribution of global-mean daily precipitation are dominantly driven by GHG changes, but by aerosols when averaged regionally over Asia and Europe.

Next, the impacts of two major policy-relevant emission drivers of 1970-2010 aerosol changes, energy use growth and technology advances, are investigated. Energy use growth dominates the total aerosol changes and associated climate impacts, from and within Asia in particular. However, technology advances outweigh the impacts of energy use growth over Europe and North America. The temperature response per unit aerosol ERF varies significantly across many factors, including location and magnitude of aerosol-related emission changes, questioning again the utility and robustness of ERF, and related metrics, in interpreting climate change. The 1970-2010 changes in air pollution are driven predominately by anthropogenic emissions while climate change (i.e., changes in air pollutants attributable to changes in meteorologies driven by GHGs, solar radiation, etc.) also contributes. The overall changes in air pollution lead to an

extra 1.7 million deaths per year due to $PM_{2.5}$ and 87,000 yr^{-1} related to O_3, and losses of 166 million tons yr^{-1} of staple crop production with value 53 billion USD_{2010} yr^{-1}. The effects attributable to anthropogenic emissions reflect a "tug-of-war" between energy use growth and emission control measures, emphasizing the key role of policymaking in influencing global environmental wellbeing.

Aerosol-related emissions are expected to decline in the future; this may generate large impacts on climate extremes on top of modulating mean climate. This thesis thus makes use of transient model simulations under the Representative Concentration Pathway 8.5, and seeks to understand how future aerosol reductions will influence climate extremes, focusing particularly on heatwaves worldwide and precipitation extremes over Asia. Results show that there will be more severe heatwaves globally due primarily to mean warming, with minor contributions from future temperature variability changes. These changes are mainly associated with GHG increases, while aerosol reductions contribute significantly over the Northern Hemisphere (particularly Europe and China). Further, per unit of global surface warming, aerosol reductions, compared to GHG increases, induce a disproportionally stronger response in heatwave metrics via aerosol-cloud interactions. The Asian monsoon region will get progressively warmer and wetter as GHGs increase, while precipitation extremes will be significantly aggravated due to aerosol reductions. Such aggravations are driven by local-scale aerosol-cloud interactions over northern East Asia but by aerosol changes induced large-scale circulation anomalies over southern East and South Asia.

This thesis provides a comprehensive assessment of the impacts of aerosols on air quality, climate and extremes. These impacts, despite large uncertainties related to the representation of aerosols in climate models, are largely under the direct control of policy interventions, offering policymakers significant influence on future global habitability. The importance of aerosols in changing climate up to the present-day is very relevant for projections of future climate, and climate extremes and related risk management in particular.

The above findings shed light on, and provide motivation for, further studies aimed at reducing uncertainties in aerosol effects, and constraining aerosol processes in climate models for reliable future climate projections.

Lay Summary

Anthropogenic aerosols are small particles originating from human activities; they have important influences on global air quality and climate through a variety of complex processes. After decades of extensive studies, however, our understanding of the characteristics and impacts of aerosols are still incomplete. To improve air quality, it is expected that aerosols-related emissions are expected to reduce significantly during the 21st century worldwide. This highlights the urgency to improve our understanding of the impacts of changes in anthropogenic aerosols, to provide useful information for future climate projections and risk management.

The climate system evolves slowly (on decadal and even centennial scales) in response to emission changes, on top of the "instantaneous" response to the immediate emission changes. The transient response is a function of past changes in emissions (and how fast they changed, historically), as well as the most recent emissions. It is found that once the present-day climate has fully responded (after ~100 years) to 1970-2010 changes in greenhouse gases, anthropogenic aerosols and ozone, both the global mean temperature and precipitation responses will roughly double the ones estimated from transient model simulations. Aerosols are found to outweigh GHGs in modulating regional precipitation characteristics. Particularly, aerosol increases over Asia are shown to significantly suppress the frequency of heavy-to-extreme precipitations, while the picture is totally reversed over Europe where features aerosol reductions.

The two major policy-relevant emission drivers of 1970-2010 changes in aerosols, energy use growth and advances in emissions control technology, have significant impacts on global temperature and precipitation changes that compete with each other. Energy use plays a predominant role especially from and within Asia, while technology advances have larger impacts within regions such as Europe and North America. The 1970-2010 changes in air pollution have led to an extra 1.7 million yr^{-1} deaths related to global total $PM_{2.5}$ and 87,000yr^{-1} related to O_3, and losses of 166 million tons yr^{-1} in staple crop production, with a value of 53 billion

USD_{2010} yr^{-1}. These impacts are mainly related to anthropogenic emissions, while climate change also contributes in a minor way (less than 10%). The impacts related to anthropogenic emissions reflect a “tug-of-war” between energy use growth and pollution control measures. These indicate the importance of policymaking in controlling global air quality and hence habitability.

The impact of future aerosol reductions on heatwaves has been investigated using an existing large ensemble of model simulations. Results show that there will be more severe heatwaves primarily because of global warming, mainly associated with GHG increases. However, aerosol reductions have important influences, through interacting with clouds and radiation, and produce larger impacts compared to GHGs per unit of global surface warming. Also, the Asian monsoon region will become progressively warmer and wetter in the future as more GHGs are emitted, while precipitation extremes will be significantly worsened due to anthropogenic aerosol reductions. However, the dominant mechanisms are different between East Asia (through aerosol-cloud interactions) and South Asia (through changes in circulations).

In summary, this work provides a comprehensive assessment, and contributes to our knowledge, of the multifaceted impacts of anthropogenic aerosols on air quality, climate and extremes. Findings here may help inform future climate and environment strategies.

Acknowledgements

Finally comes the most exciting page which I reckon is the only piece most of you may read. It is, therefore, the best chance for me to dedicate my deep blame to all of you.

The supervisors

It was at 2 pm, 13 September 2016, I firstly met with David Stevenson. A gloomy, wet and windy day, just as Edinburgh normally is. I knocked David's door, nervously, awkwardly, and in panic, so the journey started. I got severe rashes on my face which was bloody red, hot and painful at that time, for which I must condemn the air quality in Edinburgh. I am sure I said Python when David asked me what programming language I use, but it took him minutes to understand I was saying it. That was my first English lesson from a native English speaker. Since then, David's patience and kindness have been constantly surprising me, and God knows how annoying I have been over the past three years. His wisdom led me through countless barriers and dilemmas, eventually to where I am now. He wrote in my annual report "*Alcide reminds me of what Claudio Ranieri said about N'golo Kante 'It's like having an extra player on the pitch*'". I printed it out, and pasted onto my bedroom door – it will company me for good. I am certain I will very soon forget all our meetings, discussions, sciences, arguments, laughter, etc. However, there are things I learnt from David that are life-long beneficial: to be kind, to be serious, to be patient, and to be fast in a slow way. I do not feel the word thanks is of any help here.

Massimo Bollasina, energetic, enthusiastic, humorous, generous and smart, made the pathway of my PhD so much fun. I must admit that, during the first few weeks of my study, I struggled to understand his accent, and I am sure he struggled much much more than I did in the same sense. Time flies, and we now make jokes about many things including English. Massimo ported the

Community Earth System Model onto the UK computer ARCHER, for which I blame him since my whole PhD thesis, so and all the substantial pains, originates from that. Also, it was Massimo who pointed me to many places and scientists worldwide to suffer from the feeling that I know nothing. Massimo to me is like a bridge towards possibilities; I hesitated, worrying about uncertainties (not as much as those related to aerosols), but thrilled the second I realise how much more amazing the other side(s) of the bridge is than I have ever imagined. He, and David, care for my life career much more than I really do, and I owe them my deep gratitude. His supervision and care, are quite precious to me, with the meaning of the English word “quite” from a Chinese dictionary.

The mothers

I very much like a line from the English drama series “Downtown *Abbey*” about mother “*She has been an important figure in my life, but I do not agree with her about everything*”.

I was raised up by my grandma and we lived together till I was 12. She is the kind that cannot be more ordinary, but is indeed the person I respect and love the most in the world. The day I told her I was going to the UK for maybe years, she tried her best to be calm, yet it was not difficult for me to see through her fears, as I know exactly all the griefs she has been through. My grandma, for me, is more than blood, but the most precious gift I have ever got.

My mama, for many reasons, was completely absent from my life until the first time I met her when I was 12. The thing I love her the most, and hate her in the same sense, is that she never tempts to make any decisions for me. She seems to stubbornly believe that her son was able to properly manage everything without interventions from others. It is her philosophy of parenting that fostered my independence and asociality in an extreme manner, and she owes me for this.

The reader

The title has nothing to do with the book “*The Reader*” by Bernhard Schlink.

During the past 34 months, I read (and listened to) around 50 books (mostly novels, biographies and history), on the train, in the airport, at Pleasance gym, before bed, and after a whole day of fighting with my keyboard. Wherever I go, there always is a book in my backpack. Wherever I visit, purchasing one book from a local bookstore is a must. Thank the reader, with his strong will and persistence, who makes the PhD life much thicker.

As Alan Bennett said in the movie "*The History Boys*": "*The best moments of reading are, when you come across with something that you would thought special, particular to you, while here it is, set down by someone else. And, it is as if a hand has come out and taken yours*". To me, it is like meeting a bunch of old friends and then waving them away. And, when you ask if they will come back again, you know yourself they would say yes and no.

The endless thanks

Ever since I began to write this thesis, I started to work on the list of names that should appear here. The list, not Arya Stark's kind of course, ended up too long to be appropriately presented. As such, I decide not to mention any of them here, but extend my deep appreciation to all of you, from all walks of my life, who played critical roles in prolonging all my sufferings through your unconditional help, support, encouragement, and trust whenever I need. Also, I would like to thank all the training, conferences, workshops, etc. for their financial support and opportunities that forced me to open my mouth, ears and eyes widely.

Now, before pencil down and the light through, a massive and endless thank you to all.

@ Desk 25, Crew Attic, The King's Buildings, Edinburgh

Thursday, 18 July 2019

List of Figures

List of Tables

Acronym and Abbreviations

AOD	Aerosol Optical Depth
AMR	Asian monsoon region
APHRODITE	Asian Precipitation Highly-Resolved Observational Data Integration Towards Evaluation
AR5	Fifth Assessment Report of the Intergovernmental Panel on Climate Change
BC	Black carbon
CAM	Community Atmosphere Model
CAMS	Copernicus Atmosphere Monitoring Service
CAM5-Chem	CAM5 with full chemistry scheme
CCN	Cloud condensation nuclei
CDER	Cloud droplet effective radius
CDNC	Cloud droplet number concentration
CLWP	Column-integrated cloud liquid water path
CESM	Community Earth System Model
CMIP5	Phase 5 of the Coupled Model Intercomparison Project
CWD	Consecutive wet days
EA	East Asia
ECMWF	European Centre for Medium-Range Weather Forecasts
EDGAR	Emissions Database for Global Atmospheric Research
ERF	Effective radiative forcing
ETCDCI	Expert Team on Climate Change Detection and Indices
FAO	Food and Agriculture Organization of the United Nations
GAEZ	Global Agro-Ecological Zones
GHG	Greenhouse gas
GPCC	Global Precipitation Climatology Center
IPCC	Intergovernmental Panel on Climate Change
ITCZ	Intertropical Convergence Zone
JJA	June-July-August
LENS	The CESM1 large ensemble project

LWCF	Longwave cloud forcing
MAM	Modal Aerosol Module
MDA8	Daily maxima of rolling 8-hour averages ozone concentration
MOZART-4	Version 4 of the Model of Ozone and Related chemical Tracers
NCAR	National Center for Atmospheric Research
NMVOCs	Non-methane volatile organic compounds
OC	Organic carbon
OH	Radical hydroxyl
PDF	Probability distribution function
$PM_{2.5}$	Particles with an aerodynamic diameter smaller than 2.5 μm
R10	Frequency of precipitation greater than 10 mm day^{-1}
R95P	Total of precipitation amount above the 95^{th} percentile
RCP8.5	Representative Concentration Pathway (RCP) 8.5
RCP8.5_FixA	RCP8.5 with aerosol fixed at 2005 levels
RX5DAY	The maximum amount of consecutive 5-day precipitation
SA	South Asia
SAT	Surface air temperature
SLCFs	Short-lived climate forcers
SFND	Southern-Flood-Northern-Drought
SOA	Secondary organic aerosol
SREX	Special Report on Managing the Risks of Extreme Events and Disasters to Advance Climate Change Adaptation
SWCF	Shortwave cloud forcing
SWCST	Clear-sky shortwave radiation at top-of-the-atmosphere
TOA	Top-of-the-atmosphere
TX	Daily maximum temperature
TX95P	The 95^{th} percentile of 1961-1990 TX
TN	Daily minimum temperature
TN95P	The 95^{th} percentile of 1961-1990 TN
VOCs	Volatile organic compounds
WACCM	The Whole Atmosphere Community Climate Model

Contents

Chapter 1 Introduction

1.1 Motivation

In order to improve air quality, emissions of anthropogenic aerosols and their precursor gases are expected to be significantly reduced worldwide in the coming decades. Aerosol reductions, however, may result in detrimental climate impacts, such as warming and exacerbating the severity and impact of climate extremes (Xu et al., 2015; Wang et al., 2016b; Samset et al., 2018). A number of future emission pathways have been developed to seek a compromise between air pollution impacts and climate outcomes in near-, medium-, and long-term (Gidden et al., 2018). However, it remains challenging to reliably project future climate changes under equally plausible future emission pathways because of our limited understanding of many aspects of the Earth System. One of the major challenges is associated with aerosols. Among all factors that influence the climate, very few are as complex as aerosols (Rosenfeld et al., 2014a; Fan et al., 2016). Aerosols remain the dominant uncertainty in our current estimates of radiative forcing of climate change (Myhre et al., 2013). Meanwhile, there are still large uncertainties (both spatially and temporally) in our understanding of both historical anthropogenic aerosol (and aerosol precursor) emissions and those under future emission pathways (Gidden et al., 2018). All the above adds urgency to reducing uncertainties associated with aerosol-related emissions and their impacts, and one of the pressing issues is to understand the major drivers and impacts of past aerosol changes. Moreover, compared to their impacts on mean climate change, it is more important to focus on changes in climate extremes as these are what really affects environmental habitability.

1.2 Atmospheric aerosols

The strict definition of 'an aerosol' is a colloidal mixture of gas and liquid/solid particles. However, it has become common to refer to the particles themselves as aerosols. Specifically, aerosols are liquid, solid or mixed-phase of particles in the air, with their sizes ranging from a few nanometres to tens of micrometres.

1.2.1 Emissions

Aerosols can come from direct emissions (termed as the primary sources). For example, wind-driven emissions of sea spray aerosols and mineral dust, as well as fossil fuel and biomass combustion produced emissions of black (BC) and organic carbon (OC) particles. Aerosol can also form through a variety of physical and chemical processes. For example, sulphate (SO_4) is one of the most important present-day anthropogenic aerosol species. It comes primarily from sulphur-containing precursor gases (e.g., sulphur dioxide (SO_2) and dimethyl sulphide (DMS)) that are oxidised by hydroxyl radical (OH), as well as by dissolved hydrogen peroxide (H_2O_2) and ozone (O_3) within cloud water droplets that can later evaporate to leave SO_4 aerosol (Jacob, 1999).

According to sources, aerosols are classified into natural and anthropogenic groups. Major natural sources include the ocean (sea-spray aerosols and DMS), soil (mineral dust), vegetation, natural wildfires, and volcanoes. Anthropogenic sources represent emissions related to human activities. For example, combustion of fossil fuel (e.g., coal, oil, and gas), biofuels (plant biomass and animal wastes) and other fuels such as peat, as well as anthropogenic (i.e., related to, or induced by, human activities) fires (Chin,

2009). Figure 1.1 shows a portrait of global aerosol distributions by types. It can be seen that the total atmospheric aerosol loading is dominated by natural sources at the global scale (Li et al., 2016). However, human activities have been contributing significantly to changes in atmospheric aerosols since the industrial revolution. For example, changes in SO_4 from power generation, as well as BC and OC from vehicle traffic (North et al., 2014).

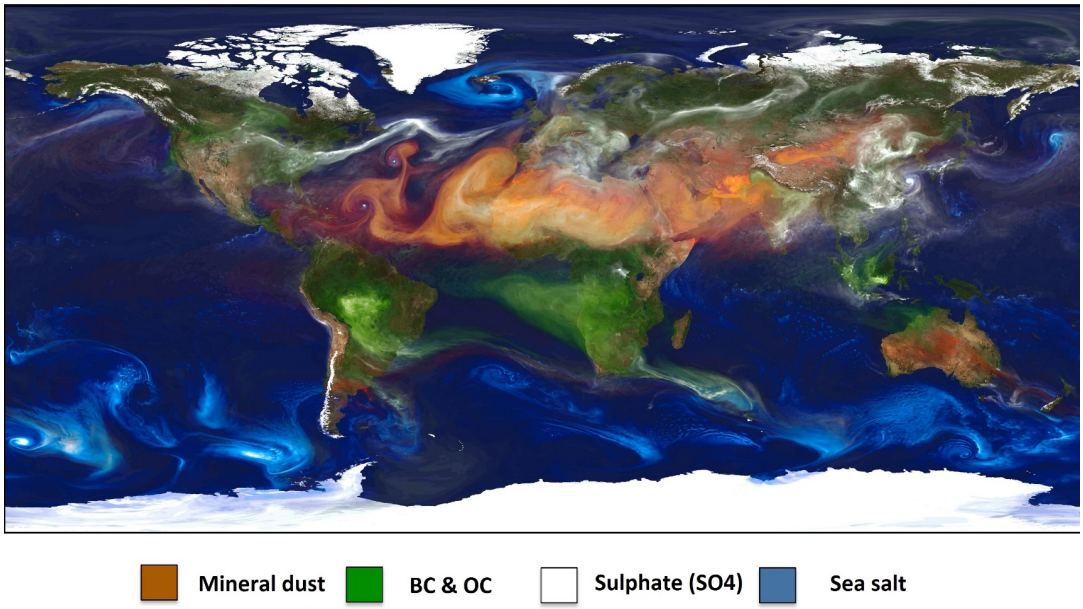

Figure 1.1 Portrait of global aerosols by species: winds-driven mineral dust (red) and sea salt (blue), black carbon and organic carbon (BC & OC; green) from fires, as well as sulphate (SO_4) aerosols (white) from volcanoes and anthropogenic emissions. The figure is taken from https://www.nasa.gov/multimedia/imagegallery/image_feature_2393.html. Data are produced by the Goddard Earth Observing System Model, Version 5 (GEOS-5) at a 10-km resolution.

Before the industrial revolution, anthropogenic aerosols came predominantly from residential biomass burning and agricultural sectors worldwide. Since around 1850, along with industrialization induced rapid increases in CO_2 emissions (Figure 1.2a), anthropogenic aerosol/precursor emissions from power generation, industry, and transportation sectors also increased rapidly (Hoesly et al., 2018). For example, the global total emission of SO_2 (Figure

1.2b) increased by a factor of 60 from 1850 to 1970 (Lamarque et al., 2010; Smith et al., 2011).

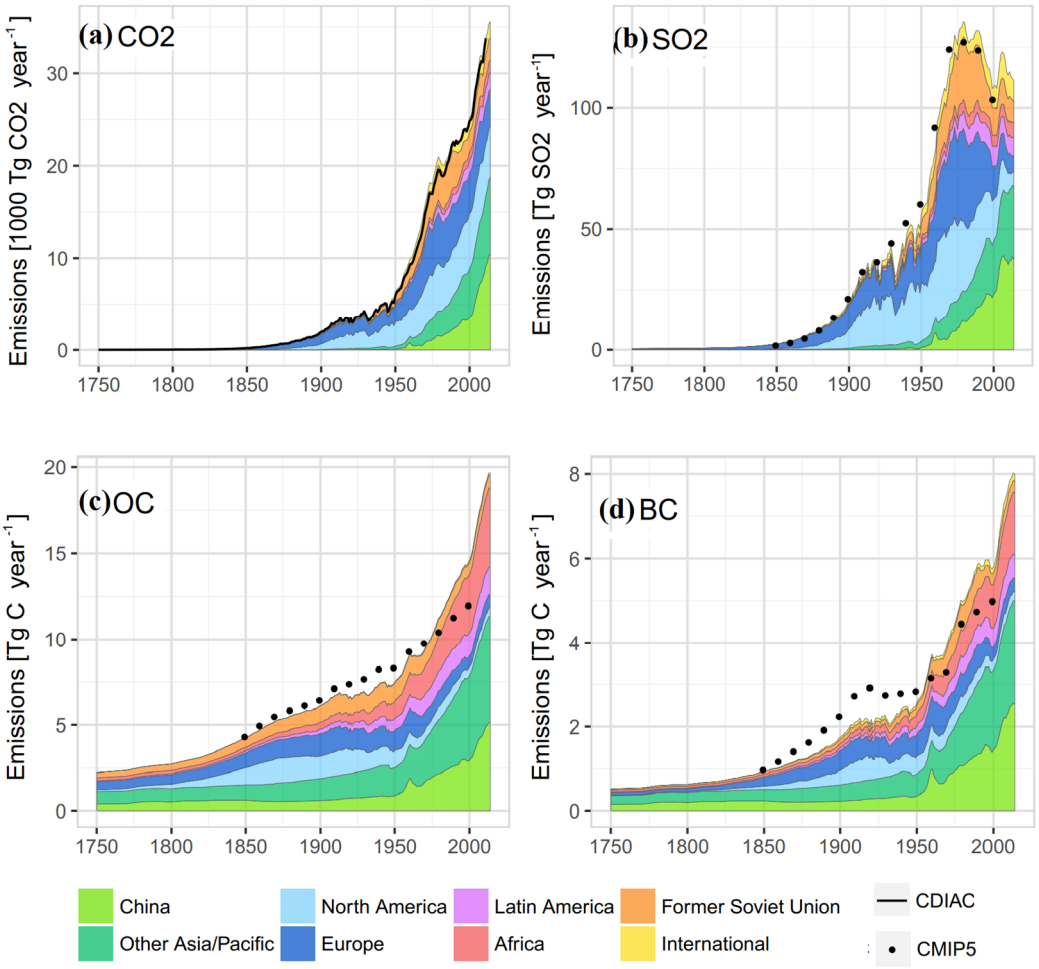

Figure 1.2 The Community Emissions Data System (CEDS) 1750–2014 anthropogenic emission trends of (a) CO_2, (b) SO_2, (c) OC and (d) BC; these values do not include aviation or agricultural waste burning on fields. The "International" region shows international shipping emissions. The dotted lines represent Phase 5 of the Coupled model intercomparison project (CMIP5) estimations. The black line in (a) denotes historical CO_2 emission from the Carbon Dioxide Information Analysis Center (CDIAC). Figures adapted from Hoesly et al. (2018).

While Asia is currently the dominant emission source of air pollutants worldwide, Europe and North America were the primary emission sources for more than a century since the industrial revolution (Lamarque et al., 2010; Smith et al., 2011). The first continental air quality directive was implemented in Europe in 1970 (Crippa et al., 2016), while country-level air quality acts have

been introduced even earlier (the mid-1960s; Auliciems and Burton (1973)). Since then legislation has been gradually introduced in industrialized regions (Europe and North America, and also Japan) aimed at reducing the impacts of acid rain and air pollution (Crippa et al., 2016). Subsequently, air pollutant emissions followed contrasting trends between developed and developing countries during the past few decades (1970-2010). For example, SO_2 emissions from developing countries (e.g., China and India; Figure 1.2b) increased steadily since the 1950s while emissions from developed regions started to decline after around 1970 (Smith et al., 2011). Only after about 2010 have some developing countries started to take pollution mitigation measures. For instance, Chinese SO_2 emissions have shown noticeable declining trend since about 2012 (Silver et al., 2018; Wang et al., 2018a; Zheng et al., 2018). As a consequence, India was recently reported to have overtaken China as the largest present-day emitter of SO_2 (Li et al., 2017). Along with changes in global anthropogenic SO_2 emissions, global OC (Figure 1.2c) and BC (Figure 1.2d)) have followed continuous increasing trends even after the 1970s, because of continued residential emissions driven by the growth of rural populations in Africa and Asia (Hoesly et al., 2018).

1.2.2 Chemical, physical and optical properties

Aerosol particles are an important part of the Earth's radiative budget, and their physical and chemical properties are key factors that determine their optical properties and climate effects (see Section 1.2.4). In order to simplify their chemical characteristics in models, aerosols are grouped by types (mineral dust, sea-salt, SO_4, BC, OC and nitrate; Section 1.2.1). Also, the concept of mixing is used to further describe the chemical properties of aerosol particles.

Specifically, it is called externally mixed when particles are chemically pure and the mixture is comprised of particles of different chemical compositions. By comparison, it is called internally-mixed when different chemical compositions are mixed within each particle (Lesins et al., 2002). The chemical composition and state of aerosol particles (solid or liquid) determine their hygroscopicity (ability to grow in size as ambient relative humidity increases), optical properties, mixing states, as well as their ability to act as cloud condensation nuclei (CCN; small particles on which water vapour condensate) and ice nuclei (Chin, 2009).

In general, size (the geometric radius of the particle) is the most important physical property of aerosol particles, because many other characteristics (surface area, volume, and mass) are related to it. However, aerosols' size can span several orders of magnitude with complex morphologies, making it difficult to be explicitly described. Also, aerosols' size can change with the hygroscopic growth process, which is particularly important for soluble species such as sulphate species. Therefore, it is useful to characterize aerosols' size distributions by the so-called aerosol modes (Figure 1.3). They are: the nucleation mode (with a radius of <0.01 μm), Aitken mode (0.01-0.1 μm), accumulation mode (0.1-1 μm), coarse mode (1-10 μm) and the giant particles (> 10 μm) (Lohmann et al., 2016). Aerosol numbers, surface and volume can thus be described with size distribution functions.

The optical properties of aerosols can be quantified by refractive index (a unitless index describing the speed that the light travels through the material) together with their sizes and shapes. The refractive index depends on the chemical composition of aerosols, and is usually approximated based on the

properties and concentrations of different compositions in the case of internally-mixing. Note that aerosol optical properties depend on the radiation wavelength (Eck et al., 1999). The optical properties of spherical aerosol particles can be described by the Mie-theory (Hergert and Wriedt, 2012). For a population of aerosol particles, optical properties are usually integrated over the size distribution. For example, the Aerosol Optical Depth (AOD), defined as the integrated extinction coefficient (scattering plus absorption) over a vertical column of unit cross-section, is commonly used to measure the degree to which aerosols prevent the transmission of light by absorption or scattering of light (Equation 1.1):

$$L=L_0*e^{-AOD}, \quad (1.1)$$

where L is the transmitted radiation, and L_0 incident radiation.

1.2.3 Atmospheric processes

Once emitted, aerosol particles may undergo a series of processes (Figure 1.3) that determine their atmospheric lifetimes, and change their physical and chemical properties. Important processes include aerosol production (formation and growth), transport, and removal. The production processes include nucleation (transformation from gas-phase molecules to aerosol nucleus), condensation (compounds condense onto the surface of pre-existing particles), coagulation (aerosol particles agglomerate together to form larger particles), as well as in-cloud production (release of soluble species from cloud and rain droplets by evaporation). Aerosols are removed primarily by wet deposition (processes in which atmospheric chemicals are accumulated in the rain, snow, or fog droplets, and are subsequently deposited onto Earth's

surface) including in-cloud (during the formation of precipitation) and below-cloud (because of the downward flux of precipitating water) scavenging processes. Dry deposition (processes in which atmospheric compositions are deposited onto the Earth's surface through such processes as settling, impaction, and adsorption) is also important for regions with little precipitation. Smaller aerosols can be deposited to the surface by turbulent fluxes, while larger aerosols can be removed quickly from the atmosphere by sedimentation. Finally, aerosols can be transported by advection and convection processes, which are important to explain their spatial distributions and radiative forcing (Chin, 2009; Lohmann et al., 2016; Seinfeld and Pandis, 2016).

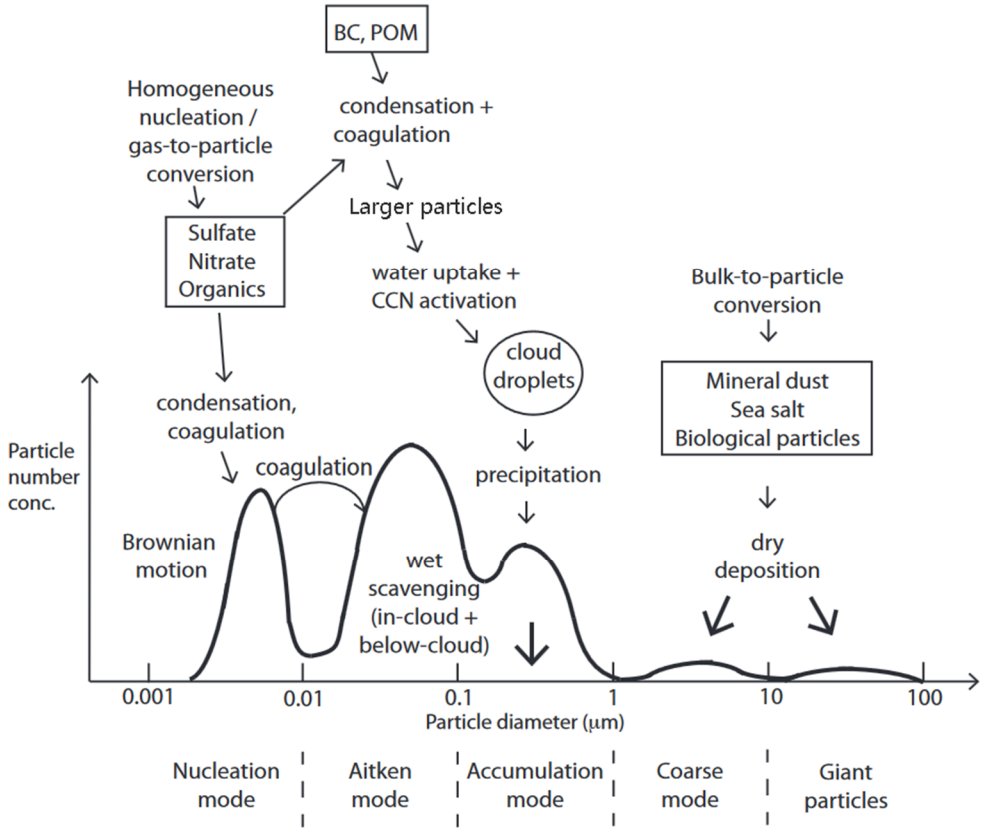

Figure 1.3 Schematic of aerosol modes, and major aerosol processes as a function of size. The figure is taken from Jacob (1999).

New particles formed through nucleation have very small sizes, and are hence negligible in mass compared to the rest of the distribution spectrum (Figure 1.3), whereas their numbers can be huge and can even dominate the total number concentration. Collisions between particles typically result in coagulation that effectively shifts the aerosol-size spectrum towards larger particle sizes. This occurs mostly between small particles and larger ones (i.e., typically between the Nucleation and Aitken mode, as reflected by the dip between the two modes in Figure 1.3). Therefore, it can be viewed as a major process of removing particles within the nucleation and Aitken modes. New particles may avoid coagulation rapidly and travel beyond their source regions, condensing semi-volatile or reactive vapours (e.g., H_2SO_4, organics, HNO_3, and NH_3), and grow in sizes. Particles in the accumulation mode -- resulting from primary emissions, condensation of secondary sulphates, nitrates, and organics from the gas phase, and coagulation of smaller particles -- can absorb water vapour under favourable conditions (e.g., supersaturated environments), leading their mass to increase by a few factors and form cloud droplets. Consequently, they can be removed through wet scavenging processes and precipitation (Figure 1.3). Finally, particles in the coarse mode are usually produced by mechanical processes, such as wind or erosion (dust, sea salt, pollens, etc.), and are mainly removed through dry deposition (Figure 1.3).

1.2.4 Radiative forcing and climate

Aerosols can perturb the Earth's radiative budget (the balance between the energy that the Earth receives from the Sun and the energy the Earth radiates back into outer space) and therefore influence climate, by directly scattering or

absorbing solar (and, to a much lesser extent, terrestrial) radiation, as well as associated rapid adjustments of the atmosphere (aerosol-radiation interactions; Figure 1.4a; Haywood and Ramaswamy (1998)). Also, by acting as CCN and ice nuclei, aerosols modify cloud microphysical properties (aerosol-cloud interactions; Figure 1.4b) and therefore influence precipitation through complex mechanisms (Boucher et al., 2013; Polson et al., 2014; Fan et al., 2016; Lohmann et al., 2016). The aerosol-cloud interactions can be further divided into the cloud albedo effect and lifetime effect (Figure 1.4b). The albedo effect is also called the Twomey effect: assuming that the cloud cover water content is fixed, a higher concentration of cloud-active aerosols would lead to increase in the concentration but decrease in the average size of cloud droplets. Consequently, the total scattering cross-section and hence cloud albedo may increase (Twomey, 1977). The lifetime effect refers to the mechanism that by increasing CCN and subsequently changing the size and number concentration of cloud droplets, clouds may live longer, since that smaller particles are removed more slowly and the processes of coalescence into raindrop take longer. However, the evaporation of rain droplets may also be reinforced. As a result, clouds may persist longer or shorter than if aerosols were not present. That is, the magnitude and sign of the aerosol lifetime effects may vary, which is so far still less understood (Albrecht, 1989). Further, absorbing aerosols embedded in (or near) a cloud layer heat that layer and promote cloud evaporation; this effect may be enhanced as cloud loss may reinforce the absorbing effect of BC (Koch and Del Genio, 2010), resulting in “burn off” of the clouds (the semi-direct effect) and hence perturb the thermal structure of the atmosphere through heating the layers where they reside (Koch and Del Genio, 2010).

Overall, aerosols cause a net cooling of the Earth; almost a third of the warming from increases in GHGs is thought to have been counteracted by cooling due to increased anthropogenic aerosols since the 1950s (Stocker et al., 2013). This is well-established as the aerosol dimming effects. However, the fraction of cooling is uncertain, and hence the source of climate uncertainty associated with aerosols. Also, it is challenging to link the time evolution of aerosol changes to that of temperature, since there are also many other factors (e.g., the variability of the ocean and sun) taking effects.

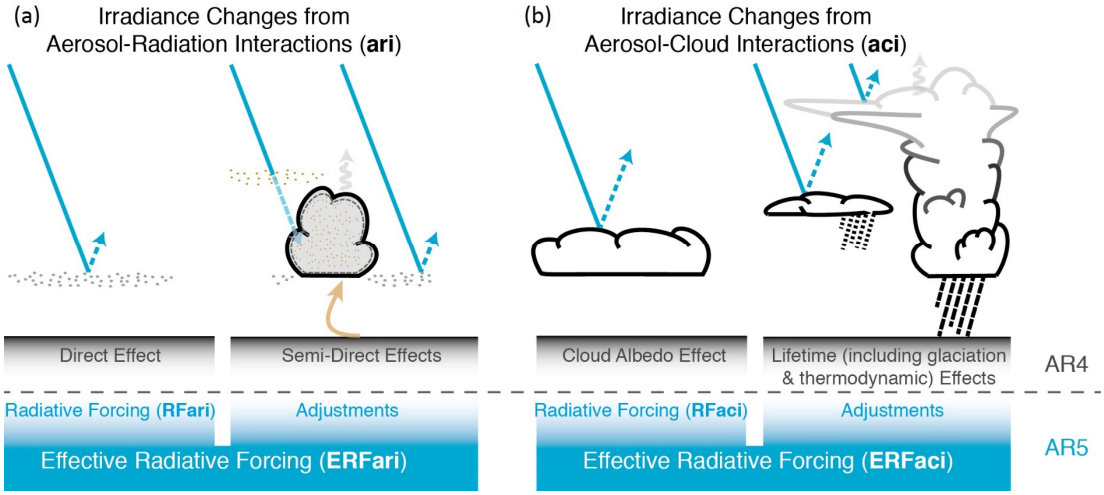

Figure 1.4 Schematic of (a) aerosol-radiation interaction, and (b) aerosol-cloud interaction. Blue arrows for solar radiation, grey arrows for terrestrial radiation, and the brown arrow for surface-cloud layer coupling. The black and blue labels at the bottom refer to the terminologies used in the fourth (AR4) and fifth (AR5) Assessment Report of the Intergovernmental Panel on Climate Change (IPCC). The figure is taken from Boucher et al. (2013).

The surface cooling due to the extinction of solar flux by aerosols, coupled with the heating of the atmosphere by elevated absorbing aerosols (notably BC), can perturb atmospheric stability. Also, as described above, aerosols may modify cloud microphysics (Andreae and Rosenfeld, 2008). All these changes may modulate precipitation (Rosenfeld et al., 2014b). However, the sign and magnitude of aerosol-cloud-precipitation interaction can vary substantially depending on emission locations, aerosol types as well as meteorological

conditions (Rosenfeld et al., 2008; Stevens and Feingold, 2009; Yu et al., 2014; Malavelle et al., 2017; Kasoar et al., 2018). Besides, the subsequent effects on regional to large scale dynamics and thermodynamics can lead to adjustments in regional climate systems. For example, the shift of the intertropical convergence zone (ITCZ) (Allen and Sherwood, 2011; Hwang et al., 2013; Acosta Navarro et al., 2017; Liu et al., 2018), as well as the weakening of the Asia monsoon (Bollasina et al., 2011; Liu et al., 2019).

The recent Precipitation Driver and Response Model Intercomparison Project (PDRMIP; Myhre et al. (2017b)) represents important progress in our understanding of the aerosol radiative forcing and climate impacts. Some of the important findings: the fast (time scale of months) response of the global mean precipitation to aerosol changes scales closely with the atmospheric energy absorption due directly to the forcing agent, while the slow response scales with the long-term change in global surface temperature (Samset et al., 2016). Also, it was found that sulphate aerosols from Asia, compared those from Europe, have stronger impacts on global temperature and precipitation changes. However, the picture reverses when the responses are normalized by unit radiative forcing or aerosol burden changes, Regionally, Asian aerosols are found to have larger impacts in modulating precipitation compared to European aerosols over corresponding local regions (Liu et al., 2018). Overall, the regional impacts of aerosols can be very different from their global impacts, and the impacts vary significantly across aerosol species, the region of forcing, as well as climate models (Samset et al., 2016; Stjern et al., 2017; Liu et al., 2018). However, note these conclusions are not without caveats, since that

the aerosol perturbations in these model experiments are scaled in an extreme/ arbitrary manner in order to maximise the signal-to-noise ratio.

Despite the above described extensive studies in the last decade that has made significant progress in our understanding of aerosols (Ming and Ramaswamy, 2009; Shindell and Faluvegi, 2009; Allen and Sherwood, 2011; Bollasina et al., 2011; Ming and Ramaswamy, 2011; Ming et al., 2011; Boucher et al., 2013; Hwang et al., 2013; Wilcox et al., 2013; Xie et al., 2013; Shindell, 2014; Wang et al., 2015), there are still large uncertainties associated with the impacts of aerosols on climate (Carslaw et al., 2013; Fan et al., 2016; Lee et al., 2016; Fletcher et al., 2018). In fact, aerosols remain the largest uncertainty in the radiative forcing on climate since the preindustrial era (Boucher et al., 2013). For example, the Intergovernmental Panel on Climate Change (IPCC) Fifth Assessment Report (AR5) estimates a 1750-2011 aerosol effective radiative forcing (ERF, defined as changes in energy flux at the top-of-the-atmosphere, taking effects of both the stratospheric and tropospheric rapid adjustments, due to a change in a component external to the climate system,) of -0.9 W m^{-2}, but with a large uncertainty range from -1.9 to -0.1 W m^{-2} (Myhre et al., 2013). This is because of their compounding uncertainties associated with the large spatial and temporal variability of aerosols, their short lifetimes, their diverse physical and chemical properties, and complex interactions that take place with radiation and microphysical processes (Boucher et al., 2013; Fan et al., 2016). These uncertainties lead to diverging aerosol schemes in present generation climate models, and thereby making aerosols one of the largest uncertainties in future climate projections.

1.3 Aerosol and ozone pollution

1.3.1 Tropospheric ozone and chemistry

O_3 is present in the troposphere and stratosphere, with 85-95% found in the latter. It is a radioactively active gas that interacts with shortwave and longwave radiation, and therefore is an important part of the radiative forcing of climate change (Forster et al., 2007; Gunnar Myhre et al., 2017). The amount of O_3 in the atmosphere (i.e., the O_3 budget) is determined by the rates of O_3 production and loss (chemical destruction and dry deposition to the Earth's surface). Stratospheric O_3 is produced primarily through molecular oxygen photolysis, while tropospheric O_3 is produced through very complicated ways (Fowler et al., 2008).

Tropospheric O_3 is thought to have increased significantly since the pre-industrial era, and have a greenhouse gas effect on the Earth's climate (Godin‐Beekmann, 2016; Checa‐Garcia et al., 2018). It is produced mainly through sunlight driven chemical reactions between NO_X, CO, VOCs and many other more complex compounds (Fowler et al., 2008; Stevenson et al., 2013), while downward transport from the stratosphere is also an important source (Hsu and Prather, 2009). It is removed through both chemical destructions and dry depositions to the surface (mainly to vegetation), while the latter remains poorly understood (Monks et al., 2015; Gaudel et al., 2018). Below is a brief introduction to tropospheric O_3 chemistry. For more details, please refer to (Godin‐Beekmann, 2016; Seinfeld and Pandis, 2016; Gaudel et al., 2018).

The free radical immediate (O('D)), mainly formed through O_3 photolysis (Eq. 1.2), is key in the reaction cycles of O_3 production and destruction. O('D) is

electronically-excited oxygen atom and can react with water vapour (Eq. 1.3) to form hydroxyl radical (OH), or reform O_3 (Eq. 1.4) following collision with an inert molecule (denoted as "M").

$$O_3 + \lambda\nu \rightarrow O(\text{'D}) + O_2 \quad (1.2)$$

$$O(\text{'D}) + H_2O \rightarrow OH + OH \quad (1.3)$$

$$O(\text{'D}) + M \rightarrow O(^3P) + M \quad (1.4)$$

$$O(^3P) + M + O_2 \rightarrow O_3 + M \quad (1.5)$$

Tropospheric O_3 photochemical production occurs through OH oxidation of CO, CH_4 and non-methane hydrocarbons (generally referred to as NMHC) in the presence of NOx. Ozone production from long-lived hydrocarbons (e.g., CH_4) is greatest in the tropical lower troposphere, where OH radical concentrations are high (Fiore et al., 2008). When NOx are present (e.g., in continental regions and parts of the free troposphere) in sunlight, O_3 formation occurs as NO_2 being oxidised at wavelengths <424 nm (Eq. 1.6-1.7). Once formed, O_3 reacts with NO to regenerate NO_2 (Eq. 1.8).

$$NO_2 + \lambda\nu \rightarrow NO + O\ (^3P) \quad (1.6)$$

$$O\ (^3P) + O_2 + M \rightarrow O_3 + M \quad (1.7)$$

$$O_3 + NO \rightarrow NO_2 + O_2 \quad (1.8)$$

In the remote troposphere, O_3 formation is sustained by CO and CH_4 oxidisation through reacting with OH. In the urban and regional atmosphere, O_3 formation is mainly through oxidisation of short-lived VOCs. The largest Chemical destruction of ozone occurs in the lower troposphere where has abundant water vapour, as well as in highly polluted regions where the high NO concentrations remove O_3 directly (Eq. 1.8). Also, Localised halogen

catalysed O_3 destruction may influence surface ozone in polar regions during the springtime (Fowler et al., 2008).

1.3.2 Socioeconomic impacts of aerosol and ozone pollution

In addition to their climate impacts, short-lived (having a lifetime less than a few years, and effectively less than a few months) air pollutants (typically aerosols and ozone, and their precursor gases) also have detrimental impacts on atmospheric visibility, human health and ecosystems.

Epidemiological studies demonstrate that both short-term and long-term exposure to particulate matter (particularly that with a diameter less than 2.5 μm, $PM_{2.5}$) and O_3 are associated with elevated premature mortality which is a measure of unfulfilled life expectancy (Death that occurs before the average age of death in a certain population) (Jerrett et al., 2009; Lepeule et al., 2012). Several recent studies (Anenberg et al., 2010; Fiore et al., 2012; Silva et al., 2013; Lelieveld et al., 2015; Silva et al., 2016b; Cohen et al., 2017; Kinney, 2018; Liang et al., 2018), including the 2015 Global Burden of Disease (Cohen et al., 2017), estimate 3-5 million annual premature deaths related to preindustrial to present-day changes in $PM_{2.5}$, and 0.2-0.7 million related to O_3 exposure. The elevated mortality is shown to be related to both anthropogenic emission and climate change that modulate air pollution (Silva et al., 2016b; Silva et al., 2017; Chowdhury et al., 2018; Markandya et al., 2018). A few studies have assessed the avoided deaths accrued from air quality improvements over Europe (Turnock et al., 2016; Carnell et al., 2019) and North America (Zhang et al., 2018). However, the relative contributions of the above described policy-relevant emission drivers to changes in global and

regional air pollution and the resultant impacts on human health are not well understood.

Alongside its impacts on human health, exposure to O_3 has long been recognized to damage vegetation because of its phytotoxicity, with many studies showing that O_3 presents serious threats to crop productivity, food security and forests (Ellingsen et al., 2008; Avnery et al., 2011; Deryng et al., 2014; Ainsworth, 2017; Emberson et al., 2018; Schiferl and Heald, 2018; Solazzo et al., 2018). Globally, exposure to O_3 pollution (both chronic exposure during growing seasons and acute stress above a threshold of 100 ppb) is estimated to result in a yield loss of 4–15% for wheat, 5–15% for soybean, 3–4% for rice, and 2–5% for maize (Ainsworth, 2017). Note that due to the absence of worldwide observational data, these estimates rely on modelled ozone fields and empirically derived exposure-response functions (Betzelberger et al., 2010). It is projected that global population will continue to increase over the next few decades (Lamarque et al., 2011; Gidden et al., 2018). Also, driven by variations in precursor gas (methane in particular) emissions and stratospheric influxes, tropospheric ozone may change, with large uncertainty spread, over the 21st century as well (Lamarque et al., 2011; Young et al., 2013). All the above pose great risks to future food security worldwide, but with very large uncertainties. Therefore, it is vital to quantify the major drivers of O_3 pollution and their impacts on crop production, in order to provide effective suggestions for future air quality and agriculture strategies (Schiferl and Heald, 2018).

1.4 Climate extremes

1.4.1 Definition and changes

The Special Report on Managing the Risks of Extreme Events and Disasters to Advance Climate Change Adaptation (SREX) of the IPCC defines climate extremes as climate or weather events exceeding certain thresholds near the upper (or lower) end of the range of observations (Field et al., 2012). The Fifth Assessment Report (AR5) of the IPCC concluded that “warming of the climate system is unequivocal and almost certainly caused by anthropogenic activities” (Flato et al., 2013; Stocker et al., 2013). While climate change leads to variations in a wide range of aspects, it is most directly perceived by the public through increased frequency, duration and intensity of weather and climate extremes (Hansen et al., 1998; Peterson et al., 2013; Sillmann et al., 2013a). These extreme events pose tremendous risks to the physical environment, ecosystems, as well as human or societal conditions and assets (Easterling et al., 2000; Knapp et al., 2008; Field et al., 2012; Mascioli et al., 2016; Wang et al., 2016b). For example, the 2011 floods in central and southern China affected over 36 million people with at least 355 deaths, and resulted in a direct economic loss of nearly US$ 6.5 billion (Van Rij, 2016).

While natural variability continues to be the major driver of the occurrence of climate extremes, climate change is playing an increasingly more important role through changing the odds and natural limits. In fact, a small change in mean climate may lead to large changes in extremes (Stocker et al., 2013; Lewis et al., 2017; Zhou and Khairoutdinov, 2017). For example, assuming a normal distribution of historical temperatures, a small increase in mean

temperature shifts the entire temperature distribution towards larger values (hotter temperatures; Figure 1.5a). This would lead these record heat events to become even more severe and much more frequent. Precipitation may not necessarily follow the same distribution pattern as temperature. This is particularly true over local regions where precipitation may not fit a normal distribution. However, a small shift in mean precipitation would also lead to large variations in their frequency distributions (Allan and Soden, 2008; Trenberth, 2011). Finally, changes in climate extremes can be further exacerbated if the variability (Figure 1.5b) of the distribution of climate variables also changes (Field et al., 2012; Perkins-Kirkpatrick and Pitman, 2018).

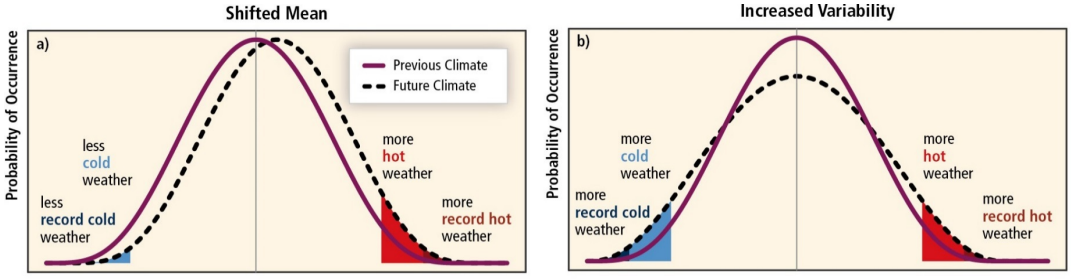

Figure 1.5 Schematic of the impacts of changes in temperature distribution on extremes. (a) The effects of a simple mean temperature shift without changes in variability, and (b) effects of increased variability without shift in the mean. The solid purple curves denote present-day distributions, while the dashed black lines are for future climate. Blue for cold extremes and red for hot extremes. The figure is taken from Field et al. (2012).

1.4.2 Aerosols and changes in climate extremes

Observations show that temperature and precipitation extremes have changed significantly over the past few decades (Field et al., 2012; Chen and Dong, 2019). For example, there are more hot extremes along with less cold extremes, as well as increases in the frequency of precipitation extremes (Alexander et al., 2006; Perkins et al., 2012; Donat et al., 2013; Perkins-

Kirkpatrick and Pitman, 2018). Rigorous model studies demonstrate that such changes cannot be reproduced without taking human influences into account (Christidis et al., 2011; Min et al., 2011; Zhang et al., 2013; Fischer and Knutti, 2015; Mascioli et al., 2016; Chen and Sun, 2017; Huixin et al., 2017; Mukherjee et al., 2018; Chen and Dong, 2019).

Aerosol changes have been shown to influence temperature and precipitation extremes. For example, studies have indicated that aerosols can influence heat extremes by changing incoming solar radiation and modulating cloud properties (Yu et al., 2014; Wang et al., 2016b; Chen and Dong, 2019), as well as by affecting soil moisture (Lenderink et al., 2007) and atmospheric circulation patterns (Xu et al., 2015; Teng et al., 2016). Also, despite the fact that aerosols' effect on precipitation and precipitation extremes are rather unclear, many modelling works have shown that aerosols can suppress extreme precipitation of various definitions (Wang et al., 2016b). Most importantly, despite ongoing debates (Feichter et al., 2004; Xie et al., 2013; Wilcox et al., 2018), a large body of studies indicate that, per unit of forcing/warming, aerosols have significantly larger impacts than GHGs on both global mean climate (Hansen et al., 2005; Shindell, 2014; Shindell et al., 2015), as well as global/regional climate extremes (Perkins, 2015; Xu et al., 2015; Lin et al., 2016; Wang et al., 2016b; Samset et al., 2018).

1.5 The Community Earth System Model (CESM1)

This thesis relies on the Community Earth System Model (CESM1; Hurrell et al. (2013)) that is the state-of-the-art fully-coupled (Figure 1.6) Earth System model developed by the National Center for Atmospheric Research (NCAR).

Below I provide a brief introduction to CESM1 which participated in phase 5 of the Coupled Model Intercomparison Project (CMIP5; Taylor et al. (2012)). CESM1 can be coupled in different configurations. For example, depending upon research aims, the atmospheric component model can be the Community Atmosphere Model 5 (CAM5; Neale et al. (2010)), CAM5 with full chemistry scheme (CAM5-Chem; Lamarque et al. (2012)), or the Whole Atmosphere Community Climate Model (WACCM; Marsh et al. (2013)).

1.5.1 The Community Atmosphere Model 5 (CAM5)

CAM5 is the eighth-generation atmospheric general circulation model released with CESM1. It has 30 vertical layers from the surface up to ~40 km, and has the flexibility of being configured into a variety of horizontal resolutions. For example, the nominal 1° (i.e., 0.9° × 1.25° for the atmosphere and 1°×1 in the ocean) used in this thesis. The atmospheric dynamics scheme in CAM5 is similar to its fourth version (CAM4). However, CAM5 includes a range of improvements in the representation of physical processes. More importantly, it is the first version of CAM that is capable of simulating aerosol-cloud interaction processes (Ghan et al., 2012; Liu et al., 2012), using the Modal Aerosol Module (MAM; Section 1.6).

The default CAM5 configuration for long-term climate simulations usually has prescribed monthly averages of atmospheric compositions (Tilmes et al., 2015). Also, concentrations of CO_2 and CH_4 are prescribed with seasonal cycles and latitudinal-gradients (Conley et al., 2012). Aerosol effects on stratiform clouds by acting as CCN and IN are represented through a two-moment stratiform cloud microphysics scheme (Morrison and Gettelman,

2008). The mass and number of cloud liquid and ice particles are predicted, and the mass and number of perceptible particles (rain and snow) are diagnosed (Hurrell et al., 2013). However, aerosol microphysical effects on deep convective clouds are still absent in CAM5 (Liu et al., 2015). Other major components of CAM5 can be found in Neale et al. (2010).

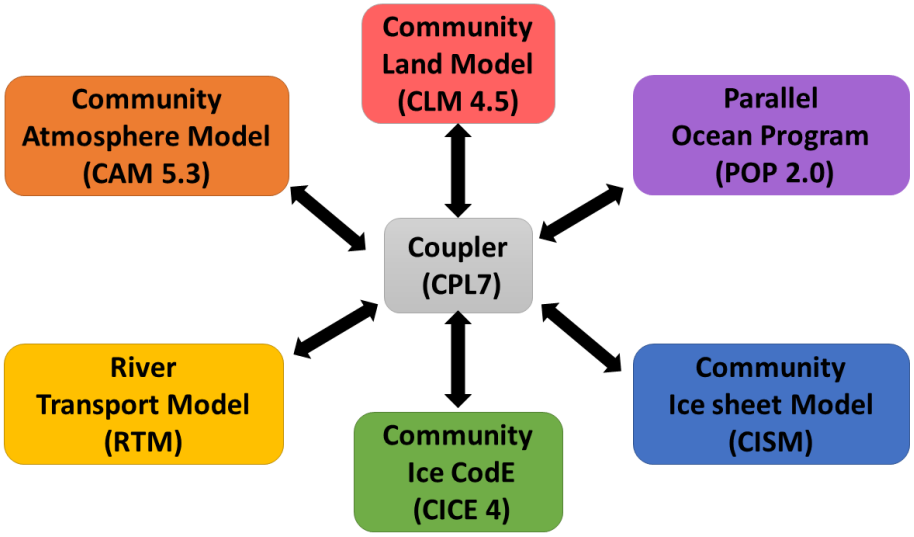

Figure 1.6 Schematic of the Community Earth System Model CESM1 (CAM5) component models and coupling: atmosphere (CAM5.3, 30 vertical levels), ocean (POP2.0, 60 vertical levels], land (CLM4.5), sea ice (CICE), River (RTM) and land ice (CISM) component models.

1.5.2 CAM5 with chemistry (CAM5-Chem)

CAM5 is capable of including chemistry of varying complexities. For example, an extensive tropospheric chemistry scheme and an extensive tropospheric and stratospheric chemistry scheme are both available in CAM5-Chem (Lamarque et al., 2012). The chemical pre-processor in both schemes are the same as version 4 of the Model of Ozone and Related chemical Tracers (MOZART-4; Emmons et al. (2010)). However, the extensive tropospheric chemistry represents a minor update of MOZART-4, while the extensive

tropospheric and stratospheric chemistry scheme implements also the full stratospheric chemistry scheme of WACCM (Liu et al., 2012).

The dynamics (including transport) and physics (radiation, convection, large-scale precipitation, as well as boundary layer diffusion) in CAM5-Chem are the same as the standard CAM5, while chemistry is included only when explicitly configured (Lamarque et al., 2012; Hurrell et al., 2013). When included, atmospheric chemistry interacts with the climate via a variety of mechanisms including radiation (gas and aerosols), aerosol deposition, and aerosol-cloud interactions (Liu et al., 2015). In the extensive tropospheric chemistry scheme, stratospheric chemistry is not explicitly represented. As such, monthly averages of the climatological distributions of some chemically-active stratospheric compositions (namely O_3, NO, NO_2, HNO_3, CO, CH_4, N_2O, and N_2O_5) are usually prescribed from WACCM simulations (Lamarque et al., 2012).

1.6 The Modal Aerosol Module (MAM)

There are several ways to represent aerosols in climate models. The bulk method (Tie et al., 2005) assumes a constant aerosol size distribution and simulates only aerosol mass concentrations. Therefore, it is not sufficient for characterizing aerosol particle properties, which is especially true for coarse-mode aerosols. The sectional method (Spracklen et al., 2005) discretises aerosol size distribution functions into size bins, and predicts explicitly the number/mass of particles in different size bins. However, it is computationally expensive. The modal method (Whitby et al., 1991) represents aerosol size

distributions by multiple lognormal functions, and is a compromise between the bulk and sectional methods.

CAM5 and CAM5-Chem adopt the modal approach, namely the modal aerosol module (MAM) that has three versions. The default three lognormal modes (MAM3; Figure 1.7) is used for long-term (decades to centuries) climate simulations (Liu et al., 2012). An optional seven lognormal modes (MAM7) that simulate ammonium and represents the size distribution of coarse aerosols (mineral dust and sea-salt) more explicitly is available (He and Zhang, 2014). Also, to account for the microphysical ageing of primary carbonaceous aerosols, a four lognormal modes (MAM4) was developed by adding an additional primary carbon mode to MAM3 (Liu et al., 2015). It was shown that the simulated column burdens of anthropogenic aerosols and cloud properties are almost identical between MAM3 and MAM7 (Liu et al., 2012). In addition, the difference between MAM3 and MAM4 lies only in primary organic matter (POM) and BC in remote regions (e.g., the Arctic; Liu et al. (2015)). As such, MAM3 is employed throughout this work. Below I provide a brief description of MAM3, and more details can be found in Liu et al. (2012). Note that nitrate and ammonium aerosols are not simulated in MAM3.

1.6.1 Basics

MAM3 has three lognormal modes: Aitken, accumulation and coarse modes. The typical size range and geometric standard deviation are prescribed for each mode (Figure 1.7). Several aerosol species (SO_4, OC, BC, sea-salt, and mineral dust) are simulated and their number concentrations and mass are prognostically calculated. Aerosol particles are assumed to be internally-mixed

within modes and externally-mixed among modes (see Section 1.2.2 for definitions of internal and external mixing). Within a single mode, the mass mixing ratios of internally-mixed species predicted. Primary carbonaceous aerosols (including BC) are emitted into the accumulation mode and age instantaneously, allowing them to be coated with soluble species (e.g., SO_4) and therefore serve as CCN (Conley et al., 2012). Also, when coated by soluble species such as SO_4 or organic material, mineral dust aerosols can readily absorb water and activate similarly as CCN (Kumar et al., 2009), meaning that mineral dust aerosols are also likely to be removed by wet deposition.

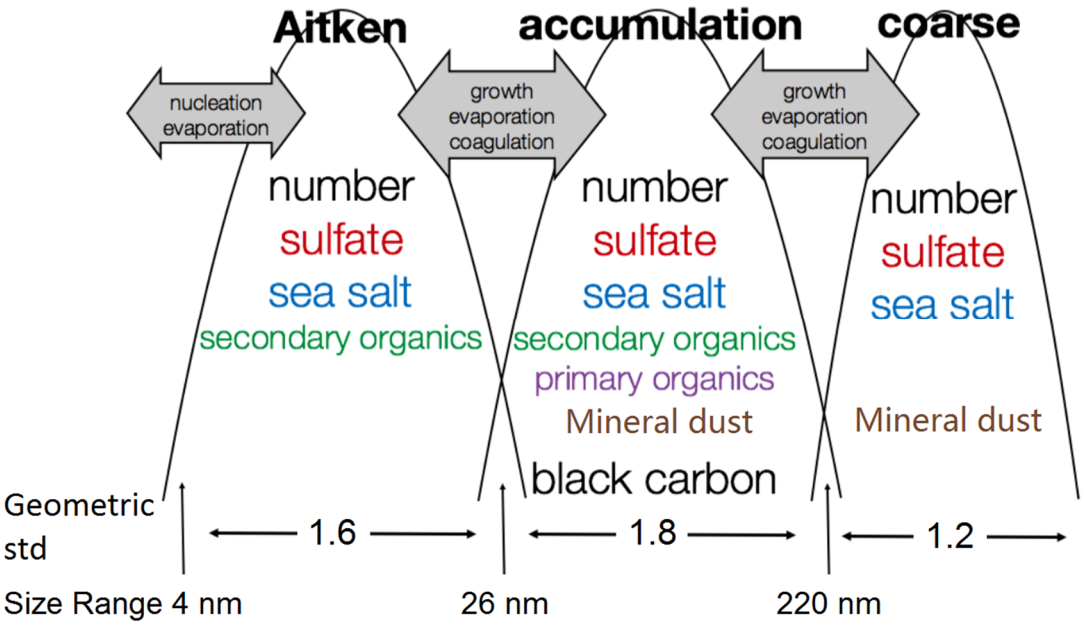

Figure 1.7 Schematic of the Modal Aerosol Module (MAM3) used in CAM5 and CAM5-Chem. The typical size range and geometric standard deviation are prescribed for each mode. Several aerosol species (SO_4, OC, BC, sea-salt, and mineral dust) are simulated and their number concentrations and mass are calculated.

MAM3 simulates a number of important processes that influence aerosol particle properties (e.g., number and mass concentration, size, refractive index, as well as chemical composition). These processes include emission,

gas and aqueous-phase chemical oxidation, particle formation and growth (nucleation, condensation and coagulation), water uptake and activation to form cloud droplets, reproduction from rain and cloud droplet evaporation, as well as removal (in-cloud and below-cloud scavenging, dry deposition and gravitational settling) and transport. Below I provide a brief summary of how MAM3 represents these processes.

1.6.2 Emissions

In MAM3, aerosols and their precursor gases are emitted in numbers of both molecules and particles. For SO_2, it is assumed that 2.5% of the molar mass is directly emitted as primary sulphate aerosols (SO_4) and the rest as SO_2 (Dentener et al. 2006). Surface sources (agriculture, waste and shipping) and elevated sources (energy, industry, forest fire and grassfire) of primary sulphate particles are emitted into the accumulation mode, while those from domestic and transportation sectors are emitted into the Aitken mode (Ghan et al. 2012). In addition, sulphate species are emitted with injection height: (1) those from agriculture, domestic, transportation, waste and shipping sectors are emitted at the surface (<100 m); (2) those from energy and industry sectors are emitted at 100-300 m above the surface; (3) those from forest fire and grassfire are emitted at higher elevations (0-6 km with 6 vertical intervals).

For OC emissions, a 1.4 POM/OC factor is applied to derive the mass of POM by including the mass of other elements (i.e., oxygen, hydrogen, and nitrogen; Seinfeld et al. (2016)). For BC and POM, emissions from energy, industry, agriculture, waste, shipping, domestic and transportation are put into the surface layer in the accumulation mode, while those from grassfire and forest

fire put into the elevated layers in the accumulation mode. Finally, natural aerosol-related (e.g., volcanic sulphur, DMS, and biogenic volatile organic compounds (VOCs)) emissions are all prescribed.

1.6.3 Atmospheric chemistry

In the standard CAM5 configurations, simple gas-phase chemistry is included for sulphate species. This includes (1) DMS oxidation by OH and NO_3 to form SO_2, (2) SO_2 being converted into H_2SO_4 (gas) through gas-phase OH oxidation, (3) SO_2 being converted into SO_4 through aqueous-phase oxidation by H_2O_2 and O_3. In CAM5 (MAM3), NH_3 and ammonium NH_4^+ cycles are not explicitly simulated, so that sulphate aerosols are assumed to be partially neutralized by ammonium in the form of NH_4HSO_4 (Liu et al., 2012). Also, monthly averages of oxidant fields (O_3, OH, H_2O_2 and NO_3) are prescribed. However, when the full chemistry scheme (CAM5-Chem) is included, the simple chemistry for aerosols is coupled with online-calculated oxidant fields from the chemistry scheme (Neale et al., 2010).

1.6.4 Aerosol formation and removal

New aerosol particle formation (nucleation) is calculated using a binary parameterization for sulphuric acid (H_2SO_4) in MAM3 (Vehkamäki et al., 2002). The nucleation process is a function of temperature, relative humidity as well as the gas-phase concentration of sulphate precursor species. Because MAM3 does not have a nucleation mode, new particles are put into the Aitken mode, and are coagulated as they grow from critical cluster size to Aitken mode size. Condensation of H_2SO_4 (irreversible) and semi-volatile organics (reversible) to various modes are simulated dynamically, using standard mass

transfer expression (Seinfeld and Pandis, 2016) that are integrated over each mode (Binkowski and Shankar, 1995). The condensation rate onto pre-existing aerosol particles is a function of the vapour pressure of the gas-phase species. MAM3 simulates intermodal and intra-modal coagulation of Aitken and accumulation modes. Note the coagulation of coarse mode is neglected as it is much slower. Coagulation within each mode reduces particle numbers but does not change the mass, while coagulation of Aitken with accumulation mode transfers aerosol particles to modes with larger sizes.

Aerosol wet removal processes include in-cloud scavenging (removal of cloud-borne particles) and below-cloud scavenging (by precipitation) for both stratiform and convective clouds (Section 1.5.5). Scavenged aerosol particles from one altitude can be reformed at a lower altitude if a rain droplet evaporates below clouds. Dry deposition processes are parameterized based on the CAM5 land information (Zhang et al., 2001), while sedimentation processes are calculated at all levels above the surface following Seinfeld and Pandis (2016). The velocity of dry deposition depends on particle wet size (i.e., the Stokes Law states that the terminal fall velocity is proportional to radius squared). For example, the droplet size for cloud-borne aerosol particles.

1.6.5 Clouds and radiation

Both stratus and cumulus clouds are represented in CAM5, and interact with radiation. For stratus, a prognostic saturation adjustment is used to account for the conversion of water vapour into stratus liquid water content (Park et al., 2012). Also, a modified double-moment formulation (Greenwald et al., 1993; Morrison and Gettelman, 2008) is used to account for stratus microphysics.

That is, the number and mass mixing ratios of cloud droplets and ice crystals are predicted, and the number and mass mixing ratio of precipitation (rain and snow) are diagnosed. For cumulus, CAM5 simulates the fraction of deep and shallow cumulus differently. Specifically, deep cumulus is represented by an empirical logarithmic function of deep convective mass flux (Neale et al., 2008), while shallow cumulus is computed using shallow convective mass flux and vertical velocity (Park and Bretherton, 2009). Note however no microphysical processes are included for cumulus, even though convective precipitation scavenges aerosols (Section 1.5.4).

Aerosol water uptake processes are represented using the relative humidity and the volume-mean hygroscopicity for each mode based on the equilibrium Köhler theory (Ghan and Zaveri, 2007). The source for the cloud droplets in stratus comes from activation processes, while sink terms include both in-cloud and below-cloud scavenging (auto-conversion of cloud droplets to form rain, instantaneous evaporation of falling droplets, and accretion of cloud droplets by rain). More specifically, interstitial aerosols (those not incorporated in a cloud droplet) are converted into cloud-born aerosols through activation processes. The activation occurs through three processes: (1) as updrafts carry air into the cloud base (Ghan et al., 1997); (2) as cloud fraction increases (Ovtchinnikov and Ghan, 2005); and (3) as air is continually cycled through clouds, assuming a three hours of in-cloud residence time (Lelieveld and Crutzen, 1990). The total number of activated particles is equal to the number of droplets nucleated. Aerosols that have become dissolved in cloud droplets can be reformed to interstitial states when cloud and droplets evaporate. On

the other hand, those interstitial aerosols can be re-activated again in “new” clouds, causing an increase in cloud droplet numbers.

The Rapid Radiative Transfer Model for General Circulation Models is used to parameterise longwave (16 spectral intervals) and shortwave (14 spectral intervals) radiative transfer. Aerosol and cloud absorption are included for longwave radiation, while extinction from aerosols, clouds and Rayleigh scattering are represented in shortwave radiation. Aerosol optical properties are parameterised through specifying their optical properties (wet refractive index and wet surface mode radius; Ghan and Zaveri (2007)) within each spectral interval. Assuming a gamma size distribution that varies with the numbers and mass mixing ratios of stratiform cloud droplet, liquid cloud optics are represented based on Mie computations (Wiscombe, 1979) for pure water droplets (Morrison and Gettelman, 2008).

1.7 The CESM1 large ensemble project (LENS)

The CESM1 Large Ensemble Project (LENS; Kay et al. (2015)) was designed to advance our understanding of internal climate variability and climate change. It has a number of simulations using the nominal 1-degree latitude/longitude version of CESM1 (CAM5 with simple chemistry). Figure 1.8 shows the LENS simulated global surface temperature anomaly (1961–90 base period) from preindustrial to the end of the 21st century under historical and the Representative Concentration Pathway (RCP) 8.5 external forcings. The RCP8.5 scenario assumes a global annual mean radiative forcing of +8.5 W m^{-2} by 2100 relative to pre-industrial times. LENS has two ~1000 year-long preindustrial control simulations that were designed to quantify the internal

climate variability in the absence of climate change. Its 30 ensemble member simulations of the 1920-2100 period under historical and RCP8.5 forcings are used to disentangle the signal of climate change from internal climate variability.

The LENS model simulations have been used widely by the community. Here, two sets of LENS experiments are utilized to investigate future changes in climate extremes (Chapter 5 and 6). The first one includes a 30-member ensemble of transient simulations driven by historical forcing during 1920-2005 and following the RCP8.5 pathway for the period 2006-2100 (Riahi et al., 2007; Van Vuuren et al., 2011). Each of the 30 members has the same forcing trajectory but starts from randomly perturbed initial atmospheric conditions (Kay et al., 2015). Secondly, a 15-member ensemble of simulations with the same time-varying forcing as RCP8.5 but with fixed aerosol/precursor emissions at 2005 levels (hereinafter RCP8.5_FixA for short) (Lin et al., 2015; Xu et al., 2015). Note, however, that aerosol concentrations in RCP8.5_FixA do evolve slightly (regional differences up to 5-10% by 2010 (Lin et al., 2015)) due to sampling different transport and removal processes associated with the different climate meterologies.

Under RCP8.5_FixA, the net warming is primarily due to changes in GHGs with minor contributions from other factors such as land-use changes (Xie et al., 2013; Paul et al., 2016). Therefore, throughout this work, changes under RCP8.5_FixA are refereed as GHG effects. Assuming linearity in the combined responses, the difference between RCP8.5 and RCP8.5_FixA represents the climate effect due to future time-evolving anthropogenic aerosol changes. Note

although non-linear interactions between GHGs and aerosol exist, such non-linearity emerges only when additional anthropogenic aerosols are present.

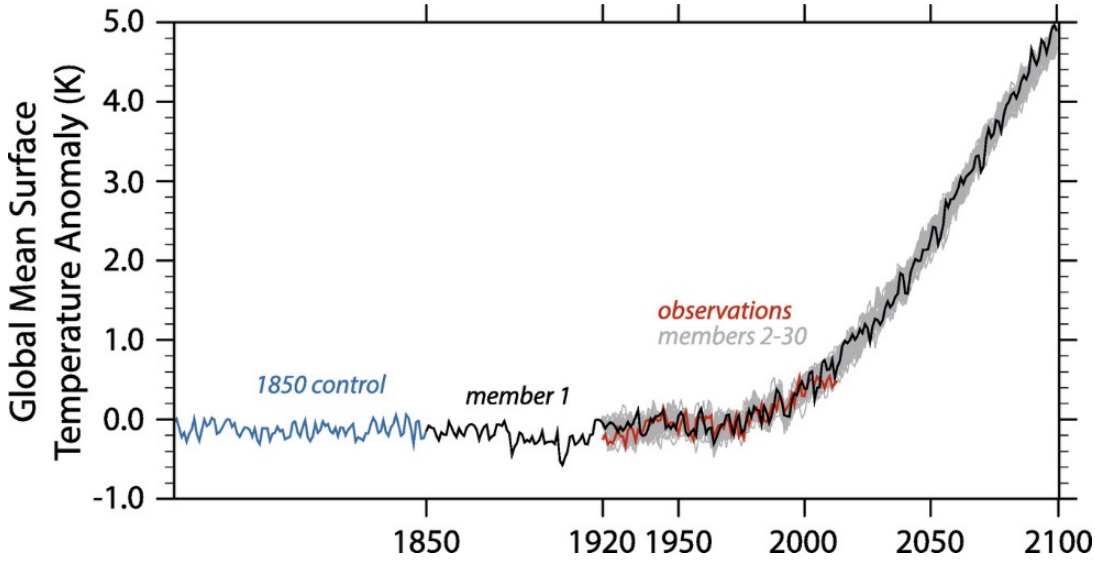

Figure 1.8 Time evolution of global annual mean surface temperature anomaly (1961–1990 base period) produced from the CESM1 large ensemble project (LENS). Blue for the 1850 control, black for individual ensemble members, and red for observations from the Met Office Hadley Centre and the Climatic Research Unit at the University of East Anglia (HadCRUT4; Morice et al. (2012)). The figure is taken from Kay et al. (2015).

1.8 Objectives and research questions

The overall aim of this thesis is to enhance our understanding of the impacts of aerosols on climate radiative forcing and response (Chapter 2-3), air pollution (Chapter 4), as well as climate extremes (Chapter 5-6), by looking at model simulations of both the recent past (1970-2010; Chapter 2-4) and the future (2006-2100; Chapter 5-6).

First, this thesis seeks to understand anthropogenic aerosol changes during the period 1970-2010, and their impacts. Specific objectives (overarching and sub-divided) for each Chapter are as follows.

1. **To examine the climate impacts of changes in each individual forcing agent during the period 1970-2010, focusing on the relative roles of anthropogenic aerosols compared to other forcing agents including GHGs and O_3 (Chapter 2).**
   a. How far is the present-day climate (i.e., the transient response) from the steady-state where the climate has fully-responded to 1970-2010 changes in all forcing agents?
   b. How do changes in each individual forcing influence global and regional surface air temperatures? Do SLCFs, and particularly aerosols, behave the same as GHGs?
   c. What is the difference between GHGs and SLCFs in modulating precipitation? Do the effects differ between global and regional scales?
2. **To understand the major drivers of past anthropogenic aerosol changes and their climate impacts (Chapter 3).**
   a. How do aerosol changes associated with 1970-2010 growth in energy use and advances in emission control technology influence surface air temperature and precipitation, both globally and regionally?
   b. Is ERF a valid indicator of surface air temperature response for aerosols? If not, why not?
   c. What non-linear processes are involved in aerosol forcing and climate response? How important are they?
   d. What are the implications for future climate mitigation and projection, as well as climate policymaking?

3. **To assess 1970-2010 changes in air quality and their impacts on human health and crop production, attributing to climate change and anthropogenic emissions (Chapter 4).**
    a. How much of 1970-2010 changes in air pollution is attributable to anthropogenic emissions, and how much to climate change? Does it differ between different air pollutants?
    b. Of the changes associated with anthropogenic emissions, how much is driven by energy use growth, and how much is associated with advances in emission control technologies?
    c. How changes in air pollution can be attributed to each of the driving factors that have influenced human health?
    d. How are changes in air pollution attributable to each of the driving factors that have influenced crop production? What does it mean for the global economy?

With the climate effects and socioeconomic impacts of past aerosol changes above in mind, this thesis then turns to the "future" (2006-2100) under the RCP8.5 emission pathway, seeking to understand the impacts of future aerosol mitigation on climate extremes. In particular, I focus on heatwaves at the global scale (Chapter 5) and precipitation extremes over Asia (Chapter 6).

4. **To understand how future GHG increases and aerosol mitigation may influence the characteristics of future heatwaves (Chapter 5).**
    a. How will future heatwave characteristics change in response to GHG increases and aerosol reductions following the RCP8.5 emission pathway?

b. Are the changes driven by the shift of mean temperature and/or changes in temperature variability? Are there seasonal differences?

c. What is the mechanism through which aerosol changes influence heatwave characteristics?

5. To understand how future GHG increases and aerosol mitigation will influence summertime precipitation and precipitation extremes over Asia (Chapter 6).

a. How will mean and extreme precipitation in Asia change in the future following the RCP8.5 emission pathway? What is the difference in response between mean and extreme precipitation?

b. What is the difference between the changes due to GHG increases and those due to aerosol reductions? Do these differ between South and East Asia?

c. How may future aerosol reductions influence the Asian summer monsoon systems?

d. What are the mechanisms through which aerosols modulate precipitation and precipitation extremes?

Chapter 2 Effective Radiative Forcing and Climate Response to Greenhouse Gases, Aerosols and Ozone

This chapter is adapted from a paper that is, at the time of writing, in review by the Journal of Geophysical Research: Atmosphere. I carried out all model experiments, performed all data analysis, and wrote the first draft of the manuscript. Dr David Stevenson and Dr Massimo Bollasina supervised the study, and provided comments on subsequent manuscript revisions. Three anonymous reviewers provided additional comments during peer-review.

Zhao A, Stevenson D.S. and Bollasina M. A., Climate forcing and response to greenhouse gases, aerosols and ozone in CESM1, in revision for Journal of Geophysical Research: Atmosphere.

2.1 Abstract

Using the Community Earth System Model (CESM1), time-slice experiments were carried out to investigate the effective radiative forcing (ERF) and climate response to 1970-2010 changes in well-mixed greenhouse gases, anthropogenic aerosols, as well as tropospheric and stratospheric ozone. The results show that, once the present-day climate has fully responded to 1970-2010 changes in all forcings, both the global mean temperature and precipitation responses are twice as large as the transient ones, with wet regions getting wetter, and dry regions drier. The temperature response per unit ERF for short-lived species varies considerably across many factors including forcing agents, and the magnitudes and locations of emission changes. This may suggest that the ERF should be used carefully to interpret the climate impacts of SLCFs. Changes in both the mean and the probability distribution of global mean daily precipitation are driven mainly by GHG increases. However, changes in the frequency distributions of regional mean daily precipitation are more strongly influenced by changes in aerosols, rather than greenhouse gases. This is particularly true over Asia and Europe where aerosol changes have significant impacts on the frequency of heavy-to-extreme precipitation.

2.2 Introduction

It is well established that human activities have altered the chemical and physical properties of the atmosphere (Acosta Navarro et al., 2017), and therefore influenced the climate system (Schmidt et al., 2014). Changes in many climate features, especially the global warming trend, have been shown

to be driven mainly by the increasing abundance of well-mixed greenhouse gases (GHGs) (Stocker et al., 2013). However, there are also significant concerns about the impacts of short-lived (i.e., having a shorter lifetime than CO_2) climate forcers (SLCFs, notably aerosols, ozone and their precursor gases) on both air quality and climate (Stocker et al., 2013; Schmale et al., 2014; Stohl et al., 2015). Unlike GHGs, concentrations of SLCFs depend strongly on the geographical location of emission sources, and their radiative forcings are largely heterogeneous and uncertain (Stohl et al., 2015; Aamaas et al., 2017). More importantly, the climate response to SLCFs differs from that of quasi-uniform forcing agents at regional scales (Lamarque et al., 2011; Aamaas et al., 2017).

The climate system evolves slowly in response to changing emissions: once a perturbation is introduced, the climate system will respond and adjust to restore a new radiative balance on decadal timescales, and even centennial timescales when accounting for the deep ocean heat uptake (Yang and Zhu, 2011). The climate in the new equilibrium can be very different from its transient state as the latter does not account for the full long-term response to the imposed forcing (Yoshimori et al., 2016). The equilibrium climate response to GHGs, and CO_2 in particular, has received much attention (Marvel et al., 2016; Rugenstein and Bloch-Johnson, 2016; Yoshimori et al., 2016; Caldwell et al., 2018). In comparison, there are fewer studies on the equilibrium climate response to changes in SLCFs, except some looking at idealized experiments where emissions/concentrations of aerosols are scaled rather arbitrarily (Kühn et al., 2014; Liu et al., 2018; Persad and Caldeira, 2018; Samset et al., 2018). However, despite their short lifetimes, a major fraction of SLCFs' impacts are

associated with the slow response of the ocean through adjustments in circulation and clouds (Allen and Sherwood, 2011; Ganguly et al., 2012; Voigt et al., 2017; Wang et al., 2017a). The slow response emerges on decadal to centennial timescales (Ganguly et al., 2012; Voigt et al., 2017; Wang et al., 2017a) even after these SLCFs are removed. For example, equilibrium model simulations indicate that the long-term slow response is more important in shaping the total equilibrium response of the Asian monsoon to aerosol forcing (Ganguly et al., 2012; Wang et al., 2017a). That is, similar to these long-lived species such as CO_2, the climate impacts of SLCFs will not be fully realised until the climate has equilibrated, suggesting the importance of studying the equilibrium climate responses to SLCFs as GHGs. Some studies compared the differences in climate responses between GHGs and aerosols using mixed layer ocean models (Feichter et al., 2004; Ming and Ramaswamy, 2009; Ocko et al., 2014; Dallafior et al., 2016; Hodnebrog et al., 2016; Chen and Dong, 2018; Tian et al., 2018). Nevertheless, to our knowledge, there are very few studies (e.g., Wang et al. (2018b)) specifically designed to systematically compare the equilibrium climate response to recent changes in major climate drivers (e.g., GHGs, aerosols and ozone) using a (or a set of) fully-coupled climate model(s). Also, the difference between equilibrium and transient climate responses have not been investigated so far. However, the evolving climate response, and consequently the equilibrium sensitivity, of SLCFs is of scientific interest, as they show significant new insights into how the climate system responds to SLCFs, and that there are important differences between SLCFs and GHGs. This provides useful implications for future long-term climate projection and policymaking in the context that we expect significant changes in future emissions of SLCFs.

This study focuses on the period 1970-2010 for the following reasons. Firstly, a very large fraction of the preindustrial to present-day global warming occurred after about 1970 (Stocker et al., 2013). Secondly, emissions of CO_2 started to increase in a dramatic way since the 1970s due to the rapid development of developing countries (Olivier et al., 2005; Figueres et al., 2018). Thirdly and most importantly, in addition to the very different trends of air pollutant emissions between developed and developing regions (Section 1.2.1), there are also distinct changes in tropospheric and stratospheric ozone during the period 1970-2010. More specifically, tropospheric ozone concentration has increased since the pre-industrial era due to increases in precursor emissions (Stevenson et al., 2013; Checa-Garcia et al., 2018), and varies inter-annually due to fluctuations in downward transport of stratospheric ozone (Hsu and Prather, 2009; Monks et al., 2015; Xie et al., 2016). Simultaneously, industrial emissions of halocarbons have led to widespread depletion of the stratospheric ozone layer since at least the 1970s (Solomon, 1999). Thanks to the Montreal Protocol and its amendments stratospheric ozone has started to recover but at a much slower rate (~3 times slower than the depletion) after about 2000 (Solomon et al., 2016; Hossaini et al., 2017; Kuttippurath and Nair, 2017; Wilmouth et al., 2017). Ozone modulates solar radiation and has a different surface impact depending on its location: stratospheric ozone absorbs UV absorption, warms the stratosphere, and cools the surface, while tropospheric ozone has a greenhouse effect that warms the surface and the lower atmosphere (Stevenson et al., 2013; Xie et al., 2016). The 1850-2014 total ozone ERF is estimated to be +0.30 W m^{-2}, primarily from changes in tropospheric ozone increase (+0.33 W m^{-2}), and

partially counteracted by stratospheric ozone depletion (-0.03 W m^{-2}) (Checa-Garcia et al., 2018).

The above indicates the particularity and importance of studying the period 1970-2010. This allows us to examine the differences and relative roles of very distinctive changes in individual forcing agent (especially GHGs versus SLCFs) during recent decades. These are important for interpreting and attributing currently observed climate change. More importantly, experiments have been specifically designed, seeking to quantify how far present-day climate is from a steady-state with current emissions. This is critical to better constrain long-term climate projections and more adequately prepare for future climate-related risks.

2.3 Data and methods

Anthropogenic aerosol and their precursor gas emissions are from the Emissions Database for Global Atmospheric Research (EDGAR) version 4.3.2 inventory for the years 1970 and 2010 (Crippa et al., 2016). The EDGAR emissions are mapped to conform to the CAM5 emission protocol following Lamarque et al. (2010). GHGs, natural aerosols and other reactive gas emissions/concentrations are from Lamarque et al. (2010) for 1970 and Lamarque et al. (2011) for 2010. Ozone concentrations for 1970 and 2010 (See Figure 2.1 for the zonal mean distribution of 1970-2010 ozone changes) are from earlier WACCM simulations (Marsh et al., 2013), as used by the CESM1 large ensemble project (LENS; see Section 1.6 and Kay et al. (2015)).

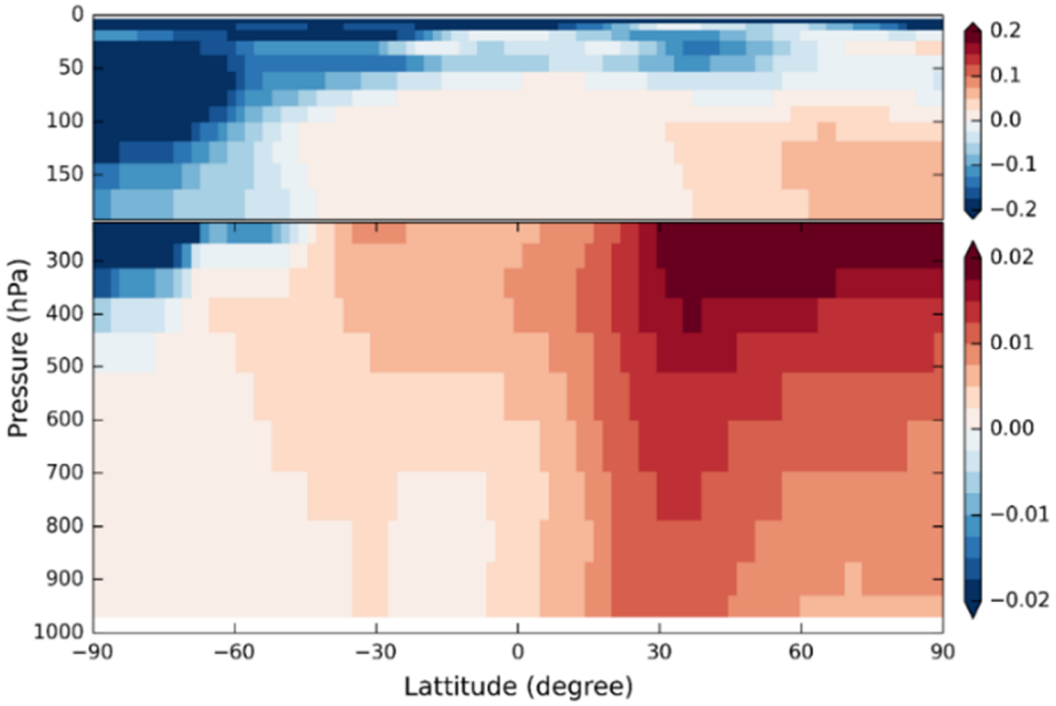

Figure 2.1 Altitude-latitude cross of 1970-2010 changes in ozone mixing ratio (ppb) prescribed in the CESM1 time-slice simulations. NB the different colour scales above and below 200 hPa.

This study employs the fully-coupled CESM1 at the nominal 1-degree resolution (Chapter 1). Using CESM1, two baseline experiments branching off from the LENS transient historical simulation at either 1970 or 2010 (See caption of Figure 2.2 for more details) were carried out. The baseline simulations were integrated into equilibrium (fully-responded to the imposed forcing where the TOA net radiative flux reaches a new balance) under the 1970 and 2010 all forcings (denoted as B70 and B10). The length of each Fcpd integration is deemed sufficient for analysis once TOA radiation imbalance no longer shows significant trends (less than 5% relative to the mean values stabilizing at ~0.3 W m^{-2}) during the last 30-50 years of each simulation, following recent works (Samset et al., 2016; Myhre et al., 2017b; Samset et al., 2018). A number of perturbation experiments, branching off from the LENS transient simulation at 2010, were also performed by alternatively keeping one

of the forcing agents at 1970 levels and the others at 2010 levels (see Table 2.1). For each experiment, a set of paired simulations were performed. The first is with fixed sea surface temperature and sea ice (hereinafter Fsst) fields derived from the LENS transient simulations. The Fsst experiment was integrated for 40 years, with the last 30 years used to diagnose ERF by the difference in the top-of-the-atmosphere (TOA, top of the model in this case) net radiative flux (Forster et al., 2016). The second is under the same forcings as the first one, but with a fully coupled ocean (Fcpd). The Fcpd experiment was integrated into equilibrium after the initial perturbation, with a repeated annual cycle of the forcings.

Table 2.1 Overview of the equilibrium model experiments. They are, the baseline runs under 1970 (B70) and 2010 forcings (B10), fixing greenhouse gases and ozone in 1970 levels (SGO), fixing anthropogenic aerosol and their precursor gases in 1970 levels (SAA), fixing tropospheric and stratospheric ozone in 1970 levels (SOZ), and fixing tropospheric ozone in 1970 levels (STO). The climate responses are resolved into changes due to each forcing as follows: All=B10–B70; GHGs=SGO – SOZ; AAs= B10SGO– SAAB70; Trop. O_3=B10–SOZSTO, Strat. O_3= STO–SOZ. The B70 simulation is initialised using the LENS transient simulation (ensemble member 34) at 1970, while all others are branched off from the LENS transient simulation (also member 34)) at 2010. All simulations are integrated into equilibrium (see the length (no. of years) of each simulation in brackets in the first column), and only the last 30 years of each run are used for analysis.

Simulation (length, years)	Initial condition	Greenhouse Gases (GHGs)	Anthropogenic aerosols (AAs)	Tropospheric ozone increase (Trop. O_3)	Stratospheric ozone depletion (Strat. O_3)
B70 (120)	1970	1970	1970	1970	1970
B10 (150)	2010	2010	2010	2010	2010
SAA (120)	2010	2010	1970	2010	2010
SGO (90)	2010	1970	2010	1970	1970
SOZ (150)	2010	2010	2010	1970	1970
STO (150)	2010	2010	2010	1970	2010

The last 30 years of each Fcpd simulation (indicated by the black boxes in Figure 2.2) are analysed to show the equilibrium climate responses. Throughout this study, differences (Table 2.1) between 1970 and 2010 are used to quantify the responses to all forcings (ALL), GHGs, anthropogenic aerosols (AAs), tropospheric ozone increase (Trop. O_3), and stratospheric

ozone depletion (Strat. O_3). It must be noted that GHGs refers to those non-ozone GHGs. Following Shindell and Faluvegi (2009), the sensitivity of the surface air temperature responses to local and global radiative forcing is estimated by normalizing area-weighted mean temperature responses against global and regional mean ERF, respectively.

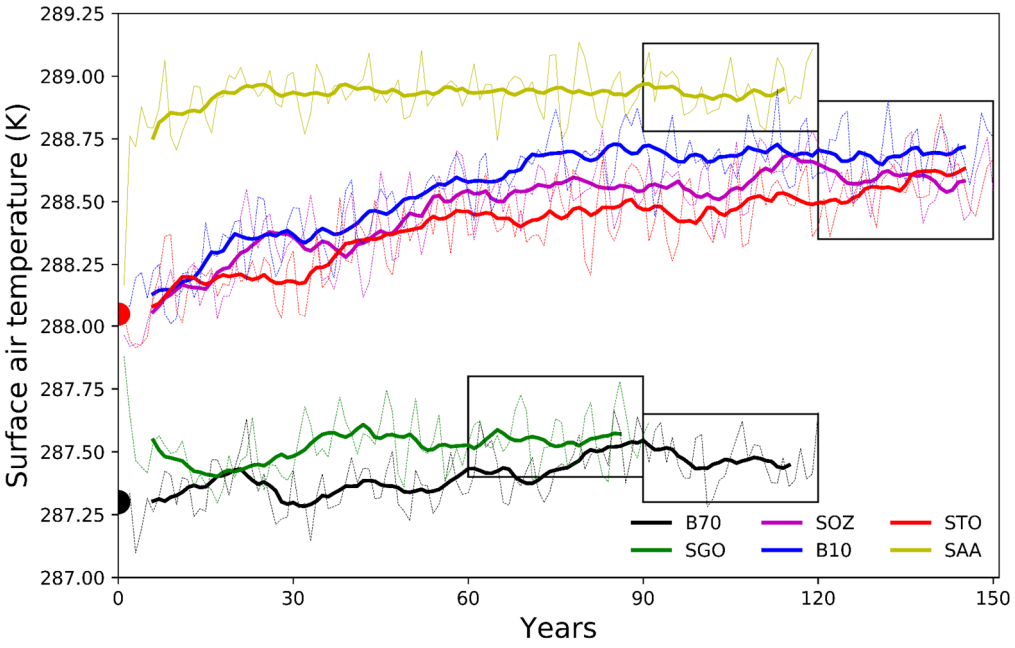

Figure 2.2 Time evolution (dashed lines and also the 11-years running mean in solid) of the global annual mean surface air temperature from the fully-coupled CESM1 baseline and perturbation runs. B70 and B10 refer to 1970 and 2010 all forcing runs, respectively. SGO, SAA, SOZ and STO represent the simulation with greenhouse gases and ozone, anthropogenic aerosols, ozone and only tropospheric ozone fixed at 1970, respectively. The black boxes denote the last 30 years of each run analysed here. Note that all simulations except for B70 started from a same 2010 dump (red half-circle) while B70 stared from a 1970 dump (black half-circle), from the CESM1 large ensemble run (LENS, no 34). Also see Table 2.1 for the detailed experiment design.

To compare the equilibrium and transient climate responses, various datasets are used: output from the LENS for both the historical (1920 – 2005) and future (RCP8.5 for 2006-2100) periods (Kay et al., 2015); monthly mean 2-m temperature from the NCEP/NCAR reanalysis (Kalnay et al., 1996); and monthly observed land-only precipitation from the Global Precipitation

Climatology Centre (GPCC) dataset (Huffman et al., 1997). For above datasets, 15 years of monthly mean fields centred on 1970 and 2010 (7 years either side as reanalysis/observation data are not available beyond 2017) are averaged to produce annual means. The difference between the two 15-year means for 1970 and 2010 from LENS is taken as the transient model response, and those from NCEP/NCAR and GPCC are taken as observational changes.

To produce spatial maps, the analysis is performed on each model grid-box using the annual mean of monthly mean fields. The statistical significance of the response, as isolated from the corresponding two sets of 30-year runs, is evaluated using the two-tailed Student t-test with a 5% significance threshold (p-value ≤0.05), and accounting for serial autocorrelation by adjusting the degrees of freedom following Nychka et al. (2000). For global and regional mean analyses, an area-weighted mean for each year of each simulation is firstly performed, and the results are shown as the mean and 25^{th}-75^{th} percentile spread of the differences between the two sets of 30-year runs.

2.4 Time evolution of global mean surface air temperature towards equilibrium

Figure 2.2 shows the time evolution (annual mean) of the global mean surface air temperature for all model experiments analysed here. Temperature generally increases from the initial condition to reach an approximate equilibrium after ~100 years. Note again that the smaller the perturbations to the initial state, the shorter is the time to reach equilibrium. In particular, the temperature difference between the B70 case in equilibrium and the 1970 initial condition is modest (~0.10 K), indicating that the 1970-2010 equilibrium

changes stem primarily from the adjustment to 2010 conditions, while the difference in the initial conditions of the two simulations may have minor impacts. It is important to point out that the global mean TOA net radiative flux converges from initial values exceeding +1.6 W m^{-2} towards zero as the experiments progress, although even after ~150 years a small imbalance is still left in the last few decades of the experiments (~0.3 W m^{-2}; Section 2.3) due to the large inertia of the deep oceanic circulation which equilibrates on time-scales of several centuries (Yang and Zhu, 2011). This residual forcing will drive additional climate anomalies further to the ones analysed here. Nevertheless, the impacts from the residual forcing are secondary, given the much larger 1970-2010 forcing changes. (Mitchell et al., 1990; Rugenstein and Bloch-Johnson, 2016; Samset et al., 2018).

Table 2.2 CESM1 simulated 1970-2010 changes in global mean aerosol burdens (mg m^{-2}) resolved into each species, as well as the 550-nm total AOD. The total changes (second column) are decomposed into that attributable to anthropogenic emissions and climate change. Percentage values in brackets denote the relative contributions to the total.

	Total net	**Anthropogenic emissions**	**Climate change**
Black carbon (mg m^{-2})	0.10	0.09 (90%)	0.01 (10%)
Organic carbon (mg m^{-2})	0.90	0.80 (89%)	0.11 (14%)
Sulphate (mg m^{-2})	0.77	0.74 (96%)	0.03 (4%)
Total AOD*100 (#)	0.81	0.71 (88%)	0.10 (12%)

The 1970-2010 changes in global and regional area-weighted mean anthropogenic aerosol/precursor emissions and burdens, as well as the spatial distribution of the 550-nm Aerosol Optical Depth (AOD), are shown in Figure 2.3. Changes in aerosol burden and AOD are predominated (around 90%; Table 2.2) by anthropogenic emissions, with the rest attributable to climate change (i.e., changes in meteorology driven mainly by GHG increases). The emissions and burdens of all aerosol species show increasing trends when

averaged globally. For example, the global mean burden of sulphate aerosol has increased by 0.77 mg m^{-2} (~22%). AOD changes are consistent with changes in emissions and burdens, with a striking dipole pattern featuring an AOD increase over Asia and a decrease over Europe and USA.

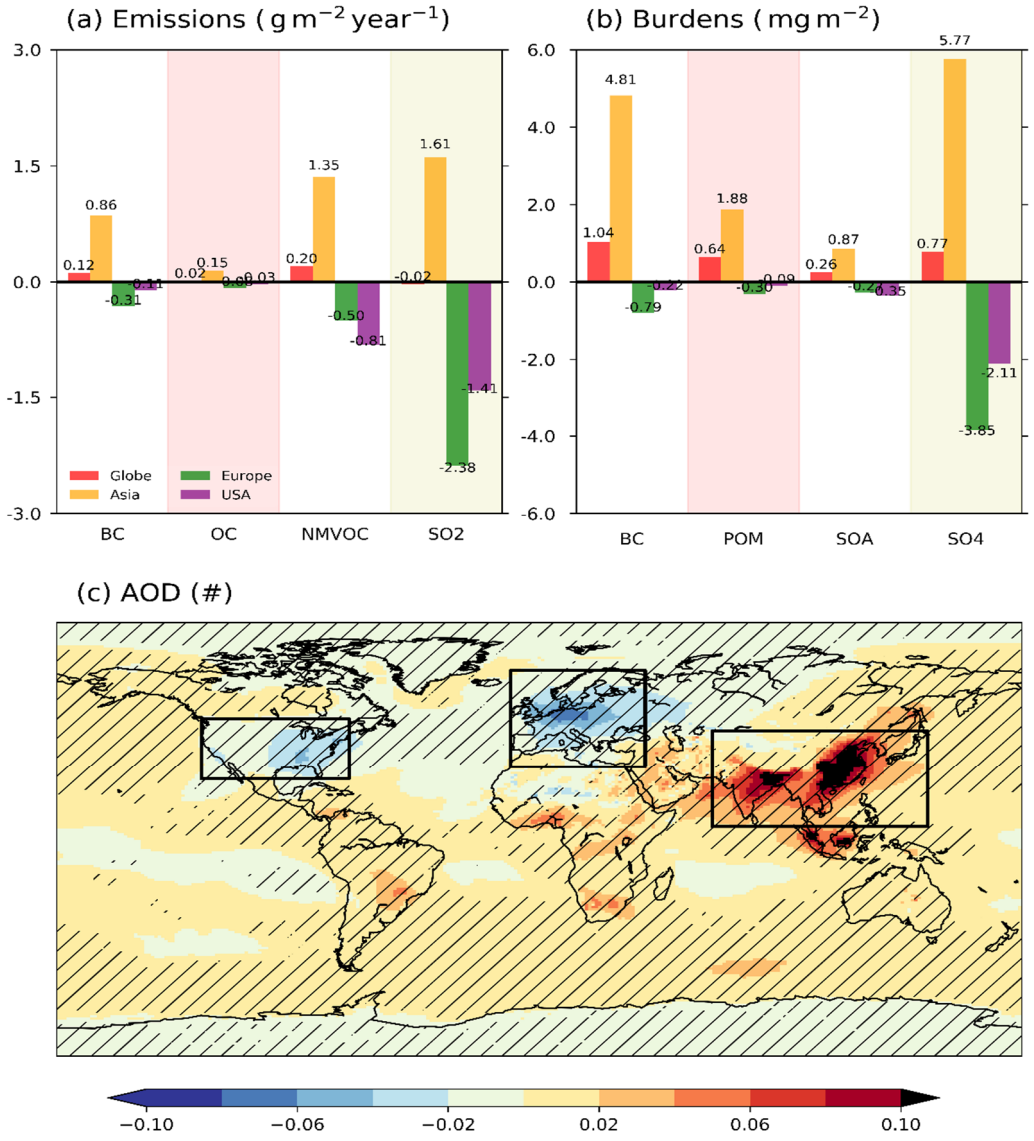

Figure 2.3 The 1970-2010 changes in (a) anthropogenic aerosol/precursor emissions (g m^{-2} yr^{-1}), (b) aerosol burdens (mg m^{-2}) and (c) spatial distribution of 550-nm Aerosol Optical Depth (AOD). Emissions and burdens are shown as the area-weighted mean over the global scale (red), Asia (yellow), Europe (green) and USA (purple). The definitions of these regions are denoted by the black boxes in (c). Hatches in (c), and also in all other figures throughout this chapter, denote a statistically significant difference (95%), derived using a two-tailed student t-test. Note the emissions and burdens of BC are multiplied by 10 for legibility.

2.5 Transient versus equilibrium climate response

To evaluate the performance of CESM1 in simulating transient climate response, the LENS ensemble mean is compared with reanalysis and observations (Figure 2.4). Further, present-day climate (transient response) is not in equilibrium in response to past emission changes, while the difference between the transient and equilibrium responses is primarily associated with the slow response of the ocean. In order to quantify such differences, the equilibrium experiments described above are compared with the LENS simulations. The spatial patterns of the 1970-2010 changes in surface air temperature show an overall agreement across datasets (Figures 2.4a-c). This is also reflected in the zonal mean profiles (Figure 2.4d). Comparison between LENS and NCEP/NCAR indicates that apart from the polar regions, the model shows reasonable agreement with reanalysis in reproducing the transient (i.e., LENS) surface air temperature changes. The equilibrium response is roughly double the transient response (Figure 2.4d), with the global mean temperature change 0.58 K larger in equilibrium than the transient warming (0.65 K).

Precipitation by nature is more heterogeneous compared to temperature, as is reflected in the spatial patterns of changes (Figures 2.4e-g). LENS simulated precipitation changes agree in general with the observed ones. However, there are noticeable differences at regional scale such as over equatorial Africa, the Middle East and Southeast Asia. These changes, for example, the wettening over Europe and the drying of the Asian monsoon, as well as the shift of the tropical rain belt, have been broadly discussed in literature as key features of the late-twentieth-century climate evolution (Ropelewski and Halpert, 1987;

Bollasina et al., 2011; Hwang et al., 2013; Liu et al., 2013; Acosta Navarro et al., 2017; Jong et al., 2018).

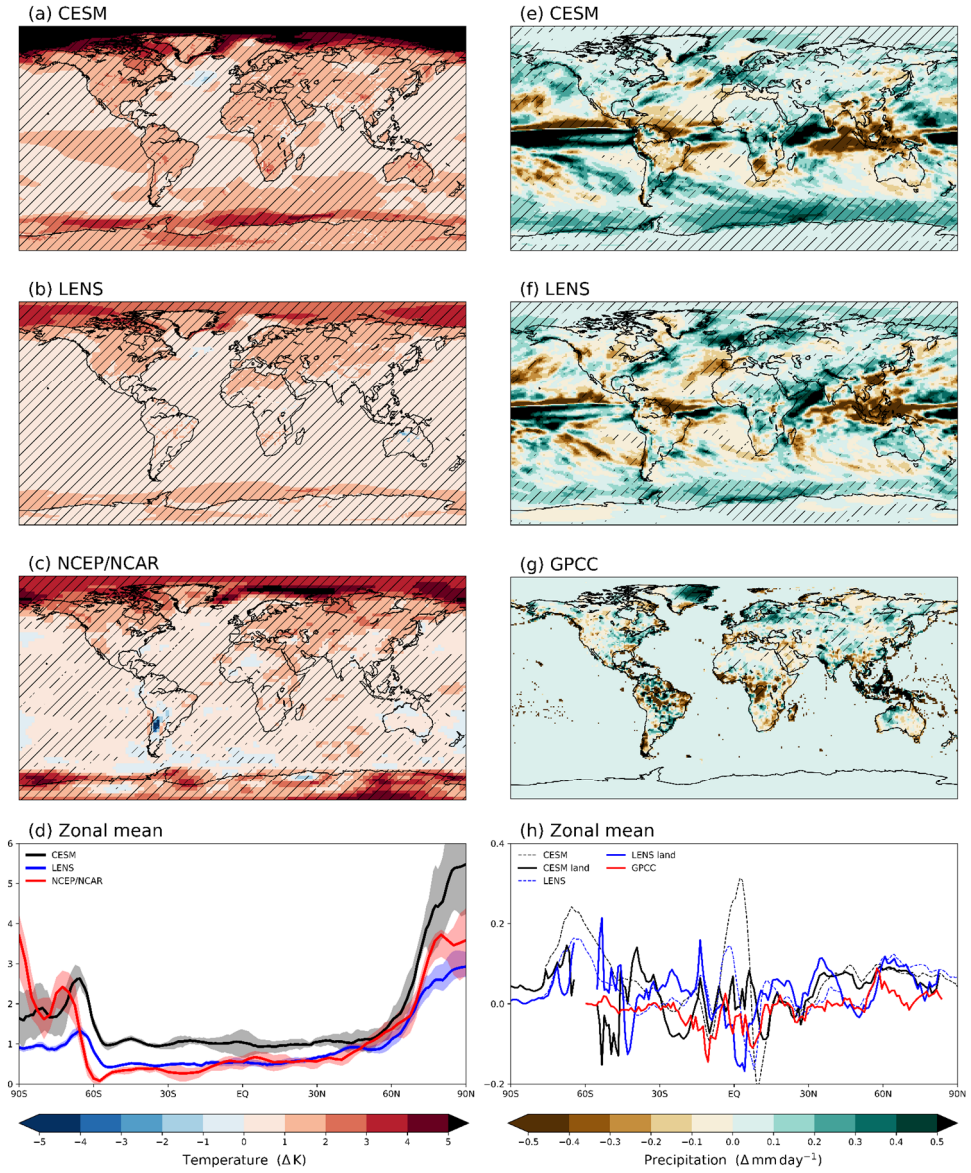

Figure 2.4 Comparisons of 1970-2010 changes in (a-d) annual mean surface air temperature and (e-h) precipitation. They are: (a, e) the difference between 1970 and 2010 equilibrium experiments in this study, (b, f) the difference between the time period 1963-1977 and 2003-2017 from the LENS ensemble mean, (c, g) the difference between time period 1963-1977 and 2003-2017 from NCEP/NCAR surface temperature reanalysis and the Global Precipitation Climatology Centre (GPCC) precipitation, as well as (d, h) their zonal means (solid for mean changes, and shadings for the 25th-75th uncertainty range). Solid curves in (h) are the corresponding land-only zonal mean precipitation changes, which are plotted to compare to the GPCC dataset that has data only over land. Hatches in the maps denote a statistically significant difference (95%), derived using a two-tailed student t-test. Note that to make the plot readable, the uncertainty range for zonal mean precipitation response is not shown.

The global precipitation pattern displays a striking resemblance between the equilibrium (Figure 2.4e) and transient (Figure 2.4f) responses, while the former features anomalies of larger magnitude. The zonal mean (land + ocean) precipitation profile in Figure 2.4h shows that, compared to the transient response, precipitation increases over the equatorial area (5°S-5°N) and high latitudes but reduces in the mid-latitudes (30°S-5°S and 5°N-40°N) in equilibrium. Globally, the 1970-2010 equilibrium precipitation increase (+0.054 mm day^{-1}) is double the transient response (+0.026 mm day^{-1}). This is not that surprising given the linkage between changes in precipitation and temperature at the global scale.

2.6 Effective radiative forcing and surface air temperature response

2.6.1 Effective radiative forcing

The rest of this chapter turns to, and focuses on, the TOA ERF and equilibrium climate responses unless otherwise stated. The spatial distribution of ERF and the corresponding surface air temperature responses are shown in Figure 2.5 (see also Figure 2.6 for the zonal mean temperature changes). Regional mean ERF values are presented in Figure 2.7. The global mean 1970-2010 ERF is 1.56±0.45 W m^{-2}, primarily associated with increases in GHGs (1.50±0.44 W m^{-2}) and tropospheric ozone (0.24±0.01 W m^{-2}), and only partially offset by aerosol changes (-0.11±0.14 W m^{-2}) and stratospheric ozone depletion (-0.07±0.15 W m^{-2}). The spatial distribution of ERF associated with GHG increases (Figure 2.5a) shows substantial uniformity and inter-hemispheric symmetry. In comparison, the ERF associated with aerosol changes (Figure

2.5b) has larger magnitudes in the Northern Hemisphere (where emissions and their changes are the largest), with significant regional differences, and shows a strong anti-correlation with the AOD pattern (Figure 2.3c). For example, anthropogenic aerosol increases in Asia result in a negative forcing of -1.07±0.91 W m^{-2} (Figure 2.7d), while aerosol reductions over Europe and USA produce positive forcings of 2.43±0.48 and 1.43±0.88 W m^{-2} (Figures 2.7e, f), respectively. In addition, the Arctic (Figure 2.7c) sees a positive aerosol forcing of 0.24±0.42 W m^{-2}, related to European and American aerosol reductions. Tropospheric ozone increase (Figure 2.5c) and stratospheric ozone depletion (Figure 2.5d), in general, lead to contrasting forcings. The former generates positive forcing, especially over the Northern Hemisphere and with the largest value over the Arctic (0.47±0.31 W m^{-2}). The latter, on the contrary, generates negative forcing, especially over the Southern Hemisphere.

2.6.2 Temperature response and sensitivity to ERF

While the spatial patterns of the surface air temperature response (Figures 2.5e-h) are broadly consistent with the ERF patterns in the corresponding experiments, there are major dissimilarities. The equilibrium 1970-2010 global mean temperature change, +1.23±0.14 K, is dominated by GHG increases (+1.03±0.16 K). This is also manifested in the zonal mean changes (Figure 2.6). The warming from GHGs is notably amplified over the Poles (Figures 2.5e and 2.6), and the Arctic in particular, despite a globally homogeneous ERF distribution. The 1970-2010 aerosol changes induce a negative global mean ERF (-0.11±0.14 W m^{-2}), resulting in an overall cooling (-0.26±0.14 K). However, the spatial pattern of the temperature response shows substantial

differences from that of the forcing. This can be clearly seen over the Arctic and large part of the oceans, which feature pronounced cooling despite the regional positive ERF.

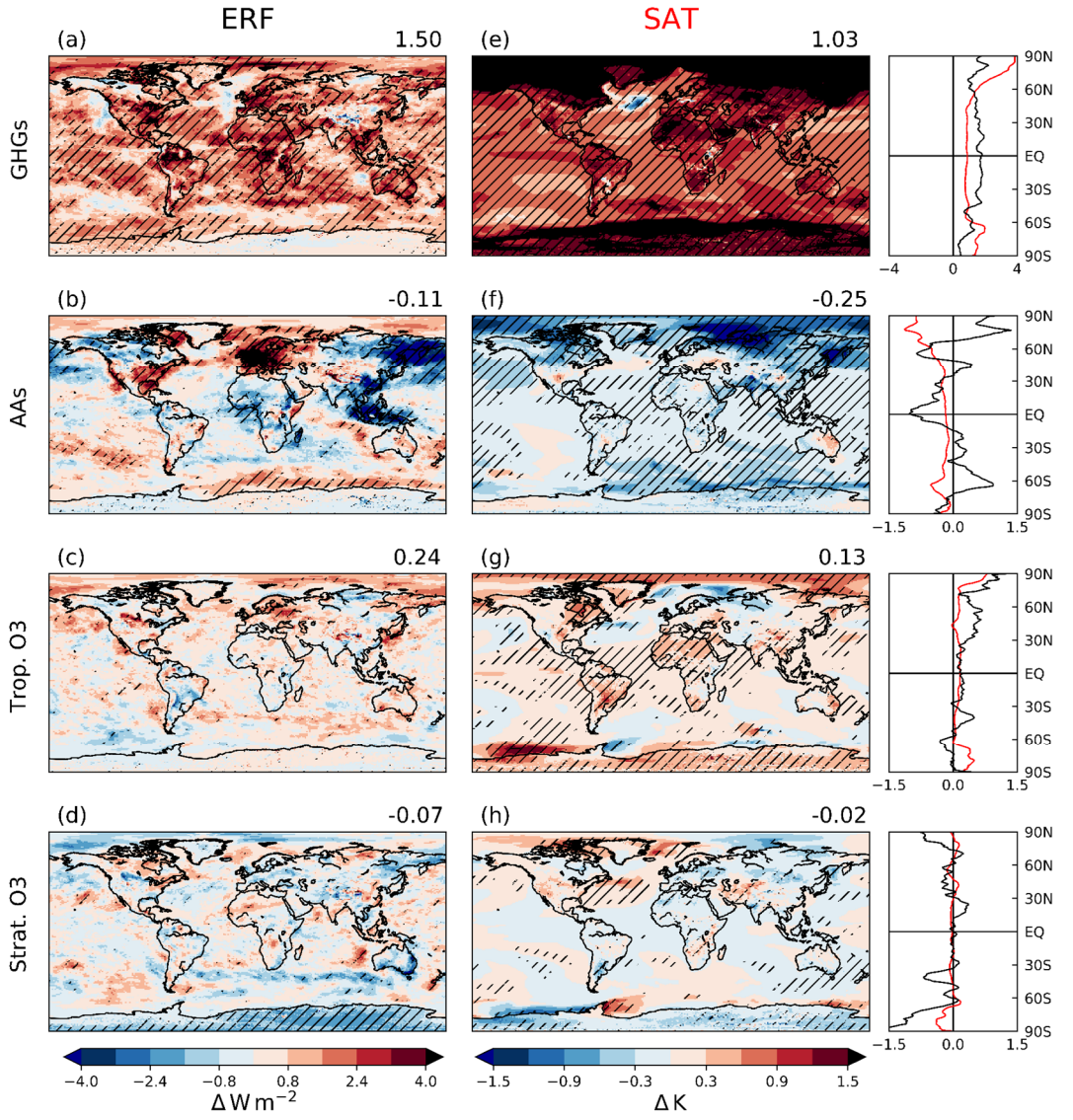

Figure 2.5 Spatial distribution of 1970-2010 (a-d) top-of-the-atmosphere effective radiative forcing (ERF) and (e-h) surface air temperature (SAT), in responses to changes in (a, e) greenhouse gases (GHGs), (b, f) anthropogenic aerosols (AAs), (c, g) tropospheric ozone increase (Trop. O_3) and (d, h) stratospheric ozone depletion (Strat. O_3). The right column shows the zonal mean changes (black for ERF and red for SAT); note the different x-axis scales between GHGs and others, as well as the different units between SAT (K) and ERF (W m^{-2}). Also see Figure 2.6 for the redrafted zonal mean temperature changes for comparison. Numbers on the top right of each panel are the area-weighted global mean values.

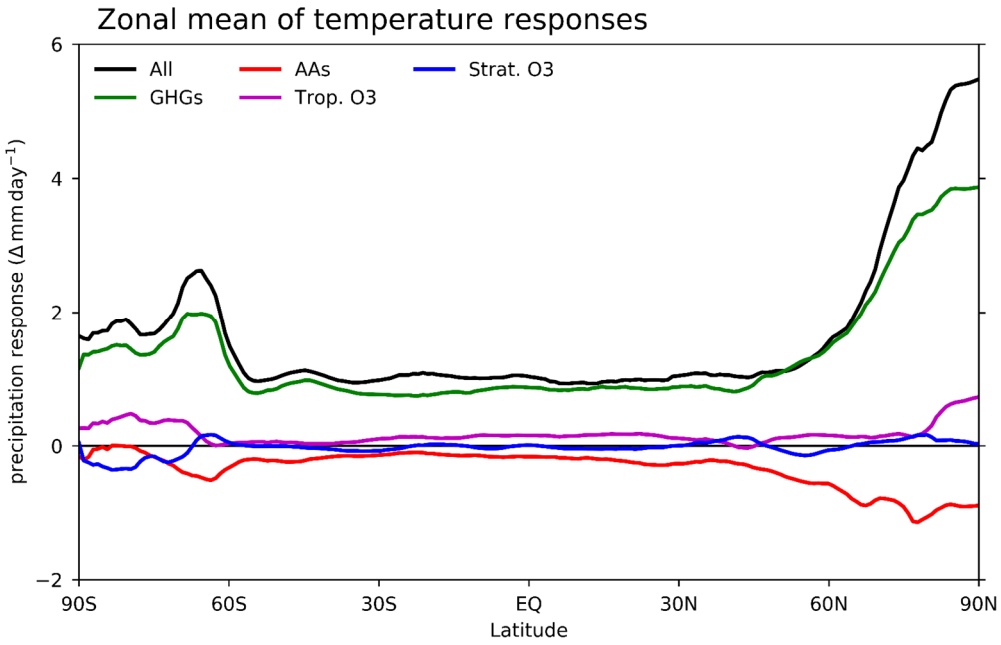

Figure 2.6 Zonal mean profiles of 1970-2010 equilibrium temperature changes (ΔK): the total change (black) are resolved into each individual forcing agent: greenhouse gases (GHG, green), anthropogenic aerosols (AAs, red), Trop. O_3 (purple) and Strat. O_3 (blue). The horizontal line denotes the zero line.

The temperature response to ozone reflects relatively more tightly the spatial pattern of ERF: warming (cooling) from positive (negative) forcing in association with tropospheric ozone increase (stratospheric ozone depletion). However, ozone-related zonal mean temperature responses are generally small in magnitude and indistinguishable from zero except over the polar regions (Figures 2.5 and 2.6). For stratospheric ozone depletion, albeit the relatively small global mean ERF and temperature response, it is reported to have significant impacts on Southern Hemisphere climate by modulating large-scale circulation (Thompson et al., 2011; Previdi and Polvani, 2014; Dennison et al., 2015; Wu and Polvani, 2017). The Antarctic cooling in response to stratospheric ozone depletion is larger than those reported by recent works (McLandress et al., 2011; England et al., 2016; Chiodo et al., 2017; Karpechko et al., 2018). This may imply that the Antarctic temperature response to

stratospheric ozone depletion can be even greater than currently estimated once the climate has fully equilibrated.

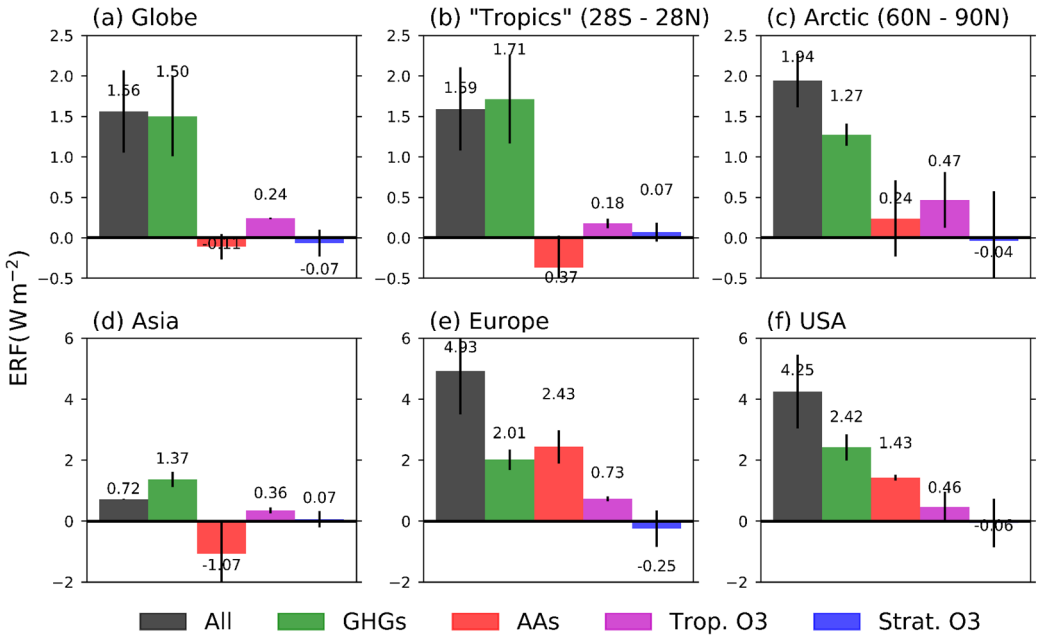

Figure 2.7 Area-weighted mean of 2010 relative to 1970 top-of-the-atmosphere ERF (W m^{-2}) over (a) global scale, (b) Tropical region (28˚S-28˚N), (c) Arctic (60˚N-90˚N), (d) Asia, (e) Europe and (f) USA. The total ERF (black) is resolved into those associated with each forcing agents: GHGs (green), AAs (red), Trop. O_3 (purple) and Strat. O_3 (blue). Error bars indicate the standard deviation spread.

The above analysis indicates that the pattern of surface air temperature response does not necessarily follow the forcing, particularly in the case of aerosols and stratospheric ozone depletion. To point this out even more clearly, the sensitivity of the temperature response per unit ERF globally as well as regionally is investigated. Figure 2.8 shows the ERF sensitivity for various forcing agents. When regional mean temperature changes are normalized by global mean ERFs, the sensitivity values, over all regions, are greater in the experiment where all forcings take effects simultaneously compared to the experiment where GHGs take effect alone. This also applies when regional mean temperature responses are normalized by regional mean

ERFs, with exceptions over the Arctic (Figure 2.8d), Europe (Figure 2.8g) and North America (Figure 2.8i).

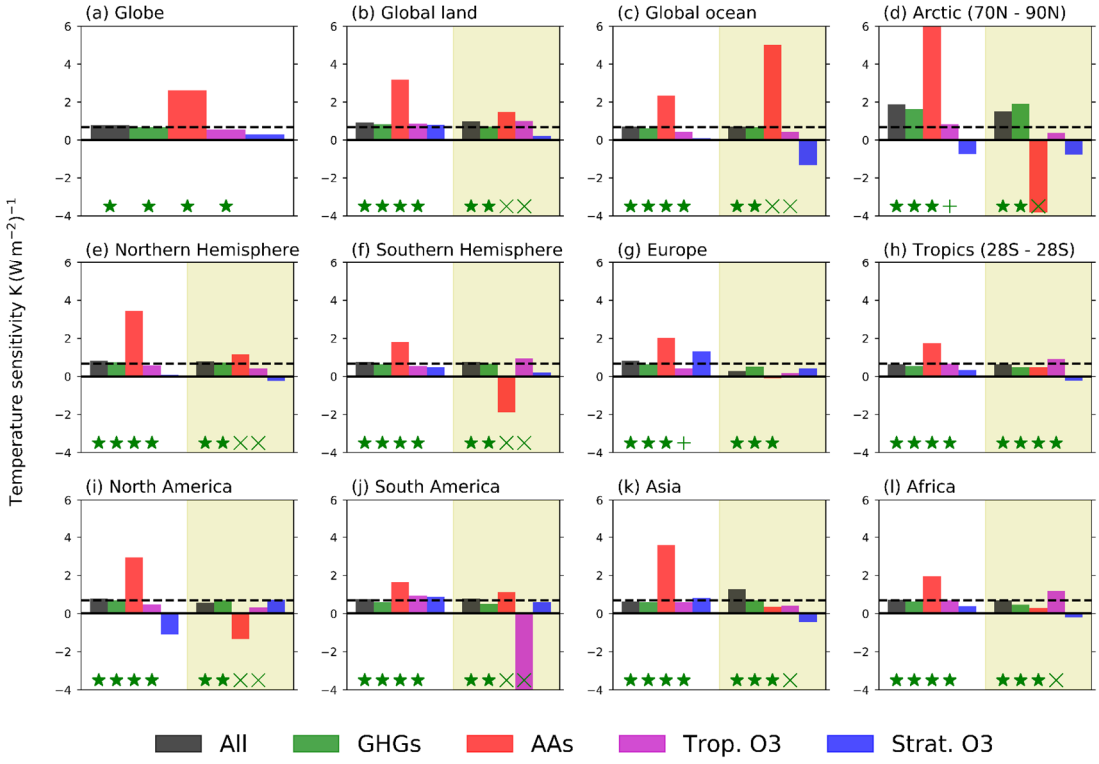

Figure 2.8 The sensitivity (K (W m^{-2})$^{-1}$) of area-weighted mean temperature responses per unit ERF from all forcings (black), GHGs (green), AAs (red), Trop. O_3 (purple) and Strat. O_3 (blue). The response is normalized by global (white background) and regional (yellow background) mean ERFs. The blue dashed lines indicate the global mean temperature response normalized by global GHG forcing (0.68 K (W m^{-2})$^{-1}$). The results are shown for (a) globe, (b) global land, (c) global ocean, (d) Arctic (70˚-90˚N), (e) Northern Hemisphere, (f) Southern Hemisphere, (g) Europe, (h) Tropics (28˚S-28˚N), (i) North America, (j) South America, (k) Asia and (l) Africa. Green stars denote that both global/regional mean ERF and temperature response are statistically significant (p-value ≤0.05, two-tailed student t-test), while green plus and cross denote, respectively, that only ERF or temperature response is statistically significant.

The sensitivity is largest over the Arctic (Figure 2.8d), due to large local sea-ice albedo-related positive feedbacks. Anthropogenic aerosols, surprisingly, result in a much larger sensitivity when normalised against global mean ERF, particularly over the Arctic, North America and Asia (Figure 2.8k), the Arctic, the Southern Ocean (Figure 8f), Europe (Figure 8g) and the USA (Figure 8i). This means that the forcing and the temperature response can be of opposite

sign for aerosols over various domains. For tropospheric ozone, the sensitivity displays large variations across regions. Note the large and negative sensitivity (<-80 K m^2 W^{-1}) over South America. This is explainable given the increase in temperature (Figure 2.5g), albeit the statistically insignificant and negative forcing (Figure 2.5c). Finally, stratospheric ozone has the smallest sensitivity at the global scale and large variability and uncertainties from region to region.

The negative relationship between aerosol forcing and temperature response warrants further discussion. Of particular interest is the large negative sensitivity value over the Arctic. Further analysis (Figure A1) shows that the pronounced Arctic cooling is associated with reduced surface net radiation and cloud fraction, an overall extension of the sea ice-covered areas, and a widespread low-tropospheric anomalous anticyclone. Interestingly, the high-latitude hemispheric-wide anomalies (e.g., temperature, sea ice extent, sea level pressure) are dominated by prominent changes in the North Atlantic and Barents Sea sector. Here, the low-level flow, part of an extensive cyclonic circulation centred over Central Europe (Figure A1a) developing in response to the large regional aerosol reduction and subsequent local warming (Figure 4f), is anomalously southward and counteracts the climatological southwesterlies. (Figure A1a) This reduced the northward transport of moisture to the Arctic region, suppressing cloud formation (Morrison et al., 2019). As clouds reduce (Figure A1b), the increase in surface downward shortwave radiation is overwhelmed by a much larger increase in the surface net longwave component, resulting in reductions in net radiation at the surface (Figure A1c). As a result, the Arctic surface cools and sea ice expands, leading to anomalous Arctic high pressure (Figure A1a) and increases in surface

albedo (Figure A1d). This further enhances the cooling through the sea-ice-albedo feedbacks. Therefore, more cold air is transported southward partially opposing the warming associated with the positive ERF. The above analysis indicates the importance of atmospheric circulation adjustments, rather than the local forcing, in influencing the surface temperature changes at high latitudes (Undorf et al., 2018).

2.7 Precipitation response

2.7.1 Spatial pattern and zonal mean

The precipitation response patterns are shown in Figure 2.9 (see also Figure 2.10 for the zonal mean changes). GHG increases enhance global mean precipitation by 0.06±0.02 mm day^{-1}, with the largest amounts in the eastern equatorial Pacific and the extratropical regions of both hemispheres. Changes in aerosols lead to a global mean precipitation reduction (Figure 2.9b) of -0.04±0.02 mm day^{-1}, with most pronounced changes over Asia (0.13±0.07 mm day^{-1}) and the Western Pacific. Also, a small but noticeable precipitation increase (+0.03±0.07 mm day^{-1}) is found over Europe associated with regional aerosol reductions. features a decrease at almost all latitudes, and particularly over the tropics. The precipitation responses (both the spatial pattern and zonal mean changes) to GHGs and aerosols closely resemble those associated with the 2×CO_2 and 5×SO_4 experiments, respectively, of the Precipitation Driver and Response Model Inter-comparison Project (PDRMIP; Samset et al. (2016)).

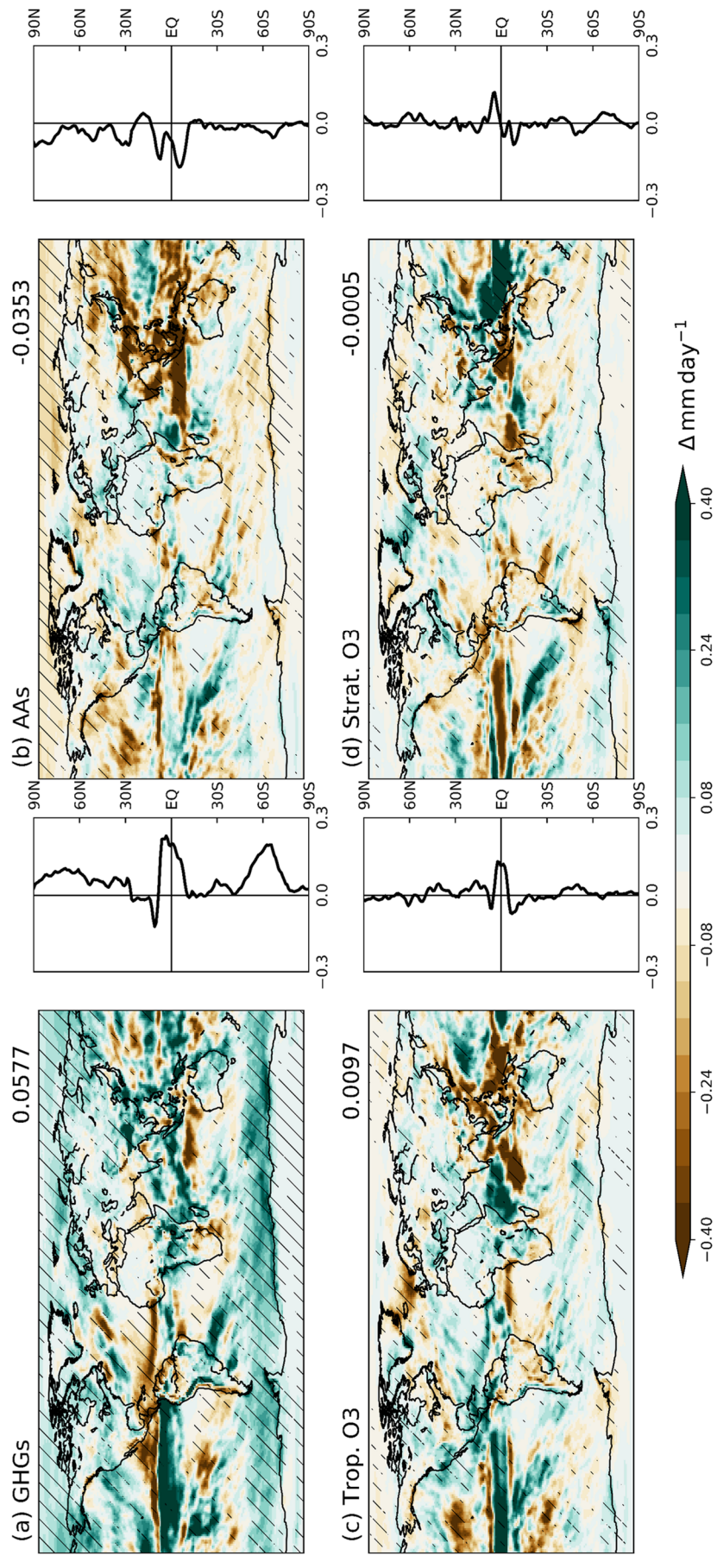

Figure 2.9 Spatial distribution and zonal mean of precipitation changes, in response to (a) GHGs, (b) AAs (c) Trop. O_3 and (d) Strat. O_3. Numbers on the top right of each panels are the global mean values. Also see Figure 2.10 for the redrafted zonal mean precipitation changes for comparison.

The precipitation response to tropospheric ozone increase (Figure 2.9c) bears resemblance to that associated with aerosol changes, particularly over East and Southeast Asia and the Pacific Ocean. However, changes in the zonal mean profile show an enhancement of precipitation at the equator, along with a global mean increase of +0.01 mm day^{-1}. Precipitation changes due to stratospheric ozone depletion (Figure 2.9d) are broadly opposite to those associated with tropospheric ozone increase. More specifically, the precipitation increases over the Western Pacific but decreases over the Eastern Pacific and the Indian Ocean, resulting in an overall weak northward shift of the ITCZ. This generally agrees with Brönnimann et al. (2017) who reported that stratospheric ozone depletion has led precipitation to increase at the northern flank of the South Pacific Convergence Zone and to decrease at the south.

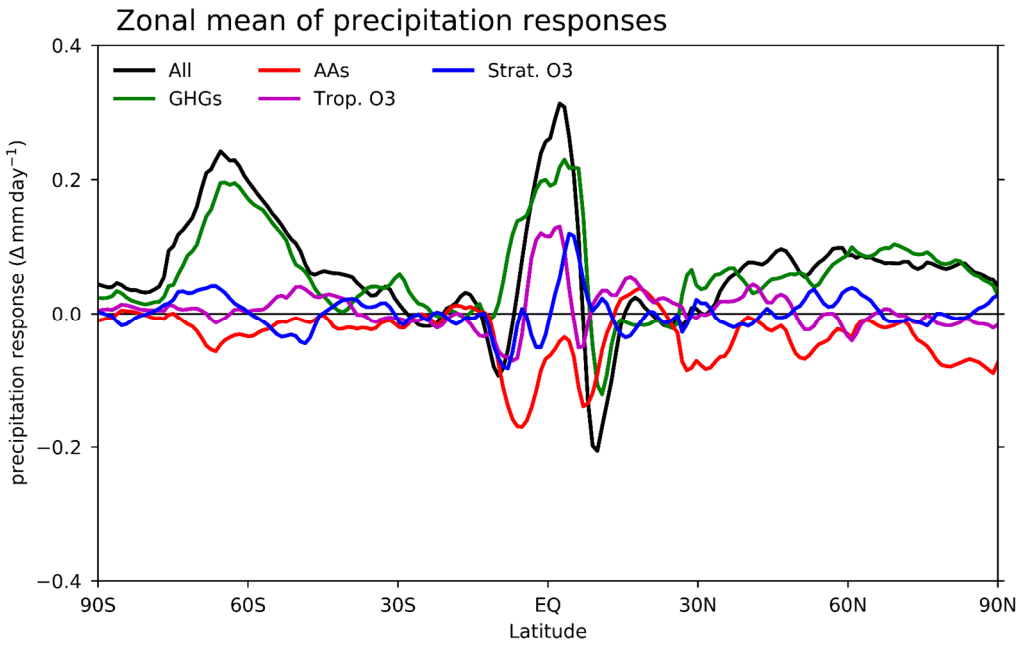

Figure 2.10 The same as Figure 2.6, but for precipitation.

The global apparent hydrological sensitivity in equilibrium is estimated to be 1.4 % K^{-1} in the all forcing experiment, while the estimate from the LENS transient response is 1.3 % K^{-1}. These estimates fit well within the range (1-3 % K^{-1}) reported by phase 5 of the Coupled Model Intercomparison Project (CMIP5; Fläschner et al. (2016)), and suggest that the global apparent hydrological sensitivity does not differ sensibly between equilibrium and transient climate responses in CESM1. However, it worth pointing out that, compared to the all forcing experiment, the sensitivity is larger in magnitude when calculated for individual forcing including GHGs, aerosols and tropospheric ozone (Table 2.3). Also, note that for aerosols, the value is negative because of the decrease in global mean precipitation (Figure 2.9b) despite the 1970-2010 global surface warming (Figure 2.5f).

Table 2.3 The 1970-2010 global apparent hydrological sensitivity (APS, % k^{-1}). Values shown include that calculated from the LENS transient response, and those from equilibrium responses in this study. For equilibrium responses, the values are also calculated for each individual forcing agent.

Experiment	**APS (% K^{-1})**
LENS transient	1.3
CESM1 in equilibrium	1.4
Greenhouse gases	1.8
Anthropogenic aerosol	4.5
Tropospheric ozone increase	2.3
Stratospheric ozone depletion	0.9

2.7.2 Changes in the probability distribution of daily precipitation

To gain further insight into the characteristics of the precipitation responses, variations in the daily precipitation distributions are examined by analysing variations in the frequency distributions (Figure 2.11). Whilst precipitation is,

by nature, spatially heterogeneous which may result, when averaged over large regions, into a partial cancellation between opposite sign anomalies over different sub-regions and thus to a smaller signal, we believe that large-scale averages provide useful information to identify large-scale patterns of changes which are directly linked to the management of country-wide resources and to the development of adaptation strategies. To facilitate quantitative discussion, three precipitation categories are defined: light (precipitation ≤10th percentile of the 1970 climatological distribution), moderate (10th-90th percentile) and heavy-to-extreme (≥90th percentile) precipitation. Note carefully these definitions are only for the purpose of quantitative analysis. Figure 2.11 shows the global (Figure 2.11a) and global land-only (Figure 2.11b) daily precipitation distributions; the remaining panels compare Asia (Figure 2.11c) to Europe (Figure 2.11d). These two regions have opposite 1970-2010 aerosol changes, albeit of different magnitude (Figure 2.3), allowing us to examine whether the corresponding daily precipitation distributions also display opposite responses.

In response to the 1970-2010 changes in all forcings, the global mean daily precipitation distribution shifts to higher values, resulting in a mean shift of the precipitation distribution by +0.06 mm day^{-1} (+1.8%). This is primarily associated with GHG increases (+1.9%). The impact of tropospheric ozone increase on the distribution is similar but secondary (+0.31%) compared to GHGs. By comparison, anthropogenic aerosol increases and stratospheric ozone depletion shift the distribution towards lower values, resulting in a mean precipitation change of -1.1% and -0.03%, respectively. Land-only precipitation changes resemble those at the global scale (land + ocean), but feature a

relatively stronger effect of ozone changes together with a smaller effect of GHGs.

Examining now regional responses, the all forcings-driven changes result in a flatter and wider distribution of daily precipitation over Asia (Figure 2.11c). This is primarily associated with aerosol increases (-4.2%, -0.13 mm day^{-1}) which outweigh the effects of GHGs (+3.4%, +0.10 mm day^{-1}) and tropospheric ozone (+0.1%, +0.00 mm day^{-1}) increase. Noticeably, aerosol increases result in an increase of light (+1.0%) and moderate (+1.3%) precipitation, concurrently with a suppression of heavy-to-extreme precipitation (-2.3%). The magnitude of these changes is larger than that associated with all forcings (+0.5%, -0.3% and -0.2%, respectively). Over Europe (Figure 2.11d), changes in daily precipitation distribution are also strongly influenced by aerosols, but in the opposite way (+0.05 mm day^{-1}, +2.6%) to Asia: aerosol reductions lead the heavy-to-extreme precipitation in Europe to increase by 3.2%, accounting for55% of the 1970-2010 total increase in heavy precipitation. Meanwhile, light and moderate precipitation are suppressed by -0.2% and -3.0%, respectively. Compared to aerosols, there is a relatively smaller contribution from GHG increases (a mean change of +0.03 mm day^{-1}, +1.3%), while the effects of tropospheric ozone increase are approximately balanced by those due to stratospheric ozone depletion.

The above-discussed changes in the daily precipitation distribution over Asia and Europe highlight the dominant role of aerosols over other forcings in modulating local precipitation. This is particularly important for heavy-to-extreme precipitation, being reduced from 10% to 7.7% by aerosol increases over Asia, and increased from 10% to 13.2% by aerosol decreases over

Europe. The contrast between Asia and Europe, therefore, demonstrates the effectiveness of increased (decreased) aerosols in weakening (enhancing) precipitation, respectively.

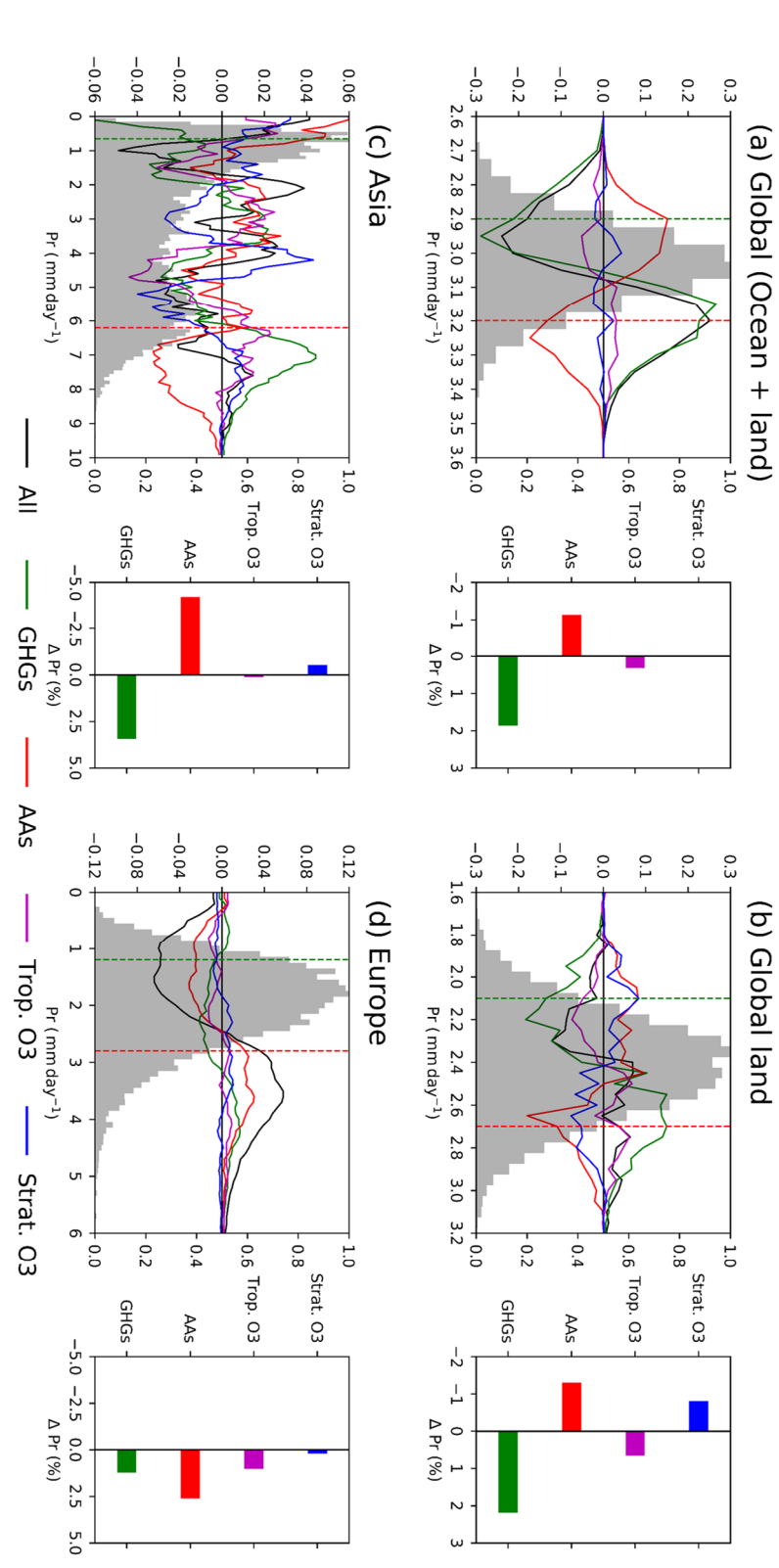

Figure 2.11 The 1970-2010 variations in the probability distribution (PDFs, curves, left axis) of area-weighted mean daily precipitation, as well as the shift of the mean value of the distribution in percent (bars). The PDFs are calculated over bins with a size of 0.05 mm day^{-1} and then normalized by the peak frequency of the corresponding 1970 climatological distribution (grey histogram). The 10th and 90th percentiles of the climatological distribution are denoted by the green and red vertical dashed lines, respectively. Note for Asia and Europe, the variations in the probability distributions (curves) are merged into larger bins (0.5 mm day^{-1}) for legibility. Results are shown for (a) globe, (b) global land, (c) Asia and (d) Europe. The 1970-2010 total changes are resolved into each individual forcings: GHGs (green), AAs (red), Trop.O_3 (purple) and Strat.O_3 (blue).

2.8 Discussion and conclusions

Human activities have altered both the composition and (chemical and physical) properties of the atmosphere since the industrial era (Acosta Navarro et al., 2017). Such changes are even more distinctive during the past four decades (1970-2010). Specifically, on top of the steady GHG increases, there are contrasting trends of air pollutant emissions between developing and developed regions (Hoesly et al., 2018; Wang et al., 2018a; Zheng et al., 2018; Aas et al., 2019), as well as opposite trends between tropospheric and stratospheric ozone changes (Checa-Garcia et al., 2018). Employing CESM1, time-slice simulations were carried out to investigate the effective radiative forcing and climate response to 1970-2010 changes in these climate forcers, emphasizing the comparison between the individual impacts of GHGs and SLCFs.

Changes in atmospheric composition during 1970-2010 brought about a TOA total ERF of 1.56±0.45 W m^{-2}, mostly due to changes in GHGs (1.50±0.44 W m^{-2}) with secondary contributions from anthropogenic aerosols, tropospheric ozone increase and stratospheric ozone depletion (-0.11±0.14, 0.24±0.01 and -0.07±0.15 W m^{-2}, respectively). These estimates are consistent with the ones reported by the AR5 for the period 1970-2010 (GHGs: 1.48 W m^{-2}; aerosols: -0.20 W m^{-2}; tropospheric ozone increase: +0.14 W m^{-2}, and stratospheric ozone depletion: 0.04 W m^{-2}, see Table AII.12, Chapter 8.1 in Stocker et al. (2013)). The value for tropospheric ozone increase is larger than the AR5 one. This is consistent with Myhre et al. (2017a) who found that ozone forcing is larger than the AR5 estimate during the period 1990-2015, likely due to an increase in NOx emissions which is twice larger than the emission data used

in AR5. The IPCC AR4 (Figure SPM.5) multi-model experiments reported that, in the case where all forcing agents are fixed at their 2000 levels, there is ~0.4 K of additional warming by 2100 due to the slow response of the ocean. The additional warming is around 1/3 of the 1900-2000 transient warming, and 2/3 of the amount occurred in the period 1970-2000 (Meehl et al., 2007). In this study, it is found that, compared to the transient changes, there is an additional global surface warming (+0.6 K) and precipitation increase (+0.03 mm day^{-1}) when present-day climate equilibrates to 1970-2010 emission changes. This in general is consistent with AR4, while the differences can be explained by differences in experiment design. The committed warming may result in changes in many other aspects of the climate system (Schlesinger, 1986; Tricot and Berger, 1987; Williams et al., 2016; Yoshimori et al., 2016) and associated impacts such as global scale precipitation changes discussed above.

The equilibrium climate responses to GHGs and aerosols, in general, agree with literature showing that the historical global mean temperature and precipitation changes are dominated by GHGs (Taylor and Penner, 1994; Min et al., 2011; Stocker et al., 2013; Wang et al., 2016a), while aerosols play important roles in regional precipitation changes (e.g., the drying trend of the Asian monsoon (Yihui and Chan, 2005; Lau and Kim, 2006; Bollasina et al., 2011; Ganguly et al., 2012; Polson et al., 2014; Song et al., 2014; Lau and Kim, 2017; Ma et al., 2017)). However, as opposed to those arguing that the spatial patterns of the climate responses to GHGs and aerosols are similar (Xie et al., 2013; Kasoar et al., 2018; Persad et al., 2018), our results demonstrate that the climate forcing and responses to SLCFs are with large

spatial heterogeneity and uncertainty (Shindell et al., 2015; Aamaas et al., 2017). Xie et al. (2016) estimated a global mean ERF of +0.46 W m^{-2}, a temperature increase of +0.36 K and precipitation increase of +0.02 mm day^{-1} due to 1850-2013 tropospheric ozone increase. These estimates all agree in sign with the estimates in this study for the period 1970-2010, and are around 2-3 times larger in magnitudes. Also, note that the spatial patterns of the precipitation response to tropospheric ozone increase show good agreement with each other (compare Figure 2.9c with Figure 5c of Xie et al. (2016)). For stratospheric ozone depletion, it is acknowledged that the annual global mean values reported here may not be able to reflect fully the impacts which are mainly through modulating austral summer atmospheric (subpolar to tropical latitudes) circulation patterns (McLandress et al., 2011; England et al., 2016; Chiodo et al., 2017; Karpechko et al., 2018). This will be explicitly investigated in future works.

Effective radiative forcing is generally deemed to be a useful indicator of temperature changes (Shindell and Faluvegi, 2009; Myhre et al., 2013; Shindell et al., 2015; Forster et al., 2016; Lewinschal et al., 2019). However, it has also been pointed out that forcing and temperature response are not necessarily collocated, due to many other climate processes and feedbacks such as the atmospheric and oceanic heat transport, and atmospheric circulation adjustments (Boer and Yu, 2003; Shindell et al., 2010; Bellouin et al., 2016; Persad and Caldeira, 2018). Nevertheless, possible links between forcing and temperature response, at least at large scale such as within latitudinal bands, has been suggested (Shindell and Faluvegi, 2009; Flanner, 2013; Shindell, 2014; Shindell et al., 2015). The major appeal behind this is

that such links, if verified, may help develop some simplified metrics for quickly evaluating the climate impacts of possible mitigation strategies in the future (Aamaas et al., 2017; Lewinschal et al., 2019). The links between forcing and temperature response found by above works, with large uncertainties and dependency upon many factors, are derived from highly idealized model experiments which represent only a few facets of the actual climate. In addition, as pointed out by Lewinschal et al. (2019), the temperature response sensitivity also depends on the magnitude of emissions. This suggests that the conclusions (sensitivity values) can vary substantially upon experimental designs with emissions of different magnitude and source location (Feichter et al., 2004; Ming and Ramaswamy, 2009; Wilcox et al., 2015). This study shows that the relationship between forcing and temperature response may work for GHGs, but not for SLCFs; the relationship shows considerable variability depending on the region and forcing agent. The results agree with recent works showing that the regional pattern of climate responses to SLCFs depend on the specific forcing agent, as well as timing and location of emissions (Aamaas et al., 2017; Persad and Caldeira, 2018; Lewinschal et al., 2019). However, the caveat is that the results/conclusions presented here may be model dependent. This is particularly the case for SLCFs, and aerosols in particular, whose climate forcing and response are highly heterogeneous and are not well constrained in present generation climate models.

Additionally, it is found that

- Once present-day climate has reached equilibrium, both the global mean temperature and precipitation changes would be twice as much as those in the transient 1970-2010 simulations.

- Increases in GHGs and tropospheric ozone enhance global mean precipitation and shift the daily precipitation distribution to larger amounts. On the contrary, the overall aerosol increases and stratospheric ozone depletion suppress global mean precipitation and shift the daily distribution toward smaller amounts.
- Compared to the global scale, the effectiveness of SLCFs in changing the characteristics of the daily precipitation distribution is stronger over regional scales. This is especially important for regions such as Asia and Europe where precipitation changes, and the frequency of heavy-to-extreme precipitation in particular, are dominated by changes in aerosols rather than GHGs.

In summary, this study shows that the present-day climate response to the recent (1970-2010) emission changes is far from being in equilibrium, implying that even with current emission levels we have perceived only a fraction of the equilibrium changes to climate and associated risks (Mauritsen and Pincus, 2017). In addition, the concept of effective radiative forcing should be used very cautiously to interpret the impacts of SLCFs. A very representative example is aerosols that are shown to outweigh GHGs in regional precipitation changes, and modulate heavy to extreme precipitation significantly. Given the possibility that emissions/concentrations of SLCFs will decline in the coming decades, it is crucial to reduce the uncertainties in our understanding of the climate impacts of SLCFs. This is critically important to achieve more robust near-future climate projections and to manage climate risks (e.g., drought, flood, heatwaves, air pollution, etc.) more effectively.

Chapter 3 Changes in Aerosols and Climate Driven by Growth in Energy Use and Advances in Emission Control Technology

This chapter is adapted from a published paper on which I am the lead author. I carried out all model experiments, performed all data analysis, and wrote the first draft of the manuscript. Dr David Stevenson and Dr Massimo Bollasina supervised the study, and provided comments on subsequent manuscript revisions. Dr Monica Crippa (Joint Research Center, European Commission) provided emission inventories, and commented on the manuscript.

Zhao, A., Bollasina, M. A., Crippa, M., and Stevenson, D. S (2019). Significant climate impacts of aerosol changes driven by growth in energy use and advances in emissions control technology, Atmos. Chem. Phys.

3.1 Abstract

Using the fully-coupled Community Earth System Model, this study quantifies the effective radiative forcing (ERF) and climate response to 1970-2010 aerosol changes associated with two major policy-relevant emission drivers: energy use growth and technology advances. Emissions from energy use growth generate a global mean aerosol ERF of -0.31±0.22 W m^{-2}, and result in a global mean cooling of -0.35±0.37 K and a precipitation reduction of -0.03±0.02 mm day^{-1}. By contrast, the avoided emissions from advances in emission control technology, which benefit air quality, generate a global mean ERF of +0.21±0.23 W m^{-2}, a global surface warming of +0.10±0.13 K and global mean precipitation increase of +0.01±0.02 mm day^{-1}. Despite the relatively small changes in global mean precipitation, these two emission drivers have profound impacts at regional scales, in particular over Asia and Europe. The total net aerosol impacts on climate are dominated by energy use growth, from Asia in particular. However, technology advances outweigh energy use growth over Europe and North America. Various non-linear processes are involved along the pathway from aerosol/precursor emissions to radiative forcing and ultimately to climate responses, suggesting that the diagnosed aerosol forcing and effects must be interpreted in the context of experiment designs. Further, the temperature response per unit aerosol ERF varies significantly across many factors, including location and magnitude of emission changes, implying that ERF, and the related metrics, need to be used very carefully for aerosols. Future aerosol-related emission pathways have large temporal and spatial uncertainties; our findings provide useful

information for both assessing and interpreting such uncertainties, and may help inform future climate change impact reduction strategies.

3.2 Introduction

Emissions of anthropogenic aerosols and their precursor gases have followed opposite trends between developed (decreases) and developing (increases) regions during the past few decades (Section 1.2.1), and are expected to be significantly reduced worldwide during the 21st century (Markandya et al., 2018). Aerosol mitigation, however, may lead to adverse climate impacts, such as the increased risk of climate extremes (Kloster et al., 2010; Samset et al., 2018). A number of plausible future emission pathways have been designed to seek a compromise between the impacts on environment and climate following aerosol reductions in the near-, medium-, and long-term (Gidden et al., 2018). This uncertainty alone represents a key limiting factor to a robust quantification and isolation of the overall aerosol impact on climate. Yet, possible differences in the climate response to varying aerosol-related emission trajectories, all the other forcings being the same, have been mostly overlooked so far (e.g., Sillmann et al. (2013a); Pendergrass et al. (2015); Bartlett et al. (2016)). This, nevertheless, is useful for partially assessing the uncertainty range of future climate projections related to uncertainties in aerosol-related emission pathways alone, despite the fact that emissions of GHGs also differ between those emission pathways.

The historical emissions of aerosols and their precursor gases, and especially those during the period 1970-2010 (Section 1.2.1), are mainly associated with three important and regulated sectors (industry, power generation and

transportation), while the residual contribution to emissions from residential and agricultural sectors is relatively stationary in time (Crippa et al., 2016; Hoesly et al., 2018). Also, such changes originate primarily from two competing policy-relevant emission drivers: economic growth and policy-driven emission controls (Crippa et al., 2016). The former is associated with energy use growth while the latter includes both air pollution abatement measures and technology advances (hereinafter technology advances for short). To quantify the impacts of these emission drivers, Crippa et al. (2016) developed the Emission Database for Global Atmospheric Research (EDGAR) retrospective air pollution emission scenarios for the period 1970-2010. Using a chemistry-climate model, Turnock et al. (2016) reported that the avoided emissions due to legislation and technology measures have improved air quality and human health over Europe, but have also led to a regional warming up to 0.45±0.11 °C.

As discussed above, energy use growth and technology advances are two of the major policy-relevant drivers of past aerosol changes via, for example, changes in power generation, industry and transportation. These drivers are very likely to continue to play important but competing roles in modulating future aerosol-related emission, as we gradually transit to a new energy structure. An analysis of the climate impact to recent changes in the two above emissions drivers is therefore critically important for future aerosol related climate projections and climate change impact reduction strategies. Here we perform time-slice model simulations using the fully-coupled Community Earth System Model (CESM1), seeking to quantify the climate forcing and impacts of aerosol changes related to the above policy-relevant emission drivers

(energy use growth and technology advances) at both global and regional scales. The aerosol scenarios used here represent the best estimates of past emissions. Therefore, compared to idealized experiments where aerosol emissions/concentrations are scaled rather arbitrarily, the implications of this study can be more informative for future decision-making.

3.3 Methods

3.3.1 The EDGAR retrospective emission scenarios

Based on the EDGAR4.3.1 best estimates for 1970 and 2010 (REF2010, Table 3.1), the EDGAR retrospective emission scenarios were designed to quantify the effectiveness of 1970-2010 changes in energy use and efficiency, technology progress and end-of-pipe emission reduction measures (Crippa et al., 2016). These retrospective scenarios focus on sectors including power generation, industry and road transport (the most regulated ones), whereas emissions from all other sectors are the same as those in REF2010. The highest emission scenario (STAG_TECH, Table 3.1) assumes no further improvements in technologies and abatement measures after 1970, but energy use and different fuel mix as REF2010. The second and lowest emission scenario (STAG_ENE) assumes stagnation of energy consumption since 1970, while fuel mix, energy efficiency, emission factors and abatement measures are the same as REF2010. Therefore, the difference between REF2010 and STAG_TECH represents the 2010-1970 emission reductions due to technology advances. Similarly, the difference between REF2010 and STAG_ENE represents the emission increase due to energy use growth. Note that the above retrospective emission scenarios were deliberately designed to

have emission changes from these two competing drivers to not add up to the total 1970-2010 changes, to quantify the associated impacts from a "what-if" perspective. For example, what would be expected assuming that we had not introduced any air pollution abatement measures since the 1970s (Crippa et al., 2016)? For more details regarding the nonlinearity associated with the retrospective emission scenarios, please refer to Crippa et al. (2016).

3.3.2 Model and experiment design

As in Chapter 2, time-slice model simulations were carried out (Table 3.1) using the fully-coupled CESM1 at the nominal 1-degree resolution (Section 1.5). Anthropogenic aerosols and their precursor emissions are from the EDGAR retrospective scenarios described above. The EDGAR emission sectors are remapped to conform to CAM5 emissions following (Lamarque et al., 2010).

Table 3.1 Overview of the fully-coupled (Fcpd) and the paired simulation (Fsst) where sea surface temperature and sea ice are fixed. They are: the baseline 2010 (B10) simulation, fixing aerosol-related emissions in 1970 levels (SAA), stagnation of anthropogenic aerosol-related emissions from energy use in 1970 levels (SEN), and stagnation of aerosol-related emissions related to technology and abatement measures in 1970 levels (STC). All Fcpd simulations are run into equilibrium (numbers in brackets denote the lengths of model integrations in years), while all Fsst runs are integrated for 40 years. Only the last 30 years of each Fcpd/Fsst run are used for analysis. Note the difference in the integration lengths of Fcpd simulations, which is determined on the criterion that the top-of-the-atmosphere radiation imbalance no longer shows significant trends (stabilizing at around ~0.3 W m^{-2} in this case) during the last few decades of each run (see the main text). The response to the best estimate of 1970-2010 anthropogenic aerosol-related emissions: best estimate = B10-SAA, energy use growth = B10–SEN; technology advances = B10–STC.

Experiment (length of Fcpd/Fsst)	Greenhouse gases	Ozone	Natural aerosols	Anthropogenic aerosols
B10 (150/40)	2010	2010	2010	2010 best estimate
SAA (120/40)	2010	2010	2010	1970 best estimate
SEN (220/40)	2010	2010	2010	2010 STAG_ENE
STC (170/40)	2010	2010	2010	2010 STAG_TECH

First, the baseline 2010 (B10) experiment analysed in Chapter 2 is used here. Also, a number of perturbation runs were performed (Table 3.1). For each case, as in Chapter 2, a paired set of two simulations were carried out: one with sea surface temperature and sea ice fixed (hereinafter Fsst), and the other with a fully coupled ocean (Fcpd). All Fcpd simulations were integrated into equilibrium (i.e., where the climate system equilibrates to imposed permutations but the deep ocean) after the initial perturbation, with repeated annual cycles of the forcings. Note that the length of each Fcpd integration is different, and is deemed sufficient for analysis once the top-of-the-atmosphere radiation imbalance does not show significant trends (less than 5% relative to the mean values stabilizing at ~0.3 W m^{-2}) during the last 30-50 years of each simulation (as in Chapter 2). The last 30 years of each time-slice simulation are analysed and the differences between baseline and perturbed simulations are shown here. Specifically, the term “best estimate” is denoted as the responses to the best estimate of 1970-2010 total net anthropogenic aerosol-related emissions, “energy use” for the response to emissions increases due to increased energy use, and “technology advances” for the response to avoided emissions due to advances in emission control technology. The statistical significance of the difference between each two (baseline and perturbed) sets of 30-yr model runs is estimated by the two-sided student t-test (p-value ≤0.05).

The paired Fsst simulation is under the same forcings as the corresponding Fcpd simulation, and is integrated for 40 years from the initial condition. The last 30-years of each Fsst simulation is used to diagnose the effective radiative forcing (ERF) by the top-of-the-atmosphere (top of the model, 3.6 hPa, in this

case) radiative flux following Forster et al. (2016). Additionally, similar Fsst simulations were carried out to diagnose the ERFs of the best estimate of 1970-2010 changes in the three major anthropogenic aerosol species (BC, OC and sulphate). For example, there is a perturbation Fsst run in which only emissions of sulphate species and the prescribed oxidants are changed back to their 1970 levels while all other forcings are the same as B10 to diagnose the ERF due to 1970-2010 sulphate aerosol changes.

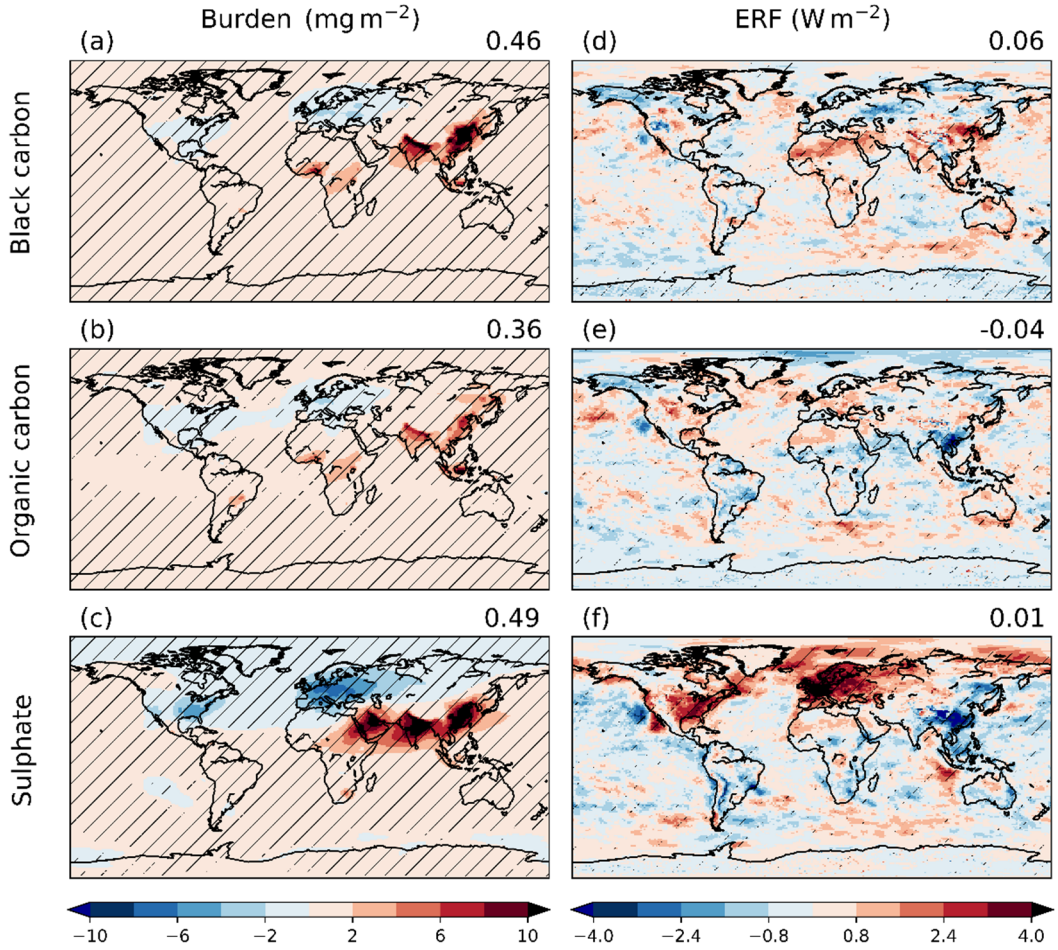

Figure 3.1 Changes in aerosol burdens (mg m^{-2}, left column) and the effective radiative forcing (ERF, W m^{-2}, right column) associated with the best estimate of 1970-2010 changes in emissions of (a, d) black carbon (BC), (b, e) organic carbon (OC) and (e, f) sulphate aerosols (SO_4). The numbers on the top right of each panel are the global means. NB the burden of BC (including the global mean value) is multiplied by a factor of 10 for legibility. Hatches, similarly in all other figures, denote 95% statistical significance level derived by a two-tailed student t-test (p-value ≤0.05).

3.4 Effective radiative forcing and climate response

3.4.1 Effective radiative forcing

Figure 3.1 shows changes in aerosol burdens and the diagnosed ERF associated with the best estimate of 1970-2010 emissions of BC, OC and sulphate aerosols. It can be seen that changes in the burdens of all aerosol species are statistically significant almost worldwide, while areas with statistically significant ERFs are rather confined.

Aerosol burdens display opposite changes between Asia and industrialized regions of Europe and North America. For instance, the burden of SO_4 increases by 5.6 mg m^{-2} in Asia but decreases by -4.0 mg m^{-2} in Europe. BC changes are shown to generate a global mean positive radiative forcing of +0.06 W m^{-2}; the spatial pattern of BC ERF is positively correlated to that of the burdens, resulting in peak values over Asia and Africa. In contrast to BC, OC changes generate a global mean negative forcing of -0.04 W m^{-2}; note also the general spatial anti-correlation between OC burdens and ERF values. The global mean ERF of sulphate aerosol changes is small in magnitude because of the partial cancellation between the negative forcing from sulphate aerosol increases over Asia and the pronounced positive forcing from sulphate aerosol reductions over Europe and North America which is amplified over the Arctic (Figure 3.1f). Yet, it can be seen that regional ERF values are dominated by sulphate species. It must be noted that the individual ERF values of each aerosol species do not add up to that due to the simultaneous changes in all these at the global scale (Figure 3.2d). A further discussion on this is provided in Section 3.5.1.

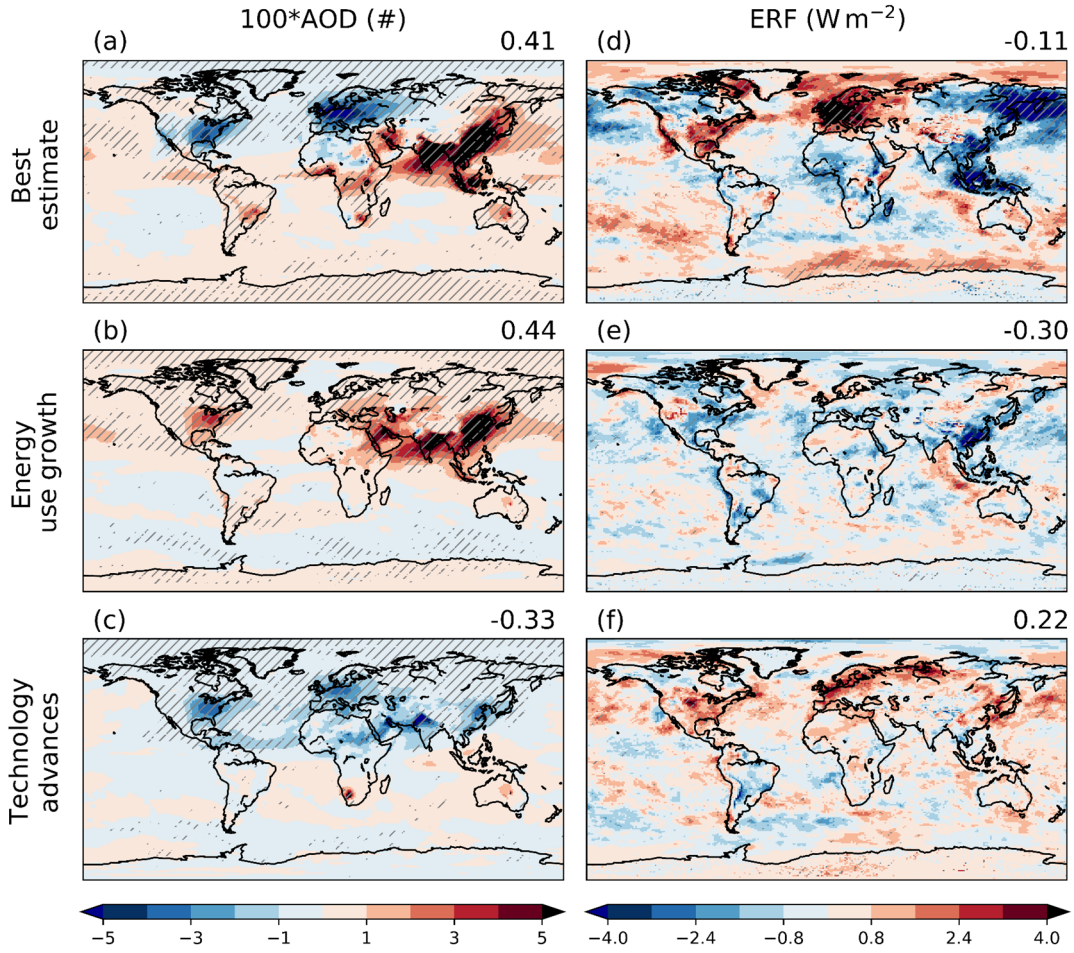

Figure 3.2 Changes in (a-c) Aerosol Optical Depth multiplied by a factor of 100 (100*AOD, 550 nm) and (d-f) the effective radiative forcing (ERF, W m^{-2}) in response to 1970-2010 anthropogenic aerosol/precursor emission changes. They are: (a, d) the best estimate of total emission changes, (b, e) changes due to energy use growth and (c, f) changes due to advances in emission control technology. The numbers on the top right of each panel are the global means (NB again the AOD ones are multiplied by a factor of 100).

The spatial patterns of the changes in the 550-nm Aerosol Optical Depth (AOD) are strongly correlated with those of aerosol burdens (compare Figure 3.1a-c to Figure 3.2a). Therefore, instead of aerosol burdens, we turn to change in the total AOD of all aerosol species for the three scenario experiments where all aerosol species change simultaneously. The total net 1970-2010 AOD changes (Figure 3.2a), not surprisingly, display a sharp contrast between Asia (+0.036) and Europe (-0.023) and North America (-

0.004). This, as described above, is mainly driven by changes in sulphate aerosols (Figure 3.1c). The 1970-2010 aerosol-related emission changes produce a global mean ERF of -0.11±0.14 W m^{-2}, with marked regional values over Europe (+2.3±1.4 W m^{-2}) and Asia (-1.06±0.72 W m^{-2}; Figure 3.3b). Aerosol changes due to energy use growth lead AOD to increase almost worldwide (Figure 3.2b), resulting in a global mean ERF of -0.31±0.21 W m^{-2}, with the most noticeable negative forcing of -0.88±0.60 W m^{-2} over Asia followed by -0.51±0.53 W m^{-2} over North America (Figure 3.3b). By contrast, the avoided emissions due to technology advances lead AOD to decrease predominately over the Northern Hemisphere (Figure 3.2c), and generate a global mean positive forcing of +0.21±0.23 W m^{-2} (Figure 3.2f). The most noticeable changes are found over Europe (+1.16±1.11 W m^{-2}) and North America (+0.53±0.49 W m^{-2}). It worth noting the AOD increases over Southern Africa due to increases in sea-salt and OC which may be related to the additional warming induced changes in meteorology in the technology advances experiment.

3.4.2 Temperature response

Figure 3.4 shows the spatial distribution and zonal mean profile of the surface air temperature responses. Also see Figure 3.3c for the regional mean values. It can be seen that the majority of statistically significant temperature changes in response to aerosol changes are over the ocean rather than the land. This is particularly true for the energy use experiment, and may reflect the fact that the equilibrium climate response is dominated by the slow response of the ocean. In response to the 1970-2010 aerosol changes, the global mean surface temperature changes by -0.26±0.14 K, while there are confined and

weak warming patterns over local regions including Eastern Europe and USA (Figure 4a). The zonal mean temperature changes show significant cooling of the Northern Hemisphere that is amplified over the Arctic (-0.83±0.60 K), together with a less pronounced cooling in the Southern Hemisphere. The sign of global mean surface temperature change due to 1970-2010 aerosol changes is consistent with that of ERF. Note, however, the inconsistency between regional mean ERFs and temperature responses (e.g., particularly over the Arctic, Europe and the Southern Ocean). Further analysis shows such inconsistency may be associated with reductions in Arctic clouds due to a widespread low-tropospheric anomalous anticyclone over the Arctic together with an extensive cyclonic circulation centred over Central Europe as well as the resultant decreases in surface net radiation (see Chapter 2) The anomalous southerlies transport cold advection southward and partially oppose the warming associated with the local positive ERF in high latitudes, leading to pronounced high-latitude cooling that is further amplified through the sea ice-albedo-cloud related feedbacks. (Kay et al., 2012; Najafi et al., 2015; Sand et al., 2015; Navarro et al., 2016; Dobricic et al., 2019). For more details, please refer to Zhao et al. (2019b).

Aerosol-related emissions from energy use result in a relatively homogenous cooling that is statistically significant almost worldwide, and over the oceans in particular (Figure 3.4b), with a global mean cooling of -0.35±0.17 K. The cooling is enhanced over the Arctic (-0.92±0.73 K). It can be seen that both the spatial pattern and zonal mean of temperature changes due to energy use growth induced aerosol changes resembles very well those of the 1970-2010 best estimate, but with much larger magnitudes of changes. This demonstrates

energy use as a major contributor to the 1970-2010 aerosol changes induced climate impacts, which is particularly the case over Asia and the Arctic.

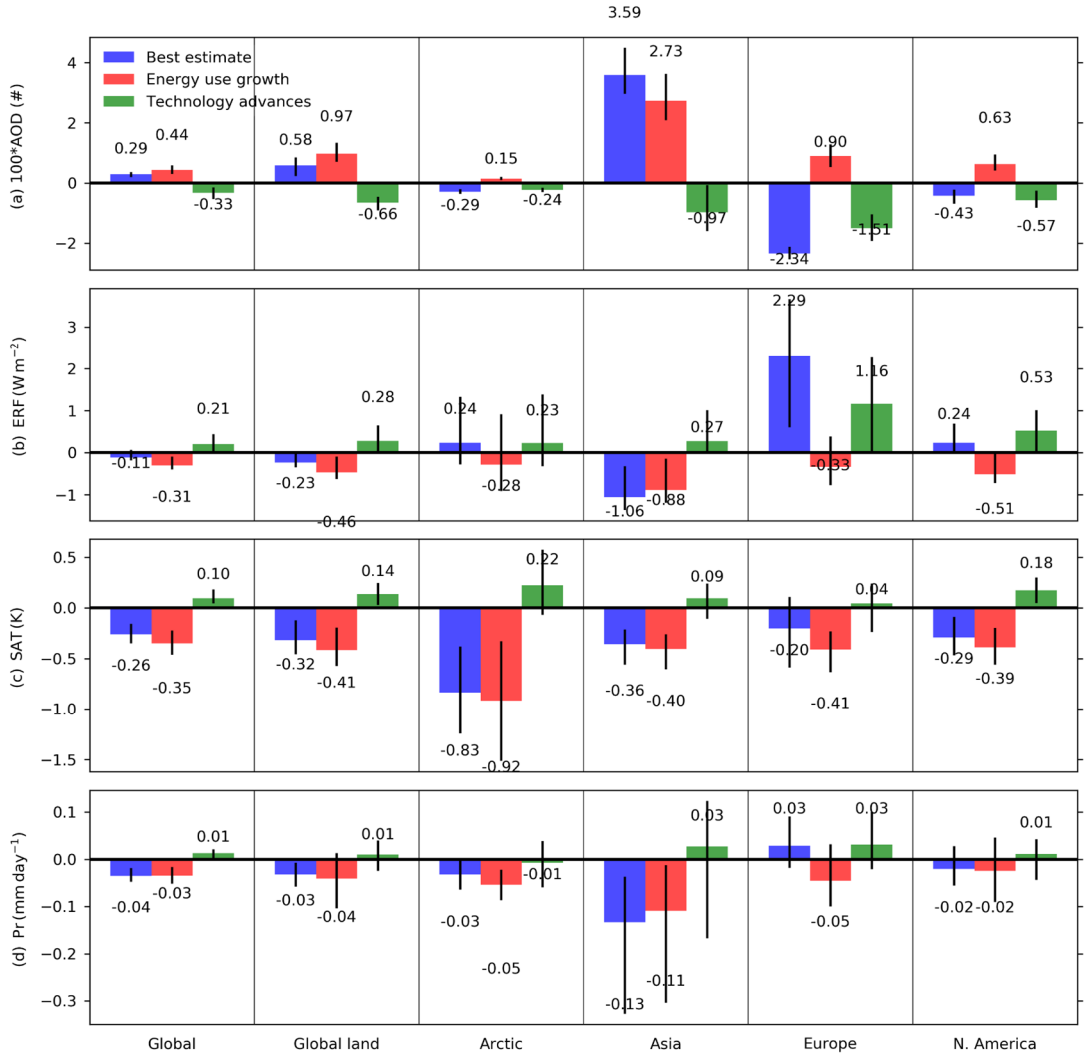

Figure 3.3 Area-weighted global and regional mean changes in (a) Aerosol Optical Depth multiplied by a factor of 100 (100*AOD), effective radiative forcing (ERF, W m^{-2}), surface air temperature (SAT, K), and precipitation (Pr, mm day^{-1}). Error bars denote the 25th–75th percentile spread of the model uncertainty. Region definitions are as follows: Arctic (0°E-360°E, 60°N–0°N), Asia (65°E–145°E, 5°N-45°N), Europe (10°W–40°E, 30°N-70°N) and North America (190°E-300°E, 12°N-70°N). Colour conventions are: blue for responses to the best estimate of 1970-2010 anthropogenic aerosol changes, red for responses to aerosol changes due to energy use growth and green for advances in emission control technology. NB the AOD values are multiplied by a factor of 100 for legibility.

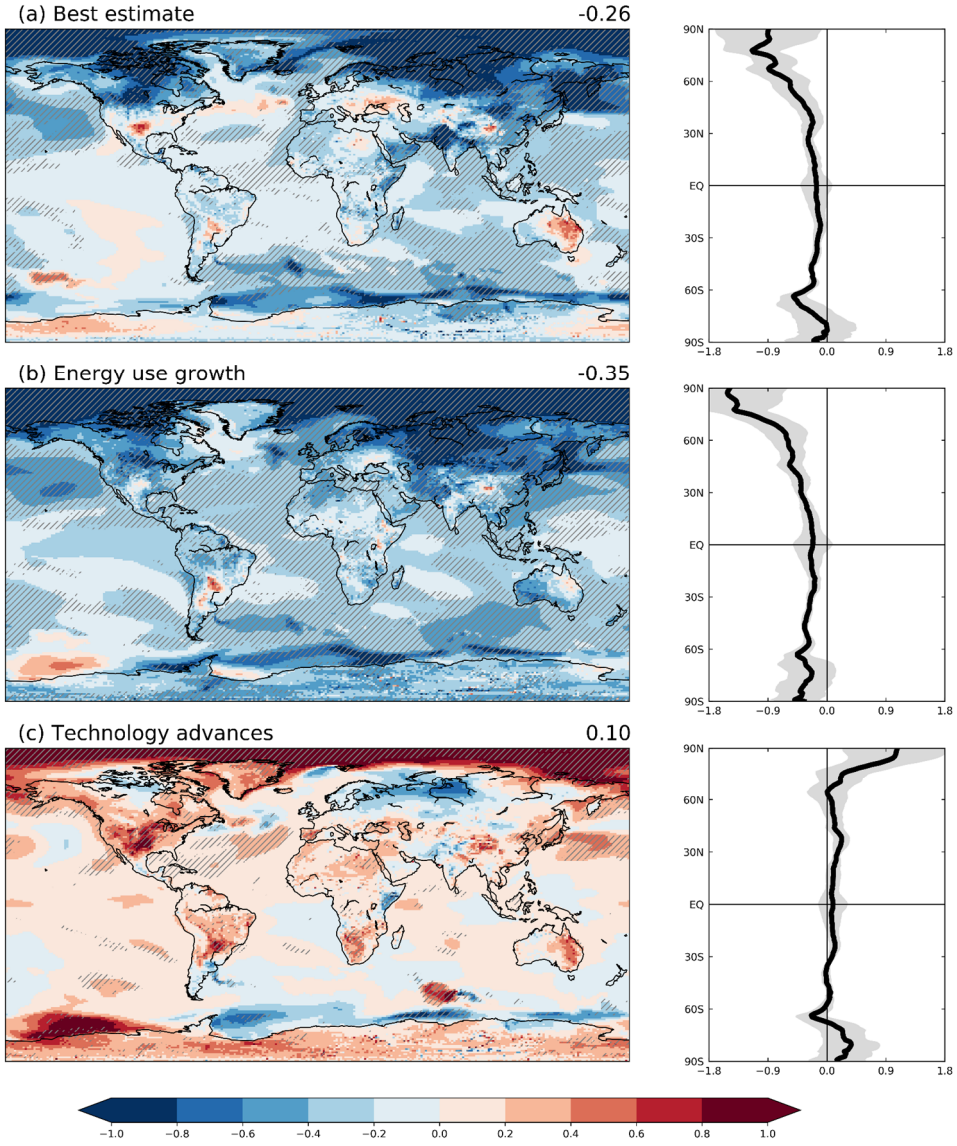

Figure 3.4 Annual mean surface air temperature change (Δ K), in response to 1970-2010 anthropogenic aerosol changes. They are: (a) the best estimate of total aerosol changes, (b) changes due to energy use growth and (c) changes due to advances in emission control technology. The numbers on the top right of each panel are the global mean values. Also shown are the mean (solid) and standard deviation (30 model years; shadings) of the zonal mean temperature response.

The avoided aerosol-related emissions from technology advances (Figure 3.2c) lead the globe to warm by +0.10±0.13 K, with the most pronounced responses over the Arctic (+0.22±0.61 K) and North America (+0.18±0.19 K). Yet, the warming effects can also be seen over other regions including Asia,

Africa, and South America, despite the relatively smaller aerosol reductions in these regions related to technology advances. Note clearly that the temperature responses are with large uncertainties. The zonal mean temperature response is only distinguishable from zero over the Northern Hemisphere mid-latitudes (~30°N) and the polar regions. It is worth pointing out the noticeable cooling pattern over Europe despite the large positive forcing (+1.16 W m^{-2}; Figure 3.2f). This is shown to be related to the adjustments in the atmospheric circulation that results in anomalous cold advection from higher latitudes, overwhelming the effects of local surface radiation increases.

The competition between technology advances (Figure 3.4c) and energy use (Figure 3.4b) growth can be clearly seen in modulating the spatial pattern of global temperature changes, with the global mean values (0.10 K and -0.35 K respectively) almost add up to that in the best estimate experiment (-0.26 K). Note however that regional mean values do not add up, with Northeast Eurasia and the Atlantic Ocean in particular, where the two drivers reinforce each other in changing local temperature changes.

As described above, despite the broad consistency between the patterns of aerosol ERF (Figure 3.2) and temperature response (Figure 3.4), there are also notable dissimilarities. This is particularly true at over the high latitudes, where changes in atmospheric circulation are shown to play important roles in local surface temperature responses. To point this out more clearly, we calculate the temperature response per unit aerosol ERF (temperature sensitivity) over various domains (Figure 3.5). It can be seen that the relationship between ERF and temperature response is far from being linear

even at the global scale and over latitudinal bands. For example, the global mean sensitivity value ranges from 0.5 K $(W\ m^{-2})^{-1}$ in the technology advances experiment to 2.4 K $(W\ m^{-2})^{-1}$ in the best estimate experiment. Also, note the negative temperature sensitivity values at various local regions (i.e., the Arctic, Europe, North America, Asia, etc.), questioning ERF as a useful predictor of temperature change for aerosols.

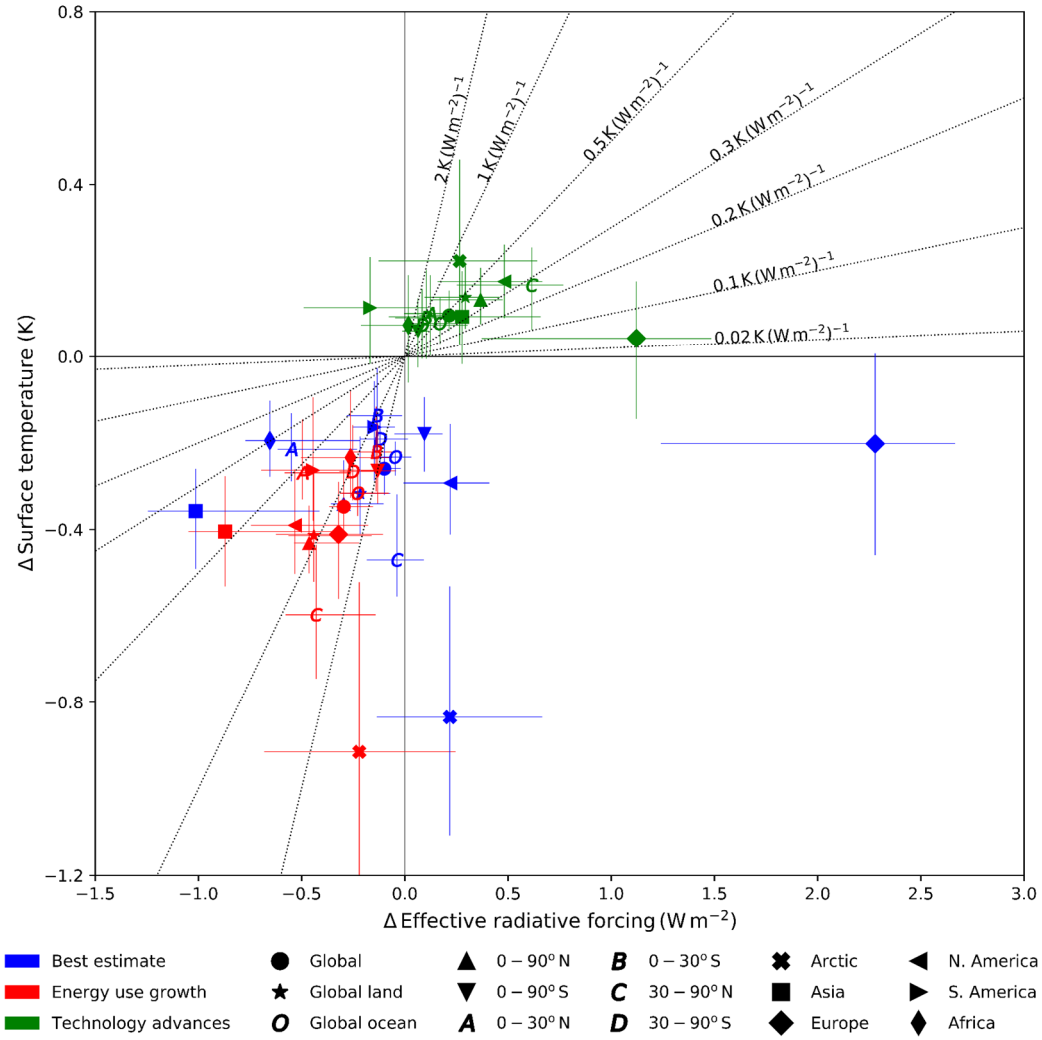

Figure 3.5 Scatterplot of surface air temperature responses (Δ K) vs. effective radiative forcing (Δ W m^{-2}). The error-bars represent the 25th-75th percentile spread of the model uncertainty. The dashed slope lines crossing the origin indicate the sensitivities of the temperature response to ERF with a unit of K $(W\ m^{-2})^{-1}$. Region definitions are as follows: Arctic (0°E-360°E, 60°N–0°N), Asia (65°E–145°E, 5°N-45°N), Europe (10°W–40°E, 30°N-70°N), North America (190°E-300°E, 12°N-70°N), South America (278°E-326°E, 56°S-12°N) and Africa (20°W-60°E,-35°S-25°N) plus latitudinal bands. Colour conventions are the same as Figure 3.3.

3.5 Precipitation response

Changes in precipitation show complex spatial patterns (Figure 3.6) and much larger uncertainties (Figure 3.3d) compared to temperature responses. Overall, the 1970-2010 aerosol changes result in a global precipitation reduction (-0.04±0.02 mm day^{-1}), with the most pronounced changes over Asia (-0.13±0.28 mm day^{-1}) and adjoining oceans (Figure 3.6a). By comparison, precipitation increase can be seen over Europe (+0.03±0.08 mm day^{-1}) and the North Atlantic Ocean. Despite the large uncertainties, the zonal mean changes show precipitation reductions at almost all latitude bands. The pronounced precipitation reductions over Asia reflect partly the 20^{th} century drying trend of the Asian monsoon (Yihui and Chan, 2005; Lau and Kim, 2006; Bollasina et al., 2011; Ganguly et al., 2012; Polson et al., 2014; Song et al., 2014; Lau and Kim, 2017; Ma et al., 2017),

The globe, especially land areas, gets even drier in response to aerosol changes from energy use growth (Figure 3.6b). The precipitation change in Asia (-0.11±0.30 mm day^{-1}) is close to that associated with the best estimate of 1970-2010 aerosol changes (-0.13±0.28 mm day^{-1}). This, as also in temperature response, suggests that aerosol changes from energy use growth exert the predominant control on precipitation changes over Asia. The precipitation reduction is also notable over Europe (-0.05±0.09 mm day^{-1}). Along with precipitation decreases at almost all latitude bands, and the tropics in particular, zonal mean precipitation changes show a weak but southward shift of the Inter-Tropical Convergence Zone (ITCZ), leading to weak precipitation increases over the Southern Hemisphere subtropics (10-30°S).

On the contrary to energy use growth, technology advances lead precipitation to increase globally (+0.01±0.02 mm day^{-1}) and particularly in the Northern Hemisphere, along with its warming effect (Figure 3.4c). There are precipitation increases over Europe, Mediterranean and Northern Africa (Figure 3.6c). In comparison, prominent precipitation decreases can still be seen over Southeast Asia and the North Indian Ocean. Meanwhile, the zonal mean precipitation profile shows a marked northward shift of the ITCZ with notable precipitation reductions over the Southern Hemisphere tropics.

Similar to temperature changes, the 1970-2010 precipitation changes induced by aerosol changes also demonstrate competition between the two emission drivers, yet the values do not add up to that in the Best Estimate case even when globally averaged. Generally, the global mean precipitation changes with temperature at a rate of 0.09-0.15 mm day^{-1} K^{-1}. This is slightly larger than the multi-model mean estimate (~28.6 mm yr^{-1} K^{-1}, i.e., ~0.08 mm day^{-1} K^{-1}) for the slow climate response component derived from the Precipitation Driver Response Model Intercomparison Project (PDRMIP; Samset et al. (2016)). Most of the global and regional mean responses follow to some extent the linear increase (compare Figure 3.3c to 3.3d), but Asia, Europe and the Arctic deviate significantly from the linear relationship. This supports previous studies demonstrating that regional precipitation responses are not simply linked to temperature through regional energy budget constraints, but also depend on other factors such as prevailing circulation patterns and remote teleconnections (Bollasina et al., 2014; Wilcox et al., 2018; Lewinschal et al., 2019). Overall, the above indicates the importance of changes in aerosol-related emissions in both global and regional precipitation changes. This is

particularly true for Asia and Europe which represent the major sources of present-day aerosol-related emissions. In addition, aerosol changes are shown to have important influences on the ITCZ that tend to shift it towards the warmer hemisphere (Allen and Sherwood, 2011; Hwang et al., 2013; Allen and Ajoku, 2016; Acosta Navarro et al., 2017; Liu et al., 2018).

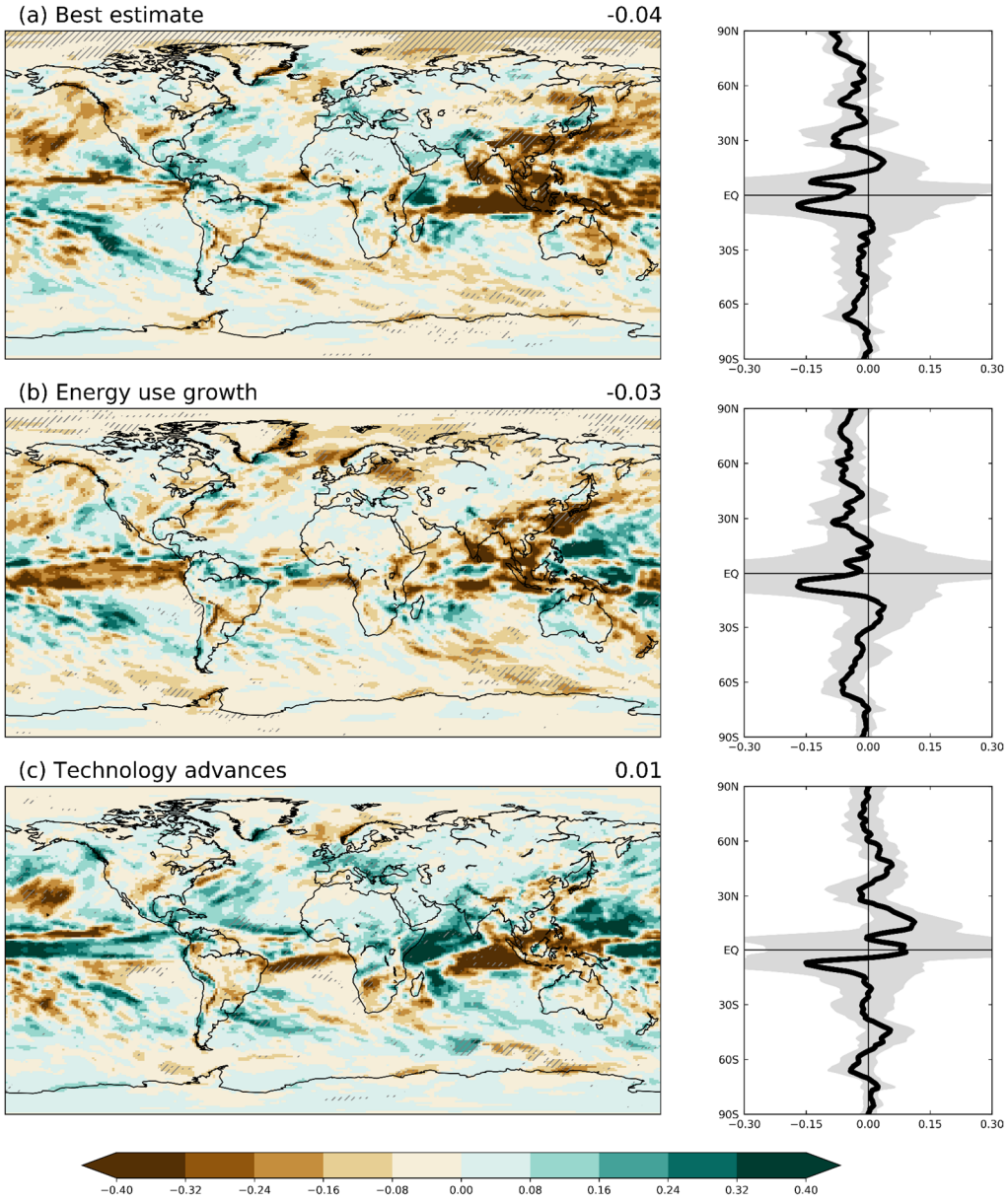

Figure 3.6 The same as Figure 3.4, but for precipitation response (Δ mm day $^{-1}$).

3.6 Discussion

3.6.1 Nonlinearities

Instead of linearly attributing the total aerosol-related emission changes into individual contributing factors, a “what-if” approach was adopted to develop the EDGAR retrospective scenarios (Crippa et al., 2016). This design is useful to assess the effectiveness of major drivers of aerosol-related emissions and allows us to show explicitly the policy-choice driven impacts, while accounting for nonlinear interplays between individual factors. However, this approach adds extra nonlinearities to the results presented here in that, as discussed throughout this study, aerosol changes from energy use and technology advances do not add up to the total net 1970-2010 emission changes. This may suggest the existence of other factors taking effects, while it is almost impossible to attribute the residuals to such factors. Nevertheless, even when total emissions are linearly decomposed into individual contributing factors, it is reasonable to expect both the radiative forcing and climate responses to not linearly add up because of a variety of intertwined mechanisms. For example, the location-dependent lifetime of different aerosol species (Liu et al., 2012), and the forcing efficacies (Kasoar et al., 2016; Aamaas et al., 2017). At the global scale, despite the nonlinearities in aerosol/precursor emissions and AOD changes, the diagnosed global mean ERF and temperature responses roughly add up (Figure 3). However, this is not the case for precipitation. When averaged regionally, the nonlinearities are more pronounced and can be seen through the pathway from emissions to AOD and ERF, and to temperature and precipitation responses.

In this study, ERF associated with changes in each individual aerosol species is diagnosed as the differences between the baseline Fsst simulation (B10) and the ones where the targeted species (e,g., BC) are kept constant at their 1970 levels while the others are as prescribed in B10. It is noted that changes in the burdens and AOD of the three aerosol species are identical to those in the experiment where all the three species change simultaneously (B10-B70). However, the ERF estimates do not linearly add up to the total. In fact, the residual (0.14 W m^{-2}) is even larger in magnitude than the 1970-2010 total net aerosol ERF (-0.11 W m^{-2}). This reflects partly the nonlinear effect associated with the mixing ratio of different aerosol species as well as the importance of background aerosol loadings. This is particularly important for BC whose effects depend also on the presence of sulphate and organic aerosols (Ramana et al., 2010). That is, given that aerosol species are internally-mixed in MAM3 (i.e. different chemical species are mixed within an aerosol particle), the hygroscopicity of aerosol particles is dominated by the volume of soluble species (organic compounds and sulphate). This means that the nonlinearity in the isolated aerosol ERF may be a reflection of the aerosol scheme in CESM1. More specifically, BC particles tend to be coated with other species (e.g., sulphate, ammonium, and organic carbon) during ageing, thereby enhancing the absorption and the subsequent impacts on cloud microphysics, as well as amplifying their radiative forcing (Haywood and Ramaswamy, 1998; Chung et al., 2012; Wu et al., 2016). That is, the radiative forcing of BC may change with the ratio of BC to SO_4. In this study, the ERF of BC is diagnosed as the difference between the baseline experiment (B10) and that with BC held at the 1970 levels, leading the latter experiment to have a smaller ratio of BC to SO_4 and therefore smaller ERF. As a consequence, the ERF estimate due

to the 1970-2010 changes in BC emissions may be overestimated and may contribute to nonlinearities in the ERF of individual species. Note that these nonlinearities can be further enhanced by processes related to the aerosol-cloud interactions, which are difficult to quantify (Fan et al., 2016; Forster et al., 2016).

Overall, the above discussion illustrates the importance of background aerosol concentrations in estimating the radiative forcing of aerosols. For example, we speculate that diagnosing the ERF of BC the other way round, namely, keeping all other aerosol species at their 1970 levels while changing BC to 2010 levels, would likely result in different ERF estimates. Therefore, it is important to carefully bear in mind the method used when interpreting the ERF and climate responses associated with aerosol changes. For example, the single forcing experiments in the Coupled Model Intercomparison Project (CMIP5; Taylor et al. (2012)), the PDRMIP and other idealized aerosol perturbation experiments (Wang et al., 2015; Samset et al., 2016; Kasoar et al., 2018; Liu et al., 2018; Persad and Caldeira, 2018), as well as the upcoming AerChemMIP (Collins et al., 2017) model experiments all need to be interpreted in the context of their experiment designs.

3.6.2 Caveats on the use of effective radiative forcing

The ERF is generally deemed to be a useful indicator of temperature changes (Shindell and Faluvegi, 2009; Myhre et al., 2013; Shindell et al., 2015; Forster et al., 2016; Lewinschal et al., 2019). Based on ERF, many metrics have been proposed to facilitate comparing the effectiveness of various forcing agents. Also, these metrics are appealing to quickly assess the climate outcomes of

possible future emission pathways, and may hence provide useful information to policymakers (Aamaas et al., 2017; Lewinschal et al., 2019). However, it is known that forcing and temperature response are not necessarily collocated, due to many other climate processes and feedbacks such as the atmospheric and oceanic heat transport, and atmospheric circulation adjustments (Boer and Yu, 2003; Shindell et al., 2010; Bellouin et al., 2016; Persad and Caldeira, 2018). Specifically, ERF and the associated metrics may work for well-mixed forcing agents such as GHGs (see Chapter 2). However, they are misleading and may open to miss-interpretation when used for aerosols and some other short-lived climate forcers.

It is important to stress again that temperature responses do not necessarily follow the ERF of aerosols. The range (0.05-2.40 K (W m^{-2})$^{-1}$) of the global mean temperature response per unit ERF is even larger than that (0.1-1.4 K (W m^{-2})$^{-1}$) reported by Persad and Caldeira (2018). Also, the results suggest that the model simulated temperature response per unit aerosol ERF can differ considerably with even subtle differences in experiment design (e.g. with different amount of aerosols emitted in different locations at different timings). Further, due to the fact that aerosol schemes are represented very differently across present generation climate models; it is highly likely that the sensitivities will differ further upon the choice of climate models. Therefore, as also pointed out by recent works (Persad and Caldeira, 2018; Lewinschal et al., 2019), the large divergence in the temperature response per unit ERF from aerosols highlights the need to use ERF and derivative metrics carefully for aerosols.

3.6.3 Implications for future climate projections

Reliable projections of future climate under different but equally plausible emission pathways are of utmost importance to better constrain the range of possible societal risks and response options. Unfortunately, there are still considerable challenges due to limitations and uncertainties in our understanding of many aspects of the Earth System (Knutti and Sedláček, 2013; Northrop and Chandler, 2014; Marotzke, 2019). Aerosols represent one of the largest sources of uncertainty (Boucher et al., 2013; Lee et al., 2016; Fletcher et al., 2018). Present-day anthropogenic aerosol/precursor emissions are largely influenced by power, industry and transport sectors. However, in some of the future emission pathways, for example, the Tier-1 Shared Socioeconomic Pathways scenarios (SSP1; Gidden et al. (2018)), aerosol-related emissions are expected to decline drastically worldwide as we transit to non-fossil-fuel-based fields together with rapid implementation of air pollution control measures and new technologies. For example, benefiting from China's transition to a less energy-intensive society, for the first time in the century the global coal consumption decreased in 2015 (World Energy Council, 2016). However, the timing and rate of such transitions are largely uncertain. On the other hand, it is also likely that aerosol/precursor emissions will increase, especially over some developing regions, under scenarios where high inequality exist between and within countries. For example, in SSP3, expanding industrial sectors over Southeast Asia will rely continually on traditional energy sources such as coal. Also, it is possible that the world may continue to rely on fossil energy sources more strongly than expected over the coming years, given the concerns about nuclear energy after the Fukushima Daiichi nuclear disaster in March 2011. As a consequence, aerosol-related

emissions from energy use in some regions are expected to increase and therefore offset aerosol reductions elsewhere.

The above reflects the large uncertainties (both spatially and temporally) in our understanding and estimates of future aerosol/precursor emission trajectories, given the possibility that very different future emission pathways may be adopted by different countries to compromise between climate/air pollution impacts and economic growth. Our findings may help better assess and interpret such uncertainties in future climate projections associated with changes in aerosols. First of all, the large impacts of present-day aerosol changes from the two competing drivers, as reported in this work, suggest that the major drivers (e.g., future energy structure and efficiency, air pollution control measurements, as well as technology progresses) of aerosol changes are likely to continue to play important roles in future climate projections. Secondly, uncertainties in future aerosol/precursor emission pathways combine with those of other climate forcing agents (e.g., greenhouse gas emissions and land-use changes). Such uncertainties influence the impacts of aerosol forcing through changing the background climate state (Frey et al., 2017; Nordling et al., 2019; Stolpe et al., 2019). More importantly, our results stress the importance of nonlinearities when comparing and assessing the impacts of different future aerosol-related emission trajectories. This adds further caveats in interpreting future climate projections related to aerosol changes in addition to uncertainties in emission pathways of both aerosols and GHGs.

3.7 Summary and conclusions

Using CESM1, time-slice simulations were carried out to investigate the ERF and climate impacts of 1970-2010 aerosol changes, focusing on two major policy-relevant emission drivers that compete: energy use growth and advances in emission control technology. The 1970-2010 anthropogenic aerosol changes generate a global mean ERF of -0.11±0.14 W m^{-2}. This is dominated by sulphate species, but the ERF estimates resolved into each individual species do not add up linearly to the total. The residual may be associated with the relative ratio of different aerosol species (Kim et al., 2008), as well as many other intertwined nonlinear processes linking aerosol changes to radiative forcing, and to temperature and precipitation responses. These nonlinearities highlight the importance that one must bear aerosol experiment designs carefully in mind when interpreting aerosol forcing and effects. In particular, the background concentration of both GHGs and aerosols may have strong influences on isolated aerosol effects using climate models (Regayre et al., 2018; Grandey and Wang, 2019).

1970-2010 energy use growth leads aerosols to increase over the Northern Hemisphere and Asia in particular, giving a global mean ERF of -0.31±0.22 W m^{-2}, and resulting in a global mean cooling (-0.35±0.17 K) and precipitation reduction (-0.03±0.02 mm day^{-1}). On the contrary, the avoided aerosol-related emissions due to technology advances generate a global mean ERF of +0.21±0.23W m^{-2}, and result in a global mean warming (+0.10±0.13 K) and precipitation increase (+0.01±0.02 mm day^{-1}). Change in aerosols and the resultant climate impacts are dominated by energy use growth over Asia but by technology advances over Europe and North America, while the global

changes reflect competition between these two drivers. Compared to the rest of the world, temperature responses in the Arctic are noticeably amplified because of sea-ice and albedo related feedback processes (Navarro et al., 2016; Wobus et al., 2016; Dobricic et al., 2019). The large temperature responses are likely to be related to changes in aerosols over Europe and North America, while our results demonstrate that aerosol-related emissions from Asia may also play an important role (Westervelt et al., 2015; Wang et al., 2018b; Dobricic et al., 2019). The temperature and precipitation responses to aerosol changes demonstrate influences of adjustments in atmospheric circulation induced by aerosol changes that can overwhelm the effects of local aerosol forcing. This is particularly important over higher latitudes such as the Arctic and Europe, and questions the usefulness of ERF as an indicator of the temperature response to aerosol forcing. We acknowledge the caveat/limitation of this study in that all our findings may be model dependent, which is particularly the case for aerosols, given the high degree of parameterisation and divergence in aerosol schemes across present generation climate models. We also note that CAM5 has a relatively larger aerosol forcing compared to other CMIP5 models (Allen and Ajoku, 2016; Malavelle et al., 2017; Toll et al., 2017; Zhou and Penner, 2017). These findings, therefore, need to be verified using other models, while identifying the possible underlying differences and reasons.

In conclusion, energy use growth and technology advances represent two major drivers of present-day aerosol changes, and have strong and competing impacts on present-day climate. We anticipate that there will be significant but uncertain changes in aerosol-related emissions over the coming decades

driven by these two drivers. Also, there are a variety of nonlinearities in the effects of aerosols, originating from many factors including aerosol experiment design. All these uncertainties and nonlinearities may translate into even larger uncertainties in future climate projections and associated impacts. Given all the findings and implications laid out above, we strongly encourage model groups to better constrain the nonlinearities and uncertainties associated with aerosols in their climate models. Also, we encourage the wider research community to verify and further develop our findings in terms of aerosol-climate interactions and projections, as well as policy-relevant aerosol-related changes and their influences on air quality and associated socio-economic impacts.

Chapter 4 Impacts of Global Air Pollution Driven by Anthropogenic Emissions and Climate Change

This chapter is adapted from a manuscript that is, at the time of writing, in preparation for the journal Nature Climate Change. I carried out all model experiments, performed all data analysis, and wrote the first draft of the manuscript. Dr David Stevenson and Dr Massimo Bollasina provided feedbacks on subsequent manuscript revisions.

Zhao A, Stevenson D.S. and Bollasina M. A., Impacts of global air pollution are policy-controlled tug-of-wars, in preparation for Nature Climate Change.

4.1 Abstract

Global air quality is influenced by both emissions and climate; it has and may undergo further changes in the context of future climate change and mitigations. With this in mind, this study assesses 1970-2010 changes in air pollution and their impacts worldwide, attributing to both climate change and two policy-relevant emission drivers (energy consumption growth as economic growth vs. advances in emission control technology). Changes in air pollution, predominately driven by anthropogenic emissions while climate change also contributes, lead to 1.7 million yr^{-1} of global total $PM_{2.5}$ deaths and 87,000 yr^{-1} attributable to O_3, and 166 million tonnes yr^{-1} of staple crop production loss that values 53 billion USD_{2010}. The impacts attributable to anthropogenic emissions reflect a “tug-of-war” between energy consumption growth and technology advances, implying the important influence of policy interventions. This adds the urgency of developing integrated mitigation policies to minimise climatic and environmental impacts.

4.2 Introduction

Air pollution and climate change are two of the most challenging risks for both human beings and global ecosystems, because of their detrimental impacts on human health (Ellingsen et al., 2008; Anenberg et al., 2010; Anderson et al., 2012; Silva et al., 2016a; Kinney, 2018; Partanen et al., 2018), ecosystem wellbeing (Knapp et al., 2008; Wernberg et al., 2013), infrastructure (DEFRA, 2011), as well as society and economy (Vermeulen, 2002). The links between the emissions of greenhouse gases from human activities and global mean warming have been relatively well established (Stocker et al., 2013). In

comparison, there are large gaps in our understanding of the emissions of short-lived (with a lifetime shorter than CO_2) air pollutants (notably aerosols, ozone, and their precursors) and their climate effects. Additionally, climate change can lead to changes in the spatial-temporal distribution of air pollutants by modifying both emissions and various atmospheric processes (Val Martin et al., 2015; Silva et al., 2017; Kinney, 2018). However, despite recent substantial progress (Fiore et al., 2015; Kinney, 2018), our understanding of the interactions between emissions of air pollutants and climate change is still incomplete and largely uncertain (Collins et al., 2017; Kinney, 2018).

Global concentrations of air pollutants have increased significantly since the industrial revolution because of human activities, in association with three most important emission sectors: industry, power generation and transportation (Crippa et al., 2016; Hoesly et al., 2018). These three sectors are strongly regulated by two policy-relevant emission drivers that typically compete: economic growth and emissions controls (Crippa et al., 2016). The former mainly reflects growth in energy consumption, while the latter is determined by both air pollution abatement measures and technology advances (termed as technology advances for short). Changes in future air pollution will be modulated by changes in both emissions and climate, with the latter modulating both sources and sinks of atmospheric compositions. On the other hand, however, the anticipated mitigation actions in the future may significantly alleviate air pollution worldwide and hence bring enormous benefits.

The climate impacts of aerosol changes driven by the above two competing drivers have been investigated in Chapter 3. This chapter provides a new holistic assessment of the global impacts of 1970-2010 air pollution changes,

attributable to both climate change and anthropogenic emissions at the global scale. Note the fraction attributable to climate change refers to the changes driven by changes in major climate forcings (i.e., greenhouse gases, solar radiation, volcanoes, etc.) but anthropogenic emissions of air pollutants. For anthropogenic emissions, the present study seeks to understand the impacts associated with the two policy-relevant emission drivers described above.

4.3 Methods

4.3.1 The EDGAR retrospective emission scenarios

The same EDGAR retrospective emission scenarios are used here as in Chapter 3. However, this study considers not only aerosol-related emissions, but other also gaseous fields including NOx, CO, NH_3, as well as non-methane volatile organic compounds (NMVOCs). Emission from sectors including industry, power and aviation are emitted in the model with injection altitudes, while those from all other sectors are lumped together and emitted at the model surface. Also, NMVOCs are re-speciated to match the VOC categories in CAM5-Chem, following previous works (Fry et al., 2013; Fry et al., 2014; Zhang et al., 2016). The EDGAR retrospective emission scenarios are briefly summarized as below.

The retrospective emission scenarios focus on the three most important and regulated sectors (power generation, industry and road transport), while emissions from all other sectors are the same as REF2010 (Table 4.1). The highest retrospective emission scenario assumes no further improvements in technologies and abatement measures after 1970 (STAG_TECH), but energy

consumption and fuel mix as in REF2010. The second and lower retrospective emission scenario assumes stagnation of energy use (STAG_ENE) at 1970 levels, while fuel mix, energy efficiency, emission factors and abatements are the same as REF2010. Therefore, the difference between REF2010 and STAG_TECH reveals the avoided emissions associated with technology advances. Similarly, the difference between REF2010 and STAG_ENE reflects increased emissions due to energy use.

Note again that the EDGAR retrospective emission scenarios were deliberately designed to have emission changes from energy consumption and technology advances to not add up to those in the EDGAR best estimates of the total 1970-2010 changes (Crippa et al., 2016). Such designs allow us to quantify the associated impacts from a “what-if” perspective. For example, what would be expected assuming that we had not introduced any air pollution control measures since the 1970s? Therefore, such quantifications may arguably be more useful than a linear decomposition, from the perspective of policymaking.

4.3.2 Model simulations

In order to more fully reveal changes in air pollution and their impacts on human health, crop production, and economy, equilibrium (i.e., time-slice), rather than transient, model simulations were designed using CESM1. To compromise between computational costs and the representation of atmospheric chemistry, CESM1 (coupled with the standard CAM5) was firstly run into equilibrium under the 1970 and 2010 all forcings (i.e., employing the baseline time-slice model simulations in Chapter 2). Then, the CAM5 is

replaced by the full-chemistry scheme (CAM5-Chem), and a number of perturbation experiments were performed. More specifically, the model dumps in equilibrium of the two baselines 1970 (B70) and 2010 (B10; Table 2.1) climate simulations were saved. Next, the atmosphere component in CESM1 is switched from CAM5 to CAM5-Chem to have both the full-chemistry scheme on and all air pollutant emissions included. The baseline B70 and B10 runs were then continued (referred to as B_1970 and B_2010 hereinafter) for an additional 40 years. Additionally, branching off from the model dump in equilibrium from the 2010 baseline climate run, three other perturbation simulations were performed, also with CAM5-Chem activated and 40 years of integration length. In the three perturbation simulations, anthropogenic emissions were set, respectively, to REF1970, STAG_ENE and STAG_TECH, while all other parameters are kept the same as in the same as B_2010 (Table 4.1 and Figure 4.1). The three perturbation runs are referred to as, respectively, P_1970A, P_ENE and P_TECH. NB anthropogenic emissions refer to all short-lived species as described in Section 4.3.1.

The difference between B_2010 and B_1970 reflects the total effects of 1970-2010 anthropogenic emission changes plus climate change. The influence of 1970 to 2010 climate change is estimated approximately as P_1970A – B_1970. Also, each of the other three simulations is subtracted from B_2010 to disentangle the impacts of anthropogenic emission changes due to each individual driver. They are, total anthropogenic emissions (B_2010-P_1970A), energy consumption (B_2010 – P_ENE), and technology advances (B_2010 – P_TECH). Through this study, the difference, averaged over the last 30 years, between the baseline and each perturbation simulation, are presented.

The statistical significance of the response is evaluated between each two (baseline and perturbed) sets of 30-yr model runs using the two-tailed student t-test (p-value ≤0.05). For regional mean statistics, both the mean differences and 25th-75th percentile model spread across the 30 years are shown.

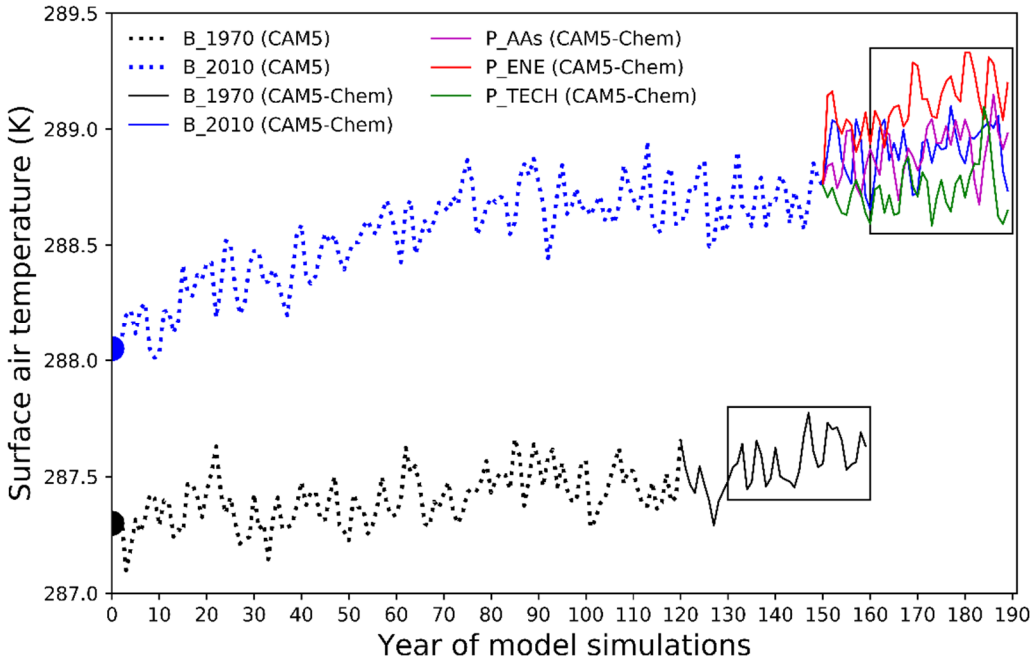

Figure 4.1 Time evolution of the global annual mean surface air temperature from the Community Earth System Model 1 (CESM1) fully coupled with the standard Community Atmosphere Model (CAM5; dotted) and then switched to the full chemistry scheme (CAM5-Chem; solid). B_1970 and B_2010 refer to the 1970 and 2010 all forcing runs, with dotted curves for baseline climate runs and solid curves for chemistry scheme activated (Table 4.1). P_AAs for the experiment where anthropogenic emissions are fixed at 1970 levels, P_ENE for energy use related emissions fixed at 1970 levels, and P_TECH for technology advances related emissions fixed at 1970 levels. The black boxes denote the last 30 years of CAM5-Chem simulations analysed here. B_2010 (CAM5) is initialized by a 2010 dump (blue half circle) while B_1970 (CAM5) is initialized by a 1970 dump (black half-circle), from the LENS (no 34).

As CAM5-Chem does not have diagnostics for total particulate matter (PM), $PM_{2.5}$ is calculated using the sum of all $PM_{2.5}$ species (SO_4, BC, POM, SOA, sea-salt and dust). Note for sea-salt and dust aerosols in the coarse mode, a constant factor of 13.6% is taken to account for the fraction that is within the $PM_{2.5}$ size range. The factor was derived based on the lognormal size

distribution of the coarse mode in MAM3 (Liu et al., 2012; Liu et al., 2015). For surface O_3, the air quality metric MDA8 (daily maxima of rolling 8-hour averages) is also computed from hourly surface ozone data.

Table 4.1 Overview of CESM1 (CAM5-Chem) model simulations analysed in Chapter 4. They are, the baseline 1970 (B_1970) and 2010 (B_2010) runs, stagnation of anthropogenic aerosol-related emissions in 1970 (P_1970A), stagnation of anthropogenic aerosol-related emissions from energy use in 1970 (P_ENE), and stagnation of aerosol-related emissions from technology and abatement measures in 1970 (P_TECH). All simulations are run into equilibrium, and only the last 30 years of each run are used for analysis.

Experiment (run length)	**Model dumps**	**Long-lived species**	**Anthropogenic emissions**
B_1970 (40)	1970	1970	1970 best estimates
B_2010 (40)	2010	2010	2010 best estimates
P_1970A (40)	2010	2010	1970 best estimates
P_ENE (40)	2010	2010	2010 STAG_ENE
P_TECH (40)	2010	2010	2010 STAG_TECH

Reanalysis dataset from the Copernicus Atmosphere Monitoring Service (CAMS; Inness et al. (2019)) is used to evaluate the performance of CESM1 (CAM5-Chem) in simulating global air pollution in 2010. CAMS is the latest global reanalysis data set of the atmospheric composition produced by the European Centre for Medium-Range Weather Forecasts (ECMWF). The CAMS reanalysis assimilates atmospheric composition fields from a variety of satellite observations with the state-of-the-art Integrated Forecast System (IFS; Flemming et al. (2017)). IFS uses an incremental 4D-Var data assimilation system with 12-hr assimilation windows (09:00 to 21:00 and 21:00-09:00 UTC). Satellite retrievals of O_3, CO, NO_2 and Aerosol Optical Depth (AOD) are assimilated. Note that because the total AOD retrievals are the only assimilated observations for all aerosol species, aerosol assimilation is less constrained than other species. The best possible forecast throughout the length of the assimilation window (12-hr) is obtained by minimizing the

differences between the model's background fields and the observations using a cost function in the 4D-Var system. More details about CAMS and the assimilation system can be found in Inness et al. (2019).

4.3.3 Health impact assessment

Cause-specific premature mortality due to long-term (annual) exposure to O_3 and $PM_{2.5}$ are estimated. A health impact function (Equation 4.1; Anenberg et al. (2010)) based on epidemiological relationships between ambient air pollution concentration and mortality in each model grid-box (Silva et al., 2013; Silva et al., 2016a; Silva et al., 2016b) is applied:

$$\Delta M = \gamma_0(1-e^{-\beta/\Delta x})Pop, \quad (4.1)$$

where ΔM is the premature mortality estimate, γ_0 the baseline mortality rate, Pop the exposed population (adults aged 30+), and ΔX changes in O_3 or $PM_{2.5}$ concentrations. β represents the concentration-response factor which is derived from relative risks (RR) estimated in long-term epidemiological studies (Jerrett et al., 2009). That is, by assuming log-linear relationships, RR is estimated per 10 ppb of extra O_3 or per 10 μg m^{-3} of extra $PM_{2.5}$, such that β =ln (RR)/10.

For O_3, following recent work (Silva et al., 2013; Lelieveld et al., 2015; Liang et al., 2018), mortalities due to respiratory diseases are considered. Note that no low-concentration threshold below which change in O_3 has no mortality effects is assumed, as there is no clear evidence for such a threshold (Silva et al., 2013; Liang et al., 2018). The RR value for O_3–related respiratory death is 1.040 (1.013-1.067; Jerrett et al. (2009)). For $PM_{2.5}$, deaths associated with

cardiopulmonary disease (RR=1.128 (1.077–1.182)) and lung cancer (RR=1.142 (1.057–1.234); Jerrett et al. (2009)) are considered. The country-level baseline mortality rates (γ_0) for respiratory disease, cardiopulmonary disease and lung cancer are obtained from WHO 2000-2016 cause-specific mortality for the population aged 30+ (WHO, 2018).

The exposed population includes adults aged 30+ in 2010 (Figure 4.2), which is used for premature mortality estimation in all the cases so that the estimates associated to each of the driving factors are relative to the same baseline. To calculate exposed population, the 2010 world population density from version 4 of the Gridded Population of the World developed by the Center for International Earth Science Information Network at Columbia University (Doxsey-Whitfield et al., 2015) is used. The country-level fraction of population aged 30+ in 2010 was obtained from the United Nation Population Division (2017). When country-level data are unavailable, continental estimates are used to substitute.

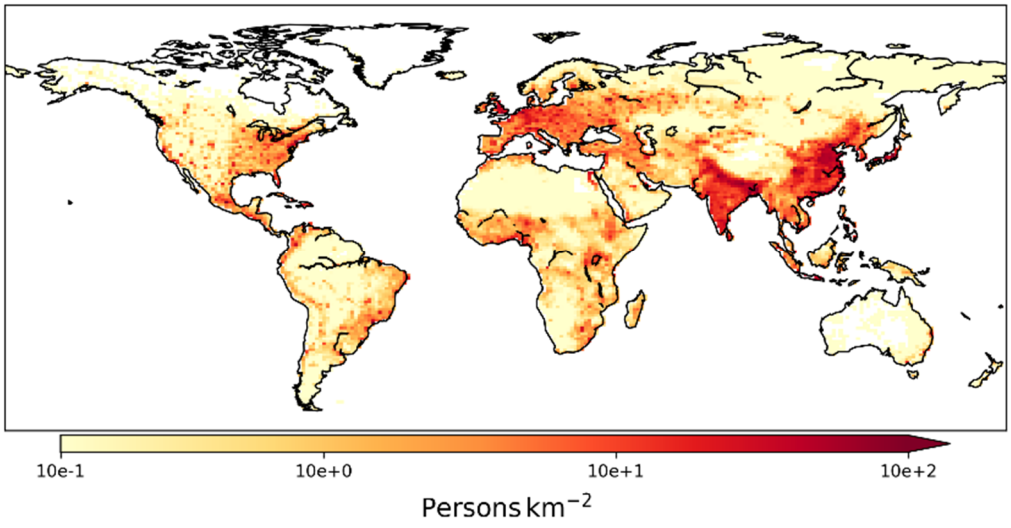

Figure 4.2 Spatial distribution of the exposed population (adults aged 30+, person km^{-2}) in 2010. Note the log scale of the colour-bar.

4.3.4 Ozone exposure and crop production loss

Following recent studies (Mills et al., 2007; Ainsworth, 2017; Emberson et al., 2018; Schiferl and Heald, 2018), the ozone exposure metric AOT40 (accumulated exposure over a threshold of 40 ppb during daylight hours; Equation 4.2) is computed for four staple crops: maize, rice, soybean and wheat. The AOT40 metric is derived using hourly surface ozone concentration during daylight hours from CESM1 (CAM5-Chem) over the last 92 days of a growing season:

$$\mathrm{AOT40}=\sum_{t=08:00}^{t=19:59} 10^{-3}([O_3]_t-40), \qquad (4.2)$$

where $[O_3]_t$ is the hourly surface ozone concentration in ppb, t the local time in summation.

Table 4.2 Exposure: response equations for relative yield loss (RYL) of maize, rice, soybean and wheat. Note the relative yield (RY) is relative to base yield where O_3 impacts are removed, and RYL is calculated by subtracting RY from unity (i.e., 100% yield without O_3 damages).

Crop	Relative yield loss	Reference
Maize	1-0.00356×AOT40	Mills et al. (2007)
Spring Wheat	1-0.0163×AOT40	
Winter Wheat	1-0.0163×AOT40	
Rice	1-0.00415×AOT40	
Soybean	1-0.00116×AOT40	
Winter Wheat, China	1-0.0228×AOT40	Wang et al. (2012)
Rice China	1-0.00949×AOT40	

The growing season information for the above four crops is obtained from the Crop Calendar Dataset determined by the Center for Sustainability and the Global Environment at the University of Wisconsin-Madison (Sacks et al., 2010). The mean harvest date (Figure 4.3) from the 0.5°-filled dataset is used to ensure input data for calculation over each model grid-box. Note that mutual exclusivity (i.e., only one crop being cultivated once within a growing season)

is assumed for each crop despite double-cropping over some regions. Therefore, the impacts on crop production and related statistics are possiblely slightly underestimated.

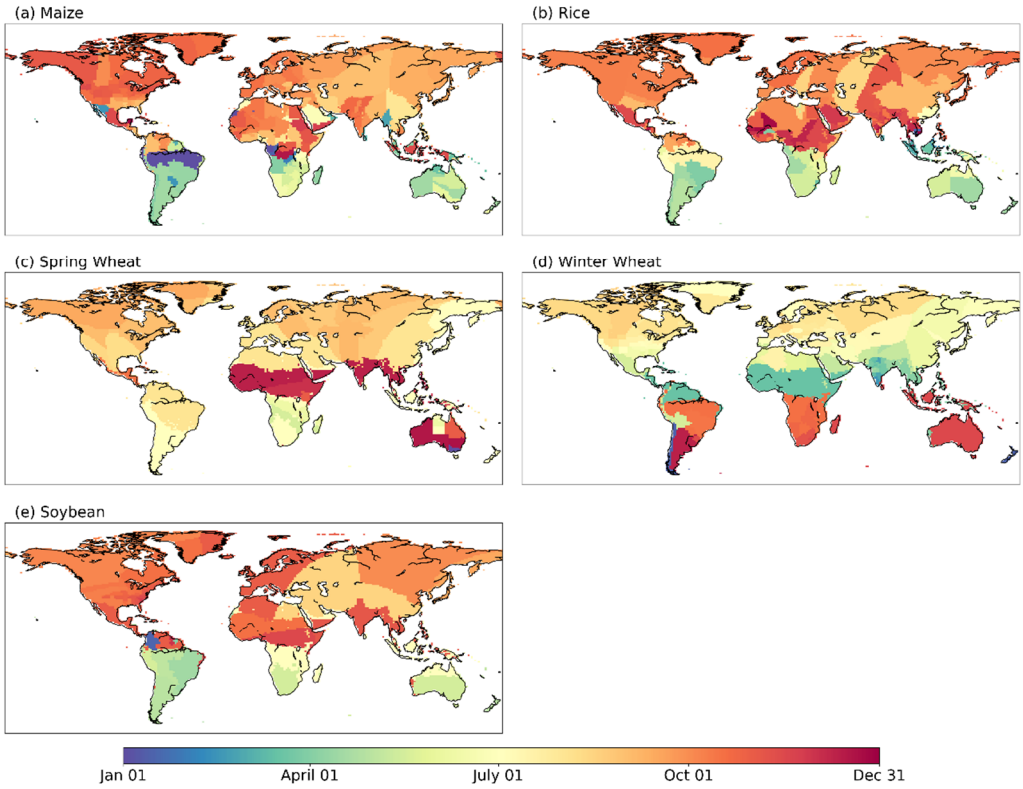

Figure 4.3 Mean harvest date of (a) maize, (b) rice, (c) spring wheat, (d) winter wheat and (e) soybean. Data are from the 0.5° crop calendar developed by the Centre for Sustainability and the Global Environment at the University of Wisconsin-Madison. Note the extrapolated data is used to ensure that every model grid-box has input for ozone metric calculation.

Using AOT40, the relative yield loss (RYL) is calculated using empirical relationships as listed in Table 4.2. The crop yield loss (CYL) is then estimated using Equation 4.3:

$$CYL = \frac{RYL}{1-RYL} \times CY, \qquad (4.3)$$

where CY represents the base crop yield. The base crop yield comes from the Global Agro-Ecological Zones (GAEZ; Fischer et al. (2012)) assessment for

2000 developed by the Food and Agriculture Organization (FAO) of the United Nations along with the International Institute for Applied Systems Analysis (IIASA, 2012). The base crop yield for 2000 is then scaled to 2010 (Figure 4.4) using the 2000-2010 country-level trend determined by the FAO Statistics Division (FAOSTAT, 2017). Finally, to assess economic losses due to crop yield losses, the 2010 annual mean producer prices (Figure 4.5) determined by the FAO Statistics Division are used.

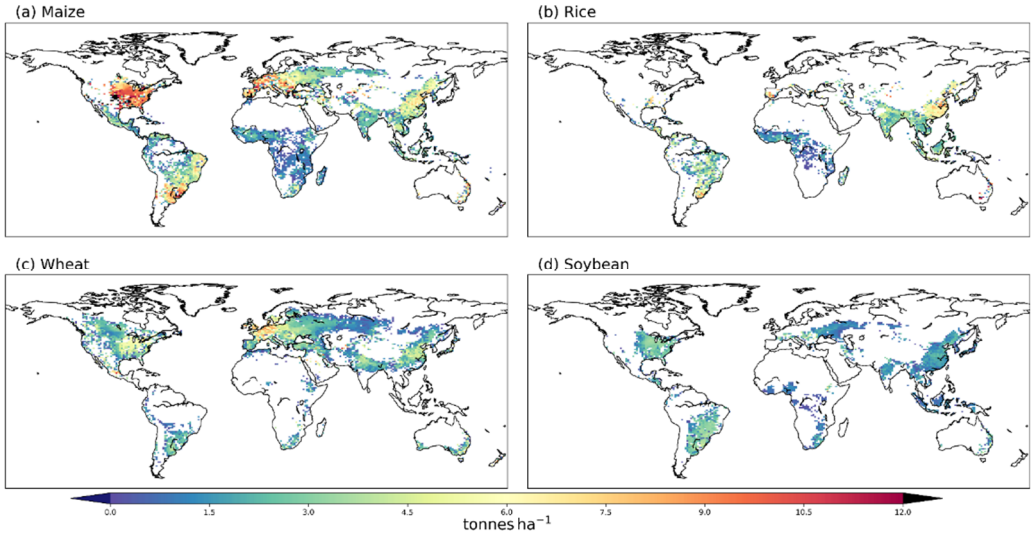

Figure 4.4 The 2010 crop yield (kg ha^{-2}) for (a) maize, (b) rice (c) wheat and (d) soybean. Data are from the 2000 Global Agro-Ecological Zones (GAEZ) which is scaled to 2010 using country-level trends from the Food and Agriculture Organization of the United Nations statistics (FAOSTAT).

4.4 Model evaluation in simulating 2010 air pollution

The performance of CAM5-Chem in simulating tropospheric and surface air pollutants including aerosols, CO, O_3 and NOx have been thoroughly evaluated at both global and regional scales (Lamarque et al., 2012; Emmons et al., 2015; He et al., 2015; Tilmes et al., 2015; Yu et al., 2015; Gaubert et al., 2016). Figure 4.6 presents a further evaluation of the performance of CAM5-

Chem by comparing annual mean surface concentrations of anthropogenic (excluding sea salt and dust) $PM_{2.5}$, as well as O_3, NOx, and CO between the CAM5-Chem 2010 baseline simulation (B_2010) to those derived from the CAMS reanalysis for 2010 (Inness et al., 2019). Albeit with significant gaps for some pollutants (especially O_3 and its precursor gases such as NO_2) due to uncertainties in atmospheric chemistry parameterizations (Huijnen et al., 2019), CAMS represents a convenient route to model evaluation. CAM5-Chem shows overall good agreement with CAMS in reproducing both the spatial patterns and magnitudes of these air pollutants except for O_3. Also, the scatterplots in Figure 4.6 show that the majority of CAM5-Chem simulated surface air pollutant concentrations lie in the 0.5:1 to 2:1 correspondence range when compared to CAMS, with the R^2 ranging from 0.55 to 0.77.

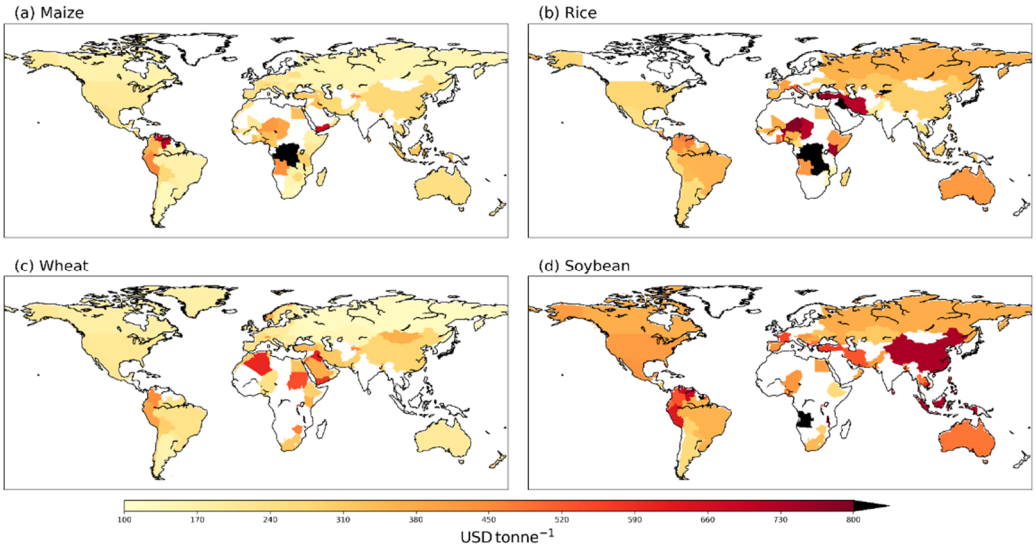

Figure 4.5 The 2010 annual mean producer crop price (USD tonne^{-1}) for (a) maize, (b) rice, (c) wheat and (d) soybean. Data are from the Food and Agriculture Organization of the United Nations statistics (FAOSTAT).

For surface O_3, although CAM5-Chem shows good agreement with other climate models (Ellingsen et al., 2008; Fowler et al., 2008), it is partially biased from that of CAMS. Such biases (overestimations) are particularly noticeable

over the Northern Hemisphere. Meanwhile, CAM5-Chem tends to slightly underestimate the concentrations of other air pollutants (e.g., CO). The biases between CAM5-Chem may be associated with many factors. First of all, uncertainties in the parameterizations of atmospheric chemistry in CAMS, and especially the large uncertainties in OH as reported by Huijnen et al. (2019), may explain some of the biases for O_3. Secondly, note that the surface layer in CAMS spans from the surface to ~20 m in height, but ~50 m in CAM5-Chem. Such differences may also partly explain the biases between CAM5-Chem and CAMS. Also, as the experiment carried out here using CAM5-Chem is in equilibrium, where meteorologies are different to the CAMS reanalysis. It is therefore likely that some of the biases may come from different meteorological conditions. Overall, the comparisons to CAMS indicates that CAM5-Chem can reasonably reproduce the surface concentrations of major air pollutants.

As described in Section 4.3.2, this study looks at the differences between baseline and perturbation model simulations, meaning that the model biases in simulating surface air pollutants can be partially cancelled. However, It is necessary to acknowledge the implications of such biases (particularly those related to $PM_{2.5}$ and O_3) for the estimated socioeconomic impacts (refer to Sections 4.6 and 4.7). For anthropogenic $PM_{2.5}$, as shown in Figures 4.6a-c, most of the model underestimations are related to small values (particularly over the oceans). Since that only land $PM_{2.5}$ pollution is translated into premature mortality, meaning that the model biases over less polluted areas are not likely to have much influence on premature mortality estimate. The underestimations are also noticeable over heavily polluted regions such as East Asia. Therefore, the mortality estimates over these regions are likely to

be underestimated. For surface O_3, underestimations are mainly over the Southern Hemisphere oceans, which do not have appreciable influences on the estimated premature mortality and crop production. However, the noticeable overestimations over the Northern Hemisphere may lead both premature mortality and production to be biased, with the latter in particular given the 40 ppb threshold used to calculate AOT40 (Section 4.3.4). That said, note again that CAMS surface reanalysis products rely mainly on models rather than observations, demonstrating the necessity in interpreting Figure 4.6. In light of all the above, we underscore that both the model evaluation and impact assessment in this study need to be interpreted with caveats.

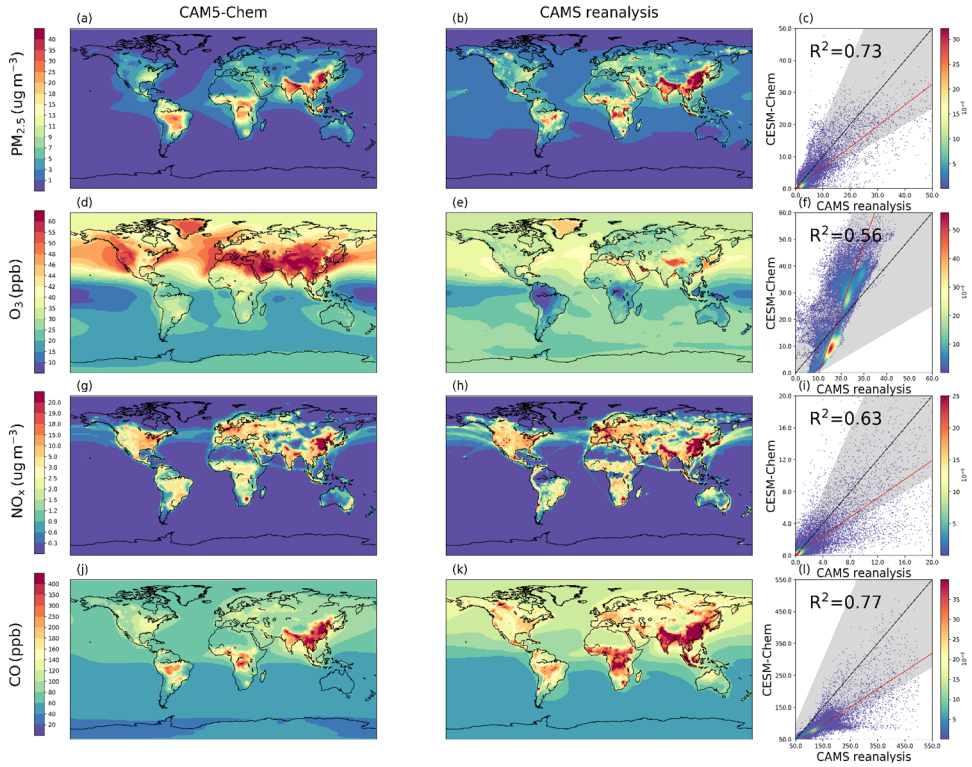

Figure 4.6 Comparisons of 2010 annual mean surface concentrations of air pollutants between CAM5-Chem simulations (first column) and the Copernicus Atmosphere Monitoring Service (CAMS, second column) reanalysis. They are: (a-c) anthropogenic $PM_{2.5}$ (sulphate + black carbon + organic carbon, μg m^{-3}), (b-f) O_3 (ppb), (g-i) NOx (μg m^{-3}), and (j-l) CO (ppb). The scatterplots coloured by density are in the format of CAM5-Chen (y-axis) vs. CAMS (x-axis). The red lines are the linear fits obtained using the reduced major axis regression, while the black lines are the 1:1 correspondence and the grey shadings represent the 0.5:1 to 2:1 ranges. Note the nonlinear colour scales of the spatial maps.

4.5 Impacts on air quality

Figure 4.7 shows 1970-2010 changes in surface concentrations of air pollutants averaged over global land and over representative regions (Asia, Europe and USA), resolving into the contribution of each individual driver. Figures 4.8-4.11 show the corresponding spatial distributions. For O_3, the daily maxima of rolling 8-hour averages (MDA8) is computed. $PM_{2.5}$ shows small trends from 1970 to 2010 at the global scale, yet with larger regional changes that present a pronounced contrast between Asia (+3.7 μg m^{-3}) and Europe (-2.8 μg m^{-3}) and USA (-2.1 μg m^{-3}). The changes have a very limited contribution from climate change (Figure 4.8a), and are driven by anthropogenic emissions (Figure 4.8b) that are dominated by energy consumption (Figure 4.8c), while technology advances (Figure 4.8d) play an important role in Europe and USA.

The ozone metric MDA8 increases worldwide, except over tropical and southern Africa (Figure 4.9). Accordingly, the global land mean MDA8 sees a statistically significant trend (+10.2 ppb) from 1970 to 2010. The change is most prominent in Asia (+31.7 ppb), but less pronounced over Europe (+4.4 ppb) and USA (+5.3 ppb). Changes in MDA8, similar to $PM_{2.5}$, are driven primarily by anthropogenic emissions (Figure 4.9b), with a minor contribution from climate change (Figure 4.9a). Energy consumption and technology advances, again, compete with each other in changing MDA8. Changes in NOx (Figure 4.7c) are similar to MDA8, showing a worldwide increase driven by anthropogenic emissions (Figure 4.10b), which are dominated by energy consumption (Figure 4.10c) and partly offset by technology advances (Figure 4.10d). Noticeably, there is a large benefit from technology advances in

Europe that reduces NOx by up to 2.2 μg m^{-2}. The reduction is around 2.4 times the 1970-2010 total change (0.9 μg m^{-2}).

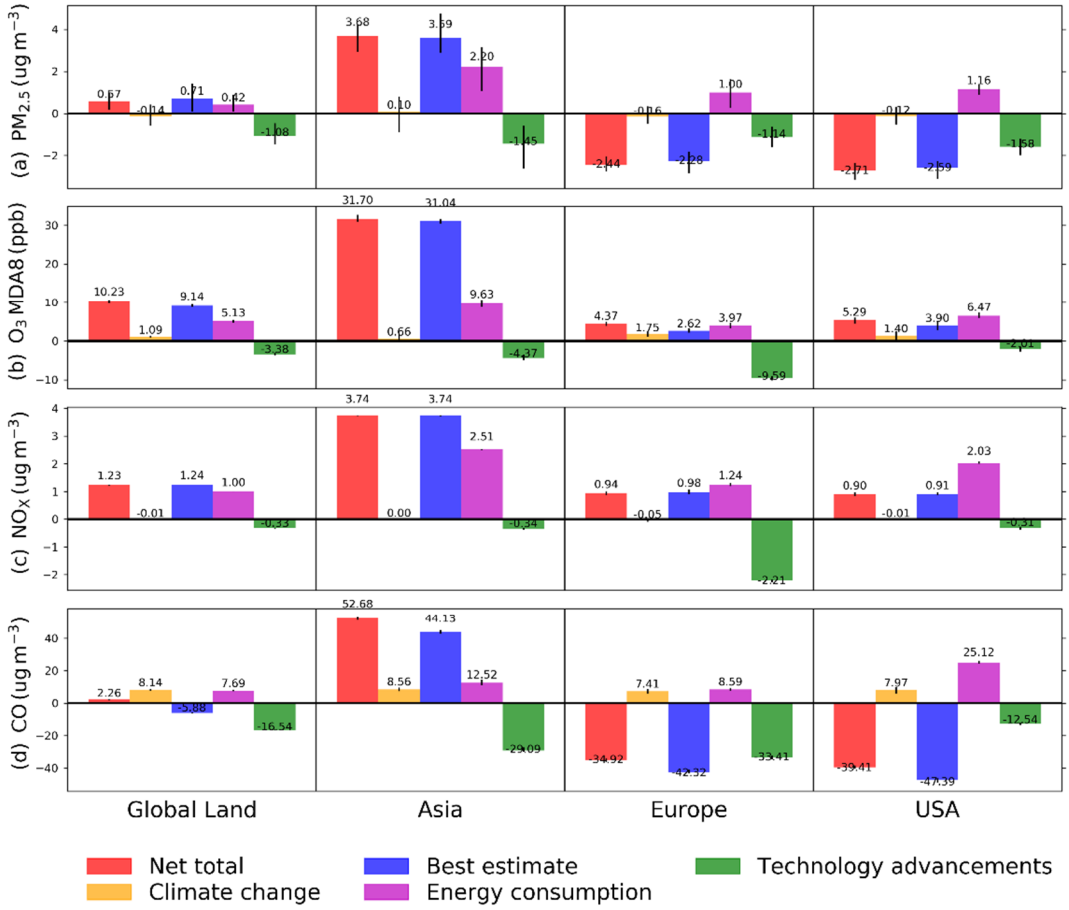

Figure 4.7 The 1970-2010 changes in global and regional mean surface concentrations of air pollutants, in response to total emissions as well as each of the individual driving factors. They are: (a) $PM_{2.5}$ (μg m^{-3}), (b) daily maximum of 8-hours running mean of surface O_3 (MDA8, ppb), (c) NOx (μg m^{-3}) and (d) CO (ppb) at global land, Asia, Europe and USA. Red bars represent the 1970-2010 total net changes, yellow for that attributable to climate change and blue to the best estimate of anthropogenic emissions. Also shown are those in response to energy consumption (purple) and technology advancements (green). The black error-bars show the 25th-75th percentile spread of the model internal variability.

The global mean CO (Figure 4.7d) shows a total net increase of 2.26 μg m^{-3} that is much less (well below 1/3) than the CO increase associated with the experiment of climate change (+8.14 μg m^{-2}). The pronounced CO increase associated with climate change is very likely due to increases in the prescribed

surface concentrations of CH_4 that serves as a long-lived precursor for CO. For the changes attributable to anthropogenic emissions, noticeably, CO is the only air pollutant that shows a global mean decreasing trend. This is mainly associated with the CO decreases in Europe and USA (Figure 4.11b), and is due to emission reductions induced by technology advances.

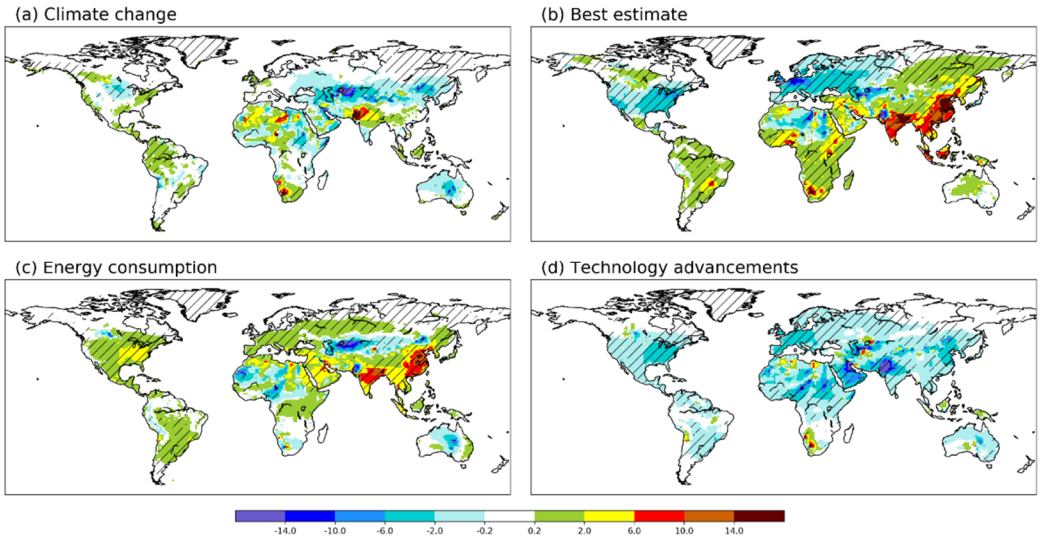

Figure 4.8 The 1970-2010 changes in annual mean surface concentration of $PM_{2.5}$ (μg m^{-3}) attributable to (a) climate change and (b) the best estimate of anthropogenic emissions. Also shown are the responses to anthropogenic emission changes due to (c) energy use growth and (d) technology advancements. All shown changes/responses are the mean differences between the last 30-years of perturbation and baseline runs. The hatches, similarly in all other figures throughout this chapter, denote a statistical significance of the difference at above 95%, derived from the two-tail student's t-test.

4.6 Impacts on premature mortality

The spatial distribution of 1970-2010 changes in premature mortality due to long term exposure to $PM_{2.5}$ and O_3 are shown in Figure 4.12, with global and regional statistics summarized in Table 4.3 and Table A1 (in the appendix). The global mortality increases by 1.7 (1.0-2.4, 5^{th}-95^{th} CI) million yr^{-1} associated with $PM_{2.5}$, mainly because of anthropogenic emissions, and with 5-6 % attributable to climate change induced $PM_{2.5}$ changes. The 1970-2010

changes in O_3 lead to a global premature mortality increase of 86,000 (29,000 -139,000) yr^{-1}, of which 7-8 % is attributable to climate change induced O_3 changes.

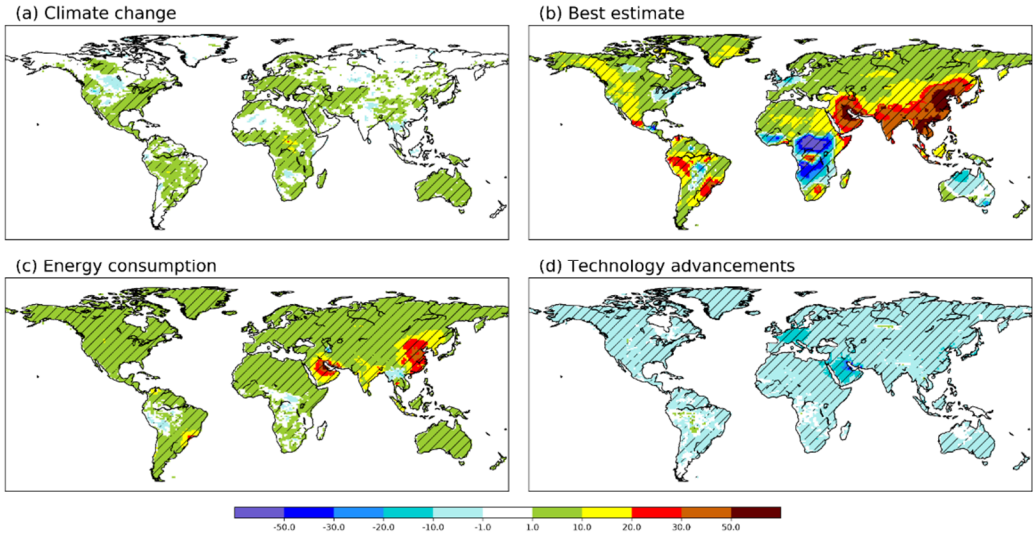

Figure 4.9 The same as Figure 4.8, but for the daily maximum of 8-hours running mean of surface O_3 (MDA8, ppb).

The $PM_{2.5}$ reduction associated with 1970-2010 climate change (Figure 4.8a) has in fact reduced mortality over a large part of the global land (Figure 4.12a), including China (-37,637 yr^{-1}), the Middle East (-17,053 yr^{-1}), Africa (-5,747 yr^{-1}), Russia (-1,858 yr^{-1}) and Europe (-1,613 yr^{-1}). By contrast, climate change increased mortality noticeably over highly populated regions of India (142,553 yr^{-1}). In contrast to $PM_{2.5}$, climate change has worsened O_3 pollution almost globally (Figure 4.9a), with only a few and very limited areas showing MDA8 decreases. Consequently, the effects of climate change on O_3 mortality are positive, with the largest increase of 1,983 (654-3,275) yr^{-1} over China followed by 1,802 (595-2,974) yr^{-1} over Europe. Note, however, again that such changes and the associated impacts may be related to increases in CH_4 concentrations in the climate change experiment.

Anthropogenic emissions account for more than 90% of the increases in pollution-attributable mortality over developing regions. This is especially true for highly populated and polluted areas such as China, Southeast Asia, India, and Africa; the total mortality increase due to anthropogenic emissions in these regions accounts for more than 70% (65%) of the global total $PM_{2.5}$ (O_3) estimates. Europe and North America, on the contrary, show reduced $PM_{2.5}$ mortality due to emission mitigations (Figure 4.12b).

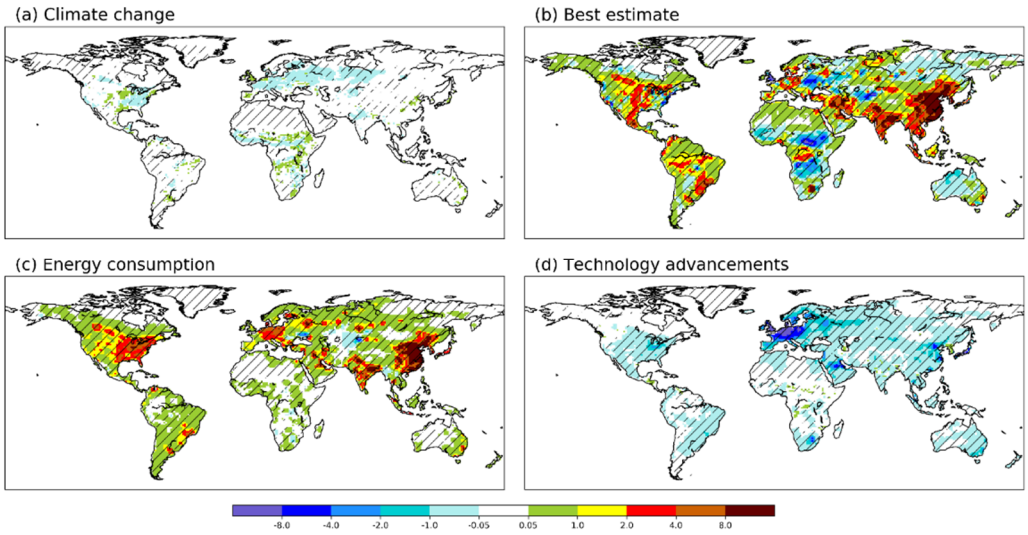

Figure 4.10 The same as Figure 4.8, but for NOx (μg m^{-3}).

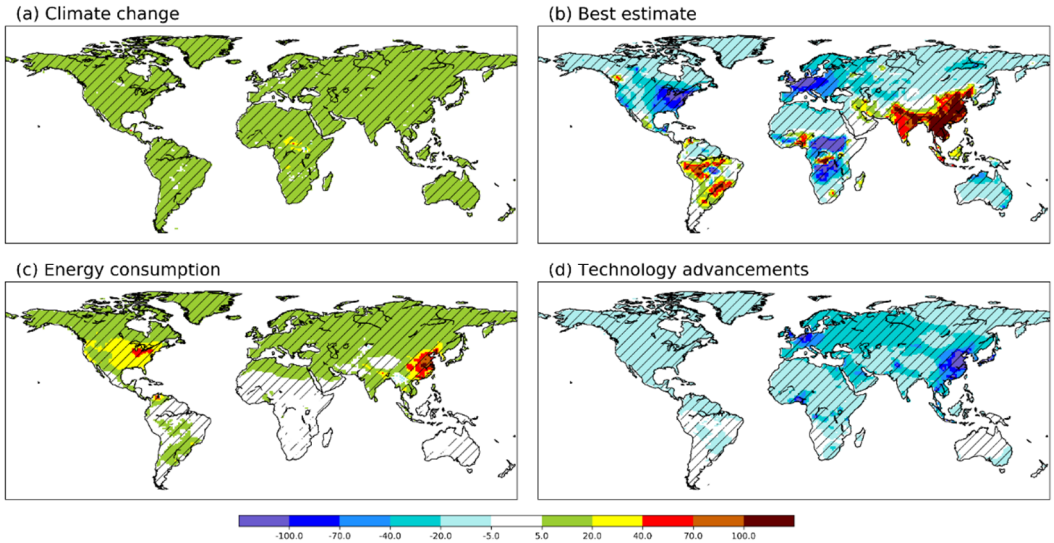

Figure 4.11 The same as Figure 4.8, but for CO (ppb).

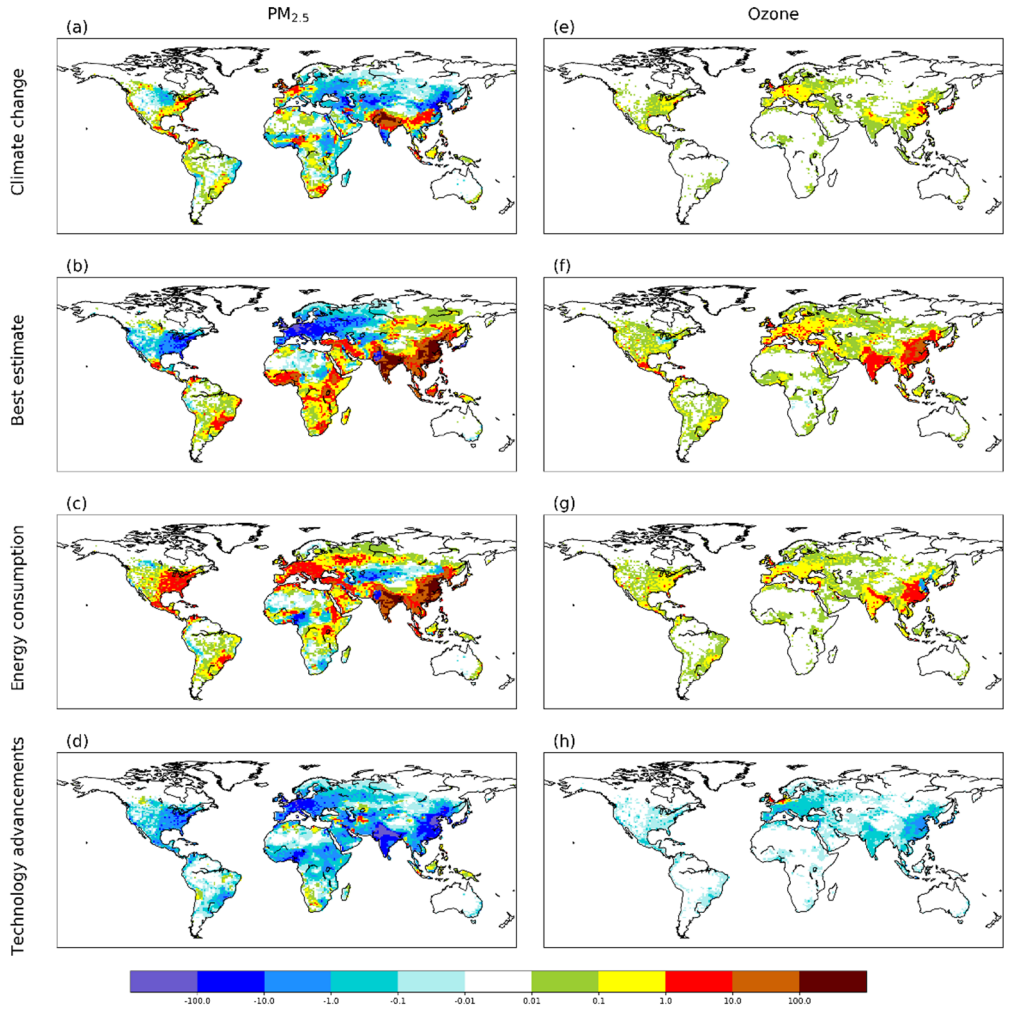

Figure 4.12 Spatial distribution of1970-2010 changes in premature mortality due to changes in air pollution. They are: deaths (per year per 1000 km^{-2}) due to long-term exposure to (a-d) $PM_{2.5}$ (Lung cancer + cardiopulmonary diseases) and (e-h) O_3 (respiratory). The 1970-2010 total net changes are resolved into that attributable to climate change (top row) and the best estimate of total net anthropogenic emission (second row), and also responses to emission changes due to energy use growth (third row) and technology advancements (bottom row).

The 1970-2010 growth in energy consumption induced $PM_{2.5}$ increase is estimated to result in 1.3 (0.7-1.8) million yr^{-1} increase in premature deaths, accounting for well over 75% of that associated with anthropogenic emissions, and 70% of the total net (with climate change taken into account). The amounts for O_3, however, are only 25% and 22%, respectively. Regionally, higher energy consumption resulted in $PM_{2.5}$ increases that lead to 0.7 (0.4-0.9) million yr^{-1} of mortality increase in China, and 0.4 (0.2-0.5) million yr^{-1} in India,

but only 25,000 (14,000 -36,000) yr^{-1} in Europe and 30,000 (18,000 -44,000) yr^{-1} in North America. For O_3, by comparison, energy consumption induced O_3 mortality increase is largest in China (6,629 yr^{-1}), followed by India (2,862 yr^{-1}) and Europe (2,113 yr^{-1}).

Table 4.3 The 1970-2010 changes in global premature mortality (10^3 yr^{-1}) from long term exposure to $PM_{2.5}$ (lung cancer + cardiopulmonary diseases) and O_3 (respiratory), as well as aggregated crop production (million metric tonnes) and economic losses (billion USD_{2010}) due to O_3 exposure. For premature deaths, the mean estimates as well as the 95% confidence intervals on the Epidemiological concentration-response functions are shown in brackets. For crop production losses, here also shows the relative crop production loss in percent relative to the 2010 bases. The economic losses are estimated as an integration of the products of crop production losses and the annual mean producer crop prices. The 1970-2010 total net changes are resolved into changes attributable to climate change and the best estimates of 1970-2010 anthropogenic emissions. Also shown are changes associated with air pollution changes due to energy use and technology advancements.

			Total net	**Climate change**	**Best estimates**	**Energy consumption**	**Technology advances**
Mortality (10^3 yr^{-1})	$PM_{2.5}$		1,749 (1,035, 2,390)	103 (62, 138)	1,646 (973, 2,252)	1,260 (731, 1,765)	-878 (-490, -1,288)
	O_3		86 (29, 139)	7 (2, 11)	79 (27, 128)	20 (66, 32)	-13 (-4, -22)
Crop production (10^6 tonnes (%))		Maize	-33 (-2.0)	-4 -0.3)	-29 (-1.7)	-18 (-1.1)	8(1.5)
		Rice	-38 (-5.2)	-2 (-0.3)	-37 (-4.9)	-15 (-2.0)	6 (0.9)
		Soybean	-22 (-4.9)	-3 (-0.6)	-19 (-4.3)	-12 (-2.7)	4 (0.9)
		Wheat	-73 (-8.4)	-8 (-0.9)	-65 (-7.5)	-30 (-3.5)	17 (2.0)
Economic loss (10^9 USD_{2010})	Gross		-53.1	-4.7	-48.4	-22.7	9.9

As a result of avoided emissions benefiting from technology advances, 0.9 (0.5-1.2) million yr^{-1} of lives were saved globally from $PM_{2.5}$ exposure, and 13,000 (4,000 -22,000) yr^{-1} from O_3 exposure. Note that the saved lives due to avoided $PM_{2.5}$ pollution from technology advances in Europe, North America and the Middle East are greater than the corresponding mortality increases due to energy consumption. On the contrary, the mortality increases related to energy consumption outweigh the numbers of saved lives related to technology advances over the rest of the world.

4.7 Impacts on crop production and economy

The O_3 exposure metric (i.e., AOT40) increases significantly during the period 1970-2010 over the Northern Hemisphere, particularly over China, India, the Middle East and the western USA (Figure 4.13). Note that AOT40 may be overestimated compared to CAMS, given that the CAM5-Chem simulated surface O_3 concentrations are partially biased from the CAMS ones (Figure 4.6). Therefore, the estimated impacts on crops may also be overestimated.

Most noticeably, AOT40 can exceed 30 ppm*hr over a large portion of Eastern China for all the crops. The globally elevated O_3 exposures are mainly associated to anthropogenic emissions, while climate change has very limited impacts that are only slightly recognizable in a few regions (Eastern USA, Mediterranean, Central Asia, and parts of Eastern China). The growth in energy consumption is the main contributor to the large AOT40 changes worldwide, but is partially counteracted by the impacts of technology advances. The corresponding spatial distribution of crop yield losses is shown in Figure 4.14, and is translated into crop production losses (Figure 4.15) and

economic losses (Figure 4.16). The global and regional integrated statistics are summarized in Tables 4.3 and Table A2 (in the appendix).

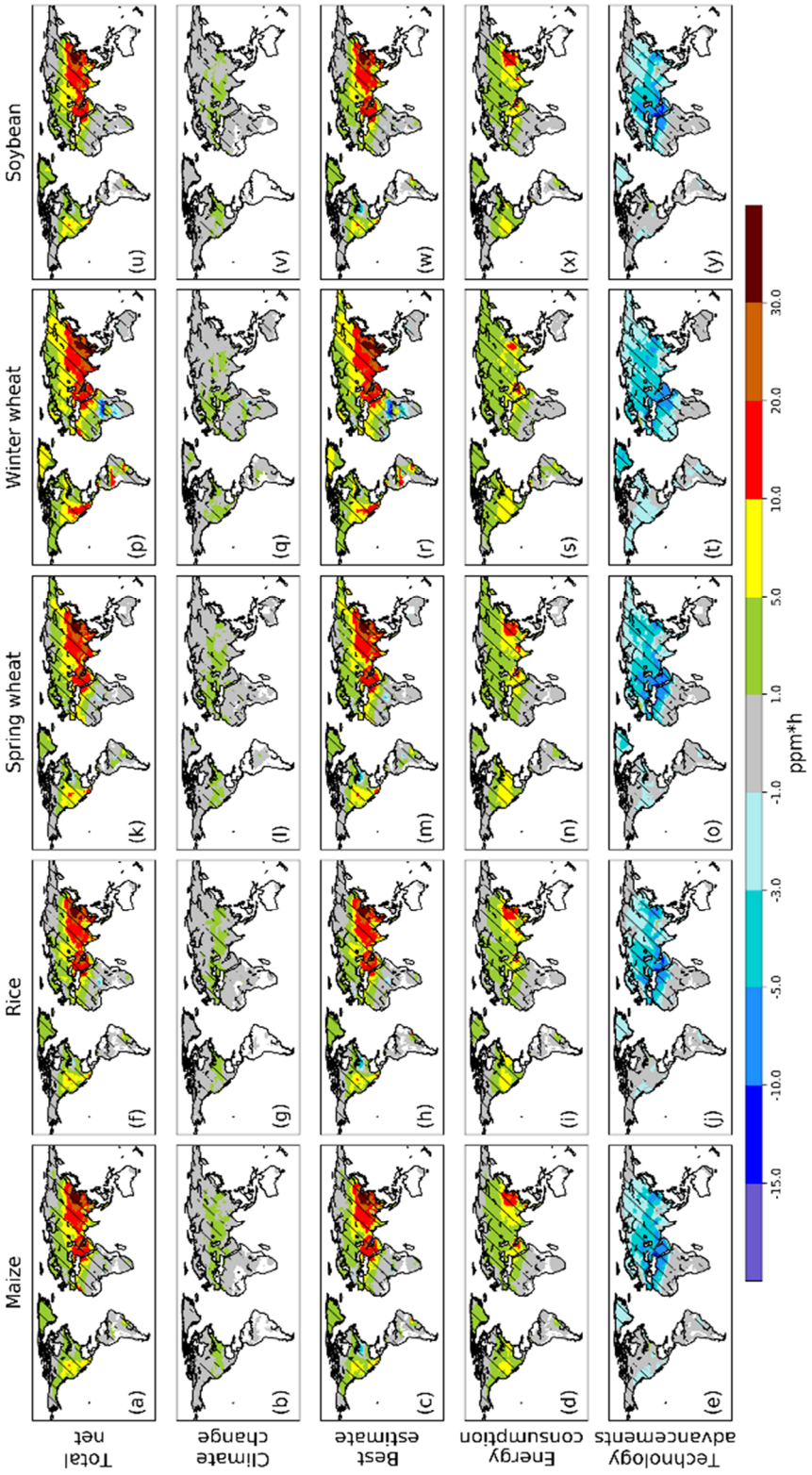

Figure 4.13 Spatial distribution of 1970-2010 changes in the ozone exposure metric AOT40 (ppm*h) integrated over the final 92 days of the growing season, for (a-e) maize, (f-j) rice and (k-o) spring wheat, (p-t) winter wheat, and (u-y) soybean. The 1970-2010 total net changes (first row) are resolved into that attributable to climate change (second row) and the best estimate of anthropogenic emissions (third row). Also shown are the responses to anthropogenic emission changes due to energy consumption (fourth row) and technology advancements (fifth row).

The 1970-2010 increase in O_3 exposure leads to a total global crop production loss of 166 million tonnes yr^{-1} (maize: 33; rice: 38; soybean: 22, and wheat: 73). The relative crop production loss, -2.0%, -5.2%, -4.9%, and -8.4% for maize, rice, soybean and wheat, respectively, agrees in general with previous estimates using different models (Dingenen et al., 2009; Avnery et al., 2011; Schiferl and Heald, 2018). The total crop production losses are worth 53.1 billion USD_{2010} yr^{-1}. This is ~2.1% of 2010 gross world product of the sum of agriculture, forestry, and fishing (2,557 billion USD_{2010}; Bank (2011)).

Of the 53.1 billion USD_{2010} yr^{-1} economic loss, 91% (48.4 billion USD yr^{-1}) is due to anthropogenic emissions. In comparison, climate change resulted into ~10% of gross economic loss (5 billion USD_{2010} yr^{-1}), associated with the sum of -0.3%, -0.3%, -0.6% and -0.9% of global maize, rice, soybean and wheat production loss, respectively. Regionally, the 1970-2010 net total crop production loss is the largest over China for all the staple crops, with a relative loss up to -21.2% for wheat. Climate change induced O_3 changes resulted in crop production losses that were the largest in China for maize (-0.8%), but in North America for soybean (-1.7%), and Europe for rice (-0.6%) and wheat (-1.6%). The 1970-2010 growth in energy consumption has led to a total crop production loss of 75 million tonnes yr^{-1} and an economic loss of 22.7 billion USD_{2010} yr^{-1}, explaining around half of the anthropogenic impacts. The impacts of energy consumption are the largest over China, followed by North America and Europe (with an economic loss of 9.8, 5.2 and 1.6 billion USD_{2010} yr^{-1}, respectively). Technology advances, on the contrary, have led to a total crop production gain of 35 million tonnes yr^{-1}, which is equivalent to an economic gain of 9.9 billion USD_{2010} yr^{-1}. The economic benefits from technology

advances are evident not only in Europe (1.9 billion USD_{2010} yr^{-1}), but also in China (2.3 billion USD_{2010} yr^{-1}) and the Middle East (1.3 billion USD_{2010} yr^{-1}). However, the economic gain in North America, 0.5 billion USD_{2010} yr^{-1}, is not as prominent as might be expected.

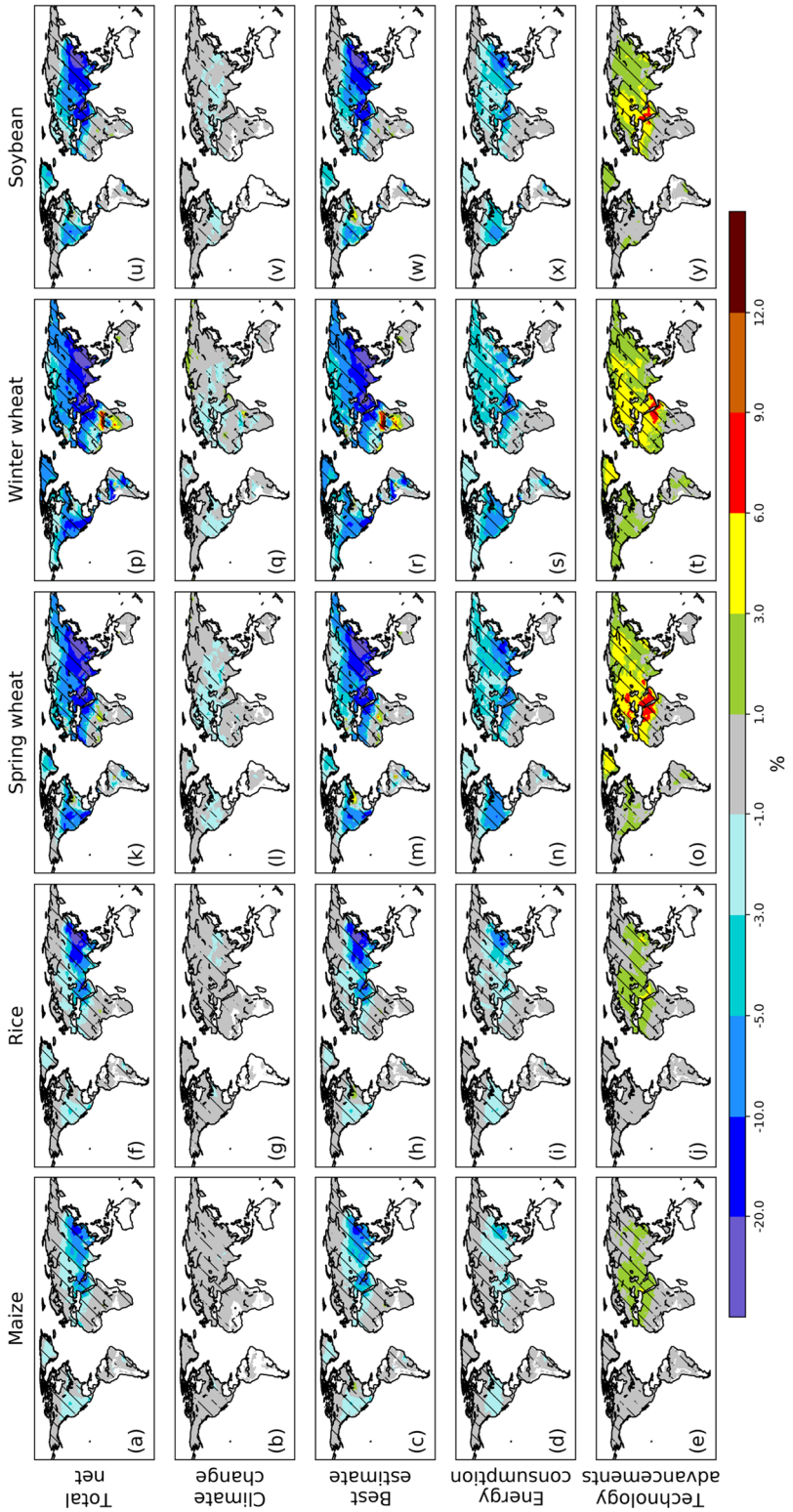

Figure 4.14 The same as Figure 4.13, but for crop yield loss (%). Note negative values for losses and positive for gains.

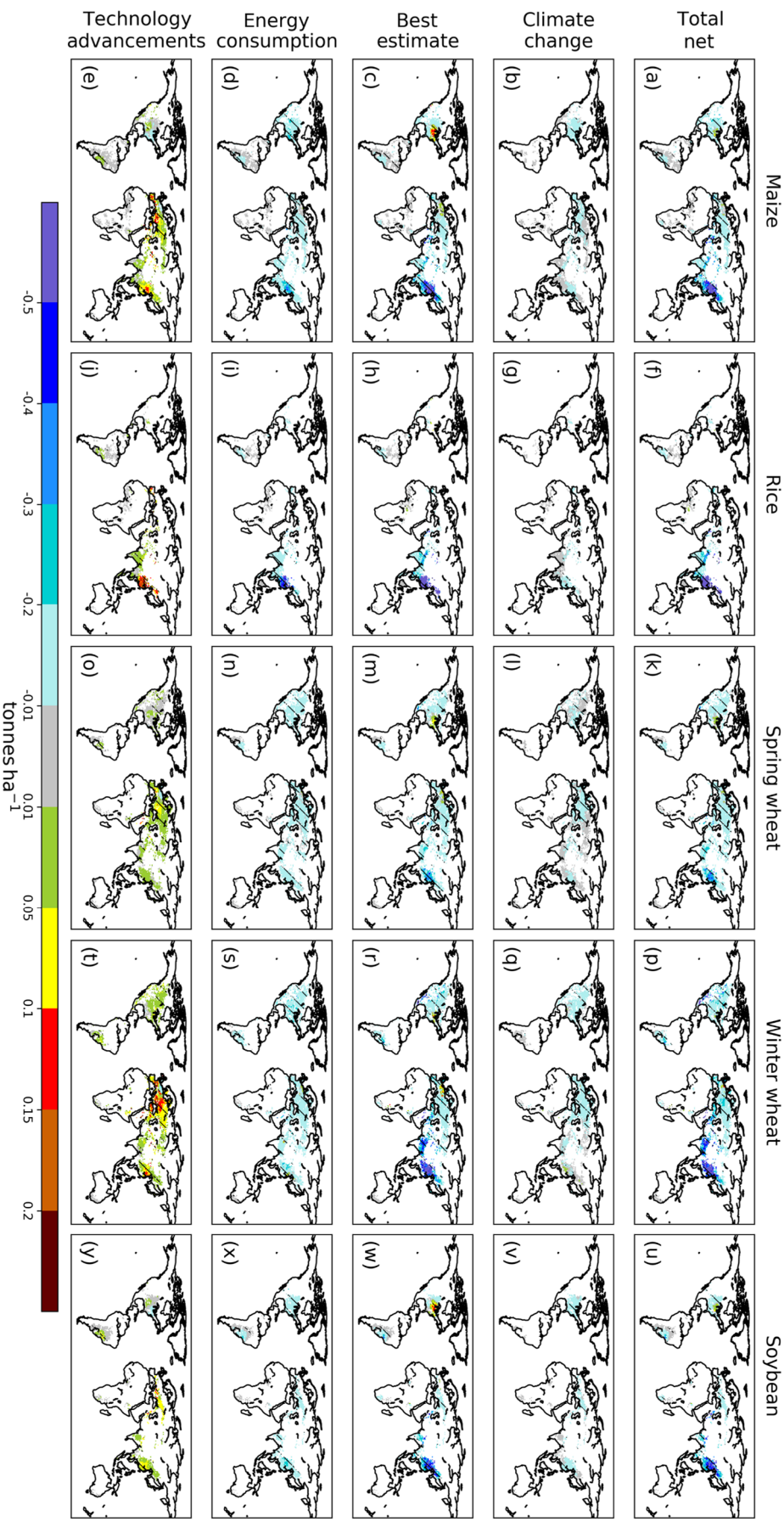

Figure 4.15 The same as Figure 4.13, but for crop production loss (tonnes ha^{-1}). Note negative values for losses and positive for gains.

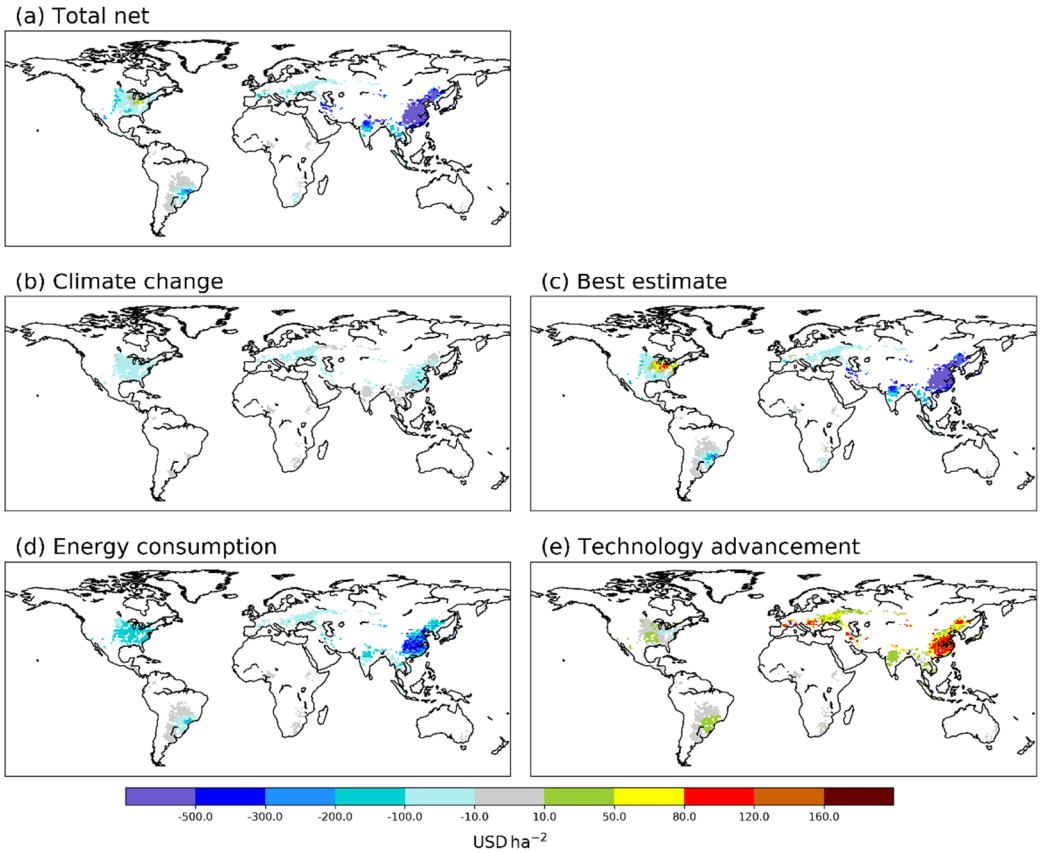

Figure 4.16 Economic loss (USD ha^{-1}) from crop production losses. Negative for loss and positive for gain. The (a) 1970-2010 total net loss is resolved into that attributable to (b) climate change and (c) the best estimate of anthropogenic emissions. Also shown are the responses to anthropogenic emission changes due to (d) energy use growth and (e) technology advancements.

4.8 Wider implications

This study provides a new holistic assessment of the global impacts of 1970-2010 air pollution changes attributable to climate change and anthropogenic emissions, as well as those associated with the two major and competing policy-relevant emission drivers at both the global and regional scales. The results suggest that both global air quality and their impacts are driven by anthropogenic emissions, which are largely regulated by policy-relevant emission interventions. This provides useful information for both assessing and interpreting the possible outcomes of future anthropogenic emission

pathways, and also for coordinating climate, air quality, agriculture, and economic strategies. The contrasts between Asia and Europe and North America reveal the fact that country-level policymaking can exert significant impacts over the region of major emission changes, yet also with global imprints. For example, the introduction of air pollution abatement measures primarily over industrialized regions of Europe and North America since around 1970 have generated important global impacts. The knowledge learnt here may provide important storylines to developing regions. For example, some developing counties such as China have pledged to improve air quality by introducing a variety of emission control measures (e.g., applying end-of-pipe pollution controls, shifting to new energy systems, and introducing new technologies) that involve many energy-intensive sectors (Li et al., 2018). Such measures can bring substantial benefits over both local regions and may also have global impacts.

This study did not calculate the economic losses due to human deaths using the so-called Value-of-a-statistical-life, to avoid discrimination issues. However, it is speculated that the total economic loss estimates will be much larger if one can take this properly into account. It is shown that, despite uncertainties, the 1970-2010 climate change has, in a relatively minor way though, modulated global air quality and their impacts. Such impacts show larger signals over some particular regions (e.g., East USA and Eastern China) than the rest of the world. Actions to mitigate climate change such as future reductions in greenhouse gas emissions, are therefore likely to bring larger benefits over regions where currently have larger climate change induced impacts. On the other hand, however, other mitigation measures such as

future reductions to emissions of aerosols and their precursor gases may lead to disproportionally exacerbated changes in climate extremes (Chapters 5 and 6), whose impacts on human health and crops are not dedicated here. The above adds the urgency of reducing greenhouse gas emissions simultaneously with short-lived air pollutants.

In short, it is shown that both the global air pollution and their socioeconomic impacts are driven by anthropogenic emission changes while climate change also contributes. The impacts associated with anthropogenic emissions are largely under policy control. This offers policymakers important influences on future global environment. However, pressingly, integrated strategies need to be developed to minimize the impacts of changes to both the climate and environment.

Chapter 5 Impacts of Future Greenhouse Gas Increases and Aerosol Reductions on Heatwaves

This chapter is adapted from a published paper on which I am the lead author. I performed all data analysis, and wrote the first draft of the manuscript. Dr David Stevenson and Dr Massimo Bollasina supervised the study, and provided comments on subsequent manuscript revisions. Two reviewers (Leighton Regayre and the other anonymous one) provided additional comments and suggestions during peer-review.

Zhao, A., Bollasina, M. A., & Stevenson, D. S. (2019). Strong influence of aerosol reductions on future heatwaves. Geophysical Research Letters, 46(9), 4913-4923.

5.1 Abstract

Using the Community Earth System Model Large Ensemble experiments (LENS), future heatwaves under the Representative Concentration Pathway 8.5 (RCP8.5) scenario are investigated, separating the relative roles of greenhouse gas increases and aerosol reductions. The results show that there will be more severe heatwaves (in terms of intensity, duration, and frequency) due to global mean warming, with minor contributions from future temperature variability changes. While these changes come primarily from greenhouse gas increases, aerosol reductions contribute significantly over the Northern Hemisphere. Furthermore, per degree of global mean warming, aerosol reductions induce a significantly stronger response in heatwave metrics relative to greenhouse gas increases. The stronger response to aerosols is associated with aerosol-cloud interactions, which are still poorly understood and constrained in current climate models. This suggests that there may exist large uncertainties in future heatwave projections, highlighting the critical significance of reducing uncertainties in aerosol-cloud interactions for reliable projections of climate extremes and effective risk management.

5.2 Introduction

The increased frequency and severity of heatwaves under global warming has raised enormous public attention during the recent years, especially after the 2003 heatwave over Central and Western Europe (Bouchama, 2004; García-Herrera et al., 2010) that broke temperature records set over the last 500-years and led to more than 70,000 deaths and economic losses in excess of 13 billion euros (De Bono et al., 2004). The past few years have witnessed numerous

heatwaves around the world reported as “record-breaking”, “abnormal”, “rare”, and “catastrophic” by the media (Coumou and Rahmstorf, 2012; Russo et al., 2015; Ceccherini et al., 2017; Chen and Li, 2017). Under projected future climate warming, the intensity, frequency, and duration of severe heatwaves are likely to increase further (Lau and Nath, 2014; Jones et al., 2015; Schoetter et al., 2015; Schär, 2016; Mora et al., 2017).

Heatwave changes can be exacerbated due to variations in many of their driving factors, including climate variability and large-scale teleconnections, changes in circulations, land-atmosphere coupling, soil moisture feedbacks, and anthropogenic forcings (Brown et al., 2008; Collins et al., 2013; Stott et al., 2013; Perkins, 2015; Horton et al., 2016; Lu and Chen, 2016; Xu et al., 2016), with potential coupled feedbacks among them (Miralles et al., 2018). However, large gaps still remain in our understanding of the mechanisms underpinning changes in heatwaves, resulting in very uncertain future projections. For example, uncertainties in future emission pathways of anthropogenic forcings and the responses of climate models to them (Booth et al., 2013). Anthropogenic aerosols represent the largest uncertainty in radiative forcing since the pre-industrial times (Stevens and Feingold, 2009; Stocker et al., 2013; Stevens, 2017). A number of studies have shown that future aerosol reductions will lead to more severe temperature/heat extremes (Levy et al., 2013; Sillmann et al., 2013a; Westervelt et al., 2015; Xu et al., 2015; Horton et al., 2016; Lin et al., 2016; Mascioli et al., 2016; Wang et al., 2016b). However, the simplified temperature metrics used by these studies, such as the maximum of daily maximum temperature, do not necessarily represent heatwave characteristics (Chen and Li, 2017), because heatwaves

are a quite distinctive type of temperature extreme where unusually hot weather occurs for several consecutive days.

Aerosol-related emissions are likely to reduce worldwide during the 21st century following stringent mitigation policies aimed at improving air quality. Therefore, it is important to know the corresponding changes in heatwaves, as well as the relative roles of increasing greenhouse gases (GHGs) and decreasing aerosols at both the global and regional scales, given their importance for policymaking and future climate risk management. Furthermore, since temperature variability may change along with climate change in the future (Schär et al., 2004), it is also critical to understand whether future changes in heatwaves will be more strongly driven by the mean temperature change or by changes in temperature variability, or a combination of both (Basarin et al., 2016). Therefore, the LENS experiments under RCP8.5 and RCP8.5_FixA are used to investigate future changes in the characteristics of heatwave events (Chen and Li, 2017). This study has three main aims: (1) to investigate future changes in the characteristics (intensity, duration, frequency and magnitude) of heatwaves at the global scale under the RCP8.5 scenario; (2) to compare the changes in heatwaves due to the shift of mean temperature and those related to changes in temperature variability; and (3) to quantify the relative roles of GHG increases and aerosol reductions.

5.3 Methods

There are many ways to define heatwaves (e.g., see Perkins (2015); Xu et al. (2016) for recent summaries). These definitions fall into two main categories according to the choice of an absolute or a percentile-based temperature

threshold. The former is crucial for evaluating their economic and environmental impacts and is more appropriate for studies of a specific and local region (Freychet et al., 2017). By comparison, the latter facilitates comparisons across locations and over time as the definition is relative to the local climatology. In this study, the percentile-based threshold is adopted. In detail, hot days are defined as days when both daily maximum (TX) and minimum (TN) are greater than their 95th percentiles; these are derived over the 1961-1990 time period, using the 30 ensemble member simulations from LENS (See Section 1.6), and denoted as TX95P and TN95P respectively. It is noted that the choice of reference period influences the magnitudes of the heatwave metrics but has no influence on the conclusions of this study. Secondly, all hot days, where both TX is greater than TX95P and TN is greater than TN95P, throughout a calendar year are identified. Then, a compound heatwave event is identified where hot days last for at least three consecutive days, by which all heatwave events are identified over a calendar year. See Figure 5.1 for a detailed schematic diagram on heatwave definition and calculations of their metrics.

To quantitatively describe the intensity and magnitude of heatwaves, the temperature excess above the 95th percentile threshold is used. The temperature excess for a specific heatwave day is defined as the mean of the differences (TX-TX95P) and (TN-TX95P) for each grid-box. Heatwaves are described by the following four metrics on an annual basis (Figure 5.1): (i) maximum duration (the maximum duration of all heatwaves across a year); (ii) peak intensity (the annual maximum heatwave intensity calculated as the average temperature excess throughout its duration); (iii) frequency (the total

number of heatwaves in a year); and (iv) total hot days (the total includes both heatwave days and hot days that persist for less than three consecutive days).

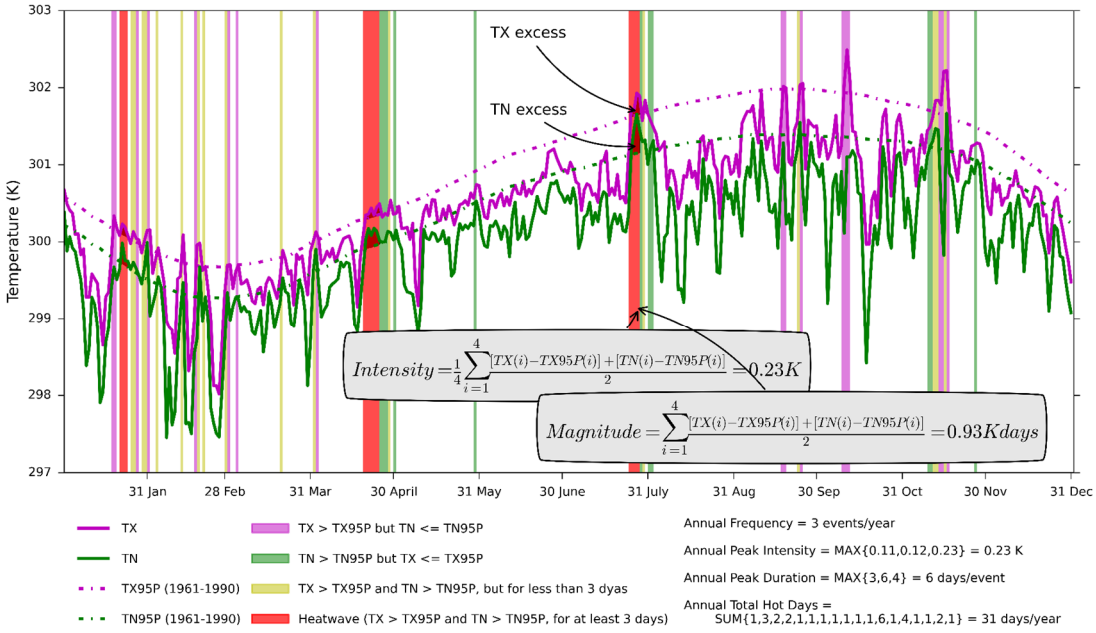

Figure 5.1 A schematic diagram of heatwave definition, produced using daily maximum (TX, magenta curve) and minimum (TN, green curve) temperature of a randomly selected year at a randomly selected grid-cell from one ensemble member of the LENS runs. The 95th percentile of TX (TX95P) and TN (TN95P) for each calendar day is computed from 1961-1990 using a 31-days moving window centred on that day. The vertical magenta spans denote days where TX is above TX95P but TN is below TN95P. The vertical green spans denote days where TN is above TN95P but TX is below TX95P. The vertical yellow spans, referred as hot days which also include heatwave days, denote days where both TX is greater than TX95P and TN is greater than TN95P, but does not meet the criteria of at least three consecutive days of duration. The identified heatwaves (three in total, referred as the annual frequency in the main text) are highlighted by the red vertical spans where both TX is greater than TX95P and TN is greater than TN95P for at least 3 consecutive days. For each heatwave, its intensity is defined as the average of temperature excess throughout its duration. The magnitude index, on the other hand, sums the temperature excess throughout the duration. The annual peak intensity and maximum duration are analysed in the main text as we focus on the extreme aspect rather than the mean aspect.

In addition to the above four metrics, the heatwave magnitude index (see the caption of Figure 5.1) is also introduced. This index, calculated by summing temperature excesses throughout the duration of a heatwave (Russo and Sterl, 2011), has the advantage of merging duration and temperature excess into a single indicator, and is therefore indicative of the overall severity of a

heatwave. Note that any heatwave metrics based on fixed (either absolute or percentile) thresholds may lose their effectiveness when the climate is warm enough. All metrics are calculated for each ensemble member for each year at each land point (excluding Antarctica). The ensemble mean and 25^{th}-75^{th} percentile spread of metrics are used in the following discussion.

For each model land grid-box, the probability that future heatwave magnitudes will exceed their present-day local records is also calculated following Lehner et al. (2016). Firstly, the "present-day record" is defined as the maximum of annual peak heatwave magnitude over 1986-2005 considering the 30 member historical simulations. That is, the "present-day record" is derived from 600 years (20 years*30 ensemble members) over each grid-cell. Then, the total number of years when the annual peak heatwave magnitude exceeds the "present-day record" is counted over all the ensemble years (600 ensemble years for RCP8.5 and 300 for RCP8.5_FixA) over two future periods 2041-2060 and 2081-2100). Finally, the exceedance probability of future heatwaves over the "present-day record" is calculated as the ratio of the total number of exceedance years to the total number of ensemble years. Note these probabilities can be biased as the LENS members are not necessarily completely independent from each other.

To evaluate the performance of LENS in simulating present-day (1986-2005) heatwave characteristics, the 1986-2005 heatwave metrics are also calculated using TX and TN from the National Centers for Environmental Prediction/National Center for Atmospheric Research reanalysis (Kalnay et al., 1996), as well as the Met Office Hadley Centre gridded daily temperatures (Caesar et al., 2006).

In order to diagnose the contribution of changes in future temperature variability to changes in heatwave characteristics, the above analysis is repeated after removing the decadal temperature trend from the raw temperature data at each grid-box. In detail, a 10-year running mean of surface air temperature (e.g., Figure 5.2) is first removed from both TX and TN to leave de-trended anomalies. New 95th percentile thresholds and heatwave metrics are then re-computed from the de-trended data.

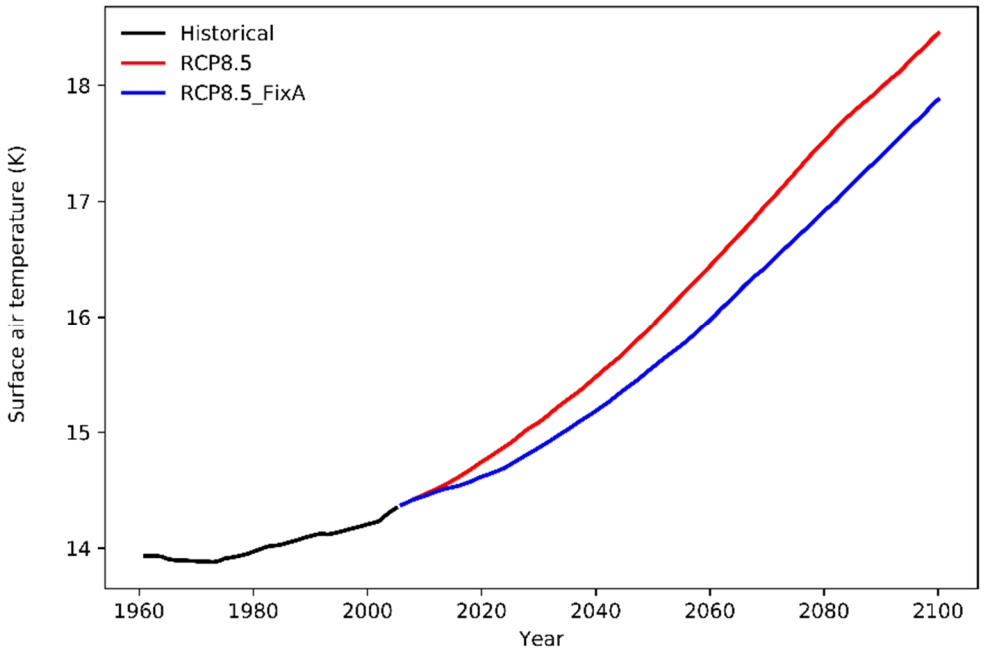

Figure 5.2 Ensemble mean of the global land area-weighted mean of 10 years running mean surface air temperature evolution. Black for the historical period (1960-2005), red (blue) for 2006-2100 under RCP8.5 (Rcp8.5_FixA), derived from the LENS experiments.

5.4 Model evaluation in capturing present-day heatwave metrics

Figure 5.3 presents the present-day (1986-2005) heatwave metrics calculated from the LENS ensemble mean (Figures 5.3a-d), as well as those derived from the National Centers for Environmental Prediction (NCEP)/National Center for

Atmospheric Research reanalysis (Figures 5.3e-h) and the Met Office Hadley Centre gridded daily temperatures (HadGHCND; Figures 5.3i-l). The density scatterplot of these metrics (reanalysis and observations vs. LENS mean) are shown in Figure 5.4. Some parts of the world (e.g., Africa and South America) lack observations; reanalysis data in these regions are also much more uncertain. The model shows good agreement with observation and reanalysis datasets in reproducing these heatwave metrics. This is evident in the Northern Hemisphere where most anthropogenic aerosols are emitted and exert the largest effects. There are however biases over certain regions. More specifically, LENS tends to slightly overestimate heatwave intensity and frequency, but underestimates heatwave duration and total hot days at high latitudes. Heatwave durations are also noticeably overestimated in North Africa compared to the reanalysis dataset.

The baselines (1961-1990) in setting the thresholds for identifying the occurrence of a heatwave are calculated from different datasets for LENS, NCEP/NCAR and HadGHCND. In addition, differences can also be associated with uncertainties in emissions, forced response in the model, biases in the model representation of circulations, etc. Overall, LENS can reasonably capture heatwave characteristics over most of the better-observed regions.

5.5 Future changes in aerosol/precursor emissions and Aerosol Optical Depth

The RCP8.5 scenario shows global GHG increases and aerosol decreases, but with aerosol trends showing strong regional variations. Figure 5.5 displays the time-evolution (2006-2100) of annual total emissions of black carbon (BC),

organic carbon (OC) and sulphur dioxide (SO_2) over specific regions and also globally, as well as the model simulated difference (RCP8.5-RCP8.5_FixA) in 550-nm Aerosol Optical Depth (AOD) averaged over 2006-2025 (Figure 5.5d) and 2081-2100 (Figure 5.5e) respectively. The declining trend of all three aerosol-related emissions can be clearly seen over most regions (Figures 5.5a-c), and China in particular after 2020. The global total SO_2 emission is projected to decrease from 113.7 Tg yr^{-1} in 2005 to 25.6 Tg yr^{-1} by 2100. India, in contrast, is projected to have increasing emissions until the mid-21st century, followed by modest declines. During 2006-2025, because aerosols do not decrease much and even increase at local regions compared to 2005, AOD increases over regions including South Asia and much of the Southern Hemisphere.

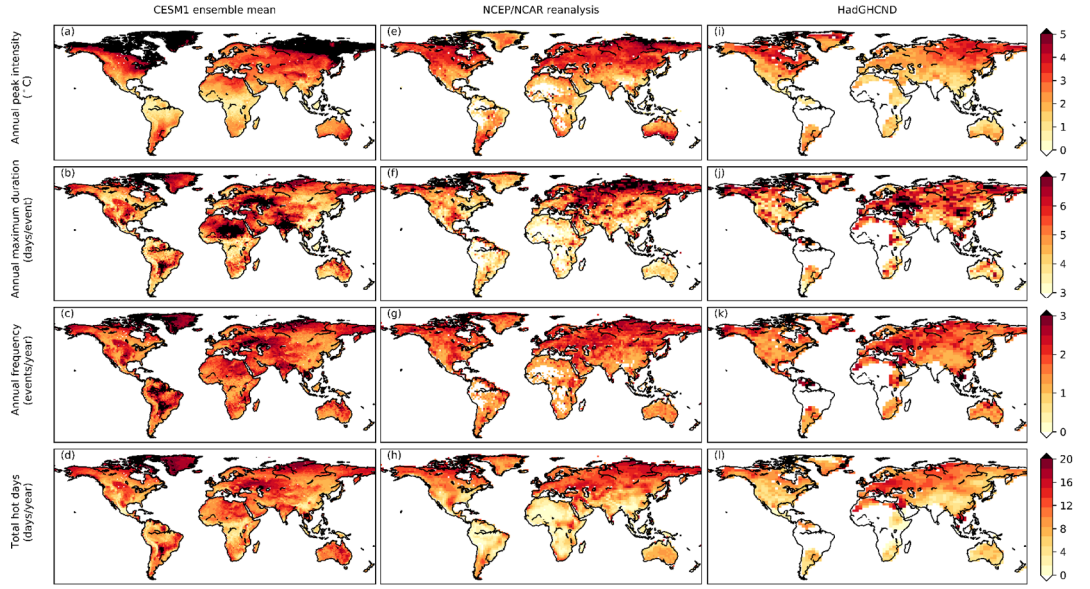

Figure 5.3 An inter-comparison of 1986-2005 mean of annual mean heatwave metrics between (a-d) CESM1 historical run (ensemble mean) and that derived from the (e-h) NCEP/NCAR reanalysis and (i-l) the Met Office Hadley Centre gridded daily temperatures (HadGHCND). They are: annual peak intensity (first row), annual maximum duration (second row), annual frequency (third row) and annual total days (fourth row). Note the white patches in (i-l, Africa, India and South America) are due to lack of observations. Calculations of these metrics are the same across the LENS ensemble members and the observation datasets, but an ensemble mean is applied to LENS to produce the maps.

By 2081-2100, due to anthropogenic emission reductions, AOD decreases sharply over land, especially in East China which sees a net AOD reduction of well over 0.20. Regional AOD increases are still found in India and much of the Southern Hemisphere. Comparing 2081-2100 to 2006-2025 (Figures 5.5d and 5.5e), AOD over oceans, however, does not differ much as anthropogenic aerosol changes. This can be explained by the short lifetime of anthropogenic aerosols and that AOD over oceans is dominated by natural aerosols (sea-salt) which does not evolve much with climate change.

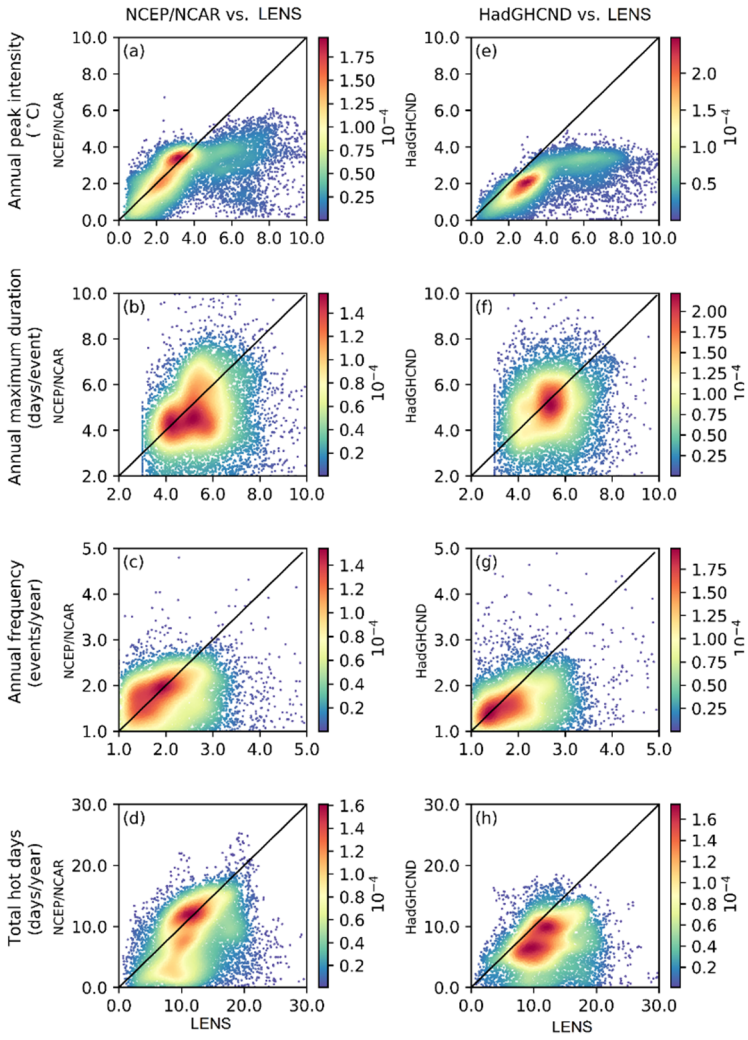

Figure 5.4 Density scatterplots of heatwave metrics between those derived from (a-d) NCEP/NCAR reanalysis and (e-h) HadGHCND and LENS mean. Data are the same as Figure 5.3. The black lines show the 1:1 correspondence.

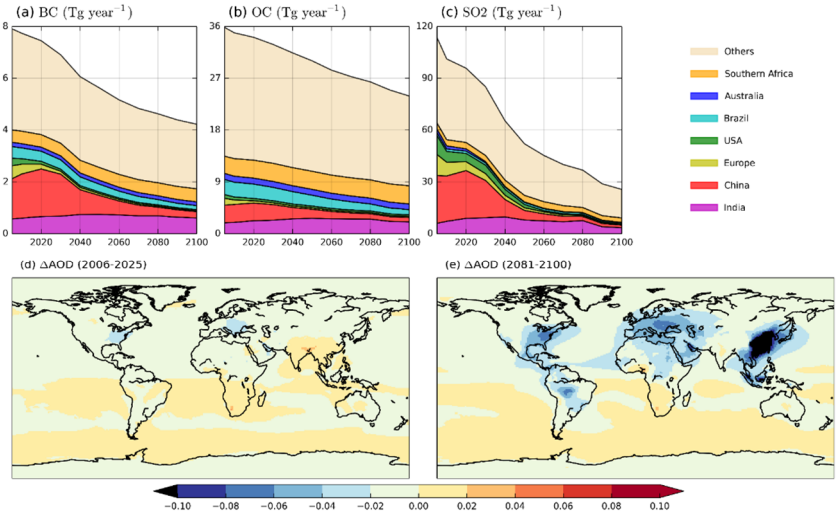

Figure 5.5 Time-evolution (2005-2100) of annual total emission (Tg yr^{-1}) of (a) black carbon (BC), (b) organic carbon (OC) and (c) sulphur dioxide (SO_2) over the globe (the total) and local regions (in different colours) in the RCP8.5 scenario. LENS simulated differences in the annual mean 550-nm Aerosol Optical Depth (AOD) between RCP8.5 and RCP.5_FixA averaged over (d) 2006-2025 and (e) 2081-2100. All regions are defined as their administrative boundaries. Alaska and Hawaii islands are not included in USA.

5.6 Present-day and future projections of heatwave characteristics

5.6.1 Changes in heatwave metrics

Figures 5.6a-d show values of the four heatwave metrics for 'present-day' (1986-2005) and for two future (2081-2100) projections (RCP8.5_FixA and RCP8.5), averaged at the global scale as well as for representative regions. Corresponding spatial patterns of changes (future vs. present-day) in these metrics due to both GHG increases and aerosol reductions are provided in Figure 5.7. Figures 5.6a and 5.7a show that GHG rises will increase global and regional mean annual peak heatwave intensities from ~2 to ~4 K. Aerosol reductions further enhance heatwave intensities by about 0.3 K (Australia) to 0.7 K (Europe and China). The annual maximum heatwave duration shows future increases, from a present-day global mean value of 3.6 days, increasing

to 21 days with GHG increases, and 28 days when aerosol reductions are also included. Heatwave duration shows strong regional variations, with the largest increases seen over Brazil (Figures 5.6b and 5.7b, f).

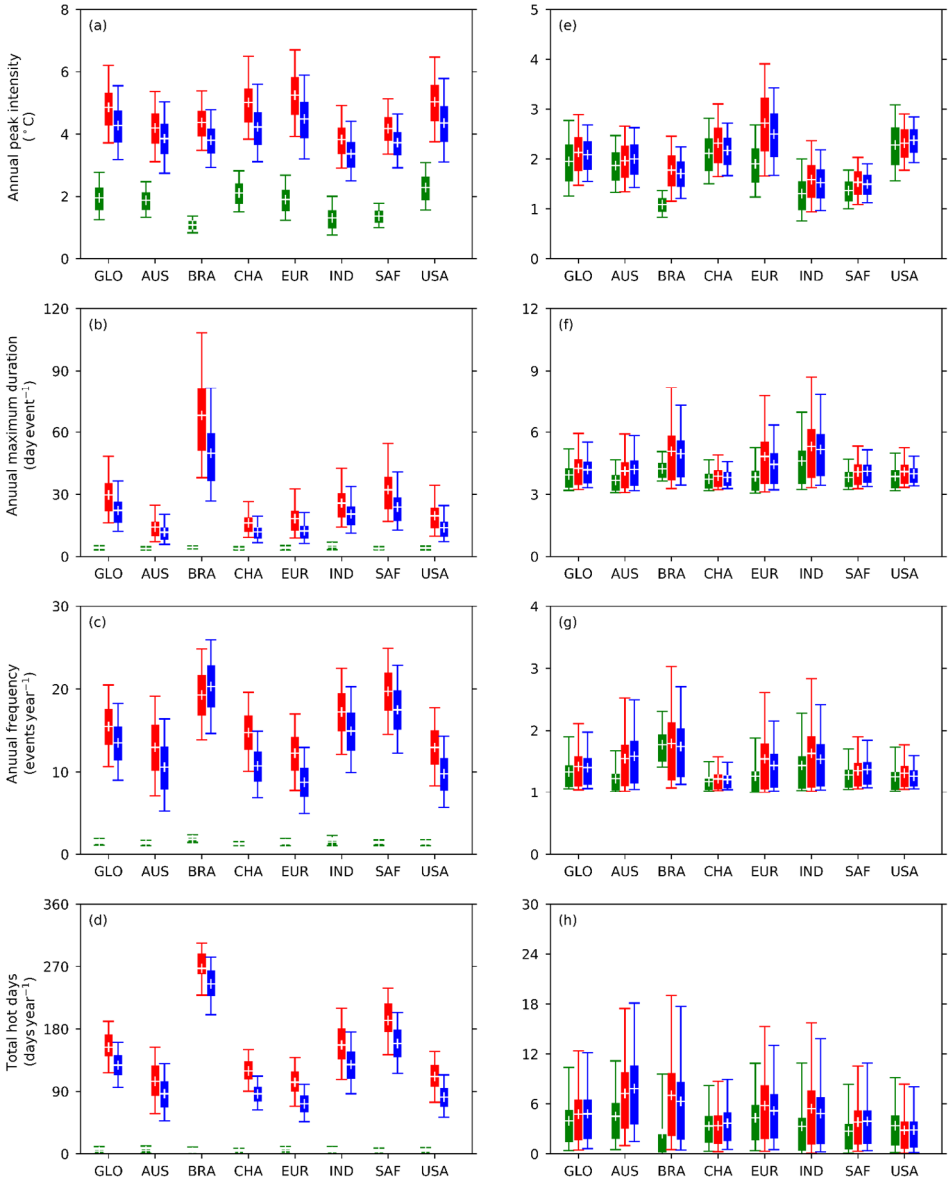

Figure 5.6 Area-weighted mean of twenty years mean of ensemble mean (white cross), 25th–75th percentile spread (box), as well as ensemble minimum and maximum (whiskers) of heatwave metrics: (a) annual peak intensity (K), (b) annual maximum duration (days event^{-1}), (c) annual frequency (number yr^{-1}) and (d) annual total days (days yr^{-1}), derived from the absolute temperatures. Green for the period 1986-2005, red for 2081-2100 under RCP8.5 and blue for 2081-2100 under RCP8.5_FixA. (e-h) are identical to (a-d), except for that (e-h) are calculated after the long-term temperature trend has been removed from the raw dataset. The results are shown for the global land (GLO), Australia (AUS), Brazil (BRA), China (CHA), Europe (EUR), India (IND), Southern Africa (SAF), and contiguous USA (USA).

Changes in annual heatwave frequency (Figure 5.6c) and total hot days (Figure 5.6d) display similar features. Note, however, there is an exception of the heatwave frequency in Brazil (and also other tropical regions) that decreases as aerosols reduce (Figure 5.7g). This is because of the significantly longer heatwave durations.

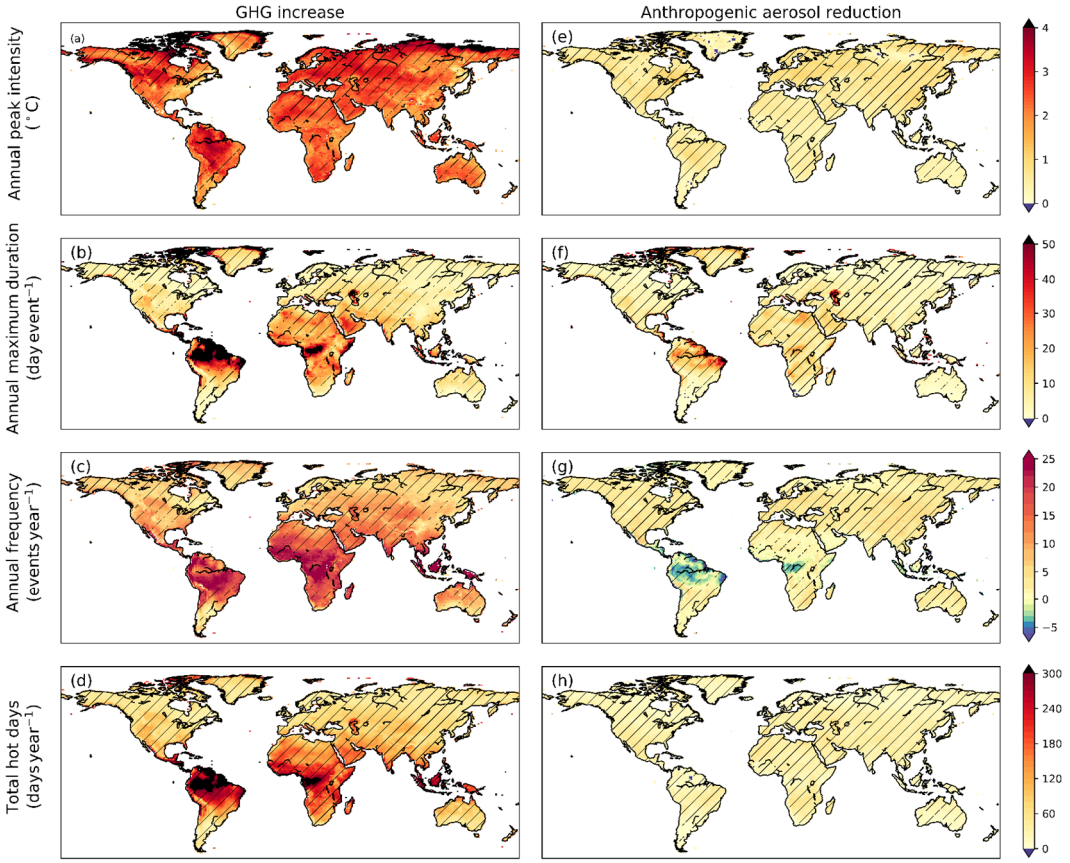

Figure 5.7 Spatial distributions of changes (from 1986-2005 to 2081-2100) in heatwave metrics: annual peak intensity (first row), annual maximum duration (second row), annual frequency (third row) and annual total days (fourth row), due to (a-d) GHG increases, and (e-h) aerosol reductions. The hatches denote at ≥95 % significance level of the changes.

5.6.2 The effects of changes in climate variability

By definition, temperature variability sets the baseline (1961-1990) values for the heatwave metrics, and that variability has changed little by 1986-2005, or by 2081-2100 (Figures 5.6e-h). This contrasts with the marked increases in

metrics based upon absolute temperature changes, suggesting that future changes are largely associated with the general warming and only slightly modulated by temperature variability changes. Specifically, the relative contribution of temperature variability changes to the various heatwave metric changes is generally under 10% (Figure 5.8), except for heatwave intensity over Europe (24%), Brazil (21%), and India (11%) under both scenarios. In addition, the difference (Figure 5.8c) between RCP8.5 and RCP8.5_FixA suggests that future aerosol reductions will generally decrease the contribution of changes in temperature variability. This is particularly true for heatwave duration: a reduction ranging from a global mean of -0.5 % to a regional peak of -2.5% over Australia. This suggests that aerosol reductions will slightly dampen temperature variability in the future (see more in Section 5.7).

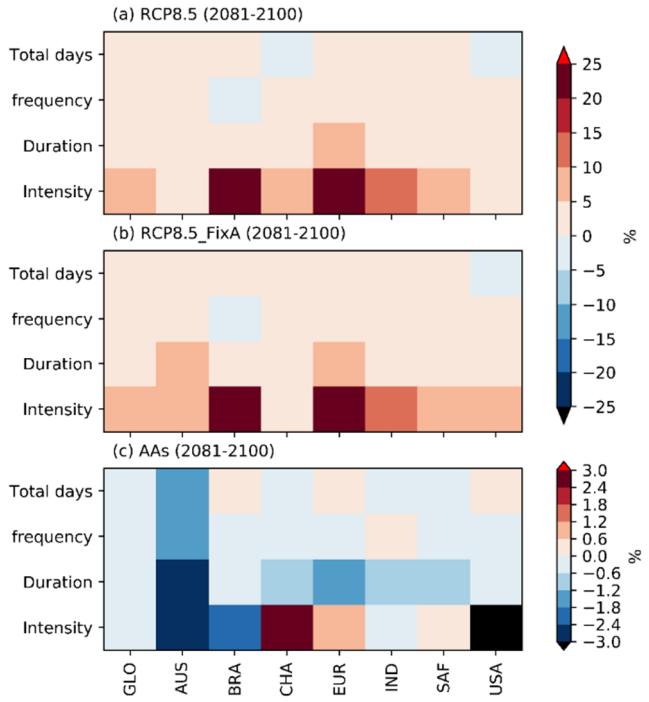

Figure 5.8 The annual mean of contribution (%) of future changes in temperature variability to absolute changes in the heatwave metrics over 2081-2100 under (a) RCP8.5 (b) RCP8.5_FixA and (c) the changes due to aerosol reductions identified as RCP8.5 – RCP8.5_FixA averaged on the globe as well as regional scales. The results are an average of the spatial mean from all the ensemble members.

5.6.3 Seasonal variations

While summer heatwaves are undoubtedly the most severe, heatwaves in other seasons can also result in significant adverse impacts, especially to agriculture, wildlife and ecosystems (Perkins, 2015). Therefore, the effect of seasonality is also investigated by performing the analysis separately for an extended summer (May-October) and winter (November-April) seasons (in the Northern Hemisphere). Note that seasons reverse over the Southern Hemisphere. The difference between summer and winter heatwave metrics are relatively small in magnitude for present-day (Table 5.1). However, such seasonal differences become prominent by 2081-2100 under both scenarios (Table 5.2), because of greater summer than winter changes in heatwave metrics (not shown). This is particularly important over northern latitudes. In addition, there is a greater seasonal difference under RCP8.5 than RCP8.5_FixA over regions (China, Europe and USA) with pronounced aerosol reductions (Figure 5.5). This indicates that aerosol reductions will lead to even more severe summer heatwaves over major aerosol/precursor emission regions. In short, it is found that there will be slightly stronger changes in summertime heatwaves compared to wintertime, and that the seasonal contrast can be amplified by aerosol reductions.

5.6.4 Section summary

In short, future GHG increases will result in future (2081-2100) heatwaves that are, when globally averaged over land, significantly more intense (2.4 K), longer (17 days), and more frequent (12 more per year), compared to present-day. These changes will be further aggravated by aerosol reductions. Namely, 0.6 K (25%), 7 days (41%) and 2 more per year (12%) of additional increases

in intensity, duration and frequency, respectively, on top those related to GHG changes. Changes to heatwaves are similar in all seasons, and are dominated by changes in mean temperature, with only minor contributions from changes in temperature variability.

Table 5.1 The annual mean (1986-2005) of difference in the heatwave metrics between the extended summertime and wintertime (i.e., summer-winter), as spatially averaged at both the global land (oceans and Antarctic excluded) and local regions. Values in the brackets are percentage differences relative to the wintertime.

Region	Intensity (K)	Duration (days/event)	Frequency (events/season)	Total days (days/season)
GLO	-0.45 (-23.3)	-0.04 (-1.0)	0.04 (4.0)	-0.20 (-14.9)
AUS	0.06 (3.6)	0.06 (1.7)	0.03 (2.5)	0.94 (82.6)
BRA	-0.17 (-15.7)	0.15 (4.2)	0.31 (24.8)	0.21 (147.5)
CHA	-0.81 (-36.8)	-0.20 (-5.8)	-0.03 (-3.0)	-0.25 (-20.9)
EUR	0.12 (7.2)	0.13 (3.9)	0.06 (5.3)	-0.40 (-24.7)
IND	-0.07 (-6.3)	0.00 (-0.0)	0.13 (11.8)	0.81 (72.1)
SAF	0.06 (5.1)	0.06 (1.8)	0.08 (7.2)	0.46 (130.2)
USA	-0.74 (-31.4)	-0.07 (-1.9)	0.06 (5.6)	-0.73 (-56.2)

Table 5.2 Seasonal differences (summer-winter) in heatwave metric changes between 2081-2100 and 1986-2005 under RCP8.5 and RCP8.5_FixA in brackets. The 1986-2005 seasonal difference is provided in Table 5.1. Al values are spatially averaged at both global land (oceans and Antarctic excluded) and regional scales. Positive values mean larger summertime heatwave metrics than wintertime, while bold font indicates that such contrast is greater under RCP8.5 than RCP8.5_FixA due to aerosol reductions.

Region	Intensity (K)	Duration (days/event)	Frequency (events/season)	Total days (days/season)
GLO	**0.40 (0.3)**	0.66 (0.7)	2.37 (2.4)	**22.68 (21.3)**
AUS	0.13 (0.1)	0.12 (0.2)	0.40 (0.8)	0.68 (3.5)
BRA	-0.09 (-0.0)	-5.53 (-2.2)	**2.88 (2.3)**	1.54 (5.2)
CHA	**0.43 (0.3)**	**1.30 (0.9)**	**4.34 (3.8)**	**37.03 (30.2)**
EUR	**0.53 (0.4)**	**2.38 (1.4)**	**3.32 (2.6)**	**37.15 (23.4)**
IND	**0.15 (0.1)**	0.37 (0.7)	2.98 (3.5)	25.95 (301.0)
SAF	-0.04 (-0.0)	-0.98 (-0.3)	0.94 (1.0)	1.93 (7.1)
USA	**0.34 (0.2)**	**2.96 (2.0)**	**4.84 (4.4)**	**51.09 (39.7)**

5.7 Probabilities of record future heatwaves and driving mechanisms

Now turns to the heatwave magnitude metric, and examines the probability that present-day heatwave magnitudes will be exceeded in future. As above, the two scenarios are used to isolate the roles of GHG increases and aerosol decreases.

5.7.1 Exceedance probability of future heatwave magnitude over present-day record

Under the RCP8.5 scenario, the tropics see earlier emergences of heatwave magnitudes exceeding their 1986-2005 records (Figure 5.9a). Further, the exceedance probability is much larger over the tropics than at higher latitudes during both time periods. An explanation is that the relatively small temperature variability in the tropics makes it easier to break the historical record with relatively small increases in mean temperature compared to higher latitudes. This agrees with existing works showing that the tropics will see the earliest emergence of significant warming (Mahlstein et al., 2011; Lehner et al., 2016). By 2081-2100, almost every year will have record-breaking heatwaves, with a global mean exceedance probability of 76% (Figure 5.9b). Not surprisingly, under the fixed aerosol scenario (Figures 5.9c, d), the probability is significantly smaller over the Northern Hemisphere, where most aerosols are emitted. For aerosols (Figures 5.9e, f), although there are some signals in the Southern Hemisphere, probability changes here are primarily associated with GHG increases (Figures 5.9c, d). In contrast, the aerosol signal is mainly over the Northern Hemisphere. For example, aerosol reductions will increase

the exceedance probability by a further 20%, on top of a 52% increase due to GHGs in Europe by 2081-2100.

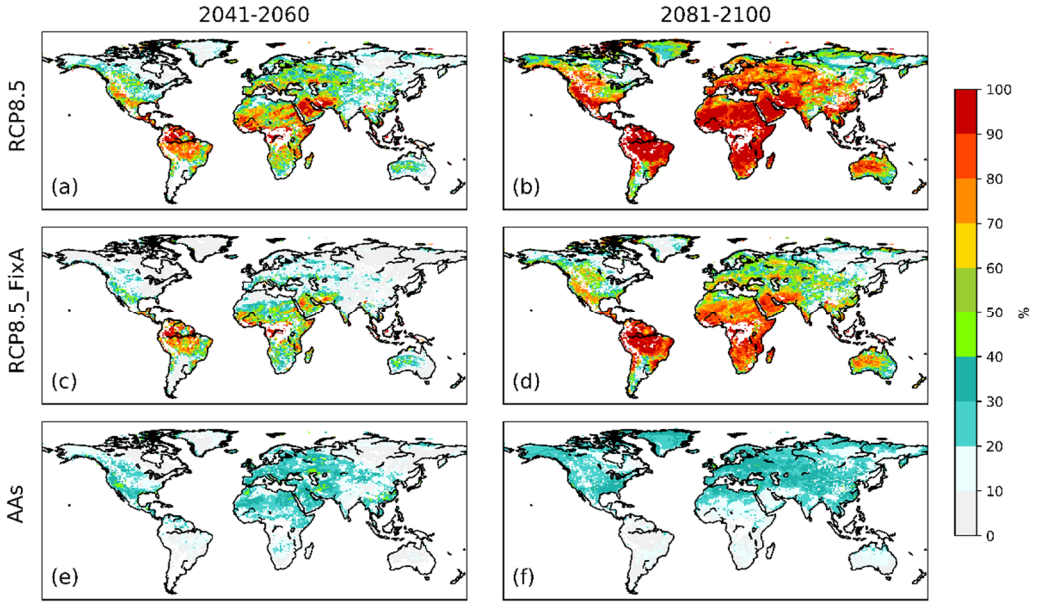

Figure 5.9 Exceedance probability of heatwave magnitude over 2041-2060 (left) and 2081-2100 (right) relative to the baseline period (1986-2005), as calculated from all the ensemble members under (a, b) RCP8.5 (greenhouse gas increases (GHG)+aerosol reductions (AAs)), (c, d) RCP8.5_FixA (GHGs only) and (e. f) the contribution from aerosol reductions.

5.7.2 Sensitivity of heatwaves to warming mechanism

As both GHG increases and aerosol reductions result in future warming, one may ask whether changes in heatwave metrics are more sensitive to one or the other. This is important because the sensitivities can be useful to assess the impacts of different future mitigation strategies. This section examines the sensitivity of future changes in heatwave metrics per unit of global land warming. The sensitivities are calculated as the slope of the linear fit between annual mean heatwave metrics and global land mean temperature changes (Figures 5 10a-c). Note the fitting was performed for 2041-2060 and 2081-2100 (Figures 5.10d-f) separately since these metrics increase exponentially with warming. The time evolution of these metrics together with other variables

used to examine the driving mechanisms of such changes are provided in Figure 5.11.

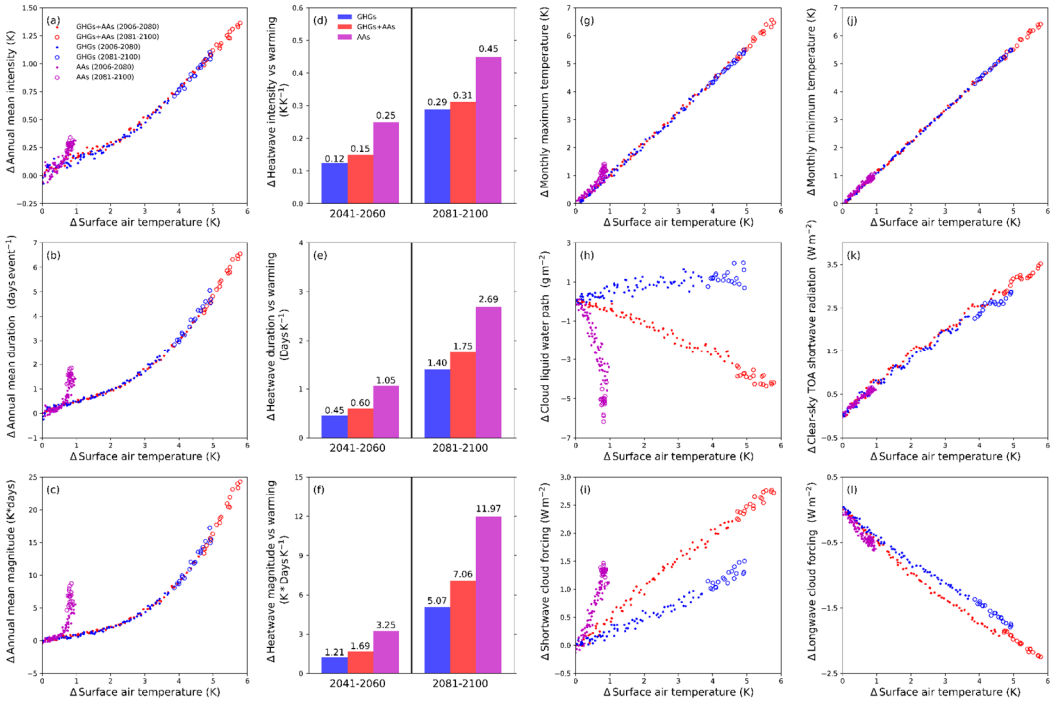

Figure 5.10 Sensitivity of heatwave metrics to warming: scatterplots of changes (ensemble mean of annual mean) in land-only area-weighted mean heatwave (a) intensity (K), (b) duration (days event^{-1}), and (c) magnitude (K*days) against global land mean surface temperature change. The sensitivity of changes in these metrics, derived as the slope of the linear fitting of the scatterplots in (a-c), are shown in (d-f) for the time period 2041-2060 and 2081-2100, respectively. Also shown are changes in the annual mean of global area-weighted mean (g) monthly maximum temperature (TX, K), (h) cloud liquid water path (CLWP, g m^{-2}), (i) shortwave cloud forcing (SWCF, W m^{-2}), (j) monthly minimum temperature (TN, K), (k) clear-sky shortwave radiation at top-of-the-atmosphere (SWCST, W m^{-2}) and (l) longwave cloud forcing (LWCF, W m^{-2}), all plotted against land area-weighted mean surface temperature change (K). All scatterplots are plotted separately for the period 2006-2080 (filled small dots) and 2081-2100 (large circles). The colour conventions are: red for RCP8.5 (GHGs + AAs), blue for RCP8.5_FixA (GHGs only) and magenta for aerosol reductions differentiated as RCP8.5-RCP8.5_FixA.

Heatwave intensity scales relatively linearly with warming from both GHG increases and aerosol reductions (Figure 5.10a), yet the latter leads to a greater heatwave intensity increase than the former per unit of warming over both the two time periods (Figure 5.10d). In fact, the larger sensitivity to warming from aerosol reductions (as compared to GHG increases) stands for

all the three heatwave metrics during both time periods (Figures 5.10d-f). The following focuses on the time period 2081-2100 unless otherwise stated. Over the period 2081-2100, surface mean temperature changes related to aerosol changes (diagnosed as the difference between RCP8.5 and RCP8.5_FixA, see Figure 5.11a) tend to stabilize at around 0.8 K. However, over the same time period, heatwave duration related to aerosols continue to rise from ~1.2 days in 2080 to 1.8 days by 2100 (Figure 5.11e). As a consequence, the sensitivity of heatwave duration to warming from aerosol reductions is two times that due to warming from GHG increases. Aerosol reductions result in changes in heatwave intensity (Figures 5.10a and 5.11d) and duration (Figures 5.10b and 5.11e), in combination (but mainly due to changes in duration), lead the heatwave magnitude to increase exponentially with warming (Figure 5.10c). This leads to an even larger (2.4 times that of GHG increases) sensitivity of heatwave magnitude to warming from aerosol reductions (Figure 5.10f).

The steepest parts of the aerosol-related curves in Figures 5.10a-c correspond to the time period when the aerosols are sufficiently low in the atmosphere (i.e., late 21st century in the RCP8.5 scenario), continuing aerosol reductions tend not to change mean temperature but increase heatwave magnitude exponentially. Because heatwaves are defined using TX and TN, it is interesting to examine if the larger sensitivity to aerosol reductions discussed above stems from changes in maximum (Figure 5.10g) and/or minimum (Figure 5.10j) temperatures. It can be seen aerosol reductions induced exponential TX changes that resemble the shape of the heatwave duration/magnitude relationship with temperature, while TN increases linearly

with warming. Therefore, it is the changes in TX that lead to dramatic increases in heatwave magnitude. This is particularly important over regions of the largest emission sources such as China, Europe, USA and. India (Figure 5.12).

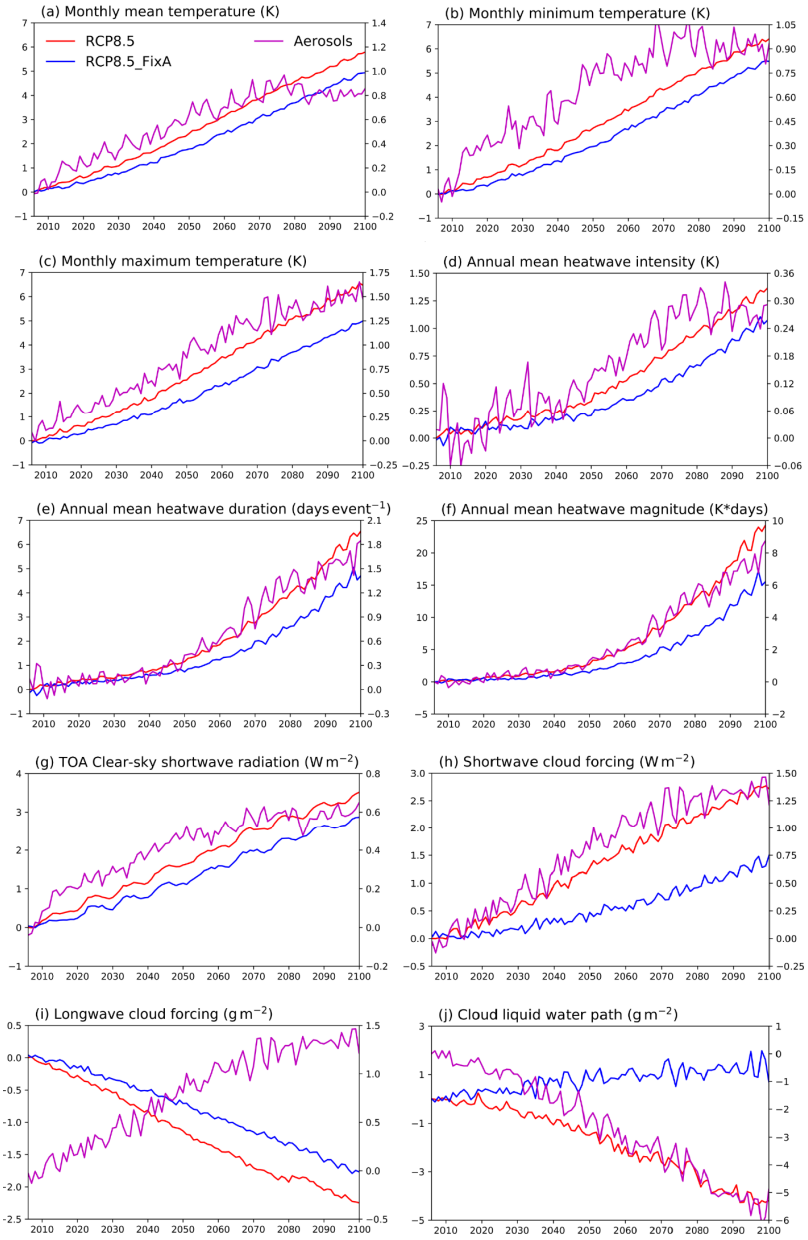

Figure 5.11 Time evolution (2006-2100) of annual mean of land-only mean: (a) monthly mean temperature (K); (b) monthly minimum temperature (K); (c) monthly maximum temperature (K); (d) annual mean heatwave intensity (K); (e) annual mean heatwave duration (days); (f) annual mean heatwave magnitude (K*days); (g) clear-sky shortwave radiation at surface (W m^{-2}); (h) shortwave cloud forcing (W m^{-2}); (i) longwave cloud forcing (W m^{-2}); and (j) cloud liquid water path (g m^{-2}). Red for RCP8.5 (left axis), blue for RCP8.5_FixA (left axis), and purple for the effects of aerosol reductions (right axis) derived as the difference between RCP8.5 and RCP8.5_FixA.

The following investigates if this is related to aerosol direct and/or indirect effects, by examining representative aerosol effect indicators: cloud liquid water path (CLWP, Figure 5.10h), shortwave cloud forcing (SWCF, Figure 5.10i) clear-sky shortwave radiation at top-of-the-atmosphere (SWCST in Figure 5.10k), as well as longwave cloud forcing (LWCF, Figure 5.10l). Note that although cloud can be influenced by dynamic and thermodynamic processes (Rosenfeld et al., 2008; Yu et al., 2014), the strong linear correlation between changes in AOD and cloud forcing (an R^2 of 0.93 for SWCF and 0.80 for LWCF; Figure 5.13) demonstrates that the aerosol-induced changes in cloud microphysics are the main drivers of the additional cloud forcing changes. Clearly, when the aerosol reductions resulted in little change in mean warming by 2081-2100, both CLWP (Figure 5.10h) and SWCF (Figure 5.10i) show dramatic changes that significantly deviate from their linear correlations with warming during 2006-2081. In contrast, SWCST and LWCF continue to show a linear correlation with temperature changes that does not differ much between GHG increases and aerosol reductions (Figures 5.10k, l). Overall, these indicate the importance of aerosol-cloud interactions rather than the aerosol direct effect in increasing TX and thereby heatwave duration/magnitude in a dramatic way. Specifically, when aerosol loading is low by 2081-2100, mean temperature and TN tend to stabilize (Figures 5.11a, b). However, TX increases exponentially (Figures 5.10i and 5.11c), because of large changes in aerosol-cloud interactions.

It is speculated that the exponential increases in TX and heatwave magnitude/duration due to aerosol-cloud interactions are related to the exponential relationship between aerosol radiative forcing, cloud microphysics

and aerosol loading as discussed by Wilcox et al. (2015). More specifically, when the aerosol loadings are sufficiently low, small changes in aerosols can lead to significantly larger responses in cloud droplet size and cloud albedo, compared to the behaviour when the aerosol loadings are high. These result in exponential increases in shortwave radiation reaching the surface (Figure 5.10i) during daytime as well as a more unstable daytime atmosphere (because cloud lifetime and amount reduce as droplet size increases). Therefore, daytime temperatures increase and become more variable while nighttime temperatures are less influenced by aerosol-cloud interactions. Consequently, unlike mean temperature and TN, TX continues to increase.

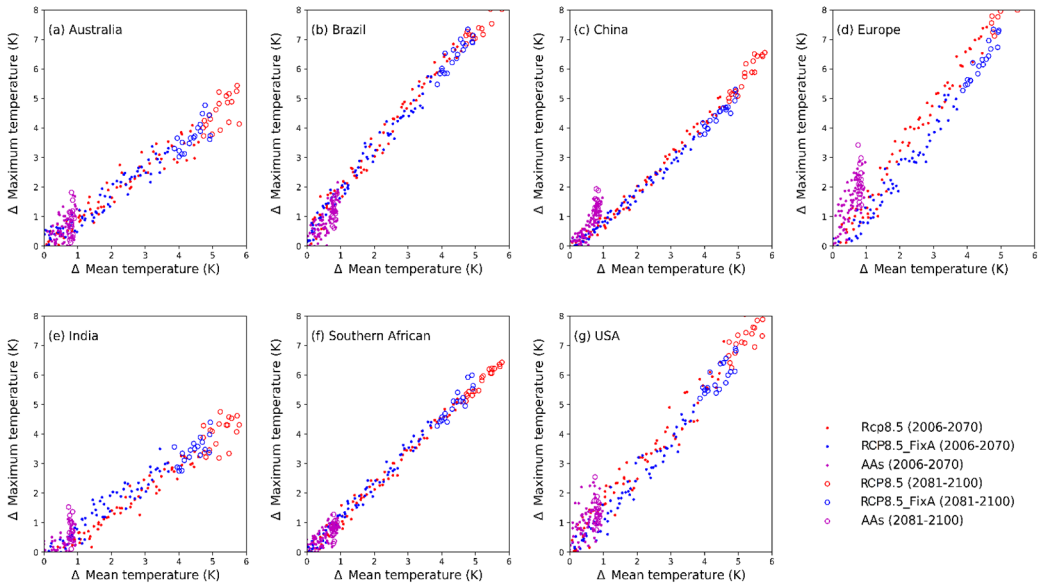

Figure 5.12 The same as Figure 10g, but for regional area-weighted mean of changes in monthly maximum temperature against global mean temperature: (a) Australia, (b) Brazil, (c) China, (d) Europe, (e) India, (f) Southern Africa, and (g) contiguous USA.

Finally, for the same amount of mean warming, TX and heatwave duration increase dramatically due to aerosol reductions (Figures 5.10b, e), but this does not occur in the case of GHG increases. This suggests that aerosol reductions dampen the day-to-day TX variability. That is, the more variable the

TX is from day to day, the fewer the consecutive days with TX above TX95P, and vice versa. The dampening of temperature variability from aerosol reductions, by reducing the chances of intermittent cool days, would lead us to suffer more from persistent heatwaves. A physical explanation is that aerosol reductions may contract the Hadley cell (Allen and Sherwood, 2011) and shift the Northern Hemisphere Hadley branch and jet stream northward (Lucas et al., 2014; Rotstayn et al., 2014; Xu and Xie, 2015; Chemke and Dagan, 2018). In combination these effects dampen atmospheric variability over the tropics and extra-tropics; this has been explicitly demonstrated by Xu et al. (2015) using the same set of model simulations.

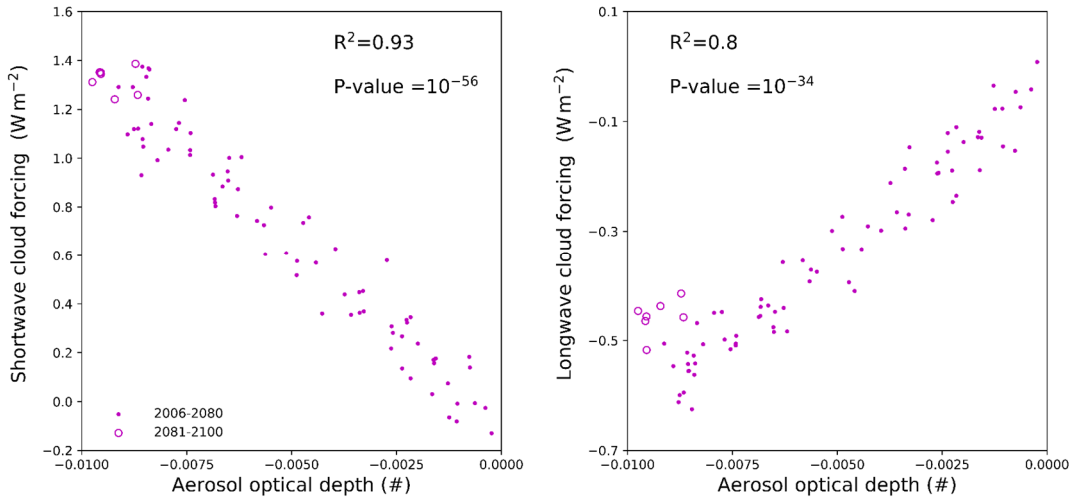

Figure 5.13 The linear correlation between 550nm Aerosol Optical Depth and shortwave (left) and longwave (right) cloud forcing (W m^{-2}), as differentiated by RCP8.5-RCP8.5_FixA. All values are ensemble mean of annual mean of the monthly mean of the area-weighted global mean.

5.8 Discussion and conclusions

A large body of literature has suggested that future GHG increases will very likely enhance the duration, intensity and frequency of heat extremes across the world (Meehl and Tebaldi, 2004; Lau and Nath, 2014; Russo et al., 2014;

Jones et al., 2015; Schoetter et al., 2015; Schär, 2016; Mishra et al., 2017; Mora et al., 2017). However, very little attention has been devoted to contrasting the roles of future GHG increases and aerosol reductions in future heatwave characteristic projections. A few studies have linked future aerosol reductions and increased temperature (or heat) extremes (Xu et al., 2015; Horton et al., 2016). However, their findings did not account for the duration of extreme temperature events, which is critical to properly characterizing a heatwave.

In this study, making use of the LENS, the effects of both changes in GHGs and aerosols on changes in future heatwave characteristics are investigated. It is found that all the heatwave metrics—intensity, duration, frequency, total hot days and magnitude—increase during the 21st century, primarily in response to the long-term warming and with a minor contribution from future temperature variability changes. Note that these heatwave metrics are influenced by the local temperature variability, and should be used in combination to interpret more fully the characteristics of heatwaves. In addition, GHG increases will account for most of these changes while aerosol reductions will exert their impact especially over the Northern Hemisphere. However, given the same amount of warming, aerosol reductions are shown to increase the heatwave magnitudes in highly non-linear ways, through aerosol-cloud interactions. The various RCP scenarios have similar aerosol—but different GHG—emission pathways (Lamarque et al., 2013). In particular, the lower GHG increases in other RCP scenarios compared to RCP8.5 may induce smaller changes in heatwave metrics. Therefore, aerosols are likely to play a more important role in future heatwave projections. Furthermore, these

heatwave metrics may differ under other future scenarios such as the shared socio-economic pathways in which the spatial patterns of emission reductions differ (Gidden et al., 2018).

The overall minor contribution of changes in temperature variability to future heatwave changes indicates the importance of the choice of the baseline (1961-1990 in this case) in setting the threshold for identifying the occurrence of a heatwave. In addition, “present-day” is defined as 1986-2005. Choosing a later period (1996-2015) result in only very minor changes, and does not influence the conclusions. It is acknowledged that the analysis here is based on one model, and it is currently unknown if the projections of changes in heatwave metrics described above hold across models. Climate models represent background aerosols differently (Carslaw et al., 2013); these may lead to differences in the magnitude of the forced response to changing aerosols between models. This is particularly important in an already aerosol-limited environment (Samset, 2018; Lewinschal et al., 2019), and may suggest that the non-linear responses in heatwave metrics to aerosol changes are model dependent. Therefore, further research, using similar methods, is needed to further assess the findings here.

To summarize, the CESM1 indicates that major changes in anthropogenic aerosols over the coming century can have very significant impacts on future heatwaves through aerosol-cloud interactions. However, the caveat is that this might only be a reflection of the specific aerosol scheme in CESM1. In fact, there still are large uncertainties in our understanding of aerosol-cloud-radiation interactions, leading to poorly-constrained and diverging aerosol schemes in present generation climate models (Wilcox et al., 2015; Lee et al.,

2016; Seinfeld et al., 2016; Malavelle et al., 2017). Therefore, our present projection of future heatwaves, and perhaps other types of climate extremes, might have large uncertainties. However, given the detrimental impacts of changes in future heatwaves and to more effectively manage climate risks, this study calls the attention of the community to prioritize efforts in reducing uncertainties in aerosol-cloud-radiation interactions.

Chapter 6 Impacts of Future Greenhouse Gas Increases and Aerosol Reductions on Precipitation Extremes over Asia

This chapter is adapted from a published paper on which I am the lead author. I performed all data analysis, and wrote the first draft of the manuscript. Dr David Stevenson and Dr Massimo Bollasina supervised the study, and provided comments on subsequent manuscript revisions. Two anonymous reviewers provided additional comments and suggestions during peer-review.

Zhao, A. D., Stevenson, D. S., & Bollasina, M. A. (2018). The role of anthropogenic aerosols in future precipitation extremes over the Asian Monsoon Region. Climate Dynamics, 1-22.

6.1 Abstract

The role of anthropogenic aerosols in future projections (up to 2100) of summertime precipitation and precipitation extremes over the Asian monsoon region is investigated, by comparing two sets of the Community Earth System Model (CESM1) large ensemble simulations (LENS) under the Representative Concentration Pathway 8.5 scenario (RCP8.5) and the corresponding scenario with aerosol fixed at 2005 levels (RCP8.5_FixA). The results suggest that the Asian monsoon region would become progressively warmer and wetter in the future under RCP8.5, while precipitation extremes will be significantly aggravated due to anthropogenic aerosol mitigation, particularly over East Asia. Specifically, aerosol reductions are found to shift the distribution of precipitation mean and extremes to larger values. For example, aerosol reductions would result in an increased likelihood of extreme precipitation (e.g., the maximum consecutive 5-day precipitation amount) and related disasters. Sensitivities of changes in mean and extreme precipitation indices to local warming from aerosol reductions are much larger than that from greenhouse gas increases. This is particularly important over East Asia in accordance with larger magnitudes of aerosol reductions compared to South Asia. Finally, by investigating the response of the climate system to aerosol changes, it is found that aerosol induced precipitation changes would be dominated by aerosol-radiation-cloud forcing over northern East Asia and aerosol forcing induced large-scale circulation anomalies over southern East and South Asia.

6.2 Introduction

Asia, the world's most populated and fastest developing region, has witnessed dramatic economic, urban and industrial growth and has been the world's largest source of aerosols and their precursors over the last few decades (Li et al., 2016). The Representative Concentration Pathway scenarios (RCPs) (Riahi et al., 2007; Lamarque et al., 2011; Van Vuuren et al., 2011) project, to varying extents, a decline of anthropogenic aerosol and their precursor emissions worldwide over the coming decades, due to positive mitigation policies aimed at alleviating air pollution (Westervelt et al., 2015). In particular, significant aerosol reductions are expected over much of Asia due to stringent legislation. Since aerosols have long been found to significantly modulate climate locally and globally, it is important to understand and quantify whether precipitation extremes may change in response to future changes in aerosols.

The availability of long-term global scale observations and improvements in climate modelling have allowed advances in our understanding of past changes of precipitation and precipitation extremes (Sen Roy and Balling, 2004; Zhai et al., 2005; Orlowsky and Seneviratne, 2012; Singh et al., 2014; Zhou et al., 2014; Freychet et al., 2015; Dong et al., 2016; Freychet et al., 2016; Wang et al., 2016b; Wang et al., 2017b). For instance, the enhancement of the hydrological cycle is suggested to lead wet (dry) regions to become wetter (drier) (Held and Soden, 2006; Tebaldi et al., 2006; Singh et al., 2013). This wet-get-wetter paradigm, especially valid in the zonal-mean sense, is projected to continue in the future in response to continued warming, especially over the Northern Hemisphere (Min et al., 2011; Sillmann et al., 2013b; Sillmann et al., 2013c; Sillmann et al., 2013a).

Changes in precipitation and precipitation extremes have so far been attributed variously to both internal natural variability (Chung and Ramanathan, 2006; Qian and Zhou, 2014) and external forcings, including greenhouse gases (GHGs) and aerosols (Polson et al., 2014; Mascioli et al., 2016; Lau and Kim, 2017; Ma et al., 2017). Changes in mean precipitation have been largely linked to the variation in the water vapour holding capacity of the atmosphere with global mean temperature in response to changes in a forcing agent – as specified by the Clausius-Clapeyron scaling, at a rate of 7% K^{-1}. However, this thermodynamical control on precipitation changes is partially offset by a slowdown of the atmospheric circulation in order to satisfy global energetic constraints, resulting in a much smaller change per unit warming (1-3 % K^{-1}) (Allen and Ingram, 2002; Wentz et al., 2007; Pendergrass and Hartmann, 2014; O'Gorman, 2015; Burke and Stott, 2017). Precipitation extremes are mainly constrained by lower-tropospheric moisture availability and supply within individual weather systems that are more related to local-scale, short time period effects rather than the global-scale energy budget. Although precipitation extremes follow the Clausius-Clapeyron relation more closely than mean precipitation (Lin et al., 2016), deviations have been observed, including changes at a super-CC scaling, due to the influence of multiple thermodynamic and dynamic factors (Caesar and Lowe, 2012; Westra et al., 2013). Besides, studies also claim that regional precipitation extremes scale more strongly with dew point temperature rather than absolute temperature, e.g., over India (Ali et al. 2017; Ali et al. 2018; Mukherjee et al. 2018).

A number of studies have shown that aerosols have substantial impacts on precipitation and precipitation extremes (Ramanathan et al., 2005; Polson et

al., 2014; Sanap et al., 2015) via complex, and in some cases, competing mechanisms. For instance, increases in aerosols during the 20th century have been found to contribute remarkably to the decrease in the Northern Hemisphere precipitation (Polson et al., 2013); the meridional shift of the Inter-Tropical Convergence Zone (Hwang et al., 2013), the weakening trend of the South Asian summer monsoon (Bollasina et al., 2011), the so-called summer "Southern-Flood-Northern-Drought" (SFND) pattern over the East China (Gong and Ho, 2002; Song et al., 2014; Deng and Xu, 2016; Li et al., 2016), as well as the shift of rainfall towards heavy mode over the East China (Ma et al., 2017). By investigating changes in temperature and precipitation extremes under different future emission scenarios, it was found that future GHG-induced changes will be strongly exacerbated under global aerosol reductions (Sillmann et al., 2013a). In addition, aerosols are suggested to have competing influences which offset GHG effects at regional scales such as over North America (Mascioli et al., 2016). More recently, it was suggested that future aerosol reductions will lead to a significant increase in precipitation extremes over Asia (Wang et al., 2016b), a topic that is investigated further here.

The extensive Asian Summer Monsoon (ASM)—spanning South Asia (SA), Southeast Asia, and East Asia (EA)—is essentially driven by the large-scale thermal contrast arising from the different heat capacities of land and ocean in response to the seasonal changes in solar radiation reaching the Earth's surface (Li et al., 2016). The ASM plays a significant role in large-scale climate variability over much of the globe, and monsoon precipitation is crucial for the socio-economic well-being and agriculture of billions of people. Despite recent advances in our understanding of aerosol-monsoon interactions, the extent to

which anthropogenic aerosols affect the monsoon and the underlying mechanisms are still largely uncertain. In particular, identifying the aerosol imprint on precipitation extremes is even more challenging. This chapter seeks to quantify the effect of anthropogenic aerosol reductions on future projections of summertime precipitation extremes over Asia using the LENS simulations (see Section 1.6).

6.3 Data and methods

In addition to the output from the LENS, observational datasets are used to evaluate the present-day model climatology. Daily precipitation from the Asian Precipitation Highly-Resolved Observational Data Integration Towards Evaluation (APHRODITE; Yatagai et al. (2012)) dataset at 0.5º × 0.5º resolution (interpolated to the model grid) was used to compute observed mean and extreme precipitation over Asia. APHRODITE is the only long-term (1951-onward) continental-scale product that makes use of a dense network of daily rain-gauge data for Asia (Yatagai et al., 2012). Additionally, LENS simulated mean surface air temperature and 850 hPa winds were compared to those from the NCEP/NCAR reanalysis (Kalnay et al., 1996) at 2.5º x 2.5º resolution.

Given the complex interplay and the existence of major differences in the underlying mechanisms between the two main sub-components of the Asian monsoon, the South Asian and East Asian monsoons (Yihui and Chan, 2005), the analysis is performed separately for South (5º-30ºN, 65º-100ºE) and East (20º-50ºN, 100º-145ºE) Asia (Giorgi and Francisco, 2000), as defined in Figure 6.1. Extreme precipitation is characterised by four indices chosen from those

defined by the Expert Team on Climate Change Detection and Indices (ETCCDI) (Alexander et al., 2006; Zhang et al., 2011), described in Table 6.1. This study focuses on the Northern Hemisphere summer (June-July-August, hereinafter JJA), when the monsoon is fully established over Asia (Wang, 2006). All the precipitation indices are computed over JJA at each land grid-cell for all the ensemble members of the two scenarios. To isolate aerosol effects, the difference between the mean of the two ensemble members are calculated, while their statistical significance is evaluated using the two-tailed student t-test.

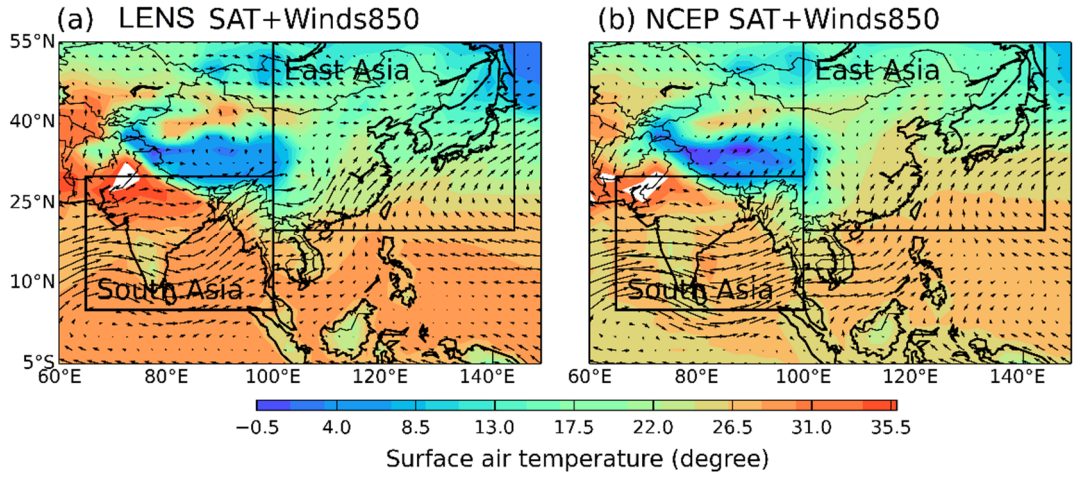

Figure 6.1 Surface air temperature (SAT, shadings, ℃) and 850 hPa winds (Winds850, arrows, m s^{-1}), 1986-2005 summertime (June-July-August, JJA) mean over the Asia monsoon region (AMR, 5ºS-55ºN, 60ºE-150ºE) derived from (a) LENS ensemble mean, and (b) NCEP reanalysis. Boxes denote South Asia (SA, 5ºN-30ºN, 65ºE-100ºE) and East Asia (EA, 20ºN-50ºN, 100ºE-145ºE) respectively.

Future change of each precipitation index is calculated as an anomaly relative to the 1986-2005 mean baseline. Note that area-averaged quantities are computed by using land-only points. To produce time series of the index over South (SA) and East Asia (EA), each index is spatially averaged for each year of each ensemble member, and the ensemble median and spread (5^{th}-95^{th} percentiles) for each year are provided. To produce spatial anomaly maps, the

index in each grid-cell is annually averaged throughout the time interval (e.g., 2031-2050) for each ensemble member. Then, the two ensemble sets of annually averaged maps (30 for RCP8.5 and 15 for RCP8.5_FixA) are used to calculate the statistical significance of the difference, and averaged across each set of ensemble members to produce the ensemble mean RCP8.5 and RCP8.5_FixA maps and their differences.

Table 6.1 Definition of the precipitation indices used in Chapter 6, wet day is referred when daily precipitation ≥1 mm, the 95th percentile threshold is calculated from the 1961-1990 daily precipitations. All the indices are calculated over the Northern Hemisphere summer (June-July-August, JJA).

Acronym	Name	Brief definition	Units
PMEAN	Mean precipitation	Mean of daily precipitation	mm day^{-1}
RX5DAY	Maximum consecutive 5-day precipitation	The maximum of consecutive 5-day precipitation	mm
R10	Moderate-to-heavy precipitation frequency	Count of days with precipitation ≥10 mm	days
CWD	Maximum duration of wet spell	Maximum number of consecutive wet days	days
R95P	Amount of extreme precipitation	Total of precipitation ≥95th percentile	mm

6.4 Model evaluation in reproducing precipitation extremes

The performance of CESM1 in capturing climate extremes has been evaluated over the globe (Kharin et al., 2013; Sillmann et al., 2013b) and local regions such as China (Wang et al., 2016b). To provide a further indication of the performance of the LENS in reproducing precipitation extremes over the Asian monsoon region (AMR), the climatology fields and precipitation extremes derived from LENS are compared to observations/reanalysis during 1986-2005. Figure 6.1 shows a comparison between observed and simulated JJA

surface air temperature and 850-hPa winds. LENS shows agreement with the reanalysis in capturing both the spatial pattern and the magnitudes of temperature as well as winds. The major monsoon trough over the South China Sea, the subtropical anti-cyclonic circulation with strong south-westerlies from the Indian Ocean that converges over the South China Sea with the easterlies from the tropical Pacific, and also the higher latitude westerlies are all notable features well represented by CESM1.

Figure 6.2 compares observed and simulated JJA mean and standard deviation of daily precipitation. Generally, both the climatological mean and variability are captured reasonably well by LENS, although when the model is averaged over the whole region it tends to produce overestimates. Such overestimates are most significant over the Himalayas-Tibetan plateau, southern India and Northeast China (Figures 6.2e, f). On the contrary, precipitation is underestimated over central India and a large proportion of South China. Quantitatively, a positive bias in mean precipitation of 0.95 mm day^{-1} (19%) and 1.56 mm day^{-1} (23%) is found over SA and EA, respectively; while the bias for precipitation variability is respectively 1.21 mm day^{-1} (14%) and 1.01 mm day^{-1} (12%). In addition, a comparison of historical changes (1986-2005 minus 1951-1970) in precipitation extremes between LENS and APHRODITE was carried out (Figure 6.3). There exist similarities between LENS and APHRODITE in capturing these historical changes, with significant differences though. It should be noted that detailed reproduction of observed changes in precipitation extreme indices is particularly challenging for a model, and some biases are inevitable and to be expected. Note that these findings are consistent with recent multi-model evaluations (Ashfaq et al., 2017), which

deemed CESM1 to be among the best performing models in simulating a number of features of the South Asian monsoon.

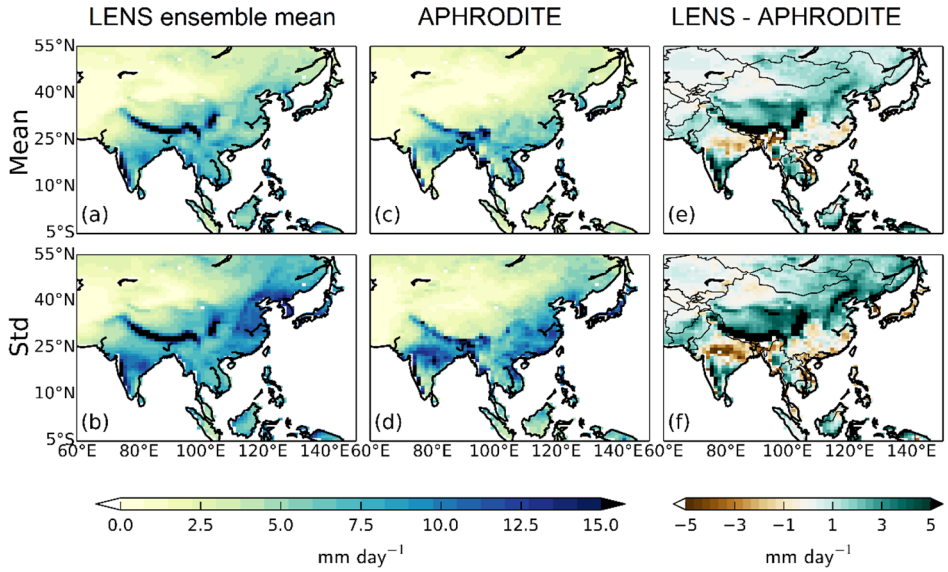

Figure 6.2 Daily precipitation (mm day^{-1}), 1986-2005 JJA (a, c) mean and (b, d) variability of derived from (a, b) APHRODITE, (c, d) LENS ensemble mean, and (e, f) the difference between LENS ensemble mean and APHRODITE. The APHRODITE data were interpolated to the LENS grid (0. 9 º×1.25º).

Albeit incomplete, the above analysis shows that CESM1 captures the key climatological features of the Asian summer monsoon, which provides a solid foundation for using it to investigate precipitation changes and extremes. Figure 6.4 shows the precipitation extreme indices (RX5DAY, R10, CWD, and R95P) averaged throughout 1986-2005 for the ensemble mean of LENS as well as APHRODITE. In general, LENS can reproduce these indices well although some biases are found regionally. The probability distribution functions (PDFs) for these extreme indices over SA and EA throughout 1986-2005, calculated from APHRODITE and the LENS ensemble members in Figure 6.4, demonstrate that LENS-simulated historical precipitation extremes generally agree with APHRODITE. However, LENS tends to produce slight overestimates. Furthermore, with the exception of CWD over EA, all of the four

precipitation extreme indices over EA and SA are greater than over the rest of the Asian continent. This indicates that at present EA and SA feature relatively more extreme precipitation compared to their surroundings. This is also noted by CMIP5 studies (Sillmann et al., 2013b) and observations (Alexander et al., 2006). In summary, the above analysis indicates that the LENS is a viable tool to study precipitation extremes over the AMR.

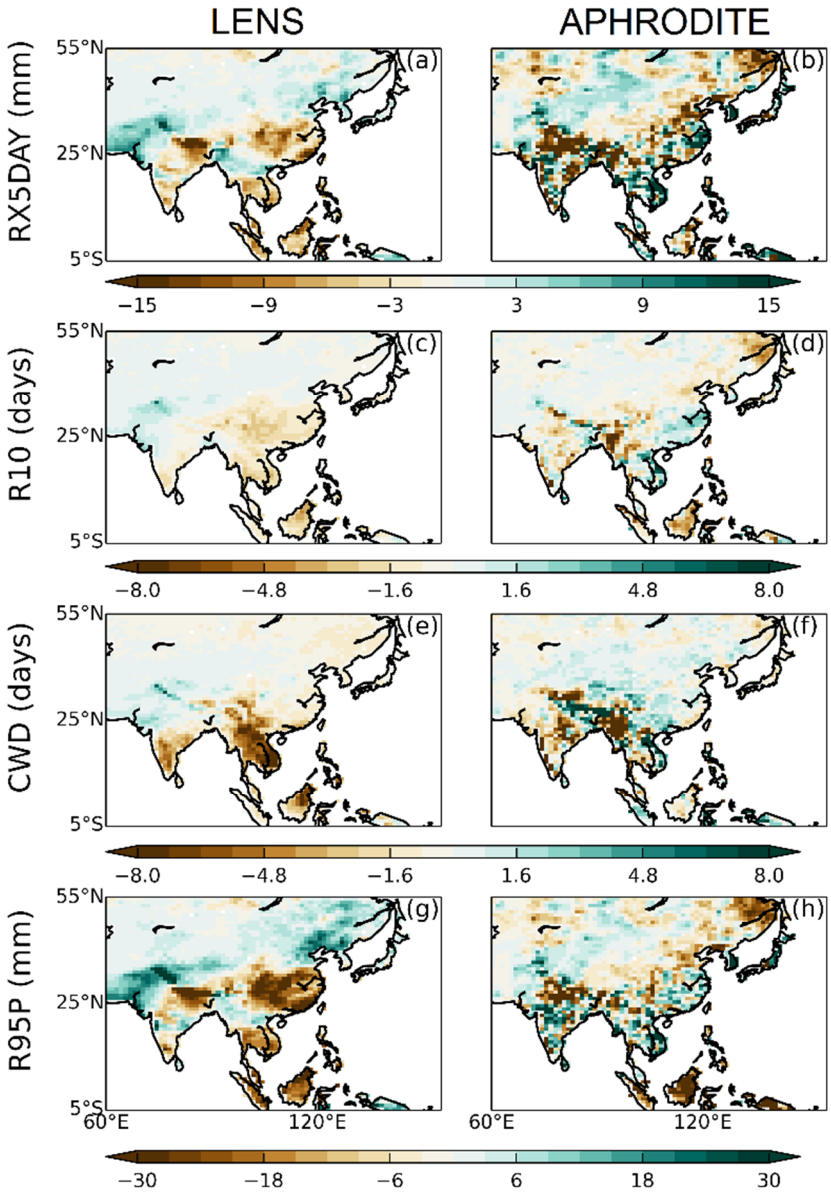

Figure 6.3 Comparisons of historical changes (1986-2005 minus 1951-1970) in precipitation extremes over the AMR. The changes are derived from (left) LENS ensemble mean, and (right) APHRODITE.

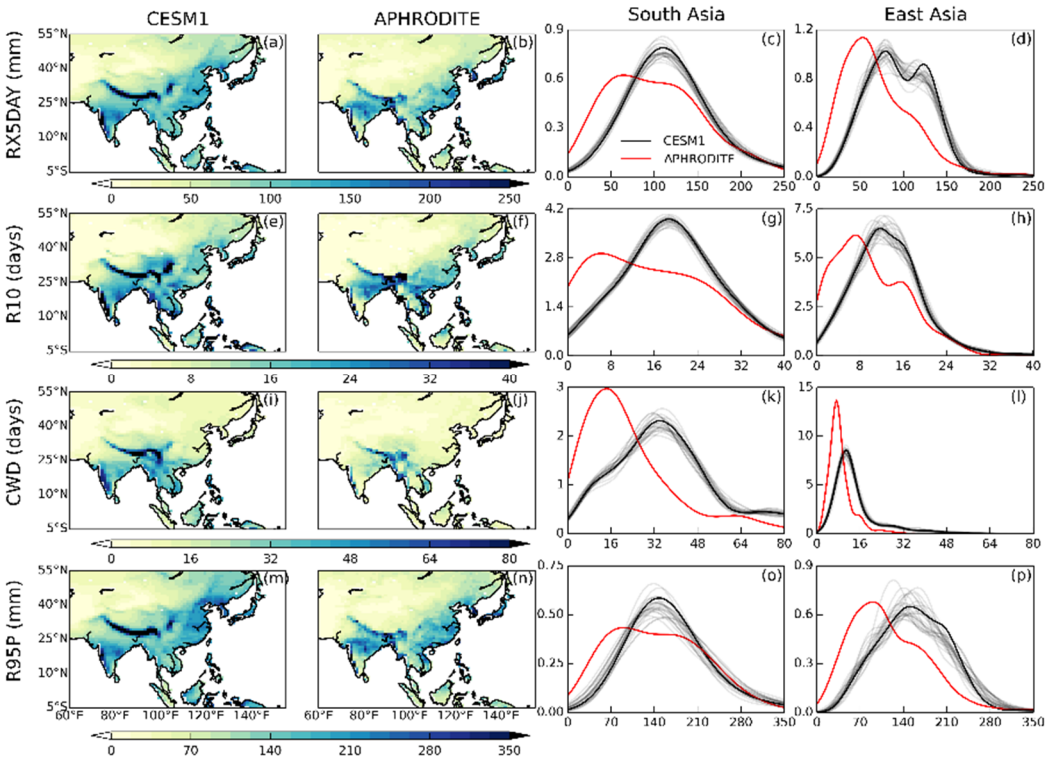

Figure 6.4 Comparison of 1986-2005 JJA extreme precipitation indices (a-d: RX5DAY (mm); e-h: R10 (days); i-l: CWD (days); and m-p: R95P (mm)), between LENS ensemble mean (first column) and derived from APHRODITE observations (second column). For definitions of indices, see Table 6.1. Third column (SA) and fourth column (EA) show probability density functions (PDFs, %) based on the spatially resolved data for each LENS ensemble member (grey lines), the ensemble mean (black line), and APHRODITE (red line), all at the model resolution of 0.9° x 1.25°).

6.5 Future projections to 2100

6.5.1 Changes in aerosol/precursor emissions and burdens

The global and regional annual mean aerosol/precursor emissions and LENS simulated AOD changes have been discussed in Section 5.5. This section presents the summertime aerosol/precursor emission changes in Asia. Figure 6.5 shows the time evolution (2006-2100) of summertime anthropogenic aerosol/precursor emissions under the RCP8.5 emission pathway together with the LENS simulated aerosol burdens over the AMR, EA and SA. Given the short aerosol residence time in the atmosphere, it is not surprising that

temporal changes in aerosol burdens closely follow those of emissions. As such, hereinafter discusses only aerosol burdens unless otherwise specified.

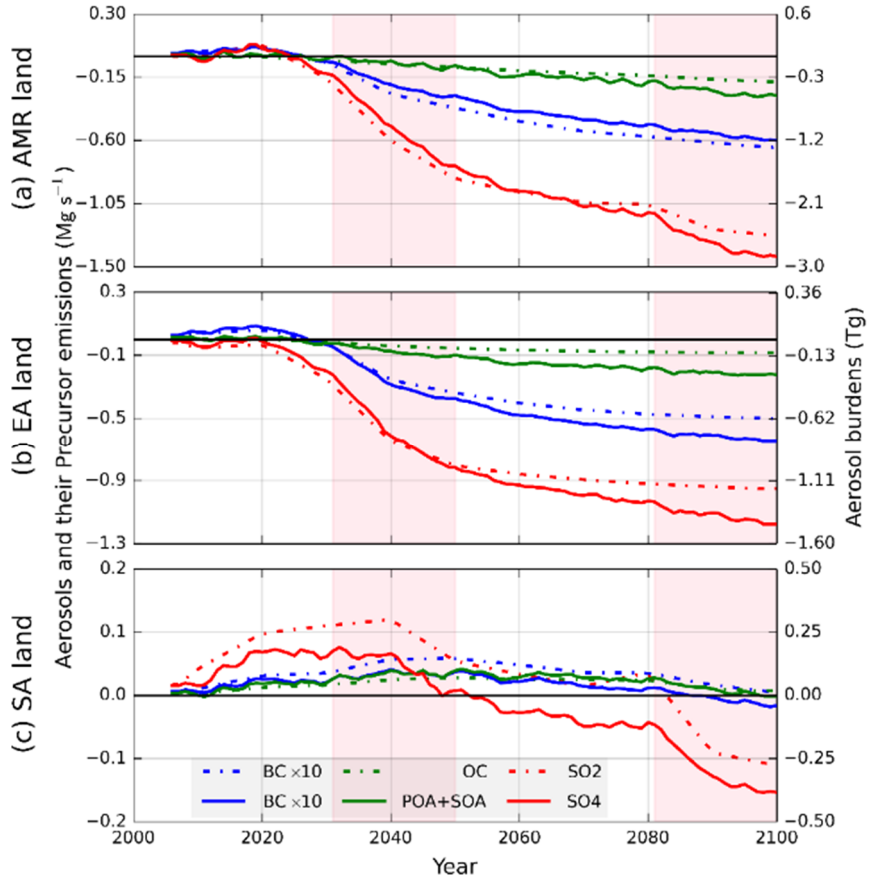

Figure 6.5 Time evolution (anomalies relative to 2005) of JJA aerosol/precursor emissions (dotted lines, left axis, blue for black carbon (BC), green for organic carbon (OC), and red for sulphur dioxide (SO_2), Mg s^{-1}), and aerosol burdens (solid lines, right axis, blue for BC, green for OC, and red for sulphate (SO_4) respectively, Tg) accumulated over land grid-cells of (a) AMR, (b) EA and (c) SA. The aerosol burdens shown are the difference between RCP8.5 and RCP8.5_FixA. The pink shadings from left to right highlight the time period 2031-2050 and 2081-2100, respectively.

Changes in sulphate aerosol (SO_4) are the most pronounced in magnitude and differ between EA and SA. More specifically, SO_4 over SA increases to peak around 2020-2040 and then declines steadily to below its 2005 level after the 2050s. By 2100, the summertime SO_4 burden over the AMR will have decreased by around 2.8 Tg (-67%) with the largest changes (1.4 Tg, -80%) arising from EA. The BC burden increases to peak around the 2010s in EA

and the 2050s in SA, then decreases relative to 2005 by around 0.12 Tg (-52%) over the AMR and 0.08 Tg (-75%) over EA by the end of this century. The BC burden over SA, by comparison, increases by 0.01 Tg (+22%) up to 2050 and then drops back to the 2005 level by the 2090s. Changes in OC tell almost the same story as BC throughout the century, except for a larger magnitude. Note the percentage changes are calculated relative to the simultaneous aerosol burdens simulated under RCP8.5_FixA.

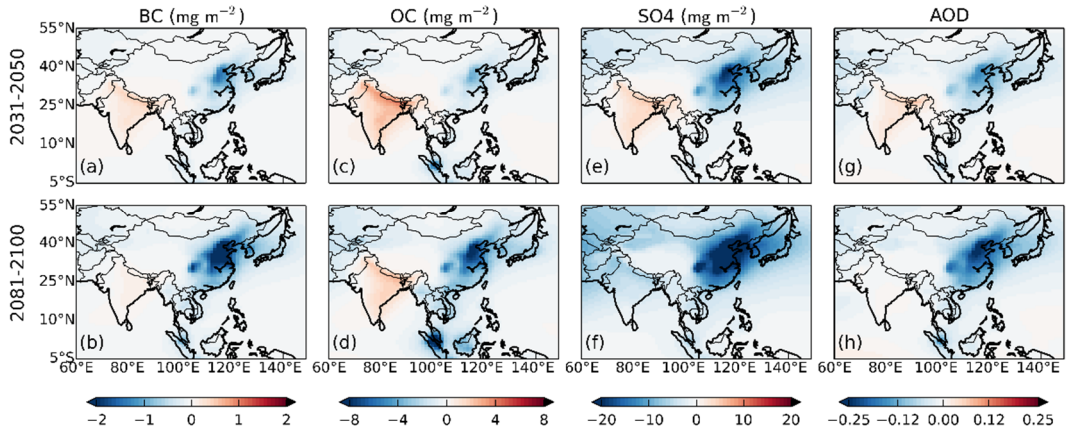

Figure 6.6 Difference in aerosol burdens (mg m^{-2}) between RCP8.5 and RCP8.5_FixA, for (a, b) BC, (c, d) OC, and (e, f) SO_4, as well as (g, h) 550-nm Aerosol Optical Depth (AOD), averaged throughout 2031-2050 (top) and 2081-2100 (bottom).

The simulated differences, averaged over 2031-2050 and 2081-2100 (highlighted by the pink shadings in Figure 6.5), of summertime BC, OC and SO_4 burden, as well as the Aerosol Optical Depth at 550nm (AOD) over the AMR, are shown in Figure 6.6. These two time periods are selected to show contrasting aerosol effects. Relative to RCP8.5_FixA, while BC, OC and SO_4 are projected to decline over EA during 2031-2050, SA shows increases in all three aerosol species, with peak relative increases of 26% (BC), 23% (OC) and 32% (SO_4) over the Indo-Gangetic plain. As a result, AOD differences between SA and EA up to 2031-2050 show changes with opposite signs, with

an average increase of 0.04 for SA and an average decrease of 0.06 for EA. By 2081-2100, the aerosol burden over EA is predicted to dramatically decrease. For SA, in comparison, increases in BC and OC can still be seen, whereas SO_4 decreases slightly. The AOD pattern (Figures 6.6g, h), mostly attributable to sulphate aerosol, shows reductions over EA (-0.074 on average) and East China (well below -0.20) in particular, but relatively minor decreases over SA (-0.006 on average) by 2081-2100.

6.5.2 Changes in precipitation and precipitation extremes

The temporal evolution of projected changes in summertime surface air temperature, mean precipitation, as well as precipitation extreme indices under RCP8.5 and RCP8.5_FixA over EA and SA, are provided in Figures 6.7 and 6.8 respectively. The spatial pattern of mean precipitation anomalies relative to the 1986-2005 climatology is presented in Figure 6.9, while Figure 6.10 shows the spatial patterns of the aerosol-induced changes in the precipitation extreme indices averaged over 2031-2050 and 2081-2100. Under RCP8.5, where both GHGs and aerosols (Figures 6.5 and 6.6) change significantly, temperature increases rapidly with time, with a net warming by 2100 of up to +5.8 K over EA (Figure 6.7a) and +4.4 K over SA (Figure 6.8a). Accompanying the warming there is also an evident increase in mean precipitation, RX5DAY, R10 and R95P over both regions, whereas CWD increases in EA but decreases in SA.

The following sections focus on the difference between RCP8.5 and RCP8.5_FixA to isolate the effects of aerosols on variations in mean and extreme precipitation indices. Over EA, the net warming (Figure 6.7a)

associated with aerosol reductions becomes progressively larger over time. In comparison, increasing aerosol loading over SA (Figure 6.5c and Figure 6.6) does not produce an appreciable temperature change before 2040 (Figure 6.8a). This can be because the cooling induced by sulphate aerosol increases is quite limited and is offset by the warming due to increases in absorbing aerosols (BC mainly). From 2040 onward, however, the net warming due to aerosol reductions becomes evident over both SA and EA, although the latter features large model internal variability. Changes in mean precipitation (Figures 6.7b and 6.8b) show generally consistent trends with warming, but features a wide ensemble spread, especially over SA (Figure 6.8b).

There are relatively larger model internal spreads in all precipitation indices compared to temperature, although statistics indicate that aerosol changes induce changes in mean and extreme precipitation indices that are significant. The relatively larger model internal spread in precipitation indices is related to the heterogeneous nature of the precipitation response while the seasonal mean temperature responses have a more uniform spatial structure. Notably, warming induced by aerosol reductions has a proportionally larger impact on mean precipitation than that induced by GHG increases. This can be clearly seen from 2060 onwards over both SA and EA. Over EA, the 1 K of warming from aerosol reductions by 2081-2100 is associated with a mean precipitation increase of approximately 0.5 mm day^{-1}, whereas 4 K of warming from GHG increases results in the same amount of mean precipitation increase. As for SA, similarly, the 0.5 K of warming from aerosol reductions has the same effects on mean precipitation as 3 K of warming from GHGs.

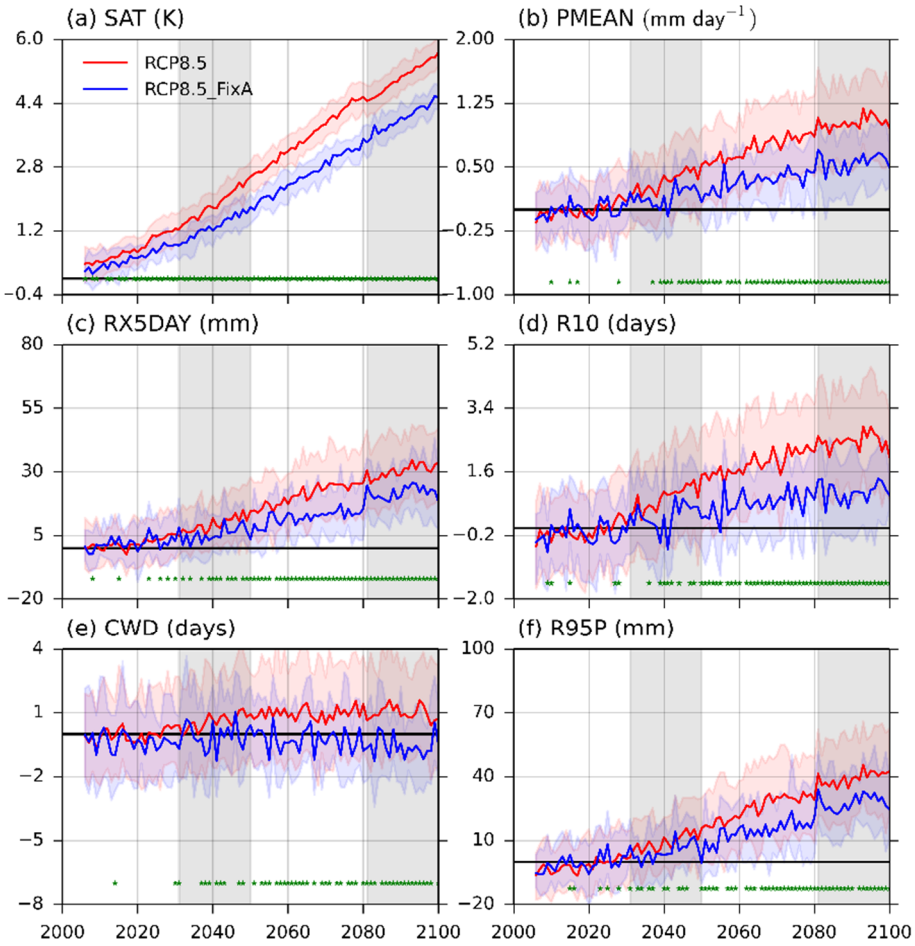

Figure 6.7 Time evolution (anomalies relative to 1986-2005 mean), over EA, of spatially averaged JJA (a) surface air temperature (SAT, K), (b) precipitation mean (mm day^{-1}), (c) RX5DAY (mm), (d) R10 (days), (e) CWD (days) and (f) R95P (mm), calculated for RCP8.5 (red, 30 ensemble members) and RCP8.5_FixA (blue, 15 ensemble members). Solid curves indicate ensemble medians and shadings are 5th to 95th percentiles spread. Green stars indicate 95% (p-value ≤0.025) statistical significance of the ensemble differences. Grey shadings highlight the time periods 2031-2050 and 2081-2100. The black horizontal line indicates no changes.

The spatial pattern of mean precipitation changes (Figure 6.9c) shows that, by 2031-2050, aerosol reductions over EA lead mean precipitation to increase over a large proportion of Asia, whereas decreases are found over parts of the Himalayas-Tibetan Plateau. By 2081-2100, as shown in Figure 6.9f, greater magnitudes of mean precipitation increase over a larger proportion of the AMR in accordance with additional aerosol reductions can be clearly seen. This is most pronounced over Southeast and East Asia. Moreover, over Eastern

China under RCP8.5_FixA (Figures 6.9b, e), there exists an evident dipole in the mean precipitation featuring a precipitation decrease to the north and strong wetting to the south along with GHG induced warming. The dipole resembles the recently observed Southern-Flood-Northern-Drought (SFND) pattern (Yu et al., 2010) which was found to be largely related to aerosol changes (Jiang et al., 2013). However, this SFND pattern is substantially reduced under RCP8.5 (Figures 6.9a, d), especially by 2081-2100 (Figure 6.9d), due to aerosol induced increases in mean precipitation (Figures 6.9c, f). Therefore, the results suggest that the SFND pattern might be alleviated with stringent emission controls adopted in the future.

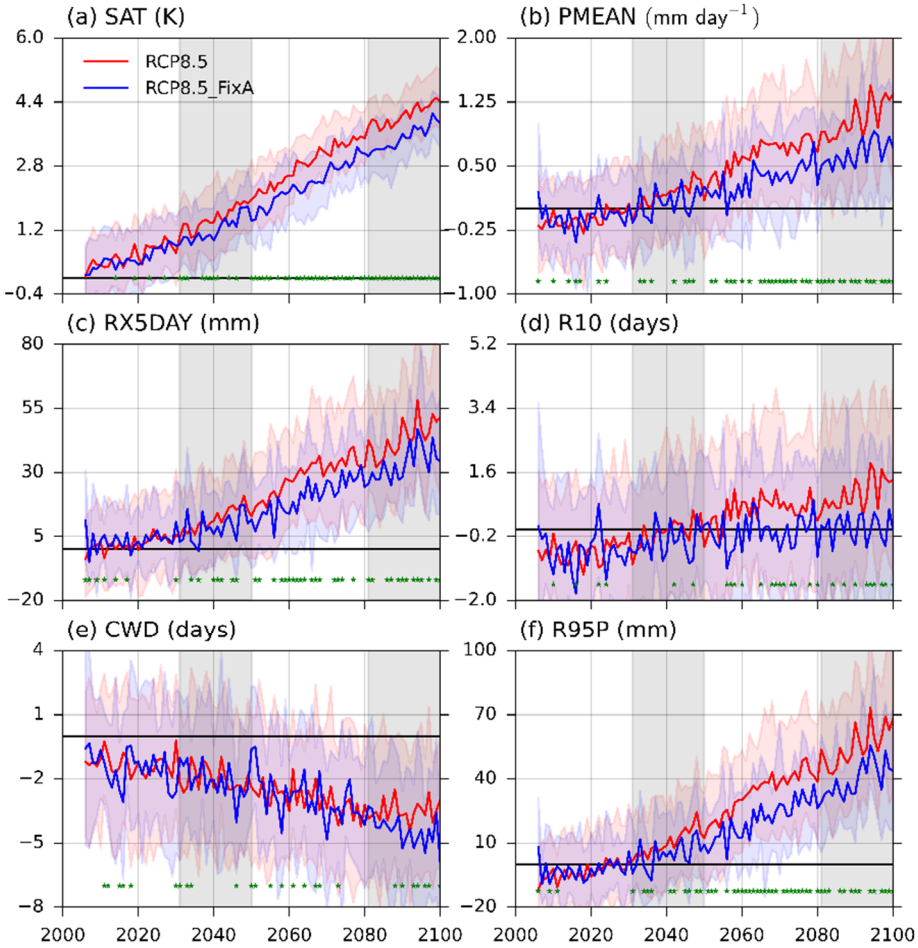

Figure 6.8 Same as Figure 6.7, but for SA.

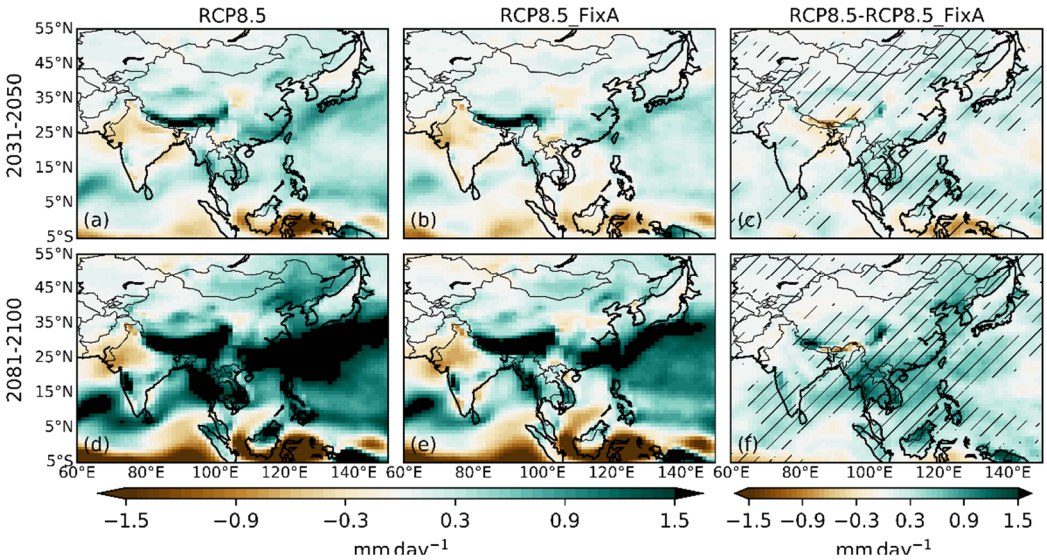

Figure 6.9 Mean JJA precipitation (relative to 1986-2005 mean, mm day^{-1}) under (a, d) RCP8.5, (b, e) RCP8.5_FixA and (c, f) their difference (RCP8.5 minus RCP8.5_FixA), averaged over 2031-2050 (top) and 2081-2100 (bottom). The dots in (c, f) denote the 95% statistical significance of the ensemble differences.

Figures 6.7-6.9 show that, along with warming and mean precipitation increases because of aerosol changes, the associated changes in precipitation extremes become progressively more pronounced (with the exception of CWD over SA). Aerosol reductions lead RX5DAY to increase over a larger portion of the AMR from 2031-2050 (Figure 6.10a) to 2081-2100 (Figure 6.10b). Given that RX5DAY represents the maximum magnitude of heavy precipitation over a 5 day period, changes in RX5DAY can be used as a proxy for flooding and related hazards (Frich et al., 2002; Sillmann et al., 2013c). Therefore, changes in RX5DAY between RCP8.5 and RCP8.5_FixA suggest that heavy precipitation associated with natural disasters will be aggravated in the future with aerosol mitigations.

Aerosol reductions increase R10 significantly over EA (Figure 6.7d) but relatively insignificantly over SA (Figure 6.8d) with time. Clearly, during 2031-2050, there is a decrease in R10 over SA and the Tibetan Plateau but an

increase over EA (Figure 6.10c), while aerosols increase over SA but decrease over EA (Figures 6.6a-d). This suggests that aerosol increases can reduce the frequency of moderate-to-heavy (≥10 mm day^{-1}) precipitation events. What is noteworthy is that SA is projected to undergo relatively small aerosol increases coinciding with insignificant R10 decreases whereas EA sees a significant R10 increase associated with substantial aerosol mitigation. This suggests that R10 is sensitive to aerosol changes. Moreover, by comparing Figures 6.9 and 6.10, it is clear that the aerosol induced changes in the spatial pattern of mean precipitation are very similar to that of R10.

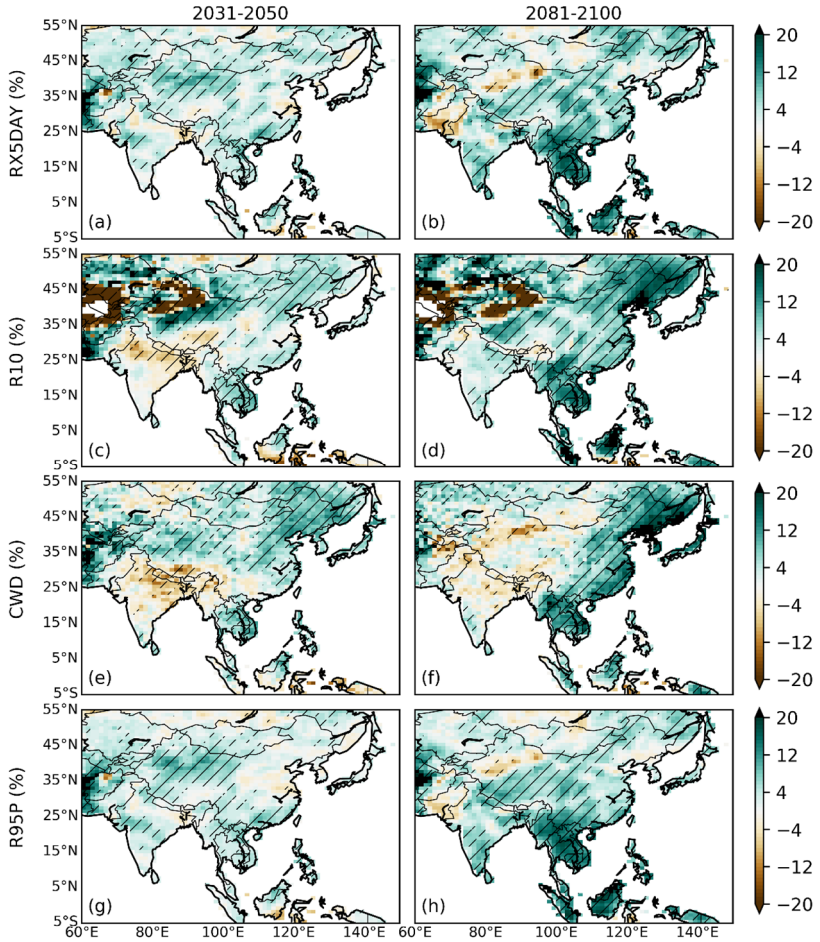

Figure 6.10 Same as Figure 6.9c, f, but for extreme precipitation indices: (a, b) RX5DAY (mm), (c, d) R10 (days), (e, f) CWD (days) and (g, h) R95P (mm) respectively, averaged over 2031-2050 (left) and 2081-2100 (right).

GHG increases result in CWD not changing much over EA (Figure 6.7e) but decreasing over SA (Figure 6.8e). Changing aerosols, by comparison, lead CWD to increase over EA but have little influence on CWD over SA. In addition, spatial differences in CWD (Figures 6.10e, f) in general show opposite changes to AOD (Figures 6.6g, h), suggesting the sensitivity of CWD to aerosols. Furthermore, the total amount of extreme precipitation (R95P) increases significantly over both SA and EA with GHG induced warming, while aerosol reductions increase R95P significantly on top of GHG effects. Changes in precipitation extremes are primarily driven by shifts in mean precipitation (Figures 6.11a, c), which lead the frequency of R10 and R95P to increase, and hence result in significant changes in these precipitation extreme indices. In contrast, changes in precipitation variability have minor contributions (Figures 6.11b, d) over both regions.

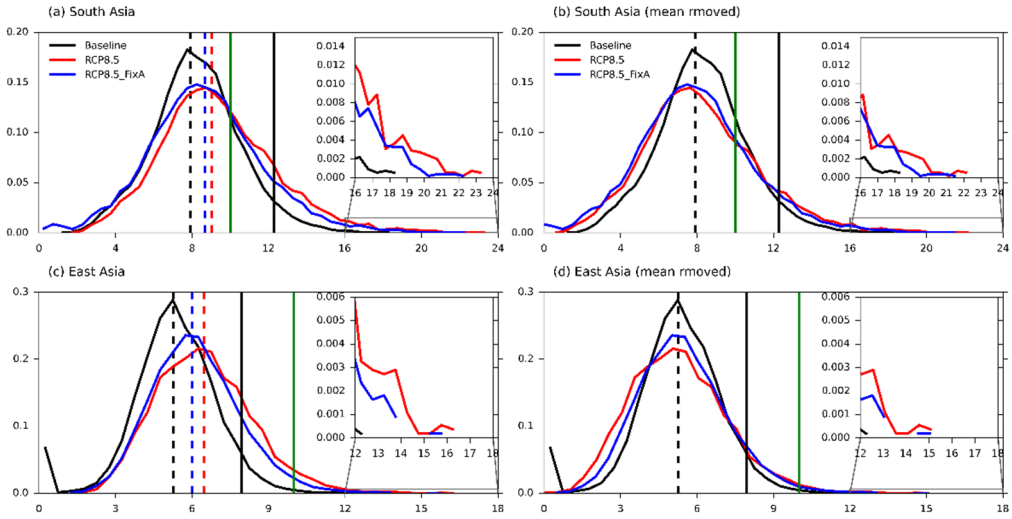

Figure 6.11 Probability distribution functions (PDFs) of area-weighted regional mean daily precipitation rate. Black for the baseline (1986-2005), red and blue for 2081-2100 under RCP8.5 and RCP8.5_FixA, respectively. The PDFs are computed using JJA precipitation rate from all ensemble members. The vertical dashed lines are the means of the distributions. The solid black lines are the 95th percentile thresholds derived from 1961-1990 historical data. The vertical green lines are the 10 mm day^{-1} thresholds used to define the precipitation index R10. The top row is for South Asia while the bottom row is for East Asia. The right-hand plots are the same as the left, but with the PDF distributions shifted so that the mean values are forced to be in the same place.

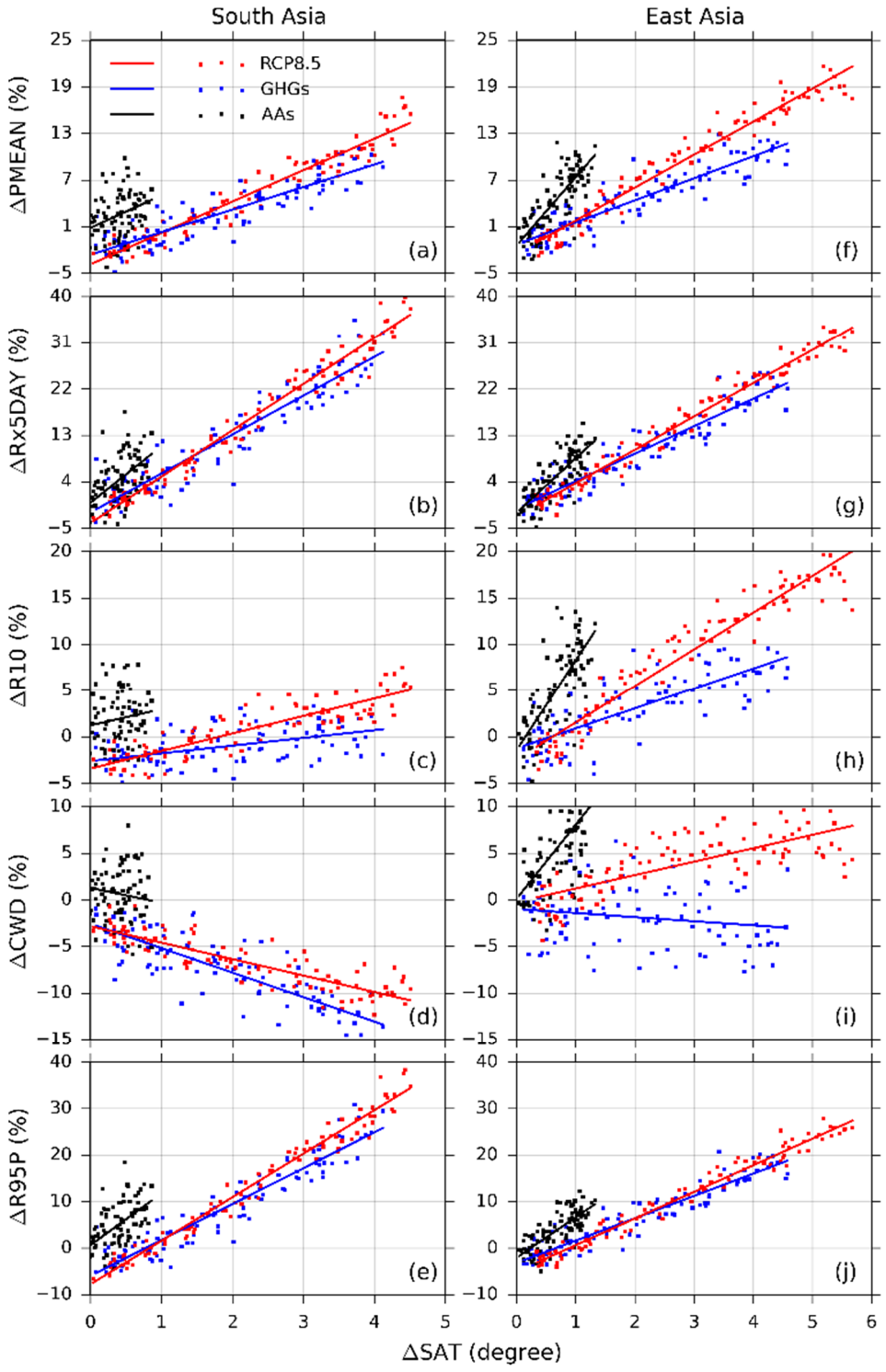

Figure 6.12 Percentage changes of (a, f) PMEAN, (b, g) RX5DAY, (c, h) R10, (d, i) CWD, and (e, j) R95P versus local surface warming over SA (left) and EA (right). Red for greenhouse gases (GHGs) plus anthropogenic aerosols under RCP8.5, blue for GHGs and black for anthropogenic aerosols only. Solid lines represent the gradients of changes derived through the least square fitting with p-value over 0.99.

Figure 6.12 displays PDFs of mean and extreme precipitation indices over SA and EA for the baseline time period (1986-2005), as well as their future projections under the two scenarios. The PDFs are calculated using all ensemble members to ensure robustness. Note that the further to the right the PDF distribution is shifted, the more extreme the precipitation indices. There are similarities between the shift of the PDFs of mean and extreme precipitation, with again an exception of CWD over SA. Because of GHG increases under RCP8.5_FixA, the PDFs are flattened, and the mean value is increased. With aerosol reductions included, the shift of the PDFs is further reinforced: the moderate events and the lower part of the distribution are weakened while the higher values are further enhanced. When compared to SA, the aerosol effects are more evident in EA – this is probably related to the larger aerosol reductions over EA by 2081-2100.

As shown in Figure 6.7 and Figure 6.8, the temporal evolution of summertime mean precipitation and extremes is related to the magnitude of warming. Therefore, the following investigates the percentage changes, relative to the 1986-2005 baseline, in spatially averaged precipitation indices in response to the warming over SA and EA. The gradients of the changes against warming are obtained by regressing percentage changes in precipitation indices to the net warming following Lin et al. (2016), using 95 pairs (2006-2100) of data. For each year, the ensemble mean net temperature and precipitation indices changes are firstly computed, and net changes as a result of aerosol changes are isolated by contrasting the two ensemble means. The net changes in precipitation indices are then converted into percentage changes with respect to the baselines (1986-2005) before regression. Note however that here the

net warming refers to local temperature increase rather than global as adopted by previous studies (Lin et al., 2016; Wang et al., 2016b). The scatterplots and least square fits are shown in Figure 6.13, and the gradients together with ensemble uncertainties are summarized in Table 6.2.

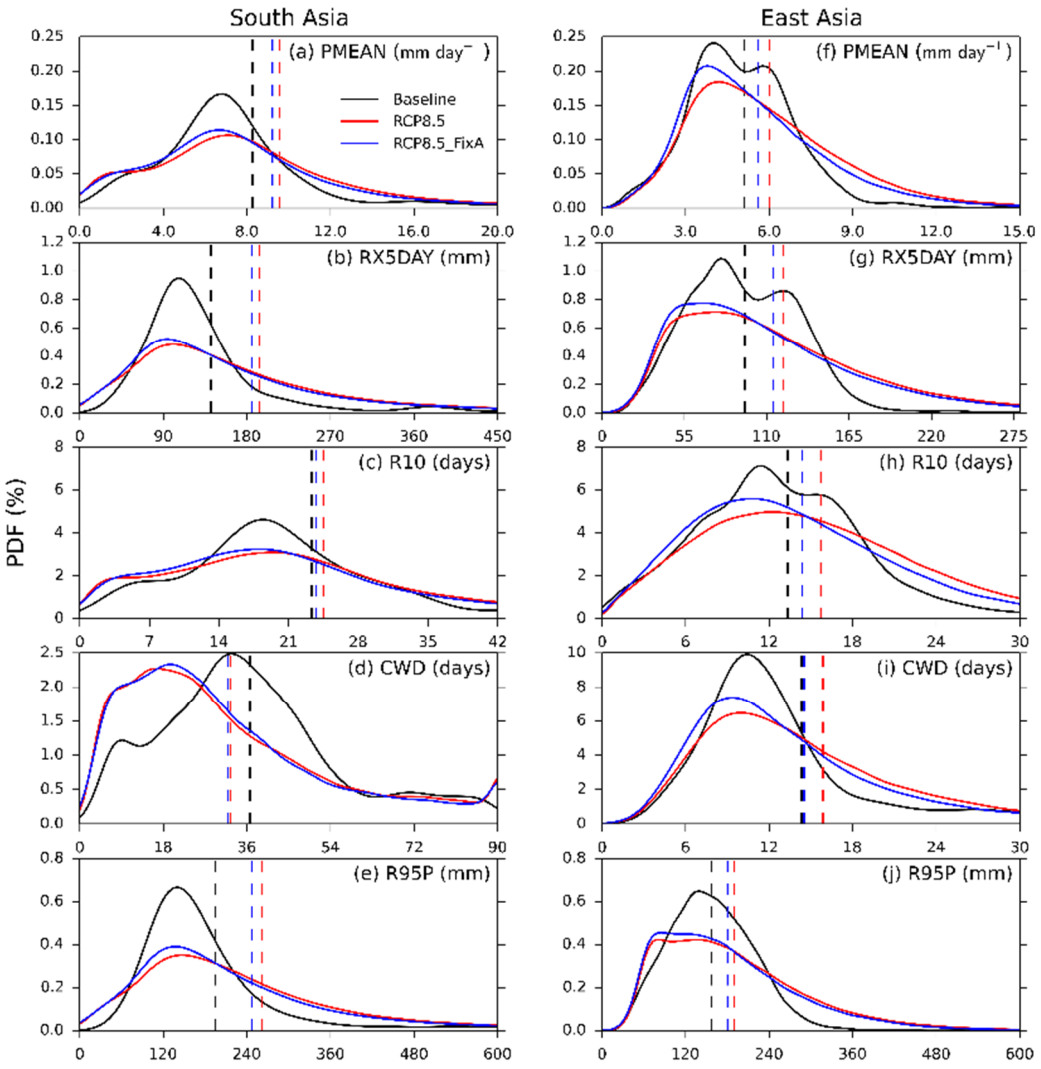

Figure 6.13 Probability density functions (PDFs) of precipitation indices over (a-e) South Asia and (f-j) East Asia. Black for the baseline (1986-2005), red for 2081-2100 under RCP8.5, and blue for 2081-2100 under RCP8.5_FixA. The vertical dashed lines are corresponding means of the PDF distributions. The PDFs are computed using 20 years of all grid-point data from all ensemble members over each region.

All the precipitation indices show a linear increase with warming from both GHG and aerosol forcing, with an exception of CWD over SA. In detail, the

gradient of the percentage change of mean precipitation does not differ much between SA and EA: 4.1 % K^{-1} (SA) and 4.2 % K^{-1} (EA) under RCP8.5, and 2.9 % K^{-1} (SA) and 2.8 % K^{-1} (EA) due to GHGs. However, a stronger response of aerosol reductions alone over EA (8.8%) is found to be double that over SA (4.2%). Table 6.2 shows that aerosols play a stronger role than GHGs in modulating precipitation extremes over EA relative to SA. For instance, with 1 K of aerosol reductions induced warming, there is an 11 % increase in RX5DAY over EA, double that due to 1 K of GHG-induced warming (5.3%). Similarly, over SA, RX5DAY increases by 11 % K^{-1} for aerosol-induced warming, but only 7.5 % K^{-1} for GHG-induced warming.

Table 6.2 Least square fitted gradients of percentage changes of precipitation indices against local warming. All results are significant at 99% levels from the student t-test. Numbers inside brackets denote ensemble variabilities.

		PMEAN	RX5DAY	R10	CWD	R95P
SA (% °C^{-1})	RCP8.5	4.14 (0.33)	8.98 (0.54)	1.89 (0.33)	-1.77 (0.33)	9.36 (0.51)
	GHGs	2.90 (0.45)	7.54 (0.90)	0.83 (0.51)	-2.63 (0.54)	7.71 (0.81)
	AAs	4.18 (3.18)	10.98 (4.89)	1.74 (3.45)	-1.58 (3.33)	11.13 (4.74)
EA (% °C^{-1})	RCP8.5	4.24 (0.27)	6.47 (0.33)	3.96 (0.33)	1.44 (0.39)	5.72 (0.30)
	GHGs	2.84 (0.39)	5.32 (0.57)	2.16 (0.51)	-0.44 (0.72)	4.80 (0.51)
	AAs	8.80 (2.01)	10.56 (2.55)	9.72 (2.61)	7.95 (3.21)	8.69 (2.28)

6.6 Response of the Asian summer monsoon

The following section analyses and discusses the overall response of the Asian summer monsoon system, i.e., beyond precipitation, to aerosol changes, focusing on the two selected time periods (2031-2050 and 2081-2100). Differences in cloud properties: low-level (surface to 850 hPa) cloud fraction (Figures 6.14a, b), vertically integrated cloud droplet number concentration (CDNC, Figures 6.14c, d), total grid-box cloud liquid water path

(CLWP, Figures 6.14e, f) and vertically averaged low-level cloud droplet effective radius (CDER, Figures 6.14g, h), are firstly examined.

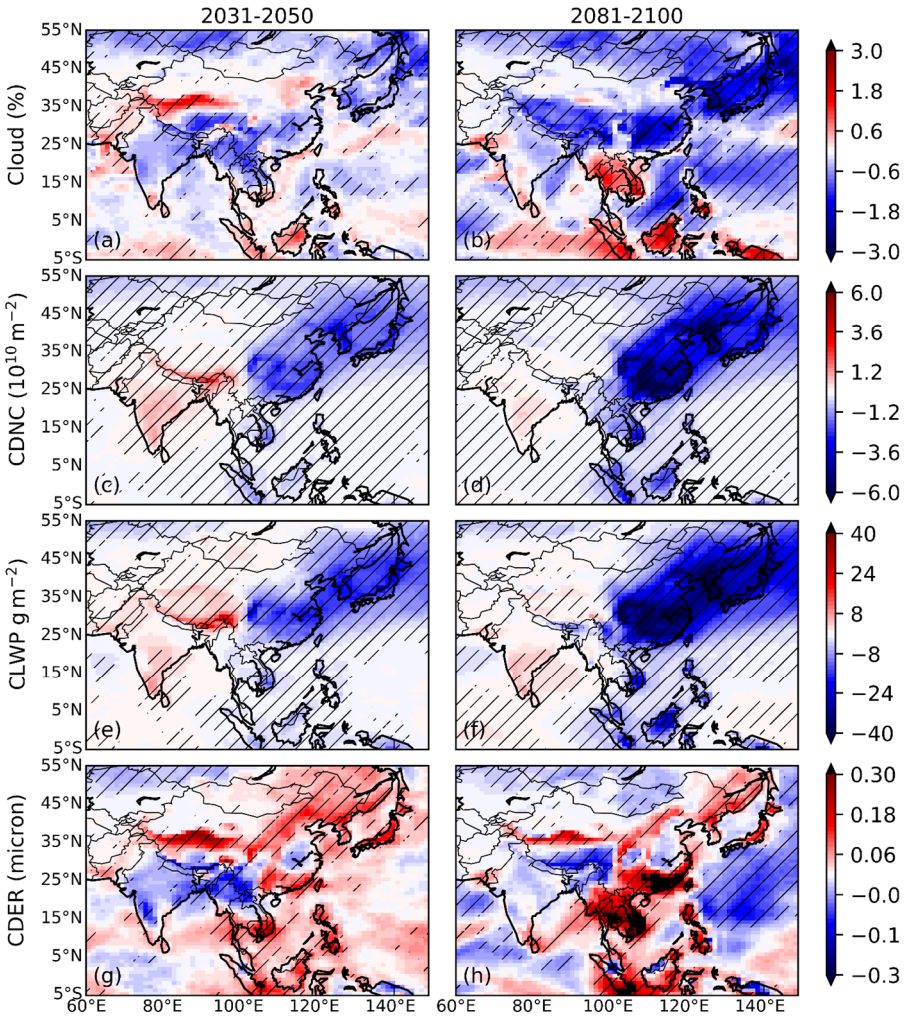

Figure 6.14 Changes in JJA cloud properties associated with changes in anthropogenic aerosols. Respectively, (a, b) low-level (below the model 850 hPa level) cloud fraction (Cloud, %), (c, d) vertically integrated cloud droplet number concentration (CDNC, 10^{10} m^{-2}), (e, f) total grid-box cloud liquid water pathway (CLWP, g m^{-2}), and (g, h) vertically averaged low-level effective cloud droplet radius (CDER, micron), averaged over 2031-2050 (left) and 2081-2100 (right). The dots denote 95% statistical significance of ensemble differences.

Despite some differences at sub-regional scales due to the multitude of small-scale processes at play, all the above variables show consistent patterns of changes at the large scale. There is a larger magnitude decrease in cloud cover over a wider region by 2081-2100 (Figure 6.14b) compared to 2031-

2050 (Figure 6.14a), due to larger aerosol reductions. Cloud changes are accompanied by a significant decrease in CDNC (Figure 6.14d, up to -60% over large parts of EA) and CLWP (Figure 6.14f, up to -30%). The above changes are suggestive of the overall importance of aerosol-cloud interactions in modulating the climate response over Asia: variations in aerosols result in concurrent changes in CDNC, with the ensuing cloud-lifetime effect further leading to consistent variations in CLWP. Note however that CDNC is also dependent on environmental conditions, especially the updraft velocity. More specifically, cloud condensation nuclei decreases lead to CDNC decreases because of reductions in cloud-active aerosols. With fewer cloud condensation nuclei, the conversion from cloud droplets into raindrops speeds up. These raindrops are precipitated efficiently, leading CLWP to drop substantially. Consequently, fewer cloud droplets are held in the clouds. The vertically average low-level CDER (Figures 6.14g, h), as might be expected, sees therefore broadly opposite trends to CDNC and CLWP, although some local inconsistencies exist.

Variations in aerosol loading and cloud properties can be related to changes in radiation. Figure 6.15 displays changes in clear-sky shortwave flux at the surface (FSNSC, Figures 6.15a, b), the all-sky shortwave flux at the surface (FSNS, Figures 6.15c, d), and surface evaporation (Figures 6.15g, h). Changes in FSNSC show general opposite trends to AOD (Figures 6.6g, h). This is indicative of surface dimming from the aerosol direct effect. Aerosol-cloud interactions, together with water vapour changes (Figures 6.14e, f), contribute to the difference between FSNS and FSNSC. For example, by 2081-2100, there is a widespread significant positive difference between

FSNS (Figure 6.15d) and FSNSC (Figure 6.15b) over EA where a substantial aerosol reduction occurs under RCP8.5. That is, aerosol-cloud forcing, i.e., aerosol reduction induced decreases in low-level cloud fraction (Figures 6.14a, b) and CLWP (Figures 6.14e, f) and hence cloud albedo (not shown), results in more shortwave radiation reaching the surface. Furthermore, aerosol reductions lead to a significant increase in surface evaporation (Figures 6.15e, f). This to some extent shows spatial agreement with precipitation changes (Figure 6.9c, f). In fact, careful comparisons between changes in evaporation and changes in mean precipitation indicate that evaporation changes appear to explain the precipitation changes over northern EA. However, it was noted that the largest precipitation changes occur over Southeast Asia but the radiative forcing changes are over the northern part. This implies that precipitation changes over southern SA are driven by other factors such as changes in dynamics.

Given the dominant role of atmospheric dynamics in the seasonal evolution of the Asian monsoon, an analysis of atmospheric circulation changes provides important insights into the fundamental mechanism governing the monsoon system. Figure 6.16 shows that aerosol forcing has a significant impact on the large scale monsoon circulation. By 2031-2050, a net warming of around +0.7 K associated with aerosol reductions can be found over EA. In contrast, owing to continued aerosol increases over SA, the magnitude of warming over the Indian continent and the Northern Indian Ocean is relatively smaller, around +0.3 K (Figure 6.16a). The SLP anomaly (Figure 6.16c) features a strong anticyclone centred over Northwest India, developing as an adjustment to increased regional aerosols and the muted warming compared to the

neighbouring areas. This results in anomalous low-level north-easterlies over the Bay of Bengal and easterlies across Southern India, which obstruct the climatological south-westerlies from the Arabian Sea, and lead to anomalous moisture divergence (Figure 6.16e) over Eastern India and the Bay of Bengal. Over EA, the large reduction in aerosols leads to a pronounced land warming compared to the ocean to the south and east, strengthening the land-sea thermal contrast, and to a collocated SLP reduction, reinforcing the climatological SLP gradient. As a result, the low-level south-westerlies are enhanced, and are accompanied by anomalous surface moisture convergence over a large part of EA and the South China Sea. In summary, by 2031-2050, aerosol reductions over EA and increases over SA result in a stronger East Asian summer monsoon circulation but a weaker South Asian summer monsoon circulation.

Atmospheric circulation changes are even more pronounced by 2081-2100, due to greater aerosol reductions over both SA and EA, thereby reversing and further continuing the trend during the first half of the 21st century, respectively. A distinct anomalous warming core, exceeding 1.5°C, is located between north-eastern EA and Japan, resulting in a large reduction in SLP and an anomalous lower-tropospheric cyclonic circulation and associated anomalous northerlies over the EA land. This, as shown in Figure 6.16f, impedes the north-eastward march of the moisture flux from the South China Sea to the land, leading to anomalous moisture divergence over the North China Plain but anomalous moisture convergence over South China and Southeast Asia. SA, on the contrary, sees reinforced monsoonal circulation most evident over the Northern Indian Ocean and the Bay of Bengal, along with larger SLP increases

over the ocean than the land (Figure 6.16d). Moisture convergence anomalies over Southern India can also be seen. In summary, by the end of the century, with further aerosol reductions, the South Asian summer monsoon circulation is strengthened while the East Asian monsoon circulation is weakened.

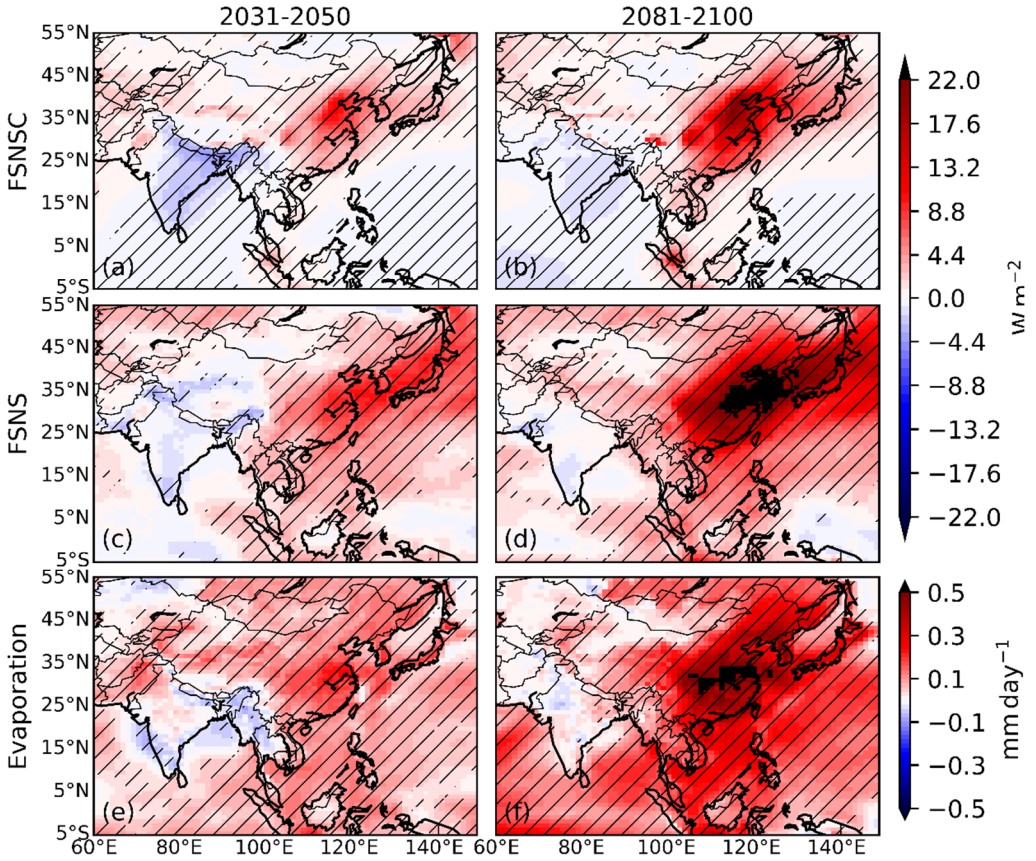

Figure 6.15 Changes in JJA radiative and evaporative fluxes associated with changes in aerosols. Respectively, (a, b) clear-sky surface shortwave radiation (FSNSC, W m^{-2}), (c, d) all-sky shortwave radiation at surface (FSNS, W m^{-2}), (e, f) surface evaporation (mm day^{-1}).

The above analysis indicates an interplay between aerosol effects on clouds and radiation and atmospheric dynamics in determining the mean seasonal precipitation change over Asia. Specifically, over northern EA despite a weaker atmospheric circulation and moisture divergence anomaly, precipitation increases due to the impacts of aerosol-radiation-cloud interactions on precipitation processes by 2081-2100. Conversely, over SA and southern EA,

changes in precipitation by the end of the 21st century appear to be more directly linked to aerosol-induced changes in the large-scale circulation. This is supported by the enhanced moisture convergence anomalies which coincide well with changes in mean precipitation (compare Figures 6.9f with 16f), and insignificant changes in cloud features and radiation.

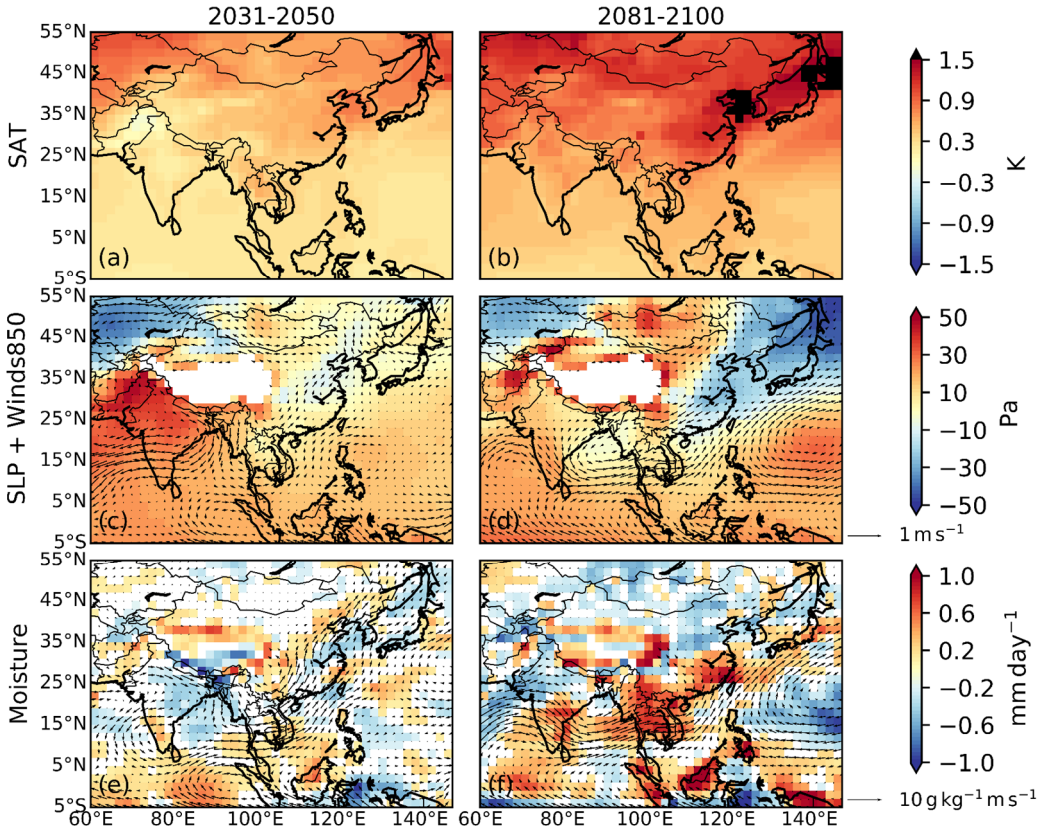

Figure 6.16 Changes in JJA thermodynamic and dynamic fields associated with changes in anthropogenic aerosols. Respectively, (a, b) Surface air temperature (K), (c, d) sea level pressure (SLP, Pa, shadings) overlapped with Winds850 (m s^{-1}, arrows), and (e, f) vertically integrated moisture convergence (mm day^{-1}, shadings, positive for convergence) overlapped with 850 hPa moisture flux (g kg^{-1} m s^{-1}, arrows). Note that SLP and circulation fields over the Tibetan Plateau are masked off.

6.7 Discussion and concluding remarks

Detecting the influence of aerosols on present-day precipitation extremes has proven to be a challenging task so far, critically limiting our confidence in

identifying the drivers of past variations in extremes and our ability to robustly project and understand future changes. Internal variability of the climate system associated with atmospheric circulation has been recognised as a major hindering factor, as variability makes it hard to detect a signal amongst the 'noise'. Further, the Asian monsoon region is particularly sensitive to variations in precipitation, including extremes, due to the critical importance of precipitation for the agriculture and socioeconomic well-being of billions of people living there. Additionally, despite stringent emission controls in the near future, aerosols are likely to continue to play a major role in the coming decades over this region given the high present-day levels.

In this work, the roles of anthropogenic aerosols in future summertime precipitation extremes over the AMR is investigated, by comparing ensemble simulations under the RCP8.5 scenario to those also under RCP8.5 but with fixed global aerosol/precursor emissions at 2005 levels. Note throughout the article such differences between RCP8.5 and RCP8.5_FixA are attributed to anthropogenic aerosol changes. Of course, the results can also be interpreted as the emergence of an underlying GHG signal as aerosols reduce, in the context that aerosols mask GHG effects in the present-day climate. The responses of cloud properties, radiative forcing, as well as thermodynamics and dynamics fields to aerosol changes were also investigated to elucidate the possible governing mechanisms. Key findings are:

- Under the future RCP8.5 pathway following aerosol/precursor emission controls, we would expect a warmer and wetter climate over the Asian monsoon region, compared to the fixed 2005 aerosol scenario. Consequently, the drying trend of the Asian monsoon during the

historical period will be alleviated. Also, the recently observed "Southern-Flood-Northern-Drought" pattern over Eastern China will tend to reduce.

- Aerosol mitigation will lead to more severe precipitation extremes, including an increased likelihood of heavy precipitation related disasters during summertime over both SA and EA, more heavy precipitation days; more extreme precipitation and lengthier periods of consecutive wet days. There is a shift in the PDFs of precipitation extremes toward higher values over land by 2081-2100, over EA in particular.
- Aerosols induce much stronger responses in extreme precipitation indices compared to GHGs, for the same amount of local surface warming: almost double the effect, as also pointed out by related works (Samset et al 2018; Lin et al. 2016). This is speculated to be related to the higher aerosol efficiency than GHG in modulating solar radiation, surface energy fluxes, and cloud microphysics and dynamics, and hence induce stronger hydrological responses. Furthermore, the ratios between aerosol and GHG induced percentage changes of precipitation indices against local warming are larger over EA than SA.
- Aerosols generate a large response not only over the emission regions, but also far away. A representative example is over southern EA where precipitation increases, while aerosol reductions are more limited to the northern EA.
- The aerosol-induced imprint on precipitation changes appear to be mediated by different mechanisms over EA and SA, while aerosol-cloud interactions are the major contributor to the response over EA, atmospheric circulation changes dominate the response over SA.

It is shown that aerosol mitigations would increase precipitation in the future. This agrees with previous studies which concluded that the increasing anthropogenic aerosol forcing during the historical period, which was the dominant driver of the summer drying trend seen over the AMR, will be alleviated in the future with stringent aerosol/precursor emission legislations (Li et al., 2015). In general, the South Asian summer monsoon circulation sees a weakening trend when aerosols from SA increase during 2031-2050, but a strengthening trend when aerosols reduce during 2081-2100. However, the East Asian summer monsoon circulation is projected to be reinforced during 2031-2050 with aerosol reductions, but weakened during 2081-2100 with additional aerosol reductions. The weakening of the East Asian summer monsoon circulation by 2081-2100 is driven by local thermodynamic and dynamic adjustments: the southward expansion of the Mongolia High towards northern China continent accompanying by an anomalous low over East and Northeast China and the adjacent oceans. This forces the Western Pacific Subtropical High (WPSH) to shift to south of the Yangtze River, and leads to the weakening of the East Asian summer monsoon circulation in northern and eastern land of China. This mechanism was also documented by previous studies (e.g., Huang et al. (2007); Zhou et al. (2009)).

Here, aerosol effects are isolated, by comparing RCP8.5 and RCP8.5_FixA, under the assumption that aerosol effects can be linearly added to other forcing agents. However, the non-linear interactions between GHGs and aerosols should be carefully noted. Also, despite the dominant role of local aerosols in determining the local responses, there can also be contributions from remote aerosols. E.g., localised AOD changes may give rise to localised radiative

forcing, but these changes to the energy budget affect climate much more widely (Shindell and Faluvegi, 2009). Bollasina et al. (2014) found that local aerosols dominate precipitation changes over India while remote aerosols contribute as well over the late 20th century. Guo et al. (2015) indicated that remote aerosols contribute to changes in the large-scale background precipitation. In addition, this study is based upon only one model which has limitations in many aspects. For instance, the representation of aerosol effects, and especially the indirect effects. A caveat that needs to be clarified is that the cloud droplet lifetime effect in CAM5 has been recently questioned from observational evidence (Malavelle et al., 2017). This was further investigated by Zhou and Penner (2017) who found that the increase of the liquid water path in CAM5 is caused by a large decrease of the auto-conversion rate when cloud droplet number increases. As such, the conclusions should be interpreted in the context of the structural limitation of CESM1, although the large ensemble experiments do provide a solid framework to provide information on internal variability.

To summarize, the CESM1 indicates that major changes in anthropogenic aerosols over the coming century are likely to have significant impacts on precipitation extremes over Asia, and will likely further enhance the rainfall changes brought about by continued GHG increases. These projections have large uncertainties, related to poorly constrained model representations of certain processes, with different mechanisms operating in different regions. Given the consequences of these projected changes for society, constraining these uncertainties will be crucially important. Therefore, careful studies on the interactions between future Asian aerosol/precursor emissions trajectories and

regional to large-scale climate dynamics are critical for effective climate risk management in this highly populated and vulnerable region.

Chapter 7 Conclusions

7.1 Thesis overview

Anthropogenic aerosols play important roles in the Earth's radiation balance and climate. Also, there are growing concerns about their impacts on human health and the environment. Our knowledge of aerosols, however, is still incomplete and largely uncertain. This thesis aims to enhance our understanding of aerosols, by providing a new holistic assessment of the impacts of anthropogenic aerosols on radiative forcing and climate, air quality and related socioeconomic outcomes, as well as climate extremes.

This thesis makes use of the state-of-the-art Community Earth System Model (CESM1) at the nominal 1-degree resolution. A number of time-slice model experiments have been carried out for the period 1970-2010 that represents a particularly important period of changes in atmospheric composition and global mean climate. To start with, the effects of changes in each individual forcing agent including greenhouse gases (GHGs), anthropogenic aerosols, and ozone have been investigated. To further understand aerosol changes and impacts, the climate impacts of aerosol changes are explicitly quantified, focusing particularly on two major policy-relevant emission drivers (i.e., growth in energy use and advances in emission control technologies). Next, changes in air quality and their socioeconomic impacts have been assessed, attributing to the two above emission drivers, as well as climate change.

With the climate impacts of 1970-2010 anthropogenic aerosol changes in mind, this thesis then turns to the future (2006-2100) under the Representative Concentration Pathway 8.5 (RCP8.5). The CESM1 large ensemble project (LENS) has been employed to examine the impacts of future aerosol

reductions on changes in climate extremes, focusing on heatwaves globally and precipitation extremes over Asia. The underlying mechanisms that drive the disproportionally larger impacts of aerosol changes on climate extremes (compared to GHG changes), for the first time, have been revealed.

7.2 Summary of key findings

The following is a summary of the major results/findings addressing the objectives and research questions outlined in Section 1.7.

1. **Time-slice model experiments have been carried out to diagnose the effective radiative forcing (ERF), and to examine the climate responses to 1970-2010 GHG increases, anthropogenic aerosol changes, tropospheric ozone increases, as well as stratospheric ozone depletion (Chapter 2).**
    a. Once the present-day climate has reached equilibrium, both the global mean temperature and precipitation changes would be roughly twice as large as the transient 1970-2010 changes.
    b. Changes in temperature and precipitation are dominated by GHG increases globally. However, short-lived climate forcers (SLCFs, including aerosols and ozone) also have important impacts. For example, they are shown to have significant impacts on the amplified Arctic temperature responses, and the shift of the inter-tropical convergence zone (ITCZ).
    c. Unlike GHGs, the temperature response can be of opposite sign to that of ERF for SLCFs at various regional scales. This is especially the case for aerosols and ozone, and suggests that ERF may not be

a useful metric for SLCFs, and needs to be used carefully for quantifying the climate effects of SLCFs.

d. Increases in GHGs and tropospheric ozone enhance global mean precipitation and shift the daily precipitation distribution towards higher values. On the contrary, the overall aerosol increases and stratospheric ozone depletion suppress global mean precipitation and shift the distribution towards smaller amounts.

e. Compared to the global scale, the impacts of SLCFs in changing the characteristics of the daily precipitation distribution is stronger over land. This is especially important for regions such as Asia and Europe where precipitation changes, and the frequency of heavy-to-extreme precipitation, in particular, are dominated by changes in aerosols rather than GHGs.

2. **The ERF and climate response to 1970-2010 changes in anthropogenic aerosols have been explicitly investigated, focusing particularly on the impacts of the two major policy-relevant emission drivers, namely growth in energy use and advances in emission control technologies (Chapter 3).**

   a. Aerosol changes due to the above two drivers have significant and competing impacts on the global mean ERF and climate. Specifically, emissions from energy use generate a global mean aerosol ERF of -0.31±0.22 W m^{-2}, and result in a global mean cooling (-0.35±0.17 K) and precipitation reduction (-0.03±0.02 mm day^{-1}). By contrast, the avoided aerosol-related emissions associated with advances in emission control technology generate a global mean ERF of

+0.21±0.23 W m^{-2}, a global surface warming (+0.10±0.13 K) and precipitation increase (+0.01±0.02 mm day^{-1}).

b. Energy use growth dominates the 1970-2010 total net aerosol changes and impacts, particularly from and within Asia. In comparison, technology advances outweigh energy use growth over Europe and North America.

c. Various intertwined nonlinear processes are related to aerosols' effects, and the diagnosed aerosol forcing and effects must be interpreted in the context of experiment designs. This is particularly the case for black carbon (BC) whose impacts depend on the background concentration of soluble species such as sulphate.

d. ERF is again found to be not useful for quantifying the effects of aerosols at regional scales, and may be open to misleading interpretations. Therefore, any climate metrics related to, or based on, aerosol ERF need to be used very cautiously.

e. Future aerosol-related emissions have large temporal and spatial uncertainties associated with the above two policy-relevant emission drivers. This, together with a variety of nonlinearities and uncertainties in the effects of aerosols, implies even larger uncertainties in future climate projections and associated impacts.

3. **The full chemistry scheme (CAM5-Chem) is fully-coupled with CESM1 to examine 1970-2010 changes in air quality, attributing to both climate change and anthropogenic emissions. Changes associated with anthropogenic emissions in response to the two major policy-relevant drivers (i.e., energy use growth and technology advances) have been investigated. The impacts of air**

pollution changes on human health, crop production and economy have been assessed (Chapter 4).

a. The 1970-2010 changes in the global surface concentrations of air pollutants (i.e., $PM_{2.5}$, O_3, NO_X and CO) are predominately driven by anthropogenic emissions. However, climate change contributes in a minor way (less than 10% of the total), which differ between different air pollutants. However, the mechanisms (e.g., changes in emissions, or chemistry) through which climate change affects the pollutants need to be further investigated.

b. Growth in energy use competes with advances in emission control technology in changing global air quality. Also, emissions from energy use dominate over Asia while technology advances play an important role in Europe and North America.

c. The 1970-2010 global mortality associated with $PM_{2.5}$ is 1.7 (1.0-2.4) million yr^{-1}, with around 5-6% attributable to climate change induced air pollution changes, and 75% associated with emission changes due to energy use. The avoided emissions due to technology advances saved 0.9 (0.5-1.2) million lives globally associated with avoided $PM_{2.5}$ exposure.

d. The 1970-2010 global mortality associated with O_3 is 86,000 (29,000 -139,000) yr^{-1}, with around 7-8% attributable to climate change induced air pollution changes, and 25% associated with emission changes due to energy use. The avoided emissions due to technology advances saved 13,000 (4,000 -22,000) yr^{-1} lives globally associated with avoided O_3 exposure.

e. The 1970-2010 changes in surface O_3 pollution leads to 166 million tonnes yr^{-1} of extra staple crop production loss (maize: 33; rice: 38; soybean: 22, and wheat: 73) that values 53 billion USD_{2010} yr^{-1}. About 91% of the total economic loss is because of anthropogenic emissions. Regionally, the loss is greatest over China for all the staple crops, with a relative loss up to -21.2% for wheat.

f. The 1970-2010 growth in energy use has led to a total crop production loss of 75 million tonnes yr^{-1} and an economic loss of 22.7 billion USD_{2010} yr^{-1}, explaining around half of the anthropogenic impacts. Technology advances, on the other hand, have led to a total crop production gain of 35 million tonnes yr^{-1} which is equivalent to an economic gain of 9.9 billion USD_{2010} yr^{-1}.

g. Global air quality and its impacts are largely under coordinated global policy intervention, offering policymakers chances to have significant influences on the future global environment. Also, the contrasts between Asia and developed regions of Europe and North America reveal the fact that country-level decision-making can exert significant regional impacts, yet the associated socioeconomic impacts can be seen globally.

4. **Using the LENS experiments, future changes in the characteristics of heatwaves under the RCP8.5 scenario at the global scale have been investigated. The relative roles of GHG increases and aerosol reductions have been quantified. The mechanisms through which aerosol changes have disproportionally larger impacts on changes in heatwaves have been revealed for the first time (Chapter 5).**

a. All the heatwave metrics—intensity, duration, frequency, total hot days and magnitude—increase during the 21st century under the RCP8.5 emission pathway.
b. Changes to heatwaves are similar in all seasons, and are driven by long-term warming, with only minor contributions from changes in future temperature variability.
c. GHG increases will account for most of these changes. Aerosol reductions will contribute most strongly to changes in heatwaves in the Northern Hemisphere extra-tropics.
d. Per unit of global mean surface warming, aerosol reductions, compared to GHG increases, lead to disproportionally stronger changes in heatwave characteristics, by changing daily maximum temperature through aerosol-cloud interactions.

5. **Also using the LENS experiments, future changes in summertime precipitation extremes under the RCP8.5 scenario in Asia have been investigated. The relative roles of GHG increases and aerosol reductions have been quantified. The impacts of aerosol changes on the Asian monsoon system have been examined. (Chapter 6)**
   a. Following the future RCP8.5 emission pathway, the Asian monsoon region will get warmer and wetter. Consequently, the drying trend of the Asian monsoon during the historical period will be alleviated. Also, the recently observed “Southern-Flood-Northern-Drought” pattern over Eastern China will tend to reduce.
   b. Aerosol reductions will lead to further aggravated precipitation extremes over Asia, on top of the effects of GHG increases. This is particularly important over East Asia where there is an evident shift

in the probability distribution of precipitation extremes toward higher values by the end of the 21st century.

c. Aerosols induce much stronger responses in precipitation extreme indices compared to GHGs, for the same amount of local surface warming: almost double the effect.

d. The aerosol-induced impacts on changes in mean and extreme precipitation indices appear to be mediated by different mechanisms over East and South Asia. While aerosol–radiation–cloud interactions are the major contributor to the response over East Asia, atmospheric circulation changes dominate the response over South Asia.

7.3 Significance and Implications

This work, the first of its kind in many aspects, provides a new holistic assessment, and contributes to our knowledge, of the impacts of anthropogenic aerosols, by addressing a range of cutting-edge research questions. Firstly, for the first time to our knowledge, the equilibrium climate responses to the historical changes (1970-2010) in both GHGs and SLCFs have been investigated, focusing particularly on the differences between GHG and aerosol changes. Secondly, the impacts of aerosol changes due to past energy use growth and emission control technologies have been assessed at both the global and regional scales; the results provide important implications for both the scientific community and policymakers in the context of future climate changes and air pollution mitigations. Thirdly, this thesis provides an integrative assessment of the impacts of anthropogenic aerosols on climate,

air quality, human health, as well as the agriculture-related economy. Fourthly, the underlying mechanisms through which future aerosol reductions modulate future changes in climate extremes have been explicitly studied.

The identified differences between transient and equilibrium climate responses imply that there are large amounts of additional warming and associated impacts yet to be seen, once the climate has fully-responded to past anthropogenic emission changes. This needs to be taken into account when developing long-term climate and environment strategies. The relative importance of SLCFs in changing present-day climate is very relevant for both understanding present-day climate changes and for future projections in the context of future climate changes and mitigations. Also, the assessment on the impacts of anthropogenic air pollution, particularly those associated with the two policy-drivers, have implications for future policymaking in terms of climate, environment, agriculture and public health. This offers policymakers significant influences on future global habitability.

This thesis, as a whole, reveals that aerosols have significant impacts on global and regional climate that are very different from well-mixed GHGs. The concept of ERF has been shown not to be useful for quantifying the effects of SLCFs (i.e., aerosols and ozone), and may be open to misleading interpretation. This implies that any climate metrics related to, or based on, ERF must be interpreted with caution. Further, for aerosols, the results show that the diagnosed climate forcing and responses may be dependent on model experiment design and methods used. This provides caveats on interpreting a variety of climate model intercomparison projects, including the upcoming Aerosols and Chemistry Model Intercomparison Project (AerChemMIP; Collins

et al. (2017)) for the next Intergovernmental Panel on Climate Change assessment report (IPCC AR6).

This thesis, for the first time, reveals that future aerosol reductions induced warming has disproportionally larger impacts on climate extremes (e.g., heatwaves) mainly through aerosol-cloud interactions. However, there are still large uncertainties in our understanding of aerosol-cloud-radiation interactions, leading to poorly-constrained and diverging effects related to aerosol schemes in present generation climate models. Therefore, our present projections of future climate extremes have large uncertainties (i.e., the magnitude, and even the sign, of extreme indices may vary substantially across climate models, because of differences in the representations of aerosol-cloud interaction, all the other factors being the same). Given the detrimental impacts of changes in future heatwaves and to more effectively manage climate risks, this thesis calls the attention of the community to prioritize efforts in reducing uncertainties in aerosol-cloud interactions.

7.4 Limitation and future works

A major limitation of this thesis is that the whole work is based on a single model, namely the CESM1, despite the fact that a number of ensemble simulations have been carried out and/or employed. The model has been evaluated thoroughly in the literature and in each research chapter regarding specific research questions. However, many processes in the model, especially those related to aerosols, still have a high degree of uncertainty. Some of these uncertainties should be particularly noted. First of all, CESM1 (CAM5) has a relatively larger aerosol forcing compared to other Coupled

Model Intercomparison Project Phase 5 (CMIP5) models, likely due to the large cloud adjustments through cloud water path in MAM3 (Allen and Ajoku, 2016; Malavelle et al., 2017; Zhou and Penner, 2017). Therefore, the estimated climate impacts due to aerosol changes using CESM1 (CAM5) are likely to be stronger than other CMIP5 models (Taylor et al., 2012). Secondly, some anthropogenic aerosol species (e.g., nitrate and ammonia aerosols) are not explicitly represented in MAM3. Although this is also the case for many other CMIP5 models (Bian et al., 2017), it may influence the results presented here, but is difficult to quantify with the current model configuration. Thirdly, there are still large uncertainties in background aerosol-related emissions (i.e., preindustrial aerosol load) that has great influences on estimates of aerosol radiative forcing and the subsequent impacts on climate (Wilcox et al., 2015; Regayre et al., 2018). Last but not the least, uncertainties in anthropogenic emissions (both spatially and temporally), and especially the aerosol-related emissions under future emission pathways, add further uncertainties in estimating their relative impacts.

In light of all the above, we underscore that all results and conclusions should be interpreted in the context of CESM1 (CAM5). Nevertheless, our findings are important in the sense that such model-dependent aerosol schemes need to be better understood and constrained in present generation climate models. These findings could be further developed/expanded in a variety of ways that form possible future research directions, including but not limited to:

- As laid out above, the major results/conclusions may be model dependent, and need to be verified using as many other models as possible, while identifying the possible differences and reasons behind

differences. This would help understand the diversities and uncertainties in our present generation climate models, in terms of the representations of aerosols and related processes. Also, as described above, it is important to examine if the specific uncertainties related to aerosols in CESM1 (CAM5) are general across present generation climate models, and the same for the subsequent influences on the results presented here.

- The conclusion that the diagnosed aerosol forcing and climate responses may be influenced by specific experiment design needs to be explicitly investigated. That is, explicitly designed sensitivity experiments are needed to further investigate in depth how different experiment designs may influence the diagnosed climate forcing and response to aerosols. A possible approach to consider is to make use of the upcoming AerChemMIP experiments (Collins et al., 2017). The specific research question should focus on the nonlinearities associated with aerosols in each model, and differences across models.
- Given that various nonlinearities and uncertainties exist in aerosols' effects, it is important to have a better understanding of where they come from, along the entire translation pathway from emissions to concentrations, to radiative forcing, and ultimately to climate responses. Specific research questions include the differences between aerosol species, the dependence on aerosol schemes in different models, as well as the possibility to simplify these processes into emission/concentration based metrics. Given that such metrics have recently been widely used and are appealing to decision-makers for

quick decision-making, it is crucially important to provide a comprehensive assessment of their validity.

- In Chapters 2-4, a number of model experiments have been carried out and analysed. However, there are still many questions that can be addressed using these model experiments. Examples include but are not limited to, such as, climate extremes, the polar climate response, and the response of the Southern Hemisphere climate to stratospheric ozone. These model experiments will be shared (e.g., through JASMIN) with the wider research community, to promote more research ideas. Additionally, the importance of aerosol mixing ratios (especially, BC and sulphate aerosols) in the diagnosed aerosol radiative forcing and climate impacts (Chapter 3) needs to be further investigated by a range of sensitivity model experiments.
- In Chapters 5 and 6, the impacts of future aerosol reductions on climate extremes are examined, and it has been found that the impacts may be dependent on the background concentration of both GHGs and aerosols. This could be further explained by looking at preindustrial times where the atmospheric abundance of both GHGs and aerosols are low. Also, this study looks at only one future emission pathway (i.e., RCP8.5), while future scenarios for aerosols have large temporal and spatial uncertainties (e.g., in the Shared Socioeconomic Pathways; Gidden et al. (2018)). Therefore, the results could be expanded under a variety of the SSP emission pathways, making use of the Scenario Model Intercomparison Project (ScenarioMIP; O'Neill et al. (2016)).
- The finding that aerosol-cloud interactions play important roles in modulating climate extremes (Chapter 5 and 6) can be possibly verified

through sensitivity model experiments where the aerosol-cloud interaction schemes are carefully switched off. To save computational costs, the atmosphere-only model(s) experiments may be considered.

Appendix

Supplementary files and tables

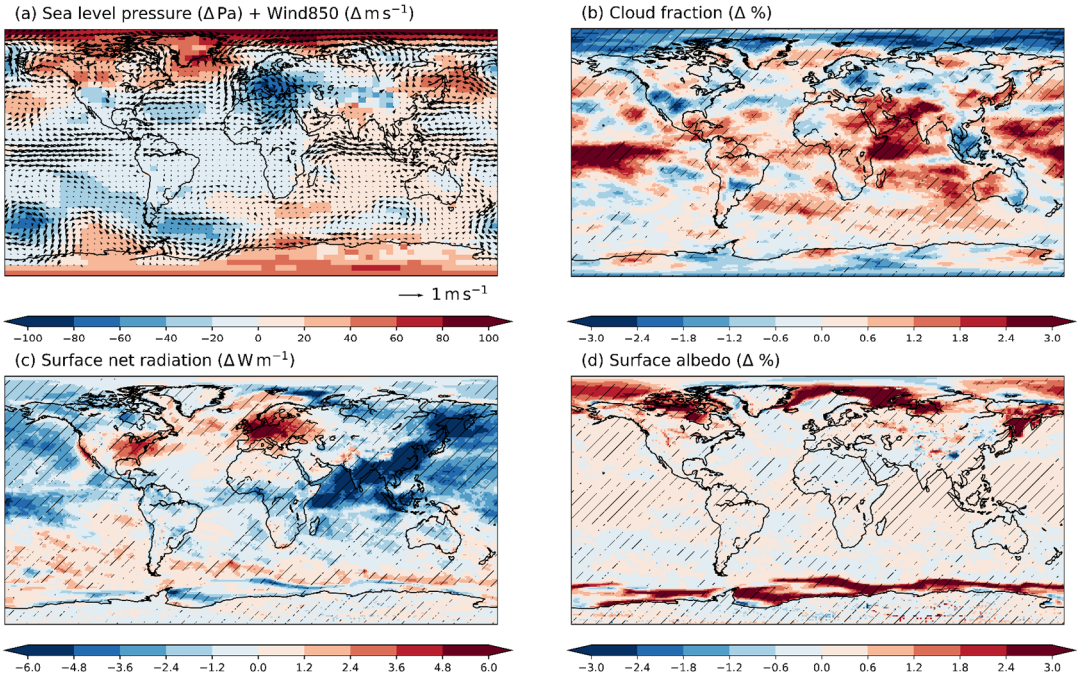

Figure A1 The 1970-2010 anthropogenic aerosols changes induced changes in (a) sea level pressure (shadings, Pa) and 850 hPa winds (vectors, m s^{-1}), (b) vertically-integrated total cloud (%), (c) surface net radiation (positive downward), and (d) surface albedo (%).

Table A1 The same as premature deaths in Table 4.3, but resolved into regional statistics. The values shown are the mean estimates and the 95% confidence intervals (in brackets) on the epidemiological concentration-response functions. The deaths are attributed to pollution changes due to climate change, anthropogenic emissions, as well as those associated with changes due to energy consumption and technology advancements.

		Climate Change	Best estimates	Energy consumption	Technology advancements
Africa	$PM_{2.5}$	-5747 (-3156, -8629)	101094 (59300, 141982)	-2735 (-1409, -4327)	-53049 (-30395, -76383)
	O_3	89 (29, 147)	755 (252, 1231)	251 (83, 413)	-247 (-81, -410)
Australia	$PM_{2.5}$	44 (26, 62)	-69 (-40, -99)	228 (132, 323)	-235 (-136, -335)
	O_3	23 (8, 38)	41 (14, 68)	42 (14, 70)	-41 (-13, -68)
China	$PM_{2.5}$	-37637 (-21037, -54683)	976185 (571962, 1350630)	666793 (386214, 933371)	-182029 (-101939, -263893)
	O_3	1983 (654, 3275)	41499 (14075, 66704)	6629 (2218, 10790)	-6408 (-2102, -10637)
Europe	$PM_{2.5}$	-1613 (-936, -2307)	-202931 (-116307, -293994)	25534 (14980, 36098)	-89978 (-52186, -128727)
	O_3	1802 (595, 2974)	6021 (1999, 9877)	2113 (698, 3482)	-2161 (-707, -3594)
India	$PM_{2.5}$	142553 (82282, 200941)	583355 (343446, 805967)	384818 (223097, 540065)	-282113 (-155911, -416433)
	O_3	474 (156, 781)	9146 (3118, 14627)	2862 (953, 4681)	-852 (-280, -1413)
Middle East	$PM_{2.5}$	-17053 (-8770, -27966)	-5170 (-1833, -10628)	1510 (1617, 239)	-52957 (-28447, -82657)
	O_3	130 (43, 214)	1735 (588, 2790)	557 (185, 912)	-596 (-194, -993)
North America	$PM_{2.5}$	5748 (3309, 8193)	-81670 (-46095, -118871)	30972 (17877, 44025)	-41175 (-23500, -59225)
	O_3	1237 (408, 2040)	3881 (1297, 6325)	2573 (851, 4235)	-725 (-238, -1200)
Russia	$PM_{2.5}$	-1858 (-1119, -2607)	-11941 (-7136, -16880)	4065 (2454, 5688)	-3281 (-1975, -4602)
	O_3	48 (16, 79)	607 (201, 997)	212 (70, 350)	-216 (-71, -359)
South America	$PM_{2.5}$	1241 (712, 1769)	12637 (7275, 17953)	8568 (4919, 12206)	-8406 (-4778, -12102)
	O_3	90 (30, 149)	1985 (667, 3218)	903 (301, 1479)	-256 (-84, -425)
Southeast Asia	$PM_{2.5}$	565 (323, 806)	93819 (54936, 130986)	37062 (21366, 52562)	-7652 (-4355, -11006)
	O_3	85 (28, 140)	4587 (1565, 7334)	1329 (443, 2170)	-476 (-156, -790)

Table A2 The same as the crop production (10^4 metric tonnes) and economic losses (million USD_{2010}) in Table 4.3, but for regional aggregations. The total net changes (third column) are resolved into those attributable to climate change and the best estimates of 1970-2010 anthropogenic emissions. Also shown are changes associated with energy consumption and technology advancements. The relative changes (‰) in crop production relative to 2010 are shown in brackets.

		Total net	Climate Change	Best estimates	Energy consumption	Technology advancements
Africa	Maize	-13.1 (-0.9)	-0.1 (-0.0)	-13.0 (-0.9)	-4.5 (-0.3)	6.5 (0.4)
	Rice	-0.2 (-0.0)	-0.6 (-0.1)	0.5 (0.1)	-1.5 (-0.2)	2.8 (0.4)
	Soybean	-22 (-4.9)	-3 (-0.6)	-19 (-4.3)	-12 (-2.7)	4 (0.9)
	Wheat	-49.6 (-15.3)	-2.6 (-0.8)	-45.2 (-14.0)	-23.7 (-7.3)	34.8 (10.8)
	Economic loss	-244.8	-16.5	-228.3	-110.7	165.6
China	Maize	-2752.9 (-165.5)	-126.3 (-7.6)	-2626.7 (-157.9)	-1018.1 (-61.2)	394.4 (23.7)
	Rice	-1679.6 (-83.3)	-60.1 (-3.0)	-1619.5 (-80.3)	-667.6 (-33.1)	229.9 (11.4)
	Soybean	-1256.3 (-188.5)	-54.5 (-8.2)	-1201.8 (-180.3)	-475.9 (-71.4)	144.3 (21.6)
	Wheat	-2495.1 (-211.6)	-39.0 (-3.3)	-2456.1 (-208.3)	-545.0 (-46.2)	276.7 (23.5)
	Economic loss	-29004.1	-1050.3	-27953.9	-9881.7	3636.8
Europe	Maize	-242.1 (-10.3)	-100.5 (-4.3)	-141.7 (-6.0)	-136.2 (-5.8)	260.6 (11.1)
	Rice	-45.9 (-19.6)	-13.9 (-5.9)	-32.0 (-13.7)	-24.1 (-10.3)	44.7 (19.1)
	Soybean	-76.7 (-25.6)	-31.8 (-10.6)	-44.9 (-15.0)	-47.0 (-15.7)	84.5 (28.2)
	Wheat	-886.1 (-45.2)	-312.2 (-15.9)	-573.9 (-29.3)	-480.1 (-24.5)	574.4 (29.3)
	Economic loss	-2962.9	-1042.2	-1920.7	-1606.8	2259.6
India	Maize	-209.0 (-36.9)	-10.7 (-1.9)	-198.3 (-35.0)	-88.7 (-15.6)	33.4 (5.9)
	Rice	-375.8 (-49.5)	-10.6 (-1.4)	-365.2 (-48.1)	-165.9 (-21.9)	52.9 (7.0)
	Soybean	-222.4 (-119.2)	-5.4 (-2.9)	-217.1 (-116.3)	-99.8 (-53.5)	32.7 (17.5)
	Wheat	-801.6 (-197.4)	-29.8 (-7.3)	-771.8 (-190.0)	-148.9 (-36.7)	56.2 (13.8)
	Economic loss	-4892.0	-165.6	-4726.3	-1650.9	566.0

Table A2 continued.

		Total net	Climate Change	Best estimates	Energy consumption	Technology advancements
Middle East	Maize	-342.5 (-61.9)	-15.7 (-2.8)	-326.7 (-59.0)	-87.3 (-15.8)	93.2 (16.8)
	Rice	-209.8 (-74.9)	-8.6 (-3.1)	-201.2 (-71.9)	-48.0 (-17.2)	39.1 (14.0)
	Soybean	-113.2 (-157.3)	-4.5 (-6.3)	-108.7 (-151.1)	-20.4 (-28.3)	16.6 (23.1)
	Wheat	Wheat	-779.8 (-156.3)	-48.6 (-9.7)	-731.3 (-146.6)	-207.3 (-41.6)
	Economic loss	-6086.2	-305.1	-5781.1	-1494.1	1285.0
North America	Maize	-375.7 (-8.8)	-214.4 (-5.0)	-161.3 (-3.8)	-588.0 (-13.7)	-3.4 (-0.1)
	Rice	-27.3 (-6.6)	-12.2 (-2.9)	-15.1 (-3.6)	-37.6 (-9.1)	5.3 (1.3)
	Soybean	-152.1, (-16.3)	-161.1, (-17.3)	9.0, (1.0)	-337.9, (-36.2)	-8.3, (-0.9)
	Wheat	-1412.5 (-59.0)	-282.5 (-11.8)	-1130.1 (-47.2)	-1233.6 (-51.5)	242.6 (10.1)
	Economic loss	-4334.1	-1709.4	-2624.7	-5203.0	458.7
South America	Maize	-78.8 (-2.2)	-0.1 (-0.0)	-78.7 (-2.2)	-61.1 (-1.7)	26.5 (0.7)
	Rice	-46.4 (-2.4)	0.1 (0.0)	-46.5 (-2.4)	-37.1 (-1.9)	18.7 (1.0)
	Soybean	-123.3 (-9.5)	-0.0 (-0.0)	-123.3 (-9.5)	-96.7 (-7.4)	39.7 (3.0)
	Wheat	-191.7 (-33.7)	-1.5 (-0.3)	-189.3 (-33.3)	-110.7 (-19.5)	52.0 (9.2)
	Economic loss	-1181.5	-5.0	-1176.4	-832.7	363.9
Southeast Asia	Maize	-104.0 (-17.4)	-0.5 (-0.1)	-103.5 (-17.3)	-55.7 (-9.3)	19.7 (3.3)
	Rice	-209.8 (-28.3)	-7.3 (-1.0)	-202.5 (-27.3)	-82.6 (-11.1)	25.7 (3.5)
	Soybean	-81.6 (-41.1)	-2.0 (-1.0)	-79.6 (-40.1)	-39.1 (-19.7)	14.7 (7.4)
	Wheat	NA	NA	NA	NA	NA
	Economic loss	-1340.2	-33.6	-1306.7	-605.3	213.7

References

Aamaas, B., T. K. Berntsen, J. S. Fuglestvedt, K. P. Shine, and W. J. Collins (2017), Regional temperature change potentials for short-lived climate forcers based on radiative forcing from multiple models, Atmospheric Chemistry and Physics, 17(17), 10795-10809.

Aas, W., A. Mortier, V. Bowersox, R. Cherian, G. Faluvegi, H. Fagerli, J. Hand, Z. Klimont, C. Galy-Lacaux, and C. M. Lehmann (2019), Global and regional trends of atmospheric sulfur, Scientific reports, 9(1), 953.

Acosta Navarro, J. C., A. M. Ekman, F. S. Pausata, A. Lewinschal, V. Varma, Ø. Seland, M. Gauss, T. Iversen, A. Kirkevåg, and I. Riipinen (2017), Future response of temperature and precipitation to reduced aerosol emissions as compared with increased greenhouse gas concentrations, Journal of Climate, 30(3), 939-954.

Ainsworth, E. A. (2017), Understanding and improving global crop response to ozone pollution, The Plant Journal, 90(5), 886-897.

Albrecht, B. A. (1989), Aerosols, cloud microphysics, and fractional cloudiness, Science, 245(4923), 1227-1230.

Alexander, L., X. Zhang, T. Peterson, J. Caesar, B. Gleason, A. Klein Tank, M. Haylock, D. Collins, B. Trewin, and F. Rahimzadeh (2006), Global observed changes in daily climate extremes of temperature and precipitation, Journal of Geophysical Research: Atmospheres, 111(D5).

Allan, R. P., and B. J. Soden (2008), Atmospheric warming and the amplification of precipitation extremes, Science, 321(5895), 1481-1484.

Allen, M. R., and W. J. Ingram (2002), Constraints on future changes in climate and the hydrologic cycle, Nature, 419(6903), 224-232.

Allen, R. J., and S. C. Sherwood (2011), The impact of natural versus anthropogenic aerosols on atmospheric circulation in the Community Atmosphere Model, Climate dynamics, 36(9-10), 1959-1978.

Allen, R. J., and O. Ajoku (2016), Future aerosol reductions and widening of the northern tropical belt, Journal of Geophysical Research: Atmospheres, 121(12), 6765-6786.

Anderson, J. O., J. G. Thundiyil, and A. Stolbach (2012), Clearing the air: a review of the effects of particulate matter air pollution on human health, Journal of Medical Toxicology, 8(2), 166-175.

Andreae, M., and D. Rosenfeld (2008), Aerosol–cloud–precipitation interactions. Part 1. The nature and sources of cloud-active aerosols, Earth-Science Reviews, 89(1), 13-41.

Anenberg, S. C., L. W. Horowitz, D. Q. Tong, and J. J. West (2010), An estimate of the global burden of anthropogenic ozone and fine particulate

matter on premature human mortality using atmospheric modeling, Environmental health perspectives, 118(9), 1189.

Ashfaq, M., D. Rastogi, R. Mei, D. Touma, and L. R. Leung (2017), Sources of errors in the simulation of south Asian summer monsoon in the CMIP5 GCMs, Climate Dynamics, 49(1-2), 193-223.

Auliciems, A., and I. Burton (1973), Trends in smoke concentrations before and after the Clean Air Act of 1956, Atmospheric Environment (1967), 7(11), 1063-1070.

Avnery, S., D. L. Mauzerall, J. Liu, and L. W. Horowitz (2011), Global crop yield reductions due to surface ozone exposure: 2. Year 2030 potential crop production losses and economic damage under two scenarios of O3 pollution, Atmospheric Environment, 45(13), 2297-2309.

Bank, W. (2011), World development indicators, World Bank.

Bartlett, M. A. Bollasina, B. B. Booth, N. J. Dunstone, F. Marenco, G. Messori, and D. J. Bernie (2016), Do differences in future sulfate emission pathways matter for near-term climate? A case study for the Asian monsoon, paper presented at AGU Fall Meeting Abstracts.

Basarin, B., T. Lukić, and A. Matzarakis (2016), Quantification and assessment of heat and cold waves in Novi Sad, Northern Serbia, International journal of biometeorology, 60(1), 139-150.

Bellouin, N., L. Baker, Ø. Hodnebrog, D. Olivie, R. Cherian, C. Macintosh, B. Samset, A. Esteve, B. Aamaas, and J. Quaas (2016), Regional and seasonal radiative forcing by perturbations to aerosol and ozone precursor emissions, Atmospheric Chemistry and Physics, 16(21), 13885-13910.

Betzelberger, A. M., K. M. Gillespie, J. M. Mcgrath, R. P. Koester, R. L. Nelson, and E. A. Ainsworth (2010), Effects of chronic elevated ozone concentration on antioxidant capacity, photosynthesis and seed yield of 10 soybean cultivars, Plant, Cell & Environment, 33(9), 1569-1581.

Bian, H., M. Chin, D. A. Hauglustaine, M. Schulz, G. Myhre, S. E. Bauer, M. T. Lund, V. A. Karydis, T. L. Kucsera, and X. Pan (2017), Investigation of global particulate nitrate from the AeroCom phase III experiment, Atmospheric Chemistry and Physics, 17(21), 12911.

Binkowski, F. S., and U. Shankar (1995), The regional particulate matter model: 1. Model description and preliminary results, Journal of Geophysical Research: Atmospheres, 100(D12), 26191-26209.

Boer, G., and B. Yu (2003), Climate sensitivity and response, Climate Dynamics, 20(4), 415-429.

Bollasina, M. A., Y. Ming, and V. Ramaswamy (2011), Anthropogenic aerosols and the weakening of the South Asian summer monsoon, science, 334(6055), 502-505.

Bollasina, M. A., Y. Ming, V. Ramaswamy, M. D. Schwarzkopf, and V. Naik (2014), Contribution of local and remote anthropogenic aerosols to the twentieth century weakening of the South Asian Monsoon, Geophysical Research Letters, 41(2), 680-687.

Booth, B., D. Bernie, D. McNeall, E. Hawkins, J. Caesar, C. Boulton, P. Friedlingstein, and D. Sexton (2013), Scenario and modelling uncertainty in global mean temperature change derived from emission-driven global climate models, Earth System Dynamics, 4(1), 95-108.

Bouchama, A. (2004), The 2003 European heat wave, Intensive care medicine, 30(1), 1-3.

Boucher, O., D. Randall, P. Artaxo, C. Bretherton, G. Feingold, P. Forster, V.-M. Kerminen, Y. Kondo, H. Liao, and U. Lohmann (2013), Clouds and aerosols, in Climate change 2013: the physical science basis. Contribution of Working Group I to the Fifth Assessment Report of the Intergovernmental Panel on Climate Change, edited, pp. 571-657, Cambridge University Press.

Brönnimann, S., M. Jacques-Coper, E. Rozanov, A. M. Fischer, O. Morgenstern, G. Zeng, H. Akiyoshi, and Y. Yamashita (2017), Tropical circulation and precipitation response to ozone depletion and recovery, Environmental Research Letters, 12(6), 064011.

Brown, S., J. Caesar, and C. A. Ferro (2008), Global changes in extreme daily temperature since 1950, Journal of Geophysical Research: Atmospheres, 113(D5).

Burke, C., and P. Stott (2017), Impact of anthropogenic climate change on the East Asian summer monsoon, Journal of Climate(2017).

Caesar, J., and J. A. Lowe (2012), Comparing the impacts of mitigation versus non‐intervention scenarios on future temperature and precipitation extremes in the HadGEM2 climate model, Journal of Geophysical Research: Atmospheres, 117(D15).

Caesar, J., L. Alexander, and R. Vose (2006), Large‐scale changes in observed daily maximum and minimum temperatures: Creation and analysis of a new gridded data set, Journal of Geophysical Research: Atmospheres, 111(D5).

Caldwell, P. M., M. D. Zelinka, and S. A. Klein (2018), Evaluating Emergent Constraints on Equilibrium Climate Sensitivity, Journal of Climate, 31(10), 3921-3942.

Carnell, E. J., M. Vieno, S. Vardoulakis, R. C. Beck, C. Heaviside, S. Tomlinson, U. Dragosits, M. R. Heal, and S. Reis (2019), Modelling public health improvements as a result of air pollution control policies in the UK over four decades–1970 to 2010, Environmental Research Letters.

Carslaw, K., L. Lee, C. Reddington, K. Pringle, A. Rap, P. Forster, G. Mann, D. Spracklen, M. Woodhouse, and L. Regayre (2013), Large contribution of natural aerosols to uncertainty in indirect forcing, Nature, 503(7474), 67.

Ceccherini, G., S. Russo, I. Ameztoy, A. F. Marchese, and C. Carmona-Moreno (2017), Heat waves in Africa 1981-2015, observations and reanalysis, Natural Hazards and Earth System Sciences, 17(1), 115.

Checa‐Garcia, R., M. I. Hegglin, D. Kinnison, D. A. Plummer, and K. P. Shine (2018), Historical tropospheric and stratospheric ozone radiative forcing using the CMIP6 database, Geophysical Research Letters, 45(7), 3264-3273.

Chemke, R., and G. Dagan (2018), The effects of the spatial distribution of direct anthropogenic aerosols radiative forcing on atmospheric circulation, Journal of Climate, 31(17), 7129-7145.

Chen, H., and J. Sun (2017), Contribution of human influence to increased daily precipitation extremes over China, Geophysical Research Letters, 44(5), 2436-2444.

Chen, W., and B. Dong (2018), Anthropogenic impacts on recent decadal change in temperature extremes over China: relative roles of greenhouse gases and anthropogenic aerosols, Climate Dynamics, 1-18.

Chen, W., and B. Dong (2019), Anthropogenic impacts on recent decadal change in temperature extremes over China: relative roles of greenhouse gases and anthropogenic aerosols, Climate Dynamics, 52(5-6), 3643-3660.

Chen, Y., and Y. Li (2017), An Inter-comparison of Three Heat Wave Types in China during 1961–2010: Observed Basic Features and Linear Trends, Scientific Reports, 7, 45619.

Chin, M. (2009), Atmospheric aerosol properties and climate impacts, Diane Publishing.

Chiodo, G., L. Polvani, and M. Previdi (2017), Large increase in incident shortwave radiation due to the ozone hole offset by high climatological albedo over Antarctica, Journal of Climate, 30(13), 4883-4890.

Chowdhury, S., S. Dey, and K. R. Smith (2018), Ambient PM 2.5 exposure and expected premature mortality to 2100 in India under climate change scenarios, Nature communications, 9(1), 318.

Christidis, N., P. A. Stott, and S. J. Brown (2011), The role of human activity in the recent warming of extremely warm daytime temperatures, Journal of Climate, 24(7), 1922-1930.

Chung, C., K. Lee, and D. Mueller (2012), Effect of internal mixture on black carbon radiative forcing, Tellus B: Chemical and Physical Meteorology, 64(1), 10925.

Chung, C. E., and V. Ramanathan (2006), Weakening of North Indian SST gradients and the monsoon rainfall in India and the Sahel, Journal of Climate, 19(10), 2036-2045.

Cohen, A. J., M. Brauer, R. Burnett, H. R. Anderson, J. Frostad, K. Estep, K. Balakrishnan, B. Brunekreef, L. Dandona, and R. Dandona (2017), Estimates and 25-year trends of the global burden of disease attributable to ambient air pollution: an analysis of data from the Global Burden of Diseases Study 2015, The Lancet, 389(10082), 1907-1918.

Collins, M., R. Knutti, J. Arblaster, J.-L. Dufresne, T. Fichefet, P. Friedlingstein, X. Gao, W. Gutowski, T. Johns, and G. Krinner (2013), Long-term climate change: projections, commitments and irreversibility.

Collins, W. J., J.-F. Lamarque, M. Schulz, O. Boucher, V. Eyring, M. I. Hegglin, A. Maycock, G. Myhre, M. Prather, and D. Shindell (2017), AerChemMIP: quantifying the effects of chemistry and aerosols in CMIP6, Geoscientific Model Development, 10(2), 585-607.

Conley, A. J., R. Garcia, D. Kinnison, J.-F. Lamarque, D. Marsh, M. Mills, A. K. Smith, S. Tilmes, F. Vitt, and H. Morrison (2012), Description of the NCAR community atmosphere model (CAM 5.0), NCAR technical note.

Coumou, D., and S. Rahmstorf (2012), A decade of weather extremes, Nature climate change, 2(7), 491-496.

Crippa, M., G. Janssens-Maenhout, F. Dentener, D. Guizzardi, K. Sindelarova, M. Muntean, R. Van Dingenen, and C. Granier (2016), Forty years of improvements in European air quality: regional policy-industry interactions with global impacts, Atmospheric Chemistry and Physics, 16(6), 3825-3841.

Dallafior, T., D. Folini, R. Knutti, and M. Wild (2016), Mixed‐layer ocean responses to anthropogenic aerosol dimming from 1870 to 2000, Journal of Geophysical Research: Atmospheres, 121(1), 49-66.

De Bono, A., P. Peduzzi, S. Kluser, and G. Giuliani (2004), Impacts of summer 2003 heat wave in Europe.

DEFRA, U. (2011), Climate resilient infrastructure: preparing for a changing climate, edited, Stationary Office London.

Deng, J., and H. Xu (2016), Nonlinear effect on the East Asian summer monsoon due to two coexisting anthropogenic forcing factors in eastern China: an AGCM study, Climate Dynamics, 46(11-12), 3767-3784.

Dennison, F. W., A. J. McDonald, and O. Morgenstern (2015), The effect of ozone depletion on the Southern Annular Mode and stratosphere‐troposphere coupling, Journal of Geophysical Research: Atmospheres, 120(13), 6305-6312.

Dingenen, R., F. J. Dentener, F. Raes, M. C. Krol, L. Emberson, and J. Cofala (2009), The global impact of ozone on agricultural crop yields under current and future air quality legislation, Atmospheric Environment, 43(3), 604-618.

Dobricic, S., L. Pozzoli, E. Vignati, R. Van Dingenen, J. Wilson, S. Russo, and Z. Klimont (2019), Nonlinear impacts of future anthropogenic aerosol emissions on Arctic warming, Environmental Research Letters, 14(3), 034009.

Donat, M. G., L. V. Alexander, H. Yang, I. Durre, R. Vose, and J. Caesar (2013), Global land-based datasets for monitoring climatic extremes, Bulletin of the American Meteorological Society, 94(7), 997-1006.

Dong, B., R. T. Sutton, E. J. Highwood, and L. J. Wilcox (2016), Preferred response of the East Asian summer monsoon to local and non-local anthropogenic sulphur dioxide emissions, Climate Dynamics, 46(5-6), 1733-1751.

Doxsey-Whitfield, E., K. MacManus, S. B. Adamo, L. Pistolesi, J. Squires, O. Borkovska, and S. R. Baptista (2015), Taking advantage of the improved availability of census data: a first look at the gridded population of the world, version 4, Papers in Applied Geography, 1(3), 226-234.

Easterling, D. R., G. A. Meehl, C. Parmesan, S. A. Changnon, T. R. Karl, and L. O. Mearns (2000), Climate extremes: observations, modeling, and impacts, science, 289(5487), 2068-2074.

Eck, T., B. Holben, J. Reid, O. Dubovik, A. Smirnov, N. O'neill, I. Slutsker, and S. Kinne (1999), Wavelength dependence of the optical depth of biomass burning, urban, and desert dust aerosols, Journal of Geophysical Research: Atmospheres, 104(D24), 31333-31349.

Ellingsen, K., M. Gauss, R. V. Dingenen, F. Dentener, L. Emberson, A. M. Fiore, M. Schultz, D. Stevenson, M. Ashmore, and C. Atherton (2008), Global ozone and air quality: a multi-model assessment of risks to human health and crops, Atmospheric Chemistry and Physics Discussions, 8(1), 2163-2223.

Emberson, L. D., H. Pleijel, E. A. Ainsworth, M. Van den Berg, W. Ren, S. Osborne, G. Mills, D. Pandey, F. Dentener, and P. Büker (2018), Ozone effects on crops and consideration in crop models, European Journal of Agronomy, 100, 19-34.

Emmons, L., S. Arnold, S. Monks, V. Huijnen, S. Tilmes, K. S. Law, J. L. Thomas, J.-C. Raut, I. Bouarar, and S. Turquety (2015), The POLARCAT Model Intercomparison Project (POLMIP): overview and evaluation with observations, Atmospheric Chemistry and Physics, 15(12), 6721-6744.

Emmons, L. K., S. Walters, P. G. Hess, J.-F. Lamarque, G. G. Pfister, D. Fillmore, C. Granier, A. Guenther, D. Kinnison, and T. Laepple (2010), Description and evaluation of the Model for Ozone and Related chemical Tracers, version 4 (MOZART-4).

England, M. R., L. M. Polvani, K. L. Smith, L. Landrum, and M. M. Holland (2016), Robust response of the Amundsen Sea Low to stratospheric ozone depletion, Geophysical Research Letters, 43(15), 8207-8213.

Fan, J., Y. Wang, D. Rosenfeld, and X. Liu (2016), Review of aerosol–cloud interactions: Mechanisms, significance, and challenges, Journal of the Atmospheric Sciences, 73(11), 4221-4252.

FAOSTAT, F. (2017), Available online: http://www. fao. org/faostat/en/# data, QC (accessed on 2 August 2017).

Feichter, J., E. Roeckner, U. Lohmann, and B. Liepert (2004), Nonlinear aspects of the climate response to greenhouse gas and aerosol forcing, Journal of climate, 17(12), 2384-2398.

Field, C. B., V. Barros, T. F. Stocker, and Q. Dahe (2012), Managing the risks of extreme events and disasters to advance climate change adaptation: special report of the intergovernmental panel on climate change, Cambridge University Press.

Figueres, C., C. Le Quéré, A. Mahindra, O. Bäte, G. Whiteman, G. Peters, and D. Guan (2018), Emissions are still rising: ramp up the cuts, edited, Nature Publishing Group.

Fiore, A. M., V. Naik, and E. M. Leibensperger (2015), Air quality and climate connections, Journal of the Air & Waste Management Association, 65(6), 645-685.

Fiore, A. M., J. J. West, L. W. Horowitz, V. Naik, and M. D. Schwarzkopf (2008), Characterizing the tropospheric ozone response to methane emission controls and the benefits to climate and air quality, Journal of Geophysical Research: Atmospheres, 113(D8).

Fiore, A. M., V. Naik, D. V. Spracklen, A. Steiner, N. Unger, M. Prather, D. Bergmann, P. J. Cameron-Smith, I. Cionni, and W. J. Collins (2012), Global air quality and climate, Chemical Society Reviews, 41(19), 6663-6683.

Fischer, E. M., and R. Knutti (2015), Anthropogenic contribution to global occurrence of heavy-precipitation and high-temperature extremes, Nature Climate Change, 5(6), 560-564.

Fischer, G., F. O. Nachtergaele, S. Prieler, E. Teixeira, G. Tóth, H. Van Velthuizen, L. Verelst, and D. Wiberg (2012), Global Agro-ecological Zones (GAEZ v3. 0)-Model Documentation.

Flanner, M. G. (2013), Arctic climate sensitivity to local black carbon, Journal of Geophysical Research: Atmospheres, 118(4), 1840-1851.

Fläschner, D., T. Mauritsen, and B. Stevens (2016), Understanding the intermodel spread in global-mean hydrological sensitivity, Journal of Climate, 29(2), 801-817.

Flato, G., J. Marotzke, B. Abiodun, P. Braconnot, S. C. Chou, W. J. Collins, P. Cox, F. Driouech, S. Emori, and V. Eyring (2013), Evaluation of Climate Models. In: Climate Change 2013: The Physical Science Basis. Contribution of Working Group I to the Fifth Assessment Report of the Intergovernmental Panel on Climate Change, Climate Change 2013, 5, 741-866.

Flemming, J., A. Benedetti, A. Inness, R. J. Engelen, L. Jones, V. Huijnen, S. Remy, M. Parrington, M. Suttie, and A. Bozzo (2017), The CAMS interim reanalysis of carbon monoxide, ozone and aerosol for 2003–2015, Atmospheric Chemistry and Physics, 17(3), 1945-1983.

Fletcher, C. G., B. Kravitz, and B. Badawy (2018), Quantifying uncertainty from aerosol and atmospheric parameters and their impact on climate sensitivity, Atmospheric Chemistry and Physics, 18(23), 17529-17543.

Forster, P. M., G. Bodeker, R. Schofield, S. Solomon, and D. Thompson (2007), Effects of ozone cooling in the tropical lower stratosphere and upper troposphere, Geophysical Research Letters, 34(23).

Forster, P. M., T. Richardson, A. C. Maycock, C. J. Smith, B. H. Samset, G. Myhre, T. Andrews, R. Pincus, and M. Schulz (2016), Recommendations for diagnosing effective radiative forcing from climate models for CMIP6, Journal of Geophysical Research: Atmospheres, 121(20).

Fowler, D., M. Amann, F. Anderson, M. Ashmore, P. Cox, M. Depledge, D. Derwent, P. Grennfelt, N. Hewitt, and O. Hov (2008), Ground-level ozone in the 21st century: future trends, impacts and policy implications, Royal Society Science Policy Report, 15(08).

Frey, L., F. A.-M. Bender, and G. Svensson (2017), Cloud albedo changes in response to anthropogenic sulfate and non-sulfate aerosol forcings in CMIP5 models, Atmospheric Chemistry and Physics, 17(14), 9145-9162.

Freychet, N., H.-H. Hsu, C. Chou, and C.-H. Wu (2015), Asian summer monsoon in CMIP5 projections: a link between the change in extreme precipitation and monsoon dynamics, Journal of Climate, 28(4), 1477-1493.

Freychet, N., S. Tett, J. Wang, and G. Hegerl (2017), Summer heat waves over eastern china: dynamical processes and trend attribution, Environmental Research Letters, 12(2), 024015.

Freychet, N., A. Duchez, C.-H. Wu, C.-A. Chen, H.-H. Hsu, J. Hirschi, A. Forryan, B. Sinha, A. L. New, and T. Graham (2016), Variability of hydrological extreme events in East Asia and their dynamical control: a comparison between observations and two high-resolution global climate models, Climate Dynamics, 1-22.

Frich, P., L. Alexander, P. Della-Marta, B. Gleason, M. Haylock, A. K. Tank, and T. Peterson (2002), Observed coherent changes in climatic extremes during the second half of the twentieth century, Climate research, 19(3), 193-212.

Fry, M., M. Schwarzkopf, Z. Adelman, and J. West (2014), Air quality and radiative forcing impacts of anthropogenic volatile organic compound emissions from ten world regions, Atmospheric Chemistry and Physics, 14(2), 523-535.

Fry, M., M. Schwarzkopf, Z. Adelman, V. Naik, W. Collins, and J. West (2013), Net radiative forcing and air quality responses to regional CO emission reductions, Atmospheric Chemistry and Physics, 13(10), 5381-5399.

Ganguly, D., P. J. Rasch, H. Wang, and J. h. Yoon (2012), Fast and slow responses of the South Asian monsoon system to anthropogenic aerosols, Geophysical Research Letters, 39(18).

García-Herrera, R., J. Díaz, R. M. Trigo, J. Luterbacher, and E. M. Fischer (2010), A review of the European summer heat wave of 2003, Critical Reviews in Environmental Science and Technology, 40(4), 267-306.

Gaubert, B., A. F. Arellano, J. Barré, H. Worden, L. Emmons, S. Tilmes, R. R. Buchholz, F. Vitt, K. Raeder, and N. Collins (2016), Toward a chemical reanalysis in a coupled chemistry - climate model: An evaluation of MOPITT CO assimilation and its impact on tropospheric composition, Journal of Geophysical Research: Atmospheres, 121(12), 7310-7343.

Gaudel, A., O. Cooper, G. Ancellet, B. Barret, A. Boynard, J. Burrows, C. Clerbaux, P.-F. Coheur, J. Cuesta, and E. Cuevas Agulló (2018), Tropospheric Ozone Assessment Report: Present-day distribution and trends of tropospheric ozone relevant to climate and global atmospheric chemistry model evaluation.

Ghan, S. J., and R. A. Zaveri (2007), Parameterization of optical properties for hydrated internally mixed aerosol, Journal of Geophysical Research: Atmospheres, 112(D10).

Ghan, S. J., L. R. Leung, R. C. Easter, and H. Abdul - Razzak (1997), Prediction of cloud droplet number in a general circulation model, Journal of Geophysical Research: Atmospheres, 102(D18), 21777-21794.

Ghan, S. J., X. Liu, R. C. Easter, R. Zaveri, P. J. Rasch, J.-H. Yoon, and B. Eaton (2012), Toward a minimal representation of aerosols in climate models: Comparative decomposition of aerosol direct, semidirect, and indirect radiative forcing, Journal of Climate, 25(19), 6461-6476.

Gidden, M., K. Riahi, S. Smith, S. Fujimori, G. Luderer, E. Kriegler, D. P. van Vuuren, M. van den Berg, L. Feng, and D. Klein (2018), Global emissions pathways under different socioeconomic scenarios for use in CMIP6: a dataset of harmonized emissions trajectories through the end of the century, Geoscientific Model Development Discussions, 1-42.

Giorgi, F., and R. Francisco (2000), Uncertainties in regional climate change prediction: a regional analysis of ensemble simulations with the HADCM2 coupled AOGCM, Climate Dynamics, 16(2-3), 169-182.

Godin‐Beekmann, S. (2016), Stratospheric and tropospheric ozone, International Encyclopedia of Geography: People, the Earth, Environment and Technology: People, the Earth, Environment and Technology, 1-6.

Gong, D. Y., and C. H. Ho (2002), Shift in the summer rainfall over the Yangtze River valley in the late 1970s, Geophysical Research Letters, 29(10).

Grandey, B. S., and C. Wang (2019), Background Conditions Influence the Estimated Cloud Radiative Effects of Anthropogenic Aerosol Emissions From Different Source Regions, Journal of Geophysical Research: Atmospheres, 124(4), 2276-2295.

Greenwald, T. J., G. L. Stephens, T. H. Vonder Haar, and D. L. Jackson (1993), A physical retrieval of cloud liquid water over the global oceans using Special Sensor Microwave/Imager (SSM/I) observations, Journal of Geophysical Research: Atmospheres, 98(D10), 18471-18488.

Guo, L., A. G. Turner, and E. J. Highwood (2015), Impacts of 20th century aerosol emissions on the South Asian monsoon in the CMIP5 models, Atmospheric Chemistry and Physics, 15(11), 6367-6378.

Hansen, J., M. Sato, J. Glascoe, and R. Ruedy (1998), A common-sense climate index: Is climate changing noticeably?, Proceedings of the National Academy of Sciences, 95(8), 4113-4120.

Hansen, J., M. Sato, R. Ruedy, L. Nazarenko, A. Lacis, G. Schmidt, G. Russell, I. Aleinov, M. Bauer, and S. Bauer (2005), Efficacy of climate forcings, Journal of Geophysical Research: Atmospheres, 110(D18).

Haywood, J., and V. Ramaswamy (1998), Global sensitivity studies of the direct radiative forcing due to anthropogenic sulfate and black carbon aerosols, Journal of Geophysical Research: Atmospheres, 103(D6), 6043-6058.

He, J., and Y. Zhang (2014), Improvement and further development in CESM/CAM5: gas-phase chemistry and inorganic aerosol treatments, Atmospheric Chemistry & Physics, 14(17).

He, J., Y. Zhang, S. Tilmes, L. Emmons, J.-F. Lamarque, T. Glotfelty, A. Hodzic, and F. Vitt (2015), CESM/CAM5 improvement and application: comparison and evaluation of updated CB05-GE and MOZART-4 gas-phase mechanisms and associated impacts on global air quality and climate, Geoscientific Model Development Discussions, 8(8).

Held, I. M., and B. J. Soden (2006), Robust responses of the hydrological cycle to global warming, Journal of Climate, 19(21), 5686-5699.

Hergert, W., and T. Wriedt (2012), The Mie theory: basics and applications, Springer.

Hodnebrog, Ø., G. Myhre, P. M. Forster, J. Sillmann, and B. H. Samset (2016), Local biomass burning is a dominant cause of the observed precipitation reduction in southern Africa, Nature communications, 7, 11236.

Hoesly, R. M., S. J. Smith, L. Feng, Z. Klimont, G. Janssens-Maenhout, T. Pitkanen, J. J. Seibert, L. Vu, R. J. Andres, and R. M. Bolt (2018), Historical (1750–2014) anthropogenic emissions of reactive gases and aerosols from the Community Emissions Data System (CEDS), Geoscientific Model Development, 11(1), 369-408.

Horton, R. M., J. S. Mankin, C. Lesk, E. Coffel, and C. Raymond (2016), A review of recent advances in research on extreme heat events, Current Climate Change Reports, 2(4), 242-259.

Hossaini, R., M. P. Chipperfield, S. A. Montzka, A. A. Leeson, S. S. Dhomse, and J. A. Pyle (2017), The increasing threat to stratospheric ozone from dichloromethane, Nature communications, 8, 15962.

Hsu, J., and M. J. Prather (2009), Stratospheric variability and tropospheric ozone, Journal of Geophysical Research: Atmospheres, 114(D6).

Huang, R., J. Chen, and G. Huang (2007), Characteristics and variations of the East Asian monsoon system and its impacts on climate disasters in China, Advances in Atmospheric Sciences, 24(6), 993-1023.

Huffman, G. J., R. F. Adler, P. Arkin, A. Chang, R. Ferraro, A. Gruber, J. Janowiak, A. McNab, B. Rudolf, and U. Schneider (1997), The global precipitation climatology project (GPCP) combined precipitation dataset, Bulletin of the American Meteorological Society, 78(1), 5-20.

Huijnen, V., A. Pozzer, J. Arteta, G. Brasseur, I. Bouarar, S. Chabrillat, Y. Christophe, T. Doumbia, J. Flemming, and J. Guth (2019), Quantifying uncertainties due to chemistry modeling–evaluation of tropospheric composition simulations in the CAMS model (cycle 43R1).

Huixin, L., C. Huopo, and W. Huijun (2017), Effects of anthropogenic activity emerging as intensified extreme precipitation over China, Journal of Geophysical Research: Atmospheres.

Hurrell, J. W., M. M. Holland, P. R. Gent, S. Ghan, J. E. Kay, P. Kushner, J.-F. Lamarque, W. G. Large, D. Lawrence, and K. Lindsay (2013), The community earth system model: a framework for collaborative research, Bulletin of the American Meteorological Society, 94(9), 1339-1360.

Hwang, Y. T., D. M. Frierson, and S. M. Kang (2013), Anthropogenic sulfate aerosol and the southward shift of tropical precipitation in the late 20th century, Geophysical Research Letters, 40(11), 2845-2850.

IIASA, F. (2012), Global Agro-ecological Zones (GAEZ v3. 0), IIASA, Laxenburg, Austria and FAO, Rome, Italy.

Inness, A., M. Ades, A. Agustí-Panareda, J. Barré, A. Benedictow, A.-M. Blechschmidt, J. J. Dominguez, R. Engelen, H. Eskes, and J. Flemming

(2019), The CAMS reanalysis of atmospheric composition, Atmospheric Chemistry and Physics, 19(6), 3515-3556.

Jacob, D. J. (1999), Introduction to atmospheric chemistry, Princeton University Press.

Jerrett, M., R. T. Burnett, C. A. Pope III, K. Ito, G. Thurston, D. Krewski, Y. Shi, E. Calle, and M. Thun (2009), Long-term ozone exposure and mortality, New England Journal of Medicine, 360(11), 1085-1095.

Jiang, Y., X. Liu, X.-Q. Yang, and M. Wang (2013), A numerical study of the effect of different aerosol types on East Asian summer clouds and precipitation, Atmospheric Environment, 70, 51-63.

Jones, B., B. C. O'Neill, L. McDaniel, S. McGinnis, L. O. Mearns, and C. Tebaldi (2015), Future population exposure to US heat extremes, Nature Climate Change, 5(7), 652.

Jong, B.-T., M. Ting, R. Seager, N. Henderson, and D. E. Lee (2018), Role of equatorial Pacific SST forecast error in the late winter California precipitation forecast for the 2015/16 El Niño, Journal of Climate, 31(2), 839-852.

Kalnay, E., M. Kanamitsu, R. Kistler, W. Collins, D. Deaven, L. Gandin, M. Iredell, S. Saha, G. White, and J. Woollen (1996), The NCEP/NCAR 40-year reanalysis project, Bulletin of the American meteorological Society, 77(3), 437-471.

Karpechko, A. Y., A. C. Maycock, M. Abalos, H. Akiyoshi, J. M. Arblaster, C. I. Garfinkel, K. H. Rosenlof, and M. Sigmond (2018), Stratospheric Ozone Changes and Climate, Chapter 5 in Scientific Assessment of Ozone Depletion: 2018, Global Ozone Research and Monitoring Project–Report, 58.

Kasoar, M., D. Shawki, and A. Voulgarakis (2018), Similar spatial patterns of global climate response to aerosols from different regions, npj Climate and Atmospheric Science, 1(1), 12.

Kasoar, M., A. Voulgarakis, J.-F. Lamarque, D. T. Shindell, N. Bellouin, W. J. Collins, G. Faluvegi, and K. Tsigaridis (2016), Regional and global temperature response to anthropogenic SO 2 emissions from China in three climate models, Atmospheric Chemistry and Physics, 16(15), 9785-9804.

Kay, J., C. Deser, A. Phillips, A. Mai, C. Hannay, G. Strand, J. Arblaster, S. Bates, G. Danabasoglu, and J. Edwards (2015), The Community Earth System Model (CESM) large ensemble project: A community resource for studying climate change in the presence of internal climate variability, Bulletin of the American Meteorological Society, 96(8), 1333-1349.

Kay, J. E., M. M. Holland, C. M. Bitz, E. Blanchard-Wrigglesworth, A. Gettelman, A. Conley, and D. Bailey (2012), The influence of local feedbacks and northward heat transport on the equilibrium Arctic climate response to increased greenhouse gas forcing, Journal of Climate, 25(16), 5433-5450.

Kharin, V. V., F. Zwiers, X. Zhang, and M. Wehner (2013), Changes in temperature and precipitation extremes in the CMIP5 ensemble, Climatic Change, 119(2), 345-357.

Kim, D., C. Wang, A. M. Ekman, M. C. Barth, and P. J. Rasch (2008), Distribution and direct radiative forcing of carbonaceous and sulfate aerosols in an interactive size‐resolving aerosol–climate model, Journal of geophysical research: Atmospheres, 113(D16).

Kinney, P. L. (2018), Interactions of climate change, air pollution, and human health, Current environmental health reports, 5(1), 179-186.

Kloster, S., F. Dentener, J. Feichter, F. Raes, U. Lohmann, E. Roeckner, and I. Fischer-Bruns (2010), A GCM study of future climate response to aerosol pollution reductions, Climate dynamics, 34(7-8), 1177-1194.

Knapp, A. K., C. Beier, D. D. Briske, A. T. Classen, Y. Luo, M. Reichstein, M. D. Smith, S. D. Smith, J. E. Bell, and P. A. Fay (2008), Consequences of more extreme precipitation regimes for terrestrial ecosystems, Bioscience, 58(9), 811-821.

Knutti, R., and J. Sedláček (2013), Robustness and uncertainties in the new CMIP5 climate model projections, Nature Climate Change, 3(4), 369.

Koch, D., and A. Del Genio (2010), Black carbon semi-direct effects on cloud cover: review and synthesis, Atmospheric Chemistry and Physics, 10(16), 7685-7696.

Kumar, P., A. Nenes, and I. N. Sokolik (2009), Importance of adsorption for CCN activity and hygroscopic properties of mineral dust aerosol, Geophysical Research Letters, 36(24).

Kuttippurath, J., and P. J. Nair (2017), The signs of Antarctic ozone hole recovery, Scientific reports, 7(1), 585.

Lamarque, J.-F., G. P. Kyle, M. Meinshausen, K. Riahi, S. J. Smith, D. P. van Vuuren, A. J. Conley, and F. Vitt (2011), Global and regional evolution of short-lived radiatively-active gases and aerosols in the Representative Concentration Pathways, Climatic change, 109(1-2), 191-212.

Lamarque, J.-F., T. C. Bond, V. Eyring, C. Granier, A. Heil, Z. Klimont, D. Lee, C. Liousse, A. Mieville, and B. Owen (2010), Historical (1850–2000) gridded anthropogenic and biomass burning emissions of reactive gases and aerosols: methodology and application, Atmospheric Chemistry and Physics, 10(15), 7017-7039.

Lamarque, J.-F., L. Emmons, P. Hess, D. E. Kinnison, S. Tilmes, F. Vitt, C. Heald, E. A. Holland, P. Lauritzen, and J. Neu (2012), CAM-chem: Description and evaluation of interactive atmospheric chemistry in the Community Earth System Model, Geoscientific Model Development, 5(2), 369.

Lamarque, J.-F., D. T. Shindell, B. Josse, P. Young, I. Cionni, V. Eyring, D. Bergmann, P. Cameron-Smith, W. J. Collins, and R. Doherty (2013), The Atmospheric Chemistry and Climate Model Intercomparison Project (ACCMIP): overview and description of models, simulations and climate diagnostics, Geoscientific Model Development, 6(1), 179-206.

Lau, K. M., and K. M. Kim (2006), Observational relationships between aerosol and Asian monsoon rainfall, and circulation, Geophysical Research Letters, 33(21).

Lau, N.-C., and M. J. Nath (2014), Model simulation and projection of European heat waves in present-day and future climates, Journal of Climate, 27(10), 3713-3730.

Lau, W. K.-M., and K.-M. Kim (2017), Competing influences of greenhouse warming and aerosols on Asian summer monsoon circulation and rainfall, Asia-Pacific Journal of Atmospheric Sciences, 53(2), 181-194.

Lee, L. A., C. L. Reddington, and K. S. Carslaw (2016), On the relationship between aerosol model uncertainty and radiative forcing uncertainty, Proceedings of the National Academy of Sciences, 113(21), 5820-5827.

Lehner, F., C. Deser, and B. M. Sanderson (2016), Future risk of record-breaking summer temperatures and its mitigation, Climatic Change, 1-13.

Lelieveld, J., and P. Crutzen (1990), Influences of cloud photochemical processes on tropospheric ozone, Nature, 343(6255), 227.

Lelieveld, J., J. S. Evans, M. Fnais, D. Giannadaki, and A. Pozzer (2015), The contribution of outdoor air pollution sources to premature mortality on a global scale, Nature, 525(7569), 367.

Lenderink, G., A. Van Ulden, B. Van den Hurk, and E. Van Meijgaard (2007), Summertime inter-annual temperature variability in an ensemble of regional model simulations: analysis of the surface energy budget, Climatic Change, 81, 233-247.

Lepeule, J., F. Laden, D. Dockery, and J. Schwartz (2012), Chronic exposure to fine particles and mortality: an extended follow-up of the Harvard Six Cities study from 1974 to 2009, Environmental health perspectives, 120(7), 965-970.

Lesins, G., P. Chylek, and U. Lohmann (2002), A study of internal and external mixing scenarios and its effect on aerosol optical properties and direct radiative forcing, Journal of Geophysical Research: Atmospheres, 107(D10), AAC 5-1-AAC 5-12.

Levy, H., L. W. Horowitz, M. D. Schwarzkopf, Y. Ming, J. C. Golaz, V. Naik, and V. Ramaswamy (2013), The roles of aerosol direct and indirect effects in past and future climate change, Journal of Geophysical Research: Atmospheres, 118(10), 4521-4532.

Lewinschal, A., A. M. Ekman, H.-C. Hansson, M. Sand, T. K. Berntsen, and J. Langner (2019), Local and remote temperature response of regional SO 2 emissions, Atmospheric Chemistry and Physics, 19(4), 2385-2403.

Lewis, S. C., A. D. King, and S. E. Perkins-Kirkpatrick (2017), Defining a new normal for extremes in a warming world, Bulletin of the American Meteorological Society, 98(6), 1139-1151.

Li, W. M. Lau, V. Ramanathan, G. Wu, Y. Ding, M. Manoj, J. Liu, Y. Qian, J. Li, and T. Zhou (2016), Aerosol and monsoon climate interactions over Asia, Reviews of Geophysics.

Li, C. McLinden, V. Fioletov, N. Krotkov, S. Carn, J. Joiner, D. Streets, H. He, X. Ren, and Z. Li (2017), India is overtaking China as the world's largest emitter of anthropogenic sulfur dioxide, Scientific reports, 7(1), 14304.

Li, M., D. Zhang, C.-T. Li, K. M. Mulvaney, N. E. Selin, and V. J. Karplus (2018), Air quality co-benefits of carbon pricing in China, Nature Climate Change, 8(5), 398.

Li, X., M. Ting, C. Li, and N. Henderson (2015), Mechanisms of Asian summer monsoon changes in response to anthropogenic forcing in CMIP5 models, Journal of Climate, 28(10), 4107-4125.

Liang, C.-K., J. J. West, R. A. Silva, H. Bian, M. Chin, Y. Davila, F. J. Dentener, L. Emmons, J. Flemming, and G. Folberth (2018), HTAP2 multi-model estimates of premature human mortality due to intercontinental transport of air pollution and emission sectors, Atmospheric Chemistry and Physics, 18(14), 10497-10520.

Lin, L., A. Gettelman, Q. Fu, and Y. Xu (2015), Simulated differences in 21st century aridity due to different scenarios of greenhouse gases and aerosols, Climatic Change, 1-16.

Lin, L., Z. Wang, Y. Xu, and Q. Fu (2016), Sensitivity of precipitation extremes to radiative forcing of greenhouse gases and aerosols, Geophysical Research Letters, 43(18), 9860-9868.

Liu, J., B. Wang, M. A. Cane, S.-Y. Yim, and J.-Y. Lee (2013), Divergent global precipitation changes induced by natural versus anthropogenic forcing, Nature, 493(7434), 656.

Liu, L., D. Shawki, A. Voulgarakis, M. Kasoar, B. Samset, G. Myhre, P. Forster, Ø. Hodnebrog, J. Sillmann, and S. Aalbergsjø (2018), A PDRMIP Multimodel Study on the impacts of regional aerosol forcings on global and regional precipitation, Journal of Climate, 31(11), 4429-4447.

Liu, X., P.-L. Ma, H. Wang, S. Tilmes, B. Singh, R. Easter, S. Ghan, and P. Rasch (2015), Description and evaluation of a new 4-mode version of Modal Aerosol Module (MAM4) within version 5.3 of the Community Atmosphere Model, Geoscientific Model Development Discussions, 8(9).

Liu, X., R. C. Easter, S. J. Ghan, R. Zaveri, P. Rasch, X. Shi, J.-F. Lamarque, A. Gettelman, H. Morrison, and F. Vitt (2012), Toward a minimal representation of aerosols in climate models: Description and evaluation in the Community Atmosphere Model CAM5, Geoscientific Model Development, 5(3), 709.

Liu, Y., W. Cai, C. Sun, H. Song, K. M. Cobb, J. Li, S. W. Leavitt, L. Wu, Q. Cai, and R. Liu (2019), Anthropogenic aerosols cause recent pronounced weakening of Asian Summer Monsoon relative to last four centuries, Geophysical Research Letters.

Lohmann, U., F. Lüönd, and F. Mahrt (2016), An Introduction to Clouds: From the Microscale to Climate, Cambridge University Press.

Lu, R.-Y., and R.-D. Chen (2016), A review of recent studies on extreme heat in China, Atmospheric and Oceanic Science Letters, 9(2), 114-121.

Lucas, C., B. Timbal, and H. Nguyen (2014), The expanding tropics: A critical assessment of the observational and modeling studies, Wiley Interdisciplinary Reviews: Climate Change, 5(1), 89-112.

Ma, S., T. Zhou, D. A. Stone, D. Polson, A. Dai, P. A. Stott, H. von Storch, Y. Qian, C. Burke, and P. Wu (2017), Detectable anthropogenic shift toward heavy precipitation over eastern China, Journal of Climate, 30(4), 1381-1396.

Mahlstein, I., R. Knutti, S. Solomon, and R. Portmann (2011), Early onset of significant local warming in low latitude countries, Environmental Research Letters, 6(3), 034009.

Malavelle, F. F., J. M. Haywood, A. Jones, A. Gettelman, L. Clarisse, S. Bauduin, R. P. Allan, I. H. H. Karset, J. E. Kristjánsson, and L. Oreopoulos (2017), Strong constraints on aerosol–cloud interactions from volcanic eruptions, Nature, 546(7659), 485.

Markandya, A., J. Sampedro, S. J. Smith, R. Van Dingenen, C. Pizarro-Irizar, I. Arto, and M. González-Eguino (2018), Health co-benefits from air pollution and mitigation costs of the Paris Agreement: a modelling study, The Lancet Planetary Health, 2(3), e126-e133.

Marotzke, J. (2019), Quantifying the irreducible uncertainty in near‐term climate projections, Wiley Interdisciplinary Reviews: Climate Change, 10(1), e563.

Marsh, D. R., M. J. Mills, D. E. Kinnison, J.-F. Lamarque, N. Calvo, and L. M. Polvani (2013), Climate change from 1850 to 2005 simulated in CESM1 (WACCM), Journal of climate, 26(19), 7372-7391.

Marvel, K., G. A. Schmidt, R. L. Miller, and L. S. Nazarenko (2016), Implications for climate sensitivity from the response to individual forcings, Nature Climate Change, 6(4), 386.

Mascioli, N. R., A. M. Fiore, M. Previdi, and G. Correa (2016), Temperature and Precipitation Extremes in the United States: Quantifying the Responses to Anthropogenic Aerosols and Greenhouse Gases,+, Journal of Climate, 29(7), 2689-2701.

Mauritsen, T., and R. Pincus (2017), Committed warming inferred from observations, Nature Climate Change, 7(9), 652.

McLandress, C., T. G. Shepherd, J. F. Scinocca, D. A. Plummer, M. Sigmond, A. I. Jonsson, and M. C. Reader (2011), Separating the dynamical effects of climate change and ozone depletion. Part II: Southern Hemisphere troposphere, Journal of Climate, 24(6), 1850-1868.

Meehl, G. A., and C. Tebaldi (2004), More intense, more frequent, and longer lasting heat waves in the 21st century, Science, 305(5686), 994-997.

Meehl, G. A., T. F. Stocker, W. D. Collins, P. Friedlingstein, T. Gaye, J. M. Gregory, A. Kitoh, R. Knutti, J. M. Murphy, and A. Noda (2007), Global climate projections.

Mills, G., A. Buse, B. Gimeno, V. Bermejo, M. Holland, L. Emberson, and H. Pleijel (2007), A synthesis of AOT40-based response functions and critical levels of ozone for agricultural and horticultural crops, Atmospheric Environment, 41(12), 2630-2643.

Min, S.-K., X. Zhang, F. W. Zwiers, and G. C. Hegerl (2011), Human contribution to more-intense precipitation extremes, Nature, 470(7334), 378-381.

Ming, Y., and V. Ramaswamy (2009), Nonlinear climate and hydrological responses to aerosol effects, Journal of Climate, 22(6), 1329-1339.

Ming, Y., and V. Ramaswamy (2011), A model investigation of aerosol-induced changes in tropical circulation, Journal of Climate, 24(19), 5125-5133.

Ming, Y., V. Ramaswamy, and G. Chen (2011), A model investigation of aerosol-induced changes in boreal winter extratropical circulation, Journal of Climate, 24(23), 6077-6091.

Miralles, D. G., P. Gentine, S. I. Seneviratne, and A. J. Teuling (2018), Land–atmospheric feedbacks during droughts and heatwaves: state of the science and current challenges, Annals of the New York Academy of Sciences.

Mishra, V., S. Mukherjee, R. Kumar, and D. A. Stone (2017), Heat wave exposure in India in current, 1.5° C, and 2.0° C worlds, Environmental Research Letters, 12(12), 124012.

Mitchell, J., S. Manabe, V. Meleshko, and T. Tokioka (1990), Equilibrium climate change and its implications for the future, Climate change: The IPCC scientific assessment, 131, 172.

Monks, P. S., A. Archibald, A. Colette, O. Cooper, M. Coyle, R. Derwent, D. Fowler, C. Granier, K. S. Law, and G. Mills (2015), Tropospheric ozone and its precursors from the urban to the global scale from air quality to short-lived climate forcer, Atmospheric Chemistry and Physics, 15(15), 8889-8973.

Mora, C., B. Dousset, I. R. Caldwell, F. E. Powell, R. C. Geronimo, C. R. Bielecki, C. W. Counsell, B. S. Dietrich, E. T. Johnston, and L. V. Louis (2017), Global risk of deadly heat, Nature Climate Change, 7(7), 501.

Morice, C. P., J. J. Kennedy, N. A. Rayner, and P. D. Jones (2012), Quantifying uncertainties in global and regional temperature change using an ensemble of observational estimates: The HadCRUT4 data set, Journal of Geophysical Research: Atmospheres, 117(D8).

Morrison, A., J. Kay, W. Frey, H. Chepfer, and R. Guzman (2019), Cloud Response to Arctic Sea Ice Loss and Implications for Future Feedback in the CESM1 Climate Model, Journal of Geophysical Research: Atmospheres, 124(2), 1003-1020.

Morrison, H., and A. Gettelman (2008), A new two-moment bulk stratiform cloud microphysics scheme in the Community Atmosphere Model, version 3 (CAM3). Part I: Description and numerical tests, Journal of Climate, 21(15), 3642-3659.

Mukherjee, S., S. Aadhar, D. Stone, and V. Mishra (2018), Increase in extreme precipitation events under anthropogenic warming in India, Weather and Climate Extremes.

Myhre, W. Aas, R. Cherian, W. Collins, G. Faluvegi, M. Flanner, P. Forster, Ø. Hodnebrog, Z. Klimont, and M. T. Lund (2017a), Multi-model simulations of aerosol and ozone radiative forcing due to anthropogenic emission changes

during the period 1990–2015, Atmospheric Chemistry and Physics, 17(4), 2709-2720.

Myhre, P. Forster, B. Samset, Ø. Hodnebrog, J. Sillmann, S. Aalbergsjø, T. Andrews, O. Boucher, G. Faluvegi, and D. Fläschner (2017b), PDRMIP: A precipitation driver and response model intercomparison project—Protocol and preliminary results, Bulletin of the American Meteorological Society, 98(6), 1185-1198.

Myhre, G., D. Shindell, F.-M. Bréon, W. Collins, J. Fuglestvedt, J. Huang, D. Koch, J.-F. Lamarque, D. Lee, and B. Mendoza (2013), Anthropogenic and natural radiative forcing, Climate change, 423.

Myhre, G., W. Aas, R. Cherian, W. Collins, G. Faluvegi, M. Flanner, P. Forster, Ø. Hodnebrog, Z. Klimont, and M. T. Lund (2017), Multi-model simulations of aerosol and ozone radiative forcing due to anthropogenic emission changes during the period 1990–2015, Atmospheric Chemistry and Physics, 17(4), 2709-2720.

Najafi, M. R., F. W. Zwiers, and N. P. Gillett (2015), Attribution of Arctic temperature change to greenhouse-gas and aerosol influences, Nature Climate Change, 5(3), 246-249.

Navarro, J. A., V. Varma, I. Riipinen, Ø. Seland, A. Kirkevåg, H. Struthers, T. Iversen, H.-C. Hansson, and A. Ekman (2016), Amplification of Arctic warming by past air pollution reductions in Europe, Nature Geoscience.

Neale, R. B., J. H. Richter, and M. Jochum (2008), The impact of convection on ENSO: From a delayed oscillator to a series of events, Journal of climate, 21(22), 5904-5924.

Neale, R. B., C.-C. Chen, A. Gettelman, P. H. Lauritzen, S. Park, D. L. Williamson, A. J. Conley, R. Garcia, D. Kinnison, and J.-F. Lamarque (2010), Description of the NCAR community atmosphere model (CAM 5.0), NCAR Tech. Note NCAR/TN-486+ STR, 1(1), 1-12.

Nordling, K., H. Korhonen, P. Räisänen, M. E. Alper, P. Uotila, D. O'Donnell, and J. Merikanto (2019), Role of climate model dynamics in estimated climate responses to anthropogenic aerosols, Atmospheric Chemistry and Physics, 19(15), 9969-9987.

North, G. R., J. A. Pyle, and F. Zhang (2014), Encyclopedia of atmospheric sciences, Elsevier.

Northrop, P. J., and R. E. Chandler (2014), Quantifying sources of uncertainty in projections of future climate, Journal of Climate, 27(23), 8793-8808.

Nychka, D., R. Buchberger, T. Wigley, B. Santer, K. Taylor, and R. Jones (2000), Confidence intervals for trend estimates with autocorrelated observations.

O'Neill, B. C., C. Tebaldi, D. P. v. Vuuren, V. Eyring, P. Friedlingstein, G. Hurtt, R. Knutti, E. Kriegler, J.-F. Lamarque, and J. Lowe (2016), The scenario model intercomparison project (ScenarioMIP) for CMIP6, Geoscientific Model Development, 9(9), 3461-3482.

O'Gorman, P. A. (2015), Precipitation extremes under climate change, Current climate change reports, 1(2), 49-59.

Ocko, I. B., V. Ramaswamy, and Y. Ming (2014), Contrasting climate responses to the scattering and absorbing features of anthropogenic aerosol forcings, Journal of Climate, 27(14), 5329-5345.

Olivier, J. G., J. A. Van Aardenne, F. J. Dentener, V. Pagliari, L. N. Ganzeveld, and J. A. Peters (2005), Recent trends in global greenhouse gas emissions: regional trends 1970–2000 and spatial distributionof key sources in 2000, Environmental Sciences, 2(2-3), 81-99.

Orlowsky, B., and S. I. Seneviratne (2012), Global changes in extreme events: regional and seasonal dimension, Climatic Change, 110(3), 669-696.

Ovtchinnikov, M., and S. J. Ghan (2005), Parallel simulations of aerosol influence on clouds using cloud‐resolving and single‐column models, Journal of Geophysical Research: Atmospheres, 110(D15).

Park, S., and C. S. Bretherton (2009), The University of Washington shallow convection and moist turbulence schemes and their impact on climate simulations with the Community Atmosphere Model, Journal of Climate, 22(12), 3449-3469.

Park, S., C. Bretherton, and P. Rasch (2012), Global cloud simulation in the Community Atmosphere Model 5, J. Climate, submitted.

Partanen, A.-I., J.-S. Landry, and H. D. Matthews (2018), Climate and health implications of future aerosol emission scenarios, Environmental Research Letters, 13(2), 024028.

Paul, S., S. Ghosh, R. Oglesby, A. Pathak, A. Chandrasekharan, and R. Ramsankaran (2016), Weakening of Indian summer monsoon rainfall due to changes in land use land cover, Scientific Reports, 6, 32177.

Pendergrass, A. G., and D. L. Hartmann (2014), The atmospheric energy constraint on global-mean precipitation change, Journal of Climate, 27(2), 757-768.

Pendergrass, A. G., F. Lehner, B. M. Sanderson, and Y. Xu (2015), Does extreme precipitation intensity depend on the emissions scenario?, Geophysical Research Letters, 42(20), 8767-8774.

Perkins-Kirkpatrick, S., and A. Pitman (2018), Extreme events in the context of climate change, Public health research & practice, 28(4).

Perkins, S., L. Alexander, and J. Nairn (2012), Increasing frequency, intensity and duration of observed global heatwaves and warm spells, Geophysical Research Letters, 39(20).

Perkins, S. E. (2015), A review on the scientific understanding of heatwaves—their measurement, driving mechanisms, and changes at the global scale, Atmospheric Research, 164, 242-267.

Persad, G. G., and K. Caldeira (2018), Divergent global-scale temperature effects from identical aerosols emitted in different regions, Nature communications, 9(1), 3289.

Persad, G. G., Y. Ming, Z. Shen, and V. Ramaswamy (2018), Spatially similar surface energy flux perturbations due to greenhouse gases and aerosols, Nature communications, 9(1), 3247.

Peterson, T. C., R. R. Heim Jr, R. Hirsch, D. P. Kaiser, H. Brooks, N. S. Diffenbaugh, R. M. Dole, J. P. Giovannettone, K. Guirguis, and T. R. Karl (2013), Monitoring and understanding changes in heat waves, cold waves, floods, and droughts in the United States: state of knowledge, Bulletin of the American Meteorological Society, 94(6), 821-834.

Polson, D., G. Hegerl, R. Allan, and B. B. Sarojini (2013), Have greenhouse gases intensified the contrast between wet and dry regions?, Geophysical Research Letters, 40(17), 4783-4787.

Polson, D., M. Bollasina, G. Hegerl, and L. Wilcox (2014), Decreased monsoon precipitation in the Northern Hemisphere due to anthropogenic aerosols, Geophysical Research Letters, 41(16), 6023-6029.

Previdi, M., and L. M. Polvani (2014), Climate system response to stratospheric ozone depletion and recovery, Quarterly Journal of the Royal Meteorological Society, 140(685), 2401-2419.

Qian, C., and T. Zhou (2014), Multidecadal variability of North China aridity and its relationship to PDO during 1900–2010, Journal of Climate, 27(3), 1210-1222.

Ramana, M., V. Ramanathan, Y. Feng, S. Yoon, S. Kim, G. Carmichael, and J. Schauer (2010), Warming influenced by the ratio of black carbon to sulphate and the black-carbon source, Nature Geoscience, 3(8), 542.

Ramanathan, V., C. Chung, D. Kim, T. Bettge, L. Buja, J. Kiehl, W. Washington, Q. Fu, D. Sikka, and M. Wild (2005), Atmospheric brown clouds: Impacts on South Asian climate and hydrological cycle, Proceedings of the National Academy of Sciences of the United States of America, 102(15), 5326-5333.

Regayre, L. A., J. S. Johnson, M. Yoshioka, K. J. Pringle, D. M. Sexton, B. B. Booth, L. A. Lee, N. Bellouin, and K. S. Carslaw (2018), Aerosol and physical atmosphere model parameters are both important sources of uncertainty in aerosol ERF, Atmospheric Chemistry and Physics, 18(13), 9975-10006.

Riahi, K., A. Grübler, and N. Nakicenovic (2007), Scenarios of long-term socio-economic and environmental development under climate stabilization, Technological Forecasting and Social Change, 74(7), 887-935.

Ropelewski, C. F., and M. S. Halpert (1987), Global and regional scale precipitation patterns associated with the El Niño/Southern Oscillation, Monthly weather review, 115(8), 1606-1626.

Rosenfeld, D., S. Sherwood, R. Wood, and L. Donner (2014a), Climate effects of aerosol-cloud interactions, Science, 343(6169), 379-380.

Rosenfeld, D., U. Lohmann, G. B. Raga, C. D. O'Dowd, M. Kulmala, S. Fuzzi, A. Reissell, and M. O. Andreae (2008), Flood or drought: how do aerosols affect precipitation?, science, 321(5894), 1309-1313.

Rosenfeld, D., M. O. Andreae, A. Asmi, M. Chin, G. de Leeuw, D. P. Donovan, R. Kahn, S. Kinne, N. Kivekäs, and M. Kulmala (2014b), Global observations of aerosol ‐ cloud ‐ precipitation ‐ climate interactions, Reviews of Geophysics, 52(4), 750-808.

Rotstayn, L. D., E. L. Plymin, M. A. Collier, O. Boucher, J.-L. Dufresne, J.-J. Luo, K. von Salzen, S. J. Jeffrey, M.-A. Foujols, and Y. Ming (2014), Declining aerosols in CMIP5 projections: Effects on atmospheric temperature structure and midlatitude jets, Journal of Climate, 27(18), 6960-6977.

Rugenstein, M., and J. Bloch-Johnson (2016), Equilibrium and Effective Climate Sensitivity, paper presented at AGU Fall Meeting Abstracts.

Russo, S., and A. Sterl (2011), Global changes in indices describing moderate temperature extremes from the daily output of a climate model, Journal of Geophysical Research: Atmospheres, 116(D3).

Russo, S., J. Sillmann, and E. M. Fischer (2015), Top ten European heatwaves since 1950 and their occurrence in the coming decades, Environmental Research Letters, 10(12), 124003.

Russo, S., A. Dosio, R. G. Graversen, J. Sillmann, H. Carrao, M. B. Dunbar, A. Singleton, P. Montagna, P. Barbola, and J. V. Vogt (2014), Magnitude of extreme heat waves in present climate and their projection in a warming world, Journal of Geophysical Research: Atmospheres, 119(22).

Sacks, W. J., D. Deryng, J. A. Foley, and N. Ramankutty (2010), Crop planting dates: an analysis of global patterns, Global Ecology and Biogeography, 19(5), 607-620.

Samset, B., M. Sand, C. Smith, S. Bauer, P. Forster, J. Fuglestvedt, S. Osprey, and C. F. Schleussner (2018), Climate impacts from a removal of anthropogenic aerosol emissions, Geophysical Research Letters, 45(2), 1020-1029.

Samset, B., G. Myhre, P. Forster, Ø. Hodnebrog, T. Andrews, G. Faluvegi, D. Flaeschner, M. Kasoar, V. Kharin, and A. Kirkevåg (2016), Fast and slow precipitation responses to individual climate forcers: A PDRMIP multimodel study, Geophysical Research Letters, 43(6), 2782-2791.

Samset, B. H. (2018), How cleaner air changes the climate, Science, 360(6385), 148-150.

Sanap, S., G. Pandithurai, and M. Manoj (2015), On the response of Indian summer monsoon to aerosol forcing in CMIP5 model simulations, Climate Dynamics, 45(9-10), 2949-2961.

Sand, M., T. Berntsen, K. von Salzen, M. Flanner, J. Langner, and D. Victor (2015), Response of Arctic temperature to changes in emissions of short-lived climate forcers, Nature Climate Change.

Schär, C. (2016), Climate extremes: the worst heat waves to come, Nature Climate Change, 6(2), 128.

Schär, C., P. L. Vidale, D. Lüthi, C. Frei, C. Häberli, M. A. Liniger, and C. Appenzeller (2004), The role of increasing temperature variability in European summer heatwaves, Nature, 427(6972), 332.

Schiferl, L. D., and C. L. Heald (2018), Particulate matter air pollution may offset ozone damage to global crop production, Atmospheric Chemistry and Physics, 18(8), 5953-5966.

Schlesinger, M. E. (1986), Equilibrium and transient climatic warming induced by increased atmospheric CO 2, Climate Dynamics, 1(1), 35-51.

Schmale, J., D. Shindell, E. von Schneidemesser, I. Chabay, and M. Lawrence (2014), Air pollution: clean up our skies, Nature News, 515(7527), 335.

Schmidt, G. A., D. T. Shindell, and K. Tsigaridis (2014), Reconciling warming trends, Nature Geoscience, 7(3), 158.

Schoetter, R., J. Cattiaux, and H. Douville (2015), Changes of western European heat wave characteristics projected by the CMIP5 ensemble, Climate dynamics, 45(5-6), 1601-1616.

Seinfeld, J. H., and S. N. Pandis (2016), Atmospheric chemistry and physics: from air pollution to climate change, John Wiley & Sons.

Seinfeld, J. H., C. Bretherton, K. S. Carslaw, H. Coe, P. J. DeMott, E. J. Dunlea, G. Feingold, S. Ghan, A. B. Guenther, and R. Kahn (2016), Improving our fundamental understanding of the role of aerosol− cloud interactions in the climate system, Proceedings of the National Academy of Sciences, 113(21), 5781-5790.

Sen Roy, S., and R. C. Balling (2004), Trends in extreme daily precipitation indices in India, International Journal of climatology, 24(4), 457-466.

Shindell (2014), Inhomogeneous forcing and transient climate sensitivity, Nature Climate Change, 4(4), 274.

Shindell, G. Faluvegi, L. Rotstayn, and G. Milly (2015), Spatial patterns of radiative forcing and surface temperature response, Journal of Geophysical Research: Atmospheres, 120(11), 5385-5403.

Shindell, D., and G. Faluvegi (2009), Climate response to regional radiative forcing during the twentieth century, Nature Geoscience, 2(4), 294.

Shindell, D., M. Schulz, Y. Ming, T. Takemura, G. Faluvegi, and V. Ramaswamy (2010), Spatial scales of climate response to inhomogeneous radiative forcing, Journal of Geophysical Research: Atmospheres, 115(D19).

Sillmann, J., L. Pozzoli, E. Vignati, S. Kloster, and J. Feichter (2013a), Aerosol effect on climate extremes in Europe under different future scenarios, Geophysical Research Letters, 40(10), 2290-2295.

Sillmann, J., V. Kharin, X. Zhang, F. Zwiers, and D. Bronaugh (2013b), Climate extremes indices in the CMIP5 multimodel ensemble: Part 1. Model evaluation in the present climate, Journal of Geophysical Research: Atmospheres, 118(4), 1716-1733.

Sillmann, J., V. Kharin, F. Zwiers, X. Zhang, and D. Bronaugh (2013c), Climate extremes indices in the CMIP5 multimodel ensemble: Part 2. Future climate projections, Journal of Geophysical Research: Atmospheres, 118(6), 2473-2493.

Silva, R. A., Z. Adelman, M. M. Fry, and J. J. West (2016a), The impact of individual anthropogenic emissions sectors on the global burden of human

mortality due to ambient air pollution, Environmental health perspectives, 124(11), 1776.

Silva, R. A., J. J. West, Y. Zhang, S. C. Anenberg, J.-F. Lamarque, D. T. Shindell, W. J. Collins, S. Dalsoren, G. Faluvegi, and G. Folberth (2013), Global premature mortality due to anthropogenic outdoor air pollution and the contribution of past climate change, Environmental Research Letters, 8(3), 034005.

Silva, R. A., J. J. West, J.-F. Lamarque, D. T. Shindell, W. J. Collins, S. Dalsoren, G. Faluvegi, G. Folberth, L. W. Horowitz, and T. Nagashima (2016b), The effect of future ambient air pollution on human premature mortality to 2100 using output from the ACCMIP model ensemble, Atmospheric chemistry and physics, 16(15), 9847-9862.

Silva, R. A., J. J. West, J.-F. Lamarque, D. T. Shindell, W. J. Collins, G. Faluvegi, G. A. Folberth, L. W. Horowitz, T. Nagashima, and V. Naik (2017), Future global mortality from changes in air pollution attributable to climate change, Nature climate change, 7(9), 647.

Silver, B., C. Reddington, S. Arnold, and D. Spracklen (2018), Substantial changes in air pollution across China during 2015–2017, Environmental Research Letters, 13(11), 114012.

Singh, D., M. Tsiang, B. Rajaratnam, and N. S. Diffenbaugh (2013), Precipitation extremes over the continental United States in a transient, high‐resolution, ensemble climate model experiment, Journal of Geophysical Research: Atmospheres, 118(13), 7063-7086.

Singh, D., M. Tsiang, B. Rajaratnam, and N. S. Diffenbaugh (2014), Observed changes in extreme wet and dry spells during the South Asian summer monsoon season, Nature Climate Change, 4(6), 456-461.

Smith, S. J., J. v. Aardenne, Z. Klimont, R. J. Andres, A. Volke, and S. Delgado Arias (2011), Anthropogenic sulfur dioxide emissions: 1850–2005, Atmospheric Chemistry and Physics, 11(3), 1101-1116.

Solomon, S. (1999), Stratospheric ozone depletion: A review of concepts and history, Reviews of Geophysics, 37(3), 275-316.

Solomon, S., D. J. Ivy, D. Kinnison, M. J. Mills, R. R. Neely, and A. Schmidt (2016), Emergence of healing in the Antarctic ozone layer, Science, 353(6296), 269-274.

Song, F., T. Zhou, and Y. Qian (2014), Responses of East Asian summer monsoon to natural and anthropogenic forcings in the 17 latest CMIP5 models, Geophysical Research Letters, 41(2), 596-603.

Spracklen, D., K. Pringle, K. Carslaw, M. Chipperfield, and G. Mann (2005), A global off-line model of size-resolved aerosol microphysics: I. Model development and prediction of aerosol properties, Atmospheric Chemistry and Physics, 5(8), 2227-2252.

Stevens, B. (2017), Climate science: Clouds unfazed by haze, Nature, 546(7659), 483.

Stevens, B., and G. Feingold (2009), Untangling aerosol effects on clouds and precipitation in a buffered system, Nature, 461(7264), 607.

Stevenson, D., P. Young, V. Naik, J.-F. Lamarque, D. T. Shindell, A. Voulgarakis, R. B. Skeie, S. B. Dalsoren, G. Myhre, and T. K. Berntsen (2013), Tropospheric ozone changes, radiative forcing and attribution to emissions in the Atmospheric Chemistry and Climate Model Intercomparison Project (ACCMIP), Atmospheric Chemistry and Physics, 13(6), 3063-3085.

Stjern, C. W., B. H. Samset, G. Myhre, P. M. Forster, Ø. Hodnebrog, T. Andrews, O. Boucher, G. Faluvegi, T. Iversen, and M. Kasoar (2017), Rapid adjustments cause weak surface temperature response to increased black carbon concentrations, Journal of Geophysical Research: Atmospheres, 122(21), 11,462-411,481.

Stocker, D. Qin, G.-K. Plattner, M. Tignor, S. K. Allen, J. Boschung, A. Nauels, Y. Xia, V. Bex, and P. M. Midgley (2013), Climate change 2013: The physical science basis, Intergovernmental Panel on Climate Change, Working Group I Contribution to the IPCC Fifth Assessment Report (AR5)(Cambridge Univ Press, New York), 25.

Stohl, A., B. Aamaas, M. Amann, L. H. Baker, N. Bellouin, T. K. Berntsen, O. Boucher, R. Cherian, W. Collins, and N. Daskalakis (2015), Evaluating the climate and air quality impacts of short-lived pollutants, Atmospheric Chemistry and Physics, 15(18), 10529-10566.

Stolpe, M. B., I. Medhaug, U. Beyerle, and R. Knutti (2019), Weak dependence of future global mean warming on the background climate state, Climate Dynamics, 1-21.

Stott, P. A., M. Allen, N. Christidis, R. M. Dole, M. Hoerling, C. Huntingford, P. Pall, J. Perlwitz, and D. Stone (2013), Attribution of weather and climate-related events, in Climate Science for Serving Society, edited, pp. 307-337, Springer.

Taylor, K. E., and J. E. Penner (1994), Response of the climate system to atmospheric aerosols and greenhouse gases, Nature, 369(6483), 734.

Taylor, K. E., R. J. Stouffer, and G. A. Meehl (2012), An overview of CMIP5 and the experiment design, Bulletin of the American Meteorological Society, 93(4), 485-498.

Tebaldi, C., K. Hayhoe, J. M. Arblaster, and G. A. Meehl (2006), Going to the extremes, Climatic change, 79(3), 185-211.

Teng, H., G. Branstator, G. A. Meehl, and W. M. Washington (2016), Projected intensification of subseasonal temperature variability and heat waves in the Great Plains, Geophysical Research Letters, 43(5), 2165-2173.

Thompson, D. W., S. Solomon, P. J. Kushner, M. H. England, K. M. Grise, and D. J. Karoly (2011), Signatures of the Antarctic ozone hole in Southern Hemisphere surface climate change, Nature geoscience, 4(11), 741.

Tian, F., B. Dong, J. Robson, and R. Sutton (2018), Forced decadal changes in the East Asian summer monsoon: the roles of greenhouse gases and anthropogenic aerosols, Climate dynamics, 51(9-10), 3699-3715.

Tie, X., S. Madronich, S. Walters, D. P. Edwards, P. Ginoux, N. Mahowald, R. Zhang, C. Lou, and G. Brasseur (2005), Assessment of the global impact of aerosols on tropospheric oxidants, Journal of Geophysical Research: Atmospheres, 110(D3).

Tilmes, S., J.-F. Lamarque, L. Emmons, D. Kinnison, P. Ma, X. Liu, S. Ghan, C. Bardeen, S. Arnold, and M. Deeter (2015), Description and evaluation of tropospheric chemistry and aerosols in the Community Earth System Model (CESM1. 2), Geoscientific Model Development, 8, 1395-1426.

Toll, V., M. Christensen, S. Gassó, and N. Bellouin (2017), Volcano and Ship Tracks Indicate Excessive Aerosol‐Induced Cloud Water Increases in a Climate Model, Geophysical research letters, 44(24), 12,492-412,500.

Trenberth, K. E. (2011), Changes in precipitation with climate change, Climate Research, 47(1-2), 123-138.

Tricot, C., and A. Berger (1987), Modelling the equilibrium and transient responses of global temperature to past and future trace gas concentrations, Climate Dynamics, 2(1), 39-61.

Turnock, S., E. Butt, T. Richardson, G. Mann, C. Reddington, P. Forster, J. Haywood, M. Crippa, G. Janssens-Maenhout, and C. Johnson (2016), The impact of European legislative and technology measures to reduce air pollutants on air quality, human health and climate, Environmental Research Letters, 11(2), 024010.

Twomey, S. (1977), The influence of pollution on the shortwave albedo of clouds, Journal of the atmospheric sciences, 34(7), 1149-1152.

Undorf, S., M. Bollasina, B. Booth, and G. Hegerl (2018), Contrasting the Effects of the 1850–1975 Increase in Sulphate Aerosols from North America and Europe on the Atlantic in the CESM, Geophysical Research Letters, 45(21), 11,930-911,940.

United Nation Population Division (2017), World population prospects: The 2017 revision, UN.

Val Martin, M., C. Heald, J.-F. Lamarque, S. Tilmes, L. Emmons, and B. Schichtel (2015), How emissions, climate, and land use change will impact mid-century air quality over the United States: a focus on effects at national parks, Atmospheric Chemistry and Physics, 15(5), 2805-2823.

Van Rij, E. (2016), An approach to the disaster profile of People's Republic of China 1980-2013, Emergency and Disaster Reports, 3(4), 1-48.

Van Vuuren, D. P., J. Edmonds, M. Kainuma, K. Riahi, A. Thomson, K. Hibbard, G. C. Hurtt, T. Kram, V. Krey, and J.-F. Lamarque (2011), The representative concentration pathways: an overview, Climatic change, 109(1-2), 5.

Vehkamäki, H., M. Kulmala, I. Napari, K. E. Lehtinen, C. Timmreck, M. Noppel, and A. Laaksonen (2002), An improved parameterization for sulfuric acid–water nucleation rates for tropospheric and stratospheric conditions, Journal of Geophysical Research: Atmospheres, 107(D22), AAC 3-1-AAC 3-10.

Vermeulen, W. (2002), Global warming and social innovation: The challenge of a climate-neutral society, Earthscan.

Voigt, A., R. Pincus, B. Stevens, S. Bony, O. Boucher, N. Bellouin, A. Lewinschal, B. Medeiros, Z. Wang, and H. Zhang (2017), Fast and slow shifts of the zonal‐mean intertropical convergence zone in response to an idealized anthropogenic aerosol, Journal of Advances in Modeling Earth Systems, 9(2), 870-892.

Wang, S.-P. Xie, and Q. Liu (2016a), Comparison of climate response to anthropogenic aerosol versus greenhouse gas forcing: Distinct patterns, Journal of Climate, 29(14), 5175-5188.

Wang, L. Lin, M. Yang, and Y. Xu (2016b), The effect of future reduction in aerosol emissions on climate extremes in China, Climate Dynamics, 1-15.

Wang, L. Lin, M. Yang, Y. Xu, and J. Li (2017a), Disentangling fast and slow responses of the East Asian summer monsoon to reflecting and absorbing aerosol forcings, Atmospheric Chemistry and Physics, 17(18), 11075-11088.

Wang, Z. Wu, H. He, F. Wang, H. Du, and S. Zong (2017b), Changes in summer extreme precipitation in Northeast Asia and their relationships with the East Asian summer monsoon during 1961–2009, International Journal of Climatology, 37(1), 25-35.

Wang, P. Wang, N. Theys, D. Tong, F. Hendrick, Q. Zhang, and M. V. Roozendael (2018a), Spatial and temporal changes in SO 2 regimes over China in the recent decade and the driving mechanism, Atmospheric Chemistry and Physics, 18(24), 18063-18078.

Wang, J. H. Jiang, H. Su, Y.-S. Choi, L. Huang, J. Guo, and Y. L. Yung (2018b), Elucidating the role of anthropogenic aerosols in Arctic sea ice variations, Journal of Climate, 31(1), 99-114.

Wang, B. (2006), The asian monsoon, Springer Science & Business Media.

Wang, X., Q. Zhang, F. Zheng, Q. Zheng, F. Yao, Z. Chen, W. Zhang, P. Hou, Z. Feng, and W. Song (2012), Effects of elevated O3 concentration on winter wheat and rice yields in the Yangtze River Delta, China, Environmental pollution, 171, 118-125.

Wang, Y., J. H. Jiang, and H. Su (2015), Atmospheric responses to the redistribution of anthropogenic aerosols, Journal of Geophysical Research: Atmospheres, 120(18), 9625-9641.

Wentz, F. J., L. Ricciardulli, K. Hilburn, and C. Mears (2007), How much more rain will global warming bring?, Science, 317(5835), 233-235.

Wernberg, T., D. A. Smale, F. Tuya, M. S. Thomsen, T. J. Langlois, T. De Bettignies, S. Bennett, and C. S. Rousseaux (2013), An extreme climatic event alters marine ecosystem structure in a global biodiversity hotspot, Nature Climate Change, 3(1), 78-82.

Westervelt, D., L. Horowitz, V. Naik, J.-C. Golaz, and D. Mauzerall (2015), Radiative forcing and climate response to projected 21st century aerosol decreases, Atmospheric Chemistry and Physics, 15(22), 12681-12703.

Westra, S., L. V. Alexander, and F. W. Zwiers (2013), Global increasing trends in annual maximum daily precipitation, Journal of Climate, 26(11), 3904-3918.

Whitby, E. R., P. McMurry, U. Shankar, and F. Binkowski (1991), Modal aerosol dynamics modeling*Rep.*, Computer Sciences Corp., Research Triangle Park, NC (USA).

WHO (2018), Global health estimates 2016: deaths by cause, age, sex, by country and by region, 2000–2016, Geneva: World Health Organization.

Wilcox, L., E. Highwood, B. Booth, and K. Carslaw (2015), Quantifying sources of inter‐model diversity in the cloud albedo effect, Geophysical Research Letters, 42(5), 1568-1575.

Wilcox, L., N. Dunstone, A. Lewinschal, M. Bollasina, A. Ekman, and E. Highwood (2018), Mechanisms for a remote response to Asian aerosol emissions in boreal winter, Atmospheric Chemistry and Physics Discussions.

Wilcox, L. J., E. J. Highwood, and N. J. Dunstone (2013), The influence of anthropogenic aerosol on multi-decadal variations of historical global climate, Environmental Research Letters, 8(2), 024033.

Williams, R. G., P. Goodwin, V. M. Roussenov, and L. Bopp (2016), A framework to understand the transient climate response to emissions, Environmental Research Letters, 11(1), 015003.

Wilmouth, D. M., R. J. Salawitch, and T. P. Canty (2017), Stratospheric Ozone Depletion and Recovery, in Green Chemistry, edited, pp. 177-209, Elsevier.

Wiscombe, W. J. (1979), Mie scattering calculations: Advances in technique and fast, vector-speed computer codes, National Technical Information Service, US Department of Commerce.

Wobus, C., M. Flanner, M. C. Sarofim, M. C. P. Moura, and S. J. Smith (2016), Future Arctic temperature change resulting from a range of aerosol emissions scenarios, Earth's Future.

World Energy Council (2016), World energy resources 2016, World Energy Council, London, UK.

Wu, Y., and L. M. Polvani (2017), Recent trends in extreme precipitation and temperature over southeastern South America: The dominant role of stratospheric ozone depletion in the CESM Large Ensemble, Journal of Climate, 30(16), 6433-6441.

Wu, Y., T. Cheng, L. Zheng, and H. Chen (2016), Black carbon radiative forcing at TOA decreased during aging, Scientific reports, 6, 38592.

Xie, B., H. Zhang, Z. Wang, S. Zhao, and Q. Fu (2016), A modeling study of effective radiative forcing and climate response due to tropospheric ozone, Advances in Atmospheric Sciences, 33(7), 819-828.

Xie, S.-P., B. Lu, and B. Xiang (2013), Similar spatial patterns of climate responses to aerosol and greenhouse gas changes, Nature Geoscience, 6(10), 828-832.

Xu, Y., and S.-P. Xie (2015), Ocean mediation of tropospheric response to reflecting and absorbing aerosols, Atmospheric Chemistry and Physics, 15(10), 5827-5833.

Xu, Y., J.-F. Lamarque, and B. M. Sanderson (2015), The importance of aerosol scenarios in projections of future heat extremes, Climatic Change, 1-14.

Xu, Z., G. FitzGerald, Y. Guo, B. Jalaludin, and S. Tong (2016), Impact of heatwave on mortality under different heatwave definitions: a systematic review and meta-analysis, Environment international, 89, 193-203.

Yang, H., and J. Zhu (2011), Equilibrium thermal response timescale of global oceans, Geophysical Research Letters, 38(14).

Yatagai, A., K. Kamiguchi, O. Arakawa, A. Hamada, N. Yasutomi, and A. Kitoh (2012), APHRODITE: Constructing a long-term daily gridded precipitation dataset for Asia based on a dense network of rain gauges, Bulletin of the American Meteorological Society, 93(9), 1401-1415.

Yihui, D., and J. C. Chan (2005), The East Asian summer monsoon: an overview, Meteorology and Atmospheric Physics, 89(1-4), 117-142.

Yoshimori, M., M. Watanabe, H. Shiogama, A. Oka, A. Abe-Ouchi, R. Ohgaito, and Y. Kamae (2016), A review of progress towards understanding the transient global mean surface temperature response to radiative perturbation, Progress in Earth and Planetary Science, 3(1), 21.

Young, P., A. Archibald, K. Bowman, J.-F. Lamarque, V. Naik, D. Stevenson, S. Tilmes, A. Voulgarakis, O. Wild, and D. Bergmann (2013), Pre-industrial to end 21st century projections of tropospheric ozone from the Atmospheric Chemistry and Climate Model Intercomparison Project (ACCMIP), Atmospheric Chemistry and Physics, 13(4), 2063-2090.

Yu, P., O. B. Toon, C. G. Bardeen, M. J. Mills, T. Fan, J. M. English, and R. R. Neely (2015), Evaluations of tropospheric aerosol properties simulated by the community earth system model with a sectional aerosol microphysics scheme, Journal of advances in modeling earth systems, 7(2), 865-914.

Yu, R., J. Li, W. Yuan, and H. Chen (2010), Changes in characteristics of late-summer precipitation over eastern China in the past 40 years revealed by hourly precipitation data, Journal of Climate, 23(12), 3390-3396.

Yu, S., K. Alapaty, R. Mathur, J. Pleim, Y. Zhang, C. Nolte, B. Eder, K. Foley, and T. Nagashima (2014), Attribution of the United States “warming hole”: Aerosol indirect effect and precipitable water vapor, Scientific reports, 4, 6929.

Zhai, P., X. Zhang, H. Wan, and X. Pan (2005), Trends in total precipitation and frequency of daily precipitation extremes over China, Journal of climate, 18(7), 1096-1108.

Zhang, L., S. Gong, J. Padro, and L. Barrie (2001), A size-segregated particle dry deposition scheme for an atmospheric aerosol module, Atmospheric Environment, 35(3), 549-560.

Zhang, X., H. Wan, F. W. Zwiers, G. C. Hegerl, and S. K. Min (2013), Attributing intensification of precipitation extremes to human influence, Geophysical Research Letters, 40(19), 5252-5257.

Zhang, X., L. Alexander, G. C. Hegerl, P. Jones, A. K. Tank, T. C. Peterson, B. Trewin, and F. W. Zwiers (2011), Indices for monitoring changes in

extremes based on daily temperature and precipitation data, Wiley Interdisciplinary Reviews: Climate Change, 2(6), 851-870.

Zhang, Y., O. R. Cooper, A. Gaudel, A. M. Thompson, P. Nédélec, S.-Y. Ogino, and J. J. West (2016), Tropospheric ozone change from 1980 to 2010 dominated by equatorward redistribution of emissions, Nature Geoscience, 9(12), 875.

Zhang, Y., J. J. West, R. Mathur, J. Xing, C. Hogrefe, S. J. Roselle, J. O. Bash, J. E. Pleim, C.-M. Gan, and D. C. Wong (2018), Long-term trends in the ambient PM 2.5-and O 3-related mortality burdens in the United States under emission reductions from 1990 to 2010, Atmospheric Chemistry and Physics, 18(20), 15003-15016.

Zheng, B., D. Tong, M. Li, F. Liu, C. Hong, G. Geng, H. Li, X. Li, L. Peng, and J. Qi (2018), Trends in China's anthropogenic emissions since 2010 as the consequence of clean air actions, Atmospheric Chemistry and Physics, 18(19), 14095-14111.

Zhou, B., Q. H. Wen, Y. Xu, L. Song, and X. Zhang (2014), Projected changes in temperature and precipitation extremes in China by the CMIP5 multimodel ensembles, Journal of Climate, 27(17), 6591-6611.

Zhou, C., and J. E. Penner (2017), Why do general circulation models overestimate the aerosol cloud lifetime effect? A case study comparing CAM5 and a CRM, Atmospheric Chemistry and Physics, 17(1), 21-29.

Zhou, T., D. Gong, J. Li, and B. Li (2009), Detecting and understanding the multi-decadal variability of the East Asian Summer Monsoon–Recent progress and state of affairs, Meteorologische Zeitschrift, 18(4), 455-467.

Zhou, X., and M. F. Khairoutdinov (2017), Changes in temperature and precipitation extremes in superparameterized CAM in response to warmer SSTs, Journal of Climate, 30(24), 9827-9845.